OXIDATIVE STRESS IN MYOCARDIAL AND NEURAL REMODELING

EDITED BY: Thao P. Nguyen, Mansoureh Eghbali and Sally Ann Frautschy
PUBLISHED IN: Frontiers in Physiology

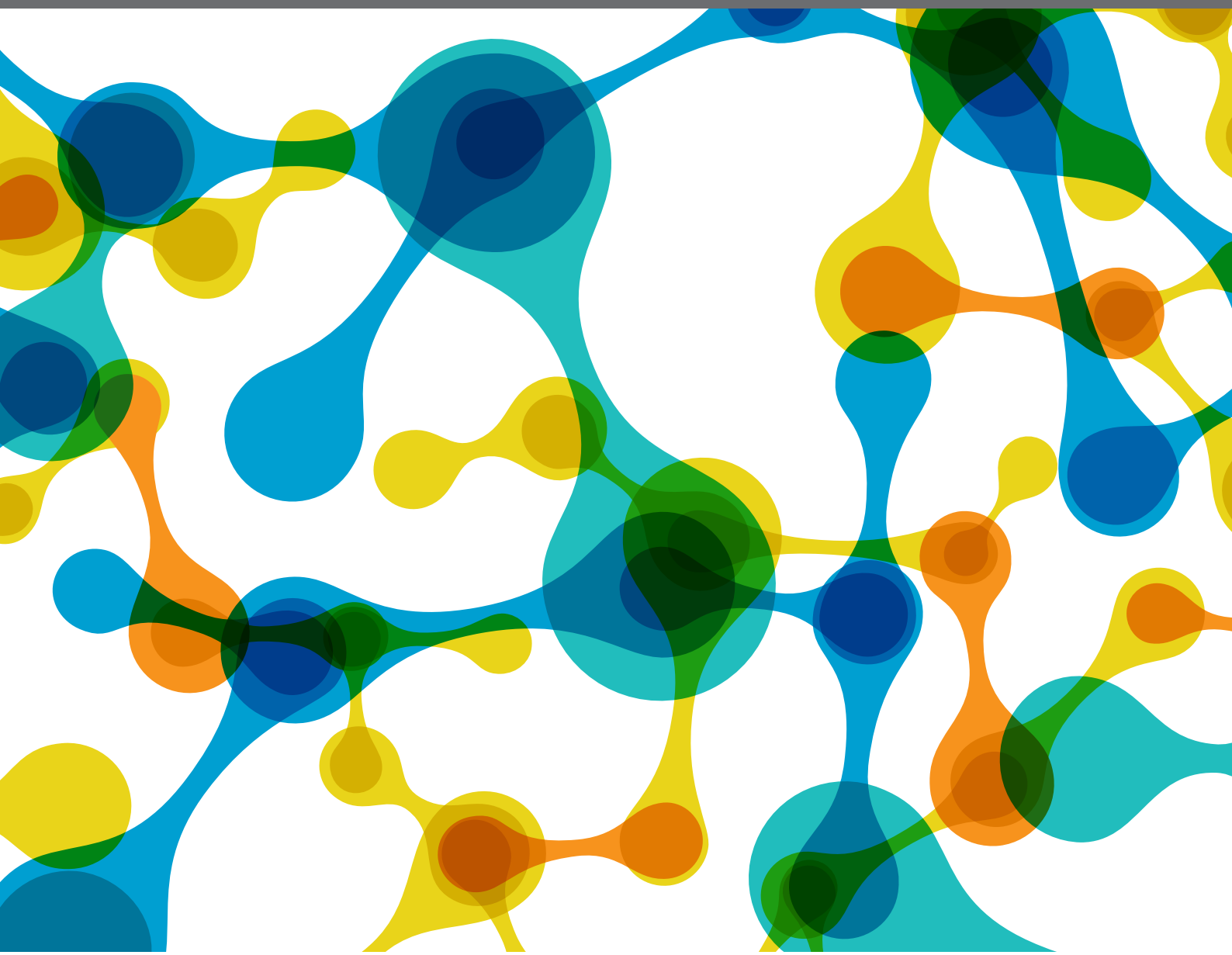

frontiers Research Topics

frontiers

ISSN 1664-8714
ISBN 978-2-88966-657-7
DOI 10.3389/978-2-88966-657-7

About Frontiers

Frontiers is more than just an open-access publisher of scholarly articles: it is a pioneering approach to the world of academia, radically improving the way scholarly research is managed. The grand vision of Frontiers is a world where all people have an equal opportunity to seek, share and generate knowledge. Frontiers provides immediate and permanent online open access to all its publications, but this alone is not enough to realize our grand goals.

Frontiers Journal Series

The Frontiers Journal Series is a multi-tier and interdisciplinary set of open-access, online journals, promising a paradigm shift from the current review, selection and dissemination processes in academic publishing. All Frontiers journals are driven by researchers for researchers; therefore, they constitute a service to the scholarly community. At the same time, the Frontiers Journal Series operates on a revolutionary invention, the tiered publishing system, initially addressing specific communities of scholars, and gradually climbing up to broader public understanding, thus serving the interests of the lay society, too.

Dedication to Quality

Each Frontiers article is a landmark of the highest quality, thanks to genuinely collaborative interactions between authors and review editors, who include some of the world's best academicians. Research must be certified by peers before entering a stream of knowledge that may eventually reach the public - and shape society; therefore, Frontiers only applies the most rigorous and unbiased reviews.
Frontiers revolutionizes research publishing by freely delivering the most outstanding research, evaluated with no bias from both the academic and social point of view. By applying the most advanced information technologies, Frontiers is catapulting scholarly publishing into a new generation.

What are Frontiers Research Topics?

Frontiers Research Topics are very popular trademarks of the Frontiers Journals Series: they are collections of at least ten articles, all centered on a particular subject. With their unique mix of varied contributions from Original Research to Review Articles, Frontiers Research Topics unify the most influential researchers, the latest key findings and historical advances in a hot research area! Find out more on how to host your own Frontiers Research Topic or contribute to one as an author by contacting the Frontiers Editorial Office: frontiersin.org/about/contact

OXIDATIVE STRESS IN MYOCARDIAL AND NEURAL REMODELING

Topic Editors:
Thao P. Nguyen, UCLA David Geffen School of Medicine, United States
Mansoureh Eghbali, University of California, Los Angeles, United States
Sally Ann Frautschy, University of California, Los Angeles, United States

Citation: Nguyen, T. P., Eghbali, M., Frautschy, S. A., eds. (2021). Oxidative Stress in Myocardial and Neural Remodeling. Lausanne: Frontiers Media SA.
doi: 10.3389/978-2-88966-657-7

Table of Contents

frontiers in Physiology

EDITORIAL
published: 05 February 2021
doi: 10.3389/fphys.2021.606484

Editorial: Oxidative Stress in Myocardial and Neural Remodeling

Thao P. Nguyen[1]*, *Sally A. Frautschy*[2] *and Mansoureh Eghbali*[3]

[1] The Cardiovascular Research Laboratory, Division of Cardiology, Department of Medicine, David Geffen School of Medicine at UCLA, Los Angeles, CA, United States, [2] Department of Neurology, David Geffen School of Medicine at UCLA, Los Angeles, CA, United States, [3] Department of Anesthesiology and Perioperative Medicine, David Geffen School of Medicine at UCLA, Los Angeles, CA, United States

Keywords: oxidative stress, reactive oxygen species, inflammation, structural remodeling, electrical remodeling, cardiac fibrosis, neurodegeneration, Alzheimer's disease

Editorial on the Research Topic

Oxidative Stress in Myocardial and Neural Remodeling

Endogenous oxidative stress arises as an attempted reparative response to injuries, including hypoxia, myocardial infarction, stroke, and radiation-induced phototoxicity. More clinically relevant than ever, oxidative stress has recently been implicated as the key player in the induction of severe acute inflammatory critical illness by the coronavirus SARS-CoV-2 (Delgado-Roche and Mesta, 2020; Wang et al., 2020), the pathogen responsible for the ongoing devastating Covid-19 global pandemic. Oxidative stress occurs when cellular generation of free radicals (reactive oxygen or nitrogen species) overwhelms cellular defense mechanisms. Although oxidative stress serves to rapidly galvanize the immune system into action, direct consequences range from lipid peroxidation, DNA damage, protein misfolding, and mitochondrial dysfunction to inflammation, structural/functional remodeling, and ultimately necrosis. The Research Topic "*Oxidative Stress in Myocardial and Neural Remodeling*" evaluates the damage of oxidative stress specifically to the cardiovascular and nervous systems, defines underlying mechanisms, and proposes novel therapeutic targets.

Starting with the heart, two reviews shed light on the cardiac-chamber specificity in oxidative stress response. Schlüter et al. review evidence that the mitochondrial defense against reactive oxygen species is lower in the right compared with left ventricle. This divergent ventricular response to oxidative stress likely accounts at least in part for the poorer ability of the right ventricle to manage the oxidative stress of pulmonary hypertension (Schlüter et al.). Indeed, in pulmonary hypertension, right ventricular function is the major determinant of survival. Mikhael et al. review evidence that in chronic pulmonary hypertension, oxidative stress induces structural remodeling of not only the pulmonary vasculature but also the right ventricle, eventually causing right heart failure. They discuss why the preclinical success of antioxidant therapies fails to translate clinically (Mikhael et al.).

Delving deeper into the mechanisms of structural remodeling by oxidative stress, Li et al. delineate a molecular pathway linking oxidative stress, diet, and inflammation with myocardial fibrosis and identify a novel potential target for antifibrotic therapy. Using mouse models of doxorubicin-induced cardiomyopathy, they demonstrate how trimethylamine N-oxide (TMAO), a gut microbiota-dependent metabolite of specific dietary nutrients, can aggravate myocardial fibrosis through activation of the Nucleotide-binding oligomerization domain (NOD)-like receptor protein 3 (NLRP3) inflammasome (Li et al.).

OPEN ACCESS

Edited by:
Mohsin Khan,
Temple University, United States

Reviewed by:
Shirin Doroudgar,
Heidelberg University Hospital, Germany

***Correspondence:**
Thao P. Nguyen
tpnguyen@mednet.ucla.edu

Specialty section:
This article was submitted to Oxidant Physiology, a section of the journal Frontiers in Physiology

Received: *15 September 2020*
Accepted: *13 January 2021*
Published: *05 February 2021*

Citation:
Nguyen TP, Frautschy SA and Eghbali M (2021) Editorial: Oxidative Stress in Myocardial and Neural Remodeling. Front. Physiol. 12:606484. doi: 10.3389/fphys.2021.606484

Zhao et al., on the other hand, investigated the mechanistic role of oxidative stress in electrical remodeling, particularly during synergy with existing structural and electrical remodeling by noncardiomyocytes, including myofibroblasts (Zhao et al.). Using a novel *in-vitro* two-dimensional model of interface between cardiomyocytes and noncardiomyocytes that they developed, the authors demonstrated a functional proof-of-concept for the contribution of oxidative stress to the dual protective and proarrhythmic roles of myofibroblasts and other noncardiomyocytes. Not only connexin43-rich noncardiomyocytes can enable passive, decremental, anisotropic impulse propagation, but they can also, independently or synergistically with oxidative stress, induce new arrhythmia triggers, dynamic functional conduction block, non-reentrant and reentrant arrhythmias.

The next three articles examine how oxidative stress causes adverse structural remodeling in both the cardiac and central nervous systems concomitantly. Carbone et al. emphasize the critical role of neutrophils in cardiac and neural remodeling mediated by the oxidative stress of ischemia-reperfusion injury as neutrophils are activated early for massive production of reactive oxygen species. The authors discuss how anatomical and functional differences between these two organs shape their responses to oxidative stress and suggest that attention to these differences may improve translational success of preclinical trials (Carbone et al.). Supporting Carbone et al.'s conclusion, Vaillancourt et al. demonstrate that the activities of reactive oxygen and nitrogen species may extend beyond local tissues. They discover how oxidative stress in pulmonary hypertensive rats induces neuroinflammation remotely in the thoracic spinal cord (Vaillancourt et al.). Denver et al., on the other hand, explore the mechanistic synergism between coexisting oxidative stress in heart and brain and the resultant clinical manifestations. Based on the insight that the central nervous system vasculature is particularly vulnerable to oxidative stress (Bennett et al., 2009; He et al., 2020), the authors develop a novel, ingenious rat model of human mixed vascular dementia by compounding the oxidative stress induced by the transgene of Alzheimer's disease with that induced by the phenotype of chronic hypertension. They discover that hypertension exacerbates the neuroinflammation of Alzheimer's dementia, leading to new fibrotic remodeling and ensuing pathology for the brain vasculature (Denver et al.).

Exploring yet another vasculature system, Ishiyama et al. discover that in Ménière's disease, endogenous oxidative stress primarily targets the vascular endothelial cells of the blood labyrinthine barrier for structural remodeling. The inflammation triggered by oxidative stress causes pericytes to degenerate and migrate, thereby compromising the structural integrity of the blood labyrinthine barrier and its critical function in ionic and fluid homeostasis (Ishiyama et al.).

Moving from pathophysiology to therapeutics, Deres et al. conduct a test of the efficacy and safety of a novel anti-inflammatory drug, bradykinin B1 receptor antagonist FGY-1153 in spontaneously hypertensive rats. The authors conclude that this novel agent provides moderate protection against the development of hypertensive cardiomyopathy and has no cardiovascular toxicities (Deres et al.). However, additional randomized preclinical and clinical trials are necessary to confirm these promising findings regarding the efficacy and safety profile of FGY-1153.

Taken together, the collection of original research and review articles presented in this Research Topic provides an overview and update of insights into the critical role of oxidative stress on myocardial and neural remodeling. We hope that this collective knowledge would inspire and drive further research for innovative and effective anti-oxidative therapeutic strategies to reduce the burden of morbidity and disability due to oxidative stress.

AUTHOR CONTRIBUTIONS

TN conceptualized this Research Topic, recruited co-editors, and wrote the original draft. All authors contributed to manuscript revision, approved the submitted version, and agreed to be accountable for all aspects of the work.

FUNDING

This work was supported by the National Institutes of Health R01HL141452 (to TN), R01AG066212 (to SF), R01HL131182 (to ME), and the Veterans Affairs Merit 1I01BX005276 (to SF).

ACKNOWLEDGMENTS

The editors thank all authors and reviewers for their invaluable contributions to this *Frontiers in Physiology* Research Topic.

REFERENCES

Bennett, S., Grant, M. M., and Aldred, S. (2009). Oxidative stress in vascular dementia and Alzheimer's disease: a common pathology. *J. Alzheimers. Dis.* 17, 245–257. doi: 10.3233/JAD-2009-1041

Delgado-Roche, L., and Mesta, F. (2020). Oxidative stress as key player in severe acute respiratory syndrome coronavirus (SARS-CoV) infection. *Arch. Med. Res.* 51, 384–387. doi: 10.1016/j.arcmed.2020.04.019

He, J. T., Zhao, X., Xu, L., and Mao, C. Y. (2020). Vascular risk factors and Alzheimer's disease: blood-brain barrier disruption, metabolic syndromes, and molecular links. *J. Alzheimers. Dis.* 73, 39–58. doi: 10.3233/JAD-190764

Wang, J. Z., Zhang, R. Y., and Bai, J. (2020). An anti-oxidative therapy for ameliorating cardiac injuries of critically ill COVID-19-infected patients. *Int. J. Cardiol.* 312, 137–138. doi: 10.1016/j.ijcard.2020.04.009

Conflict of Interest: The authors declare that the research was conducted in the absence of any commercial or financial relationships that could be construed as a potential conflict of interest.

frontiers in Physiology

ORIGINAL RESEARCH
published: 03 September 2018
doi: 10.3389/fphys.2018.01068

Oxidative Stress in the Blood Labyrinthine Barrier in the Macula Utricle of Meniere's Disease Patients

Gail Ishiyama[1], Jacob Wester[2], Ivan A. Lopez[2], Luis Beltran-Parrazal[2,3] and Akira Ishiyama[2]*

[1] Department of Neurology, David Geffen School of Medicine at UCLA, Los Angeles, CA, United States, [2] Department of Head and Neck Surgery, David Geffen School of Medicine at UCLA, Los Angeles, CA, United States, [3] Centro de Investigaciones Cerebrales, Universidad Veracruzana, Xalapa, Mexico

The blood labyrinthine barrier (BLB) is critical in the maintenance of inner ear ionic and fluid homeostasis. Recent studies using imaging and histopathology demonstrate loss of integrity of the BLB in the affected inner ear of Meniere's disease (MD) patients. We hypothesized that oxidative stress is involved in the pathogenesis of BLB degeneration, and to date there are no studies of oxidative stress proteins in the human BLB. We investigated the ultrastructural and immunohistochemical changes of the BLB in the vestibular endorgan, the macula utricle, from patients with MD (n = 10), acoustic neuroma (AN) (n = 6) and normative autopsy specimens (n = 3) with no inner ear disease. Each subject had a well-documented clinical history and audiovestibular testing. Utricular maculae were studied using light and transmission electron microscopy and double labeling immunofluorescence. Vascular endothelial cells (VECs) were identified using isolectin B4 (IB4) and glucose-transporter-1 (GLUT-1). Pericytes were identified using alpha smooth muscle actin (αSMA) and phalloidin. IB4 staining of VECS was consistently seen in both AN and normative. In contrast, IB4 was nearly undetectable in all MD specimens, consistent with the significant VEC damage confirmed on transmission electron microscopy. GLUT-1 was present in MD, AN, and normative. αSMA and phalloidin were expressed consistently in the BLB pericytes in normative, AN specimen, and Meniere's specimens. Endothelial nitric oxide synthase (eNOS), inducible nitric oxide synthase (iNOS), and nitrotyrosine were used as markers of oxidative stress. The VECs of the BLB in Meniere's had significantly higher levels of expression of iNOS and nitrotyrosine compared with normative and AN specimen. eNOS-IF staining showed similar patterns in normative and Meniere's specimens. Microarray-based gene expression profiling confirmed upregulation of iNOS mRNA from the macula utricle of Meniere's patients compared with AN. Nitrotyrosine, a marker recognized as a hallmark of inflammation, especially when seen in association with an upregulation of iNOS, was detected in the epithelial and stromal cells in addition to VECs in MD. Immunohistochemical and ultrastructural degenerative changes of the VEC suggest that these cells are the primary targets of oxidative stress, and pericyte

OPEN ACCESS

Edited by:
Thao P. Nguyen, David Geffen School of Medicine at UCLA, United States

Reviewed by:
Yong Tang, Chongqing Medical University, China
Enrique Soto, Benemérita Universidad Autónoma de Puebla, Mexico

****Correspondence:***
Gail Ishiyama
gishiyama@mednet.ucla.edu

Specialty section:
This article was submitted to Oxidant Physiology, a section of the journal Frontiers in Physiology

Received: *11 April 2018*
Accepted: *17 July 2018*
Published: *03 September 2018*

Citation:
Ishiyama G, Wester J, Lopez IA, Beltran-Parrazal L and Ishiyama A (2018) Oxidative Stress in the Blood Labyrinthine Barrier in the Macula Utricle of Meniere's Disease Patients. Front. Physiol. 9:1068. doi: 10.3389/fphys.2018.01068

pathology including degeneration and migration, likely also plays a role in the loss of integrity of the BLB and triggering of inflammatory pathways in MD. These studies advance our scientific understanding of oxidative stress in the human inner ear BLB and otopathology.

Keywords: Meniere's disease, oxidative stress, blood labyrinthine barrier, nitrotyrosine, iNOS, pericyte migration, inflammation, vestibular

INTRODUCTION

In the cardiovascular, retinal, cerebrovascular and inner ear systems, homeostasis is dependent on the integrity of the selective barrier of the microvasculature. In the auditory and vestibular system, a physical and chemical barrier, the BLB tightly controls the passage of fluids, molecules, and ions to maintain a proper environment for the cellular components and a proper ionic composition of the endolymph and perilymph, while preventing the entry of deleterious substances from the vasculature to the inner ear fluid spaces (Juhn et al., 1981, 2001). Recent studies have implicated the loss of the integrity of the BLB in diverse inner ear pathologies including acoustic trauma, autoimmune inner ear disease, presbycusis, and most recently in MD (Ishiyama et al., 2017). The BLB plays a critical role in ionic transport and the maintenance of the highly differing composition of the endolymph and the perilymph. It is believed that the BLB of the inner ear is a key player in maintaining the delicate fluid balance of the inner ear. Therefore, a disease which presents nearly universally with an excess of inner ear fluid, i.e., hydrops of the endolymphatic fluid space, may be due in part to loss of BLB integrity.

Meniere's disease is a disabling inner ear syndrome characterized by fluctuating hearing loss, recurrent episodic vertigo, aural fullness, and tinnitus with almost one-third of these patients completely disabled due to the disease and 7% of these patients suffer sudden falls, called otolithic crisis or drop attacks believed to originate from the vestibular otolithic organs, the utricle or saccule (Baloh, 2001; Ishiyama et al., 2001; Calzada et al., 2012b). Endolymphatic hydrops, a ballooning of the endolymphatic fluid space within the inner ear, is the most prominent and consistent histopathological correlate of MD, being first described in postmortem temporal bone histopathology (Hallpike and Cairns, 1938; Yamakawa, 1938). While endolymphatic hydrops is demonstrated in nearly all cases of MD (Schuknecht, 1993; Wackym, 1995) and endolymphatic hydrops can be produced in animal models (Takumida et al., 2008), researchers have been unable to replicate the spells of vertigo and hearing loss in animal models. Endolymphatic sac surgery is still practiced, however, archival human temporal bone studies and MRI imaging studies demonstrate that MD patients often have persistent hydrops on histopathology following endolymphatic sac surgery (Chung et al., 2011; Liu et al., 2016). There is growing evidence that the longitudinal flow of endolymph hypothesis of Meniere's pathophysiology needs to be reevaluated (Ishiyama et al., 2015).

We hypothesized that the pathophysiology of MD involves dysfunction of the BLB, initially noted in gadolinium-based magnetic resonance imaging (MRI) studies that enable the visualization of endolymphatic hydrops in patients. Multiple studies have demonstrated a correlation between MD and endolymphatic hydrops, audiovestibular function, and symptom severity (Zou et al., 2005; Barath et al., 2014; Naganawa and Nakashima, 2014; Sepahdari et al., 2015). In these MRI studies, MD is associated with an increased contrast enhancement in the perilymph of the affected ear (Tagaya et al., 2011; Yamazaki et al., 2012; Barath et al., 2014; Pakdaman et al., 2016; Sepahdari et al., 2016). Intravenous gadolinium is taken up into the perilymph via perfusion through the BLB, specifically the blood perilymph barrier. In the perilymph of the ipsilateral affected inner ear, increased gadolinium uptake has been reported, and this phenomenon likely reflects loss of BLB integrity in multiple otopathologies including infection, trauma, and sudden hearing loss. In our recent study comparing MD with sudden sensorineural hearing loss, the symptomatic Meniere's inner ear exhibits highly significantly increased contrast enhancement of the perilymph, consistent with a breakdown of the BLB, to a much higher degree than that noted in sudden sensorineural hearing loss (Pakdaman et al., 2016). Injection of intratympanic lipopolysaccharide (LPS), an inflammatory protein, is associated with an increased entry of serum fluorescein into the perilymph and causes ipsilateral increased gadolinium enhancement on MRI studies (Hirose et al., 2014; LeFloc'h et al., 2014), similar to the MRI findings in MD patients. Of note, the mechanism by which LPS induces increased vascular permeability may be through activation of iNOS in the inner ear (Takumida and Anniko, 1998a). While these findings are suggestive of increased permeability of the BLB in the affected inner ear of patients with MD, studies of the human inner ear microvasculature were needed to characterize in more detail the pathological process within the BLB in MD.

Despite more than a century of research since the original publication by Prosper Meniere in Ménière's, 1861, the etiology of endolymphatic hydrops and its relationship with the disabling Meniere's attacks of vertigo and hearing loss remain unknown. Our previous histopathological studies revealed neuroepithelial damage with hair cell loss, stromal edema, and subepithelial basement membrane pathology in intractable MD (McCall et al., 2009; Ishiyama et al., 2017) with questions remaining as to the cause of the neuroepithelial, stromal, and microvasculature damage. It has been shown that ischemic damage to the cochlea

Abbreviations: Alpha SMA, alpha smooth muscle actin; BBB, blood–brain barrier; BLB, blood labyrinthine barrier; eNOS, endothelial nitric oxide synthase; GLUT 1, glucose transporter 1; IB4, isolectin B4; iNOS, inducible nitric oxide synthase; MD, Meniere's disease; NTIF, nitrotyrosine immunofluorescence; ROS, reactive oxygen species; VEC, vascular endothelial cell.

triggers nitric oxide production via iNOS, and is associated with increased NO metabolites within the perilymph system (Morizane et al., 2005). We proposed that oxidative stress mediated the damage to the vestibular endorgan and the BLB in MD.

Nitric oxide is likely critical in inner ear health but may also play a role in damage and oxidative damage, and is proposed to mediate neurodegenerative changes in aging (Kregel and Zhang, 2007). Nitric oxide (NO) is an endogenous neurotransmitter in the inner ear, controlling vasodilation in response to energy needs. Round window application of NO donors increases cochlear and vestibular blood flow (Arenberg et al., 1997) and intravenous infusion of NO synthase inhibitor, *N*-nitro-L-arginine-methyl ester (L-NAME) is associated with a dose-dependent decrease in cochlear vascular conductance in one study (Hoshijima et al., 2002). The constitutive nitric oxide synthase (NOS), eNOS, is ubiquitously present in the vestibular ganglion cells, nerve fibers, cytoplasm of types I and II sensory cells, nerve fibers, dark cells, transitional cells, and subepithelial microvasculature (Takumida and Anniko, 1998b; Shi and Nuttall, 2002). The presence of the inducible NOS (iNOS) is purported to be pathological and is associated with high levels of NO (Takumida and Anniko, 1998b). When NO is produced in large amounts, or in the presence of oxidative reactants, the excess NO may be associated with oxidative stress damage through the production of peroxynitrate.

To date, there are no prior studies of oxidative stress proteins in the human inner ear capillaries of the BLB, and one prior study of the NOS in the human cochlea (Popa et al., 2001). We hypothesize that MD is associated with oxidative stress markers in the BLB cellular components, inducing damage of the BLB, causing increased permeability which allows for extravasation of fluids and proteins, damaging the extracellular matrix and perivascular basement membranes.

In the present study, we investigate the ultrastructural histopathology of the BLB in MD, identified the cellular components of the BLB, presented evidence for cytochemical changes and the possible role of oxidative stress markers in BLB breakdown. Electron microscopy demonstrated endothelial damage and pericyte migration in the BLB of MD. Using immunofluorescence markers and mRNA array, we detected upregulation of iNOS and normal levels of eNOS in the macula utricle from patients diagnosed with MD. Moreover, we detected NTIF within the microvasculature of the BLB and within the epithelial and stromal cells of Meniere's specimens. The presence of nitrotyrosine in the context of overexpression of iNOS suggests that the cellular damage is mediated by oxidative stress to the vestibular organ in MD.

MATERIALS AND METHODS

Specimens (Table 1)

The Institutional Review Board (IRB) of UCLA approved this study (IRB protocol #10-001449). All methods used in this study were in accordance with NIH and IRB guidelines and regulations. Appropriate informed consent was obtained from each patient before inclusion in the study. Postmortem microdissected human vestibular endorgans were used in the present study. The temporal bone donors were part of a National Institute of Health (NIH) funded National Temporal Bone Laboratory at UCLA through the National Institute on Deafness and Other Communication Disorders (NIDCD). The medical history for each of the patients who had donated the temporal bones was maintained and preserved in a secured electronic database. A subset of specimens embedded in resin had been obtained from patients diagnosed with MD or postmortem normative from a previous study (Ishiyama et al., 2017).

TABLE 1 | Specimens used in this study.

Specimen	Source	Diagnosis	Use	Figure/Table
1	S	AN	IF, TEM, LM	**Figures 2A,B**
2	S	AN	IF, TEM, LM	**Figures 4C**, **7A**
3	S	AN	IF, TEM, LM	**Figures 6A**, **8A,A1**
4	S	AN	RT2-PCR	**Table 3**
5	S	AN	RT2-PCR	**Table 3**
6	S	AN	RT2-PCR	**Table 3**
7	S	MD	IF, TEM, LM	**Figure 1B**
8	S	MD	IF, TEM, LM	**Figure 1C**
9	S	MD	IF, TEM, LM	**Figures 3A–C**, **4B**
10	S	MD	IF, TEM, LM	**Figures 4D**, **5B**
11	S	MD	IF, TEM, LM	**Figures 5C**, **6B**
12	S	MD	IF, TEM	**Figures 5D**, **7B**
13	S	MD	IF, TEM	**Figures 6C**, **8B,B1**
14	S	MD	RT2-PCR	**Table 3**
15	S	MD	RT2-PCR	**Table 3**
16	S	MD	RT2-PCR	**Table 3**
17	A	Normal	IF, TEM, LM	**Figure 1A**
18	A	Normal	IF, TEM	**Figure 4A**
19	A	Normal	IF, TEM	**Figure 5A**

S, surgical; A, autopsy; AN, acoustic neuroma; MD, Meniere's disease; IF, Immunofluorescence; TEM, transmission electron microscopy; LM, light microscopy; RT2-PCR reverse transcriptase, polymerase chain reaction.

Specimen Collection and Processing

Vestibular endorgans (macula utricle) were acquired at surgery from patients who required transmastoid labyrinthectomy for intractable vertigo and/or Tumarkin falls or from patients who required a translabyrinthine approach for acoustic neuroma resection (surgical controls). Microdissected vestibular endorgans obtained at postmortem temporal bone autopsy also served as normative controls.

Inclusion and Exclusion Criteria

All subjects with MD had stage IV definite intractable MD with profound non-serviceable hearing loss. Subjects met the classification of definite MD in accordance with the presenting symptoms determined by the American Academy of Otolaryngology-Head and Neck Surgery (Committee on Hearing and Equilibrium, 1995) and the Classification Committee of the Barany Society (Lopez-Escamez et al., 2015). Patients who had previously undergone intratympanic gentamicin or endolymphatic shunt surgery were excluded. Unless there was

a contraindication to MRI or contrast agent, all subjects had confirmation of unilateral endolymphatic hydrops in the inner ear ipsilateral to the profound hearing loss.

Light and Transmission Electron Microscopy

Specimens were processed as described in Ishiyama et al. (2017). Briefly, for light microscopy and transmission electron microscope (TEM): Microdissected vestibular endorgans were fixed in paraformaldehyde with glutaraldehyde. Specimen collection and processing: the vestibular endorgan, the maculae utricle, obtained during transmastoid labyrinthectomy, were placed immediately in 10% buffered formalin and transported to the laboratory for post-fixation. For this study, the macula utricle was cut approximately into two halves under the dissecting microscope using micro-scissors. One half was processed for immunofluorescence and the other half was processed for light transmission electron microscopy observations.

Tissue Processing for Immunofluorescence

Specimens were processed as described in Lopez et al. (2016). Briefly, for immunofluorescence staining one half was fixed by immersion in 10% formalin for 4 h, thereafter washed in phosphate buffered saline solution (PBS, 0.1 M, pH 7.4) for 15 min × 3 min. Tissue was then immersed in 30% sucrose diluted in PBS for 48 h. Twenty-micron thick cryostat sections were obtained using a Leica cryostat (CM1850) and mounted in Super frost plus slides (Fisher Scientific). Sections were allowed to dry at room temperature for 4 h and then stored in an ultralow refrigerator until use.

Immunofluorescence Staining

After removal from the freezer, cryostat sections of the macula utricle were incubated at room temperature for 1 h with a blocking solution containing 1% bovine serum albumin (Faction V, Sigma), Triton X-100 (0.1%) diluted in PBS. All primary antibodies used in this study were diluted in the blocking solution as described in **Table 2**. The tissue sections were then incubated in a humidity chamber at room temperature for 16 h, washed three times for 10 min in PBS. The secondary antibody mixture was prepared using horse anti-rabbit (Alexa 488) and horse anti-mouse (Alexa 488) diluted in PBS. The antibody mixture was applied to the utricle sections for 1 h before removal. Thereafter, tissue sections were washed three times for 5 min each using PBS and then mounted with Vectashield solution containing DAPI stain to visualize cell nuclei.

Immunofluorescence Controls

For positive immunofluorescence controls, cryostat sections of the cochlea were incubated with the corresponding antibodies. Negative controls: normal macula utricle sections were incubated with all reagents except for the primary antibodies, or with the primary antibodies pre-absorbed with the corresponding antigen prepared as follow: 1 μg/1 μl of the primary antibody was

TABLE 2 | Antibodies and dyes used in the present study.

Antibody/dye/Source	Dilution/antibody type	SR/immunogen	Negative control	Positive control
iNOS (Abcam) (R&D)	1:500/rabbit polyclonal 1:250/mouse monoclonal	Human, mouse/GST-tagged recombinant protein corresponding to the N-terminus of mouse iNOS/NOSII	No antibody applied or pre-absorbed with antigen in the IF staining.	Human and mouse cerebellar cortex
eNOS (Chemicon) (BD Transduction)	1:200/mouse Monoclonal 1.500/Rabbit polyclonal	Human, rat, mouse/bovine eNOS	Same as above	Human cerebellar cortex
Alpha smooth muscle actin (SIGMA) (Abcam)	1:1000/mouse monoclonal 1:250/mouse monoclonal	Human, mouse, rat/N-terminal synthetic decapeptide of alpha-smooth muscle actin	Same as above	Human cerebellar cortex
Glucose transporter-1 (Abcam)	1:1000/rabbit polyclonal 1:250 rabbit monoclonal	Human, rat/synthetic peptide	Same as above	Human cerebellar cortex
Nitrotyrosine (Millipore) (Santa Cruz)	1:500/mouse monoclonal 1:100/Mouse monoclonal	Human, mouse/nitrated KHL	Same as above	Human cerebellum 98-year-old
Griffonia simplicifolia Isolectin B4 (IB-4)/Invitrogen	1:250	–	No IB4 added	Human cochlea frozen sections
Fluorescent Phalloidin/Invitrogen	1:500	–	No phalloidin added.	Mouse cochlea

SR, species reactivity; IF, immunofluorescence.

mixed with 1 μg/1 μl of the antigen, and then this mixture was incubated at 37°C for 2 h. The pre-absorbed antibody was applied to the controls sections. No immunoreaction was seen in both negative controls (**Table 2**).

Imaging

Immunofluorescence stained macula utricle sections were viewed and imaged with an Olympus BX51 fluorescent microscope (Olympus America Inc., NY, United States) equipped with an Olympus DP70 digital camera. Images were acquired using MicroSuite™ Five software (Olympus America Inc.). Images were prepared using the Adobe Photoshop software program run in a Dell Precision 380 computer. Digital images were also obtained using a Leica (SP8) high resolution microscope, located in the Advanced Microscopy Laboratory and Spectroscopy (AML/S) of California Nanosystems Institute at UCLA (CNSI). Images were taken individually of each fluorescent marker, and the DAPI nuclei stain for the same tissue cross-section at 400× magnification. Images were prepared using the Adobe Photoshop software program run in a Dell Precision 380 computer.

Transmission Electron Microscopy (TEM)

For TEM the macula utricle was processed as previously described (Ishiyama et al., 2017). In brief: half utricle was post fixed in 4% glutaraldehyde for 12 h (diluted in 0.1% buffered sodium cacodylate, pH 7.4) and then specimens were immersed in the following solutions: 2% OsO_4 and 2% potassium ferricyanide, 0.1% thio-carbohydrazide for 1 h, 2% OsO_4 for 30 min, uranyl acetate 1% overnight, and 0.1% lead aspartate for 30 min (with intervening 5 min × 3 min washes in double distilled water between steps). Tissue is dehydrated in ascending ethanol and embedded in resin (Epon®, EMS). Thin (2 microns, for light microscopy observations) and ultrathin sections (80 nm thick) were obtained using a diamond knife (Diatome) with an AO/Reichter ultracut-E microtome. Ultrathin sections were collected on single slot carbon-formvar coated copper grids (1 mm × 2 mm).

Image Capture and Analysis

Transmission electron microscope observations and digital image capture were made using a FEI Tecnai transmission electron microscope T12 TEM −120 KV (Hillsboro, OR, United States). All sections were systematically analyzed at low (5000 magnification), and higher magnification view (22,000–25,000 magnification). Systematic analysis was performed of macula utricle sections containing blood vessels within the stroma of the maculae utricle. Sections were studied for the presence of vesicles, tight junctions in the endothelial cells, pericyte cytoplasmic organization and dendritic processes, and perivascular basement membrane alterations (i.e., thickening and disruption), and overall organization of the vestibular sensory epithelia.

Quantification of Immunofluorescence

Quantification of immunofluorescence signal was obtained and comparisons were made between MD and acoustic neuroma and MD and normative postmortem microdissected utricle stained sections. Quantitative analysis was made as described from the study (Ishiyama et al., 2010; Balaker et al., 2013), using *ImageJ* software[1] (version 1.50g). Individual images captured were opened using the *ImageJ* program and converted to gray scale (image > type 8 bit). The threshold was set (image > adjust > threshold) and adjusted to the same values for all images. Background immunofluorescence signal was measured in a small area located apart from the specific antibody staining and subtracted to show only specific staining (Process > Set Background). The image was converted to black and white, and the immunofluorescence area (blood vessel underneath the stroma) was selected using the selection tool. To determine the immunofluorescence area within the region of interest the command (analyze > analyze particles was selected), and the "mask tool" was selected. The resulting information obtained was the immunofluorescence area fraction, which is the proportion of the region of interest that was immunofluorescent. Values obtained in the normative and acoustic neuroma utricle (pixels) were considered 100%. This value was compared against Meniere's utricle stained sections.

Statistical Analysis

We tested whether the immunofluorescence area in the Meniere's utricle was statistically different from the normative and acoustic neuroma. For each specimen, mean values of the immunofluorescence area was averaged and subjected to one-way repeated measurements analysis of (ANOVA). Comparison were made between the Meniere's utricle sections and acoustic neuroma sections, and between Meniere's utricle sections and normative (autopsy) sections, for each immunofluorescence marker. A p-value ≤ 0.05 indicates a statistically significant different change in the immunofluorescence area. The Sigma Stat 3.1 software program (Jandel Scientific, San Rafael, CA, United States) was used for statistical analysis.

Gene Expression Array

We used a custom real time RT profiles PCR array™ (RT² Profiler™ PCR Array Human Oxidative Stress cat # PAHS-065Z, SABiosciences), to simultaneously evaluate the expression of 84 genes associated with oxidative stress in the macula utricle from Meniere's patients and compared their expression with acoustic neuroma group and perform a by qPCR and performed a $2^{-(\Delta\Delta CT)}$ analysis. Fold regulation was normalized [baseline expression is represented by a $2^{-(\Delta\Delta CT)} = 1$], we considered that a gene significantly increased its expression only if it was larger than five times the baseline expression, i.e., $2^{-(\Delta\Delta CT)} \geq 5$.

For this purpose, utricles were received into RNAlater (Ambion, Texas) and taken immediately to the laboratory and keep overnight in the refrigerator (4°C). Thereafter the specimens were placed at −80°C until mRNA was extracted. See **Table 1**: A pool of three utricles was used for each mRNA assay per group (Meniere's and acoustic neuroma). Total RNA was extracted using TRIzol reagent (Invitrogen) and amplified using a single-color real-time polymerase chain reaction (PCR)

[1] https://imagej.nih.gov/ij/download.html

system (Stratagene Mx3000P) as described before (Beltran-Parrazal et al., 2010; Ishiyama et al., 2010). Given that the amount of RNA obtained is minimal, RT^2 Nano Pre-AMP technology was required to synthesize cDNA from nanogram amounts of RNA samples (1–100 ng). This technique utilizes multiplex PCR-based pre-amplification to provide amplification of gene-specific cDNA target templates with minimal bias.

RT-Polymerase Chain Reaction: Pre-amplified cDNA and RT^2 qPCR SYBR Green Master Mix was then loaded onto 96-well RT^2 Profiler PCR Arrays (SABiosciences) specific for gene detection of human oxidative stress. The criteria to identify statistically significant changes from control values was a p-value less than 0.05 and a mean difference equal to or greater than twofold. Comparison was made between utricles from Meniere's specimens and acoustic neuroma specimens.

RESULTS

Vestibular Endorgans in Meniere's Disease and Normal

At the light microscopy level, there were consistent histopathological changes noted in the microvasculature, neuroepithelium, and stroma when comparing the Meniere's specimen with postmortem normative. The endorgans from Meniere's patients exhibited edematous changes of the stroma and the neuroepithelium, and subepithelial basement membrane thickening.

Normative

Figure 1A demonstrates the normative histology from a postmortem acquired vestibular utricular macula from a 70-year-old male with no auditory or vestibular pathology. The overlying neuroepithelium exhibits normal cytoarchitecture of types I and II hair cells, with supporting cells beneath, with only very mild prominence of the subepithelial basement membrane, known to occur with aging, for example, in retinal basement membranes (Nagata et al., 1986). The underlying subepithelial basement membrane is smooth, uniform, orderly, and without duplication or thickening, barely perceptible in the normative vestibular endorgan. The stromal vasculature exhibits regular arrangement of the capillaries without dilatation or necrosis.

Meniere's Disease

Figures 1B,C shows the vestibular sensory epithelia from two patients with MD. Supporting cells showed vacuoles, and the subepithelial basement membrane is thickened, disorganized. There are edematous changes throughout the vestibular stroma particularly increased in proximity to the subepithelial basement membrane, and in areas rich with perivascular stromal capillaries. The subepithelial basement membrane separating the hair cells (hc) and supporting cells (sc) from the stroma was thickened, rarefied, and ranged from mildly (as shown) to severely disorganized. The stroma exhibited edema and vacuolization. There was edema and vesicles in the supporting cells and hair cells as well. The cross-section diameter of the blood vessels underneath the stroma of the normal human utricle generally ranges from 8 to 12 μm. Blood vessels in this Meniere's specimen generally ranged from 14 to 16 μm.

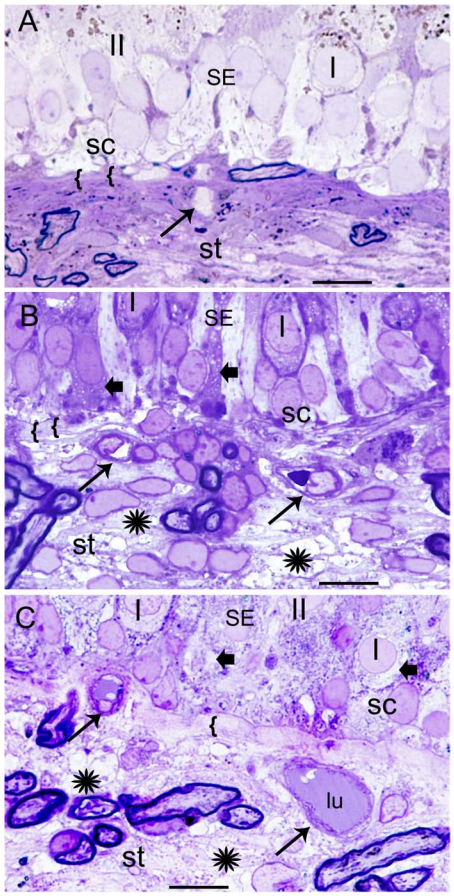

FIGURE 1 | Histological changes in the normative and Meniere's disease macula utricle. **(A)** Normal postmortem autopsy in a 70-year-old male with no vestibular dysfunction, { { points to the normal, thin, uniform basement membrane underneath the sensory epithelia. I, Type I hair cells; II, type II hair cells; st, stroma; sc, supporting cells. Arrow points to a capillary in the stroma. **(B)** Meniere's disease utricle from a patient diagnosed with intractable vertigo (65-year-old male, surgical). There is edema within the stroma, and a thickened basement membrane. **(C)** Meniere's disease with delayed hydrops, vertigo spells and Tumarkin falls. Asterisks show signs of edema in the stroma in **(B,C)**; SE, sensory epithelia. Arrowheads in the sensory epithelia indicated intracellular edema. Arrowhead point to dilated microvasculature in the stroma in **(B,C)**. { {: in **(B,C)** pronounced thickening of the basement membrane. One-micron thick plastic sections counterstained with toluidine blue. Bar is 10 microns.

Microvasculature in the Stroma of a Normal and Meniere's Disease Utricle (Transmission Electron Microscopic)

Acoustic Neuroma

The stromal capillary BLB in acoustic neuroma is relatively normal (**Figures 2A,B**). The VECs form a continuous, smooth, capillary lining with few vesicles, the lumen is without fenestrations, and the tight junctions appear to be unaltered. The VECs contain normal subcellular organelles, with several intact

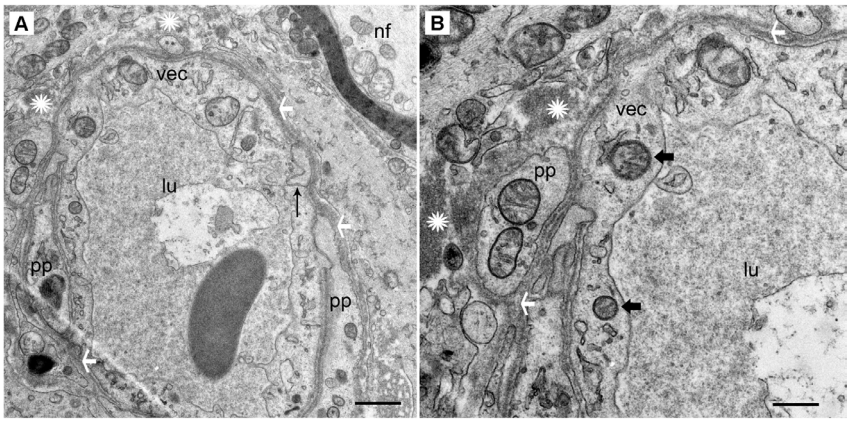

FIGURE 2 | Transmission electron photomicrographs of blood vessels in normal macula utricle (acoustic neuroma). **(A)** Cross section of a capillary (low magnification view) located in the stroma beneath the macula utricle sensory epithelia. **(B)** On higher magnification, the VECs (vec) are smooth with few vesicles, the lumen (lu) is without fenestrations, and the tight junctions (thin black arrow) appear to be unaltered. pp, pericyte processes are normal without migration or thinning, * asterisk shows the normal compact, uniform perivascular basement membrane, white arrowheads also point to the dense perivascular membrane; nf, normal nerve fiber axoplasm. Thick arrowhead: points to normal mitochondria. Magnification bar in **(A)** is 2 μm; **(B)** is 500 nm.

mitochondria noted. A pericyte process is making continuous, smooth contact with the VEC without any detachment or migration. The basement membrane is thin and uniform. Because normative inner ear surgical specimens are available only rarely, acoustic neuroma is used as normative.

Meniere's Disease

In contrast, the BLB capillaries underneath the utricle sensory epithelia from a patient with Tumarkin falls (proposed to originate from the vestibulospinal reflex in the utricle or saccule) exhibits moderately severe BLB histopathology. In this case of active MD with Tumarkin falls, within the utricle there is moderately severe with dilation of the vasculature, edema formation in the extracellular matrix, and basement membrane thickening.

Under TEM, pericyte migration and severe edematous changes are noted in the capillaries of the BLB in the utricle (**Figures 3A–C**). The VECs are swollen, the perivascular basal

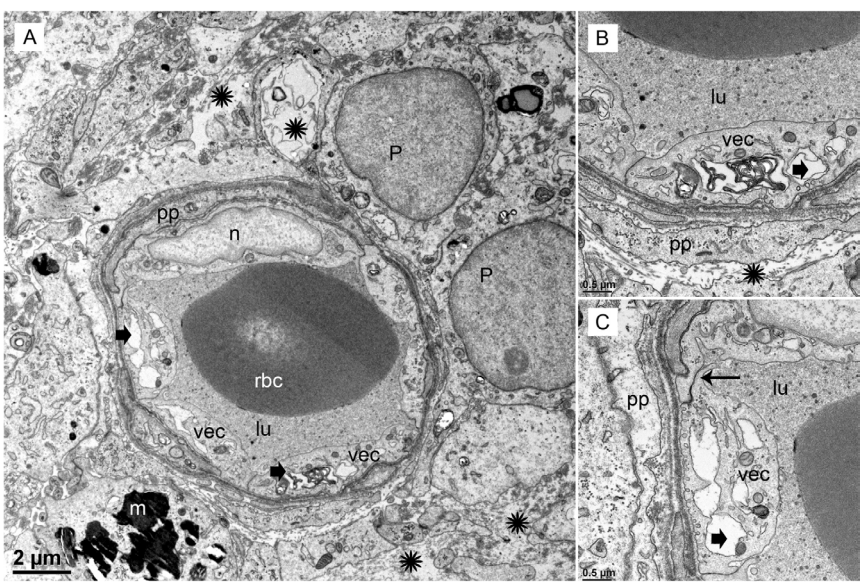

FIGURE 3 | Transmission electron photomicrographs of blood vessels in Meniere's disease macula utricle. **(A)** Low power, and **(B,C)** high power magnification shows a blood vessel with marked alterations and atrophy. The VECs (vec) are swollen, and the cytoplasm vacuolated (thick black arrowheads). The perivascular basement membrane is irregular, and there are edematous changes within the extracellular matrix (black asterisks). Multiple vesicles on the abluminal face of VEC with opening onto the perivascular basement membrane can be seen. p, pericytes; pp, pericyte process; m, melanin pigment in a putative perivascular macrophage. rbc, red blood cells; lu, lumen, thin arrow in **(C)** shows a normal tight junction between to VECs. Magnification bar in **(A)** is 2μm; **(B,C)** are 0.5 μm.

lamina is irregular, and there are edematous changes within the extracellular matrix. There is not ultrastructural evidence for disruption of the tight junctions. Higher magnification view shows that the cytoplasm of VECs is vacuolated. Multiple vesicles on the abluminal face opening onto the basal lamina can be seen. Within the VEC, there are fragments of degraded subcellular organelles. There are two pericytes with a pattern of migrating, with loss of the encircling continuous projections covering the capillary. The pericyte in the lower right side has apparent space between the process and the endothelial cell, indicating detachment. There is excessive stromal edema with large vacuoles and debris within the VEC.

Cytological Identification of VECs and Pericytes and Alterations in Cell-Specific Markers; Damaged Endothelial Cells in Meniere's Disease Exhibited Nearly Absent Isolectin B4 (IB4) Expression

Isolectin IB4 Expression in Endothelial Cells Is Nearly Absent in Meniere's Disease, While GLUT-1 Expression Appears to Be Unchanged

The VECs of the BLB are highly specialized, similar to the endothelial cells of the BBB. These cells form a single layer, tightly packed, with a greater density of mitochondria than non-neural endothelial cells. Isolectin IB4 can be used as a vascular stain for the study of VECs demonstrated in a colocalization study using IB4 (Benton et al., 2008) and a known pan-endothelial monoclonal antibody vasculature marker, RECA-1 (Duijvestijn et al., 1992; Ernst and Christie, 2006). In the specimens from MD, there was no discernable IB4 expression in the microvasculature compared with the normative postmortem control (**Figures 4A** vs. **4B**: note lack of green IB4-IF in **Figure 4B**). This likely reflects the severe degeneration of the endothelial cell. While isolectin IB4 identifies capillaries, small and medium sized arteries can be identified with von Willebrand A domain-related protein (Duong et al., 2011). Similarly, in surgical normative acoustic neuroma, the IB4-IF was noted in red, with stellate, fingerlike pericyte processes in green (**Figure 4C**) but the Meniere's specimen lacked IB4 fluorescence (**Figure 4D**).

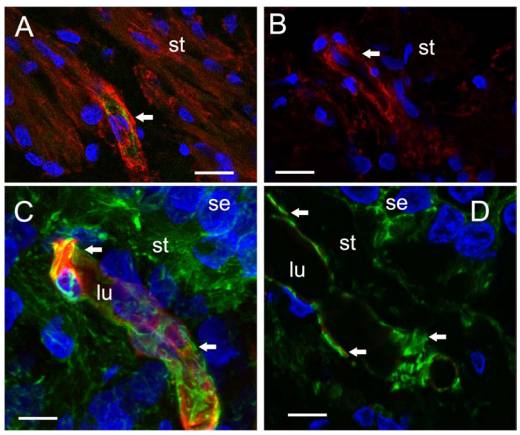

FIGURE 4 | Identification of VECs and pericytes main cellular components of the BLB. **(A)** *Normative* vs. **(B)** *Meniere's disease*: Laser confocal fluorescence micrographs showing the identification of VECs with IB4-IF, and pericytes with actin (phalloidin-F) staining in the vasculature located in the stroma of macula utricle from normal (autopsy) and Meniere's disease specimens. **(A)** Micrograph shows autopsy specimen (62-year-old-female). The pericyte processes (red phalloidin) are surrounding the capillary with VECs expressing IB4 (green IB4). **(B)** Micrograph shows a Meniere's disease specimen high magnification view. Arrowheads point to actin staining (red), IB4-IF in green. In the Meniere's specimen, there is a lack of expression of IB4. In **(A,B)** and, phalloidin was labeled with Alexa 594 (red) and IB4-IF was labeled with Alexa 488 (green). **(C)** *Normative acoustic neuroma* vs. **(D)** *Meniere's disease*: **(C)** Capillary from a normative acoustic neuroma (58 year-old-male), and **(D)** capillary from a Meniere's specimens (59 years old female). In **(C,D)**, phalloidin was labeled with Alexa 488 (green) and IB4 with Alexa 594 (red). Both **(C,D)** are laser confocal stacked images to reconstruct a 3-dimensional view. The pericytes processes can be visualized as wrapping the capillary in fingerlike processes (green, white arrowheads). VECs are also well identified by IB4 expression (red). There is a lack of IB4 staining in the blood vessel of the Meniere's specimens. DAPI stain cell nuclei (blue). St, stroma; se, sensory epithelia; lu, blood vessel luminal portion. Magnification bar in **(A,B)** is 10 microns. In **(C,D)** is 5 microns.

Pericyte Expression of α Smooth Muscle Actin (SMA) and Phalloidin Appears to Be Unaltered in Meniere's Disease Compared With Normative; In Normative, Pericytes Are Noted to Wrap in Fingerlike Projections Around the Capillary of the BLB and in Meniere's Pericytes Exhibit Degradation/Migration

There is no obvious alteration in expression of smooth muscle actin or phalloidin in MD microvasculature of the vestibular stroma. There is a hint of increased expression of SMA [but not significant alteration of expression (see **Table 3**)] which may occur in the setting of pericyte detachment and migration (**Figure 4**). **Figures 4A,B** demonstrate the expression of SMA within the pericyte is similar comparing normative surgical control (acoustic neuroma) with MD. Phalloidin staining using laser confocal microscopy allowed the full visualization of the pericyte processes: in the normative, there was the common pattern of pericytes encircling the capillary with projections that cover the capillary with fingerlike projections (**Figure 4C**).

The VECs in the Human BLB Express Glucose Transporter – 1 (GLUT-1) Similarly to the Human BBB (Figure 5A Normative and Figures 5B–D: Meniere's)

Because neurons and sensory cells require a continuous supply of energy, and use primarily glucose as fuel, the BBB endothelial cells universally express high levels of GLUT-1 in the luminal and abluminal membrane of the endothelium (Farrell and Pardridge, 1991). These integral membrane proteins help the glucose be transported down the gradient from the circulation to the endothelial cell, and then to the interstitium and then to neurons or sensory cells. GLUT-1 can be recruited when needed for extra energy to be expressed in the plasma membrane

TABLE 3 | Analysis of quantitative immunofluorescence.

Marker	MD vs. AN	% fold change from AN	MD vs. normative	% fold change from normative
Isolectin IB4	$p \leq 0.05$	**95	$p \leq 0.05$	**90
Actin	$p \geq 0.05$	*5	$p \geq 0.05$	*7
GLUT-1	$p \geq 0.05$	*2	$p \geq 0.05$	**5
iNOS	$p \leq 0.05$	*90	$p \leq 0.05$	*90
αSMA	$p \geq 0.05$	*6	$p \geq 0.05$	*4
eNOS	$p \geq 0.05$	*8	$p \geq 0.05$	*3
Nitrotyrosine	$p \leq 0.05$	*90	$p \leq 0.05$	*95

*A p-value $p \leq 0.05$ represents a statistically significant difference between immunofluorescence mean area, $p \geq 0.05$ represent no statistically significant difference. * Indicates % of increase or ** % of decrease in immunofluorescence. MD, Meniere's disease; AN, acoustic neuroma.*

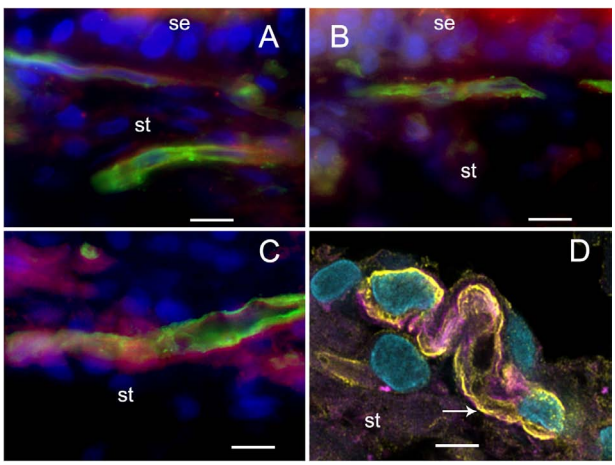

FIGURE 5 | Glucose transporter-IF (VECs, green) and Phalloidin actin (pericytes, red) **(A)**, Normative, **(B–D)**. **(A–C)** Fluorescent microscopy images. Meniere's specimens. GLUT-1-IF was consistently present in all the specimens examined (normative and Meniere's specimen). **(D)** Shows a laser confocal image yellow color (white arrow) shows GLUT1 in VECs, pink color shows actin (phalloidin) in pericytes, and clear blue shows cell nuclei (DAPI). St, stroma; se, sensory epithelia. Magnification bar **(A–C)** is 15 microns; in **(D)** is 5 microns.

(Farrell and Pardridge, 1991). The BLB endothelial cell exhibited high levels of GLUT-1, similarly localized as previous studies noted in the human BBB. There was no difference in expression of GLUT-1 in MD from normative surgical control, acoustic neuroma.

Inducible Nitric Oxide Synthase (iNOS) Is Upregulated and There Is an Increase Expression of Nitrotyrosine in the Capillaries of the BLB, the Stroma, and the Neuroepithelium in Meniere's Disease

We conducted immunohistochemical localization of iNOS and eNOS in the specimens from MD and compared with surgical normative, acoustic neuroma. iNOS was expressed in all vestibular inner ear specimens with severe intractable MD, but was not present in any of the acoustic neuroma specimens. The VECs in Meniere's specimens showed significantly higher expression of iNOS than the acoustic neuroma utricle. (**Figures 6A–C**). In contrast, eNOS, the

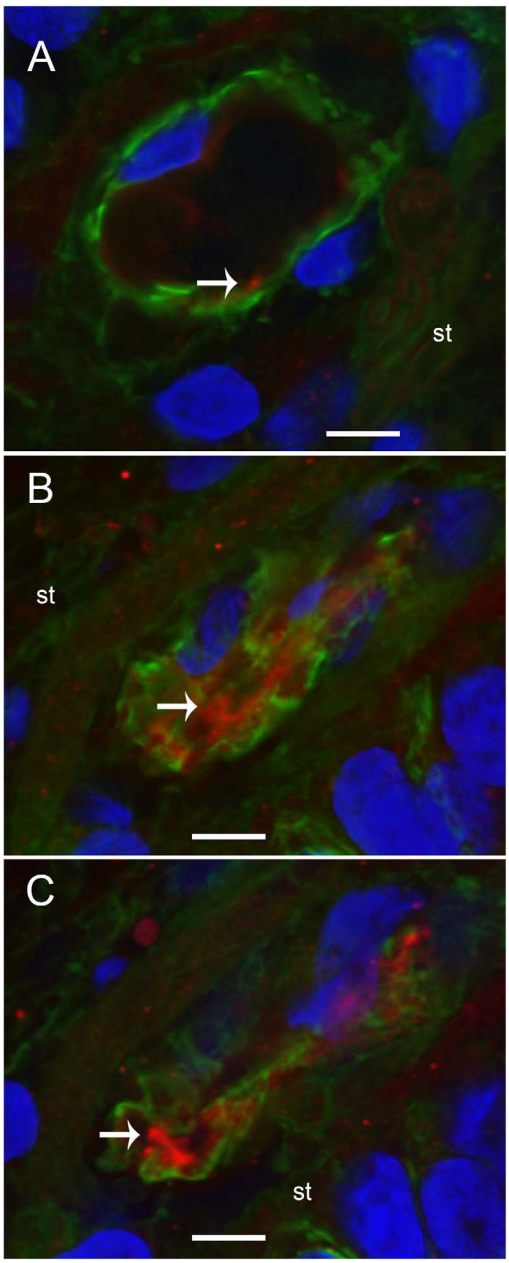

FIGURE 6 | Laser confocal photomicrographs showing the presence of inducible nitric oxide synthase-IF (iNOS-IF, red) and αSMA-IF (green) in the normal and Meniere's macula utricle vasculature. **(A)** Blood vessels in an acoustic neuroma specimen, **(B,C)** blood vessels from Meniere's disease utricle stroma (st). iNOS-IF was present in all Meniere's disease specimens examined (white arrow) while normative and acoustic neuroma showed minimum small area of iNOS-IF. Magnification bar in **(A–C)** are 5 microns.

constitutive NOS, appeared to be equally expressed within the VECs of the BLB in both surgical normative and MD (**Figures 7A,B**).

Nitrotyrosine Immunofluorescence (NT-IF) Is Noted in the Capillaries of the BLB, the Stroma, and the Neuroepithelium of Meniere's Specimens but Not in Normative Surgical Controls

Nitrotyrosine-IF was not detected in the vestibular utricular maculae from surgical normative specimen (acoustic neuroma) as noted in **Figure 8A**. In striking contrast, NT-IF was detected throughout the utricular maculae in all MD specimens examined. In the macula utricle from Meniere's patients, NT-IF was found within the cells of the sensory epithelia and stroma, as well as within the capillaries of the BLB within the stroma (**Figure 8B**). Nitrotyrosine is a post-translational modification to proteins, and the addition of a $^{-}NO_2$ group to the exposed protein tyrosine is a stable transformation that does not occur at random. Nitrotyrosine can be formed by the reactive species, peroxynitrite, and is generally believed to indicate oxidative stress (Peluffo and Radi, 2007). There are other nitrating agents, however, in the setting of co-expression of iNOS, which is normally not expressed, it is believed that nitrated proteins, nitrotyrosine, are formed due to high NO production in the setting of oxidative stress (Beckman and Koppenol, 1996). The resultant oxidative stress, in the form of NO and nitrotyrosine, may play a critical role in the loss of integrity of the BLB, and may lead to the formation of stromal and neuroepithelial degenerative changes and vacuolization of the stroma and of cellular structures.

Quantitative Analysis of Immunofluorescence

Comparison of immunofluorescence of the different markers between the specimens from MD vs. normative revealed the following significant changes (**Table 3**): isolectin IB4 exhibited a statistically significant decreased expression in the endothelial cells of the BLB of Meniere's specimens, compared with the expression in acoustic neuroma (surgical normative) and normative (autopsy). Actin, GLUT-1, αSMA, and eNOS demonstrated unaltered expression levels among the three types of specimens. In contrast both iNOS and nitrotyrosine showed statistically significant increased levels of expression in the vestibular BLB of Meniere's specimens.

Microarray-Based Gene Expression Profiling Demonstrates Significant Increase in iNOS mRNA in Meniere's Utricles

Meniere's disease utricles showed significantly iNOS mRNA increase (i.e., larger than five times) with respect to acoustic neuroma utricles (more than five times increase) (**Table 4**).

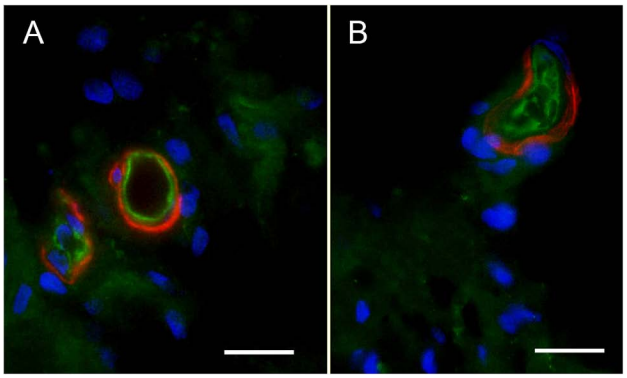

FIGURE 7 | Endothelial nitric oxide synthase (eNOS)-IF in the surgical normative (acoustic neuroma) and Meniere's macula utricle microvasculature stroma. **(A)** Shows eNOS-IF in the VECs (green), and αSMA-IF in pericytes (red) in acoustic neuroma specimen, **(B)** shows eNOS-IF in the blood vessels VECs (green) and αSMA-IF in Meniere's disease. Both specimens showed eNOS-IF in a similar intensity. Magnification bar in **(A,B)** are 10 microns.

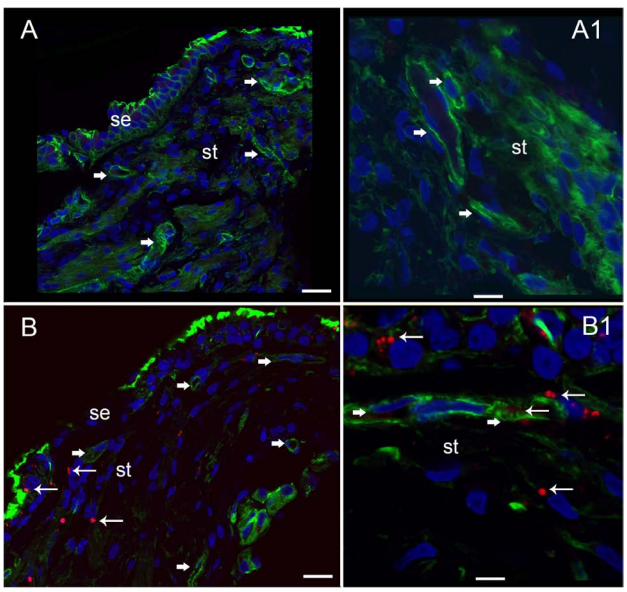

FIGURE 8 | Nitrotyrosine-immunofluorescence (NT-IF, red color) and actin (Actin-IF, green color) in the utricle of normative (acoustic neuroma) and Meniere's disease (all images obtained using laser confocal microscope). **(A)** Low magnification view showing almost complete absence of NT-IF in the normal utricle stroma (st) and epithelial cells (se), actin delineate a capillary (Phalloidin green color, arrowhead) **(A1)** high magnification showing actin (phalloidin in green) around the vasculature (arrowheads). **(B)** In contrast NT-IF (red, thin arrows), was present in the sensory epithelial (se) cells, stroma and VECs, **(B1)** is a high magnification view showing NT-IF around and inside a capillary (thin arrows); st, stroma. Magnification bar in **(A,B)** are 25 microns; **(A1,B1)** are 10 microns.

Additional mRNAs in the Meniere's specimens showed significant changes: Albumin, Dual specificity phosphatase 1, Polynucleotide kinase 3′-phosphatase, Peroxidasin, Selenoprotein P, Serine/threonine kinase 25 (**Table 4**).

TABLE 4 | Gene expression analysis by qPCR of genes related to oxidative stress in Meniere Disease (MD) vs. Acoustic neuroma (AN).

Name	ID GeneBank	$2^{-(\Delta\Delta CT)}$
Albumin ↓	NM_000477.3	**−5.1**
Arachidonate 12-lipoxygenase.	NM_001159.3	−2.2
Catalase	NM_001752.2	−4.5
24-dehydrocholesterol reductase	NM_014762.3	4.1
Dual specificity phosphatase 1 ↓	NM_004417.2	**−5.2**
Forkhead box M1	NM_021953.2	−2.2
Glutathione peroxidase 3	NM_002084.3	−2.1
Glutathione *S*-transferase zeta 1	NM_001513.2	−2.3
Lactoperoxidase	NM_006151.1	−2
Metallothionein 3	NM_005954.2	−1.8
PDZ and LIM domain 1	NM_020992.2	−2.5
Polynucleotide kinase 3′-phosphatase ↓	NM_007254.2	**−7.5**
Prion protein	NM_183079.2	1.8
Peroxidasin ↓	NM_144651.4	−8.5
Selenoprotein P ↓	NM_005410.2	−5.1
Serine/threonine kinase 25 ↓	NM_006374.3	−5
Nitric oxide synthase 2 ↑	NM_000625.3	**13.43**
Oxidation resistance 1	NM_001198532.1	−2.9

Upregulated genes (green), downregulated (red). Arrows represent statistically significant increase or decrease in fold regulation. Bolded values indicate a statistically significant increase or decrease (more that 5 times) of mRNA expression.

DISCUSSION

Vestibular Endorgans Exhibit Damage in the Vasculature, Stroma, and Neuroepithelium

The vestibular sensory endorgan in MD exhibits stromal vacuolization, neuroepithelial damage to the sensory hair cells and supporting cells, and a thickened, irregular subepithelial basement membrane. The edematous changes throughout the vestibular stroma are increased in proximity to the subepithelial basement membrane, and in areas rich with stromal capillaries. There was edema and vesicles within the supporting cells and hair cells, and the subepithelial basement membrane exhibited thickening and damage. The cross-sectional diameter of the blood vessels underneath the stroma of the normal human utricle generally ranges from 8 to 12 microns and the vessels in Meniere's specimens generally range from 14 to 16 microns.

The Blood Labyrinth Barrier

The BLB, specifically, the blood perilymph barrier, localizes to the microvasculature of the vestibular stroma, spiral ligament, spiral limbus, and modiolus (Suzuki and Kaga, 1999). The ultrastructure in the capillaries of the vestibular stroma in human demonstrates similarities with the BLB in animal models and is also similar to the cytoarchitecture of the blood–brain barrier (BBB) (Reese and Karnovsky, 1967; Nag, 2003). In the present study, we confirm that the integrity of the normative human BLB is maintained by VECs forming a continuous, non-fenestrated lining with few vesicles, sparse transcytosis, tight junctions appearing normal, smooth-lined basement membrane with pericytes intermingled and entirely encompassed within the basement membrane (Ishiyama et al., 2017). The BLB is similarly structured in the guinea pig spiral limbus and modiolus (Jahnke, 1980) and mouse strial BLB (Shi et al., 2008; Wu et al., 2014).

In the present study, we did visualize a putative melanin containing perivascular macrophage surrounding the capillary of the vestibular BLB in Meniere's specimen. The rarity with which we see the perivascular macrophage may indicate species-specific differences or differences due to pathological states. Pericytes are known to exhibit pluripotent activity, and the migrating pericyte can be seen in pathological states and may exhibit macrophage like characteristics (Dore-Duffy, 2008).

Structural and Cytochemical Changes in the BLB in Meniere's Disease

TEM of Vascular Endothelial Cell (VEC) and Pericytes

In the vestibular endorgans from MD, the VECs exhibit increased vesicular formation facing the abluminal side, edema and vacuolization of the perivascular basement membrane. The tight junctions did not exhibit changes that could be discerned at the ultrastructural level. However, it has been noted that without using tracers, the opening of the tight junctions may not be visualized (Hirano et al., 1994) and tight junctions in the BBB can demonstrate rapid reversible opening (Rapoport et al., 1972). However, we cannot rule out tight junction pathology with structural imaging, and physiological studies in patients cannot be conducted.

There was VEC degeneration with loss of organelles; and confirming the cellular damage, the marker isolectin-IB4 was nearly universally absent in the VEC of the MD specimens but was present in both acoustic neuroma and postmortem normative. It is informative to evaluate these findings in light of other systems, such as the BBB in normative and pathology. In normative conditions, the BBB endothelial cell from cerebral cortex contain only 5 caveolae per micron ^{2} likely intended to limit transcellular traffic in steady state. With hypertensive encephalopathy, there is an increase in vesicular transport in the endothelium, and there are structural changes in the tight junctions. It is believed that these structural changes occur late and are preceded by endothelial cell breakdown (Nag et al., 2011). Similar patterns of endothelial cell activation are noted in cerebral edema, which is associated with increased permeability of the BBB (Stokum et al., 2016). VEC transcytosis appears to be a critical factor in BBB dysfunction following cerebrovascular stroke (Krueger et al., 2013) and endothelial cell transcytosis is proposed to cause loss of integrity of the barrier with consequential damage to the surrounding structures.

In the present study, there were also abnormalities noted in the pericytes with edematous changes, and pericyte detachment in specimens from MD. Pericyte-endothelial interactions are known to be a critical to maintain the integrity of the BBB and the basement membrane and endothelial tight junction structure are affected by pericyte interactions (Liu et al., 2012). Pericytes contribute to the BLB function in the stria vascularis via upregulation of the tight junction proteins (Shi, 2010; Dai and

Shi, 2011; Neng et al., 2013). In the animal model of diabetic retinopathy, basement membrane thickening precedes blood retina barrier endothelial cell degradation and pericyte migration (Hainsworth et al., 2002), and oxidative stress induces loss of pericyte coverage and vascular instability (Garcia-Quintans et al., 2016). In the present study, migration of the pericyte with detachment of the pericyte processes was noted in MD, but not in normative nor in acoustic neuroma, and the loss of normal pericyte-endothelial cell interaction is likely associated with BLB damage. Normative BLB specimens exhibited pericytes characterized by fingerlike projections encircling the VEC, similar to the cerebrovascular pericytes (Dore-Duffy, 2008).

Basement Membrane

In the present study, there was thickening and disorganization of the perivascular basement membrane of the BLB in MD, and not in normative. These findings corroborate our previous work that demonstrated loss of the normal expression of collagen IV in the subepithelial and perivascular basement membranes in vestibular endorgans from MD (Calzada et al., 2012a). An intact and functional basement membrane surrounding the capillary is likely critical to the function of the BLB and abnormalities may contribute to BLB permeability alterations. The subepithelial basement membrane disruption may also be associated with an altered expression of aquaporins, and our group demonstrated that aquaporin 4 is downregulated and aquaporin 6 is upregulated in the vestibular supporting cells in MD (Ishiyama et al., 2010). It is likely that the increased permeability of the BLB is associated with damage to basement membranes, the extracellular matrix and the vestibular stroma.

Oxidative Stress and Breakdown of the BLB

Several inner ear pathologies including acoustic trauma, sudden hearing loss, presbycusis and MD are hypothesized to involve dysfunction of the microvascular circulation (Shi, 2011, 2016). Oxidative stress and ROS have been proposed as mediators for microvascular damage in systemic disorders (Beckman and Koppenol, 1996) and in sensorineural hearing loss, MD, and endolymphatic hydrops (Labbe et al., 2005; Capaccio et al., 2011; Teranishi et al., 2012). Ischemic damage to the cochlea is associated with increased expression of iNOS and NO metabolites (Shi and Nuttall, 2003). iNOS is associated with the production of large amounts of NO, which in the presence of ROS, can form peroxynitrite which mediates the nitrosylation of tyrosine. The presence of elevated levels of 3-nitrotyrosine, a marker for protein tyrosine nitration, has been implicated in the pathophysiology of diverse human diseases: Alzheimer's disease, cystic fibrosis, myocardial malfunction, lupus nephritis, cerebrovascular strokes, and diabetic retinopathy (Duncan, 2003). The presence of the nitro-group in a tyrosine residue is damaging to cell membranes and can also incite an immunological and inflammatory response (Ye et al., 1996). An increased expression of iNOS and nitrotyrosine has been noted in cerebral demyelinating lesions from the autoimmune neurological disease, multiple sclerosis (Liu et al., 2001).

In our present study, we demonstrated a significant increase in the expression of iNOS in the utricular macula from MD, corroborated with an upregulated expression of mRNA for iNOS. The constitutive eNOS was not more highly expressed in MD patients compared with normative specimens. Under normal conditions, eNOS produces NO at physiological levels, necessary for downstream cellular messengers within the inner ear (Takumida and Anniko, 2004). iNOS, on the other hand, is only detected in the inner ear under pathologic conditions (Takumida and Anniko, 1998a, 2001), and likely can be synthesized by any of the cells of the vasculature when stimulated by cytokines. It is hypothesized that the level of NO production defines its role in the cells as protective or destructive (Albrecht et al., 2003). When NO levels are elevated along with ROS, mitochondria function is blocked and cellular apoptosis may be induced (Clementi et al., 1998; Brüne et al., 1999).

Upregulation of iNOS has been described in several conditions of the inner ear including hydrops in the animal model (Takumida and Anniko, 1998b, 2001; Hess et al., 1999a,b; Shi and Nuttall, 2003). Intratympanic LPS in animal models was associated with an increase in iNOS expression, and the damage could be limited by an infusion of a competitive inhibitor of iNOS (Watanabe et al., 2000). eNOS upregulation is also seen in acoustic trauma or gentamicin injection (Heinrich et al., 2005, 2006), and eNOS can exhibit uncoupling which is associated with ROS (Vasquez-Vivar et al., 1998; Albrecht et al., 2003; Förstermann and Li, 2011; Li and Förstermann, 2013). In the setting of upregulated iNOS, high levels of NO, and nitrotyrosine, and BLB dysfunction as noted in the present study of MD vestibular endorgan, the presence of eNOS may be contributing to damage as well.

The presence of iNOS in the capillaries of the BLB, and nitrotyrosine in the BLB and the stroma, coupled with the histopathological findings of damage to the endothelial cells and the microvasculature, is strongly suggestive that oxidative stress mediates the damage to the BLB in MD leading to a cascade of events culminating in damage within the vestibular endorgan.

Other Models of BLB Damage Due to Induction of Oxidative Stress

Meniere's is a uniquely human disease, and no animal model produces the symptoms of intermittent vertigo spells with hearing loss. Therefore, it is useful to look into oxidative stress factors in animal models of other otopathologies. In the rodent model of noise-induced hearing loss, TEM analysis reveals similar strial BLB pathology as in our studies: cytoplasmic vacuolization of the endothelial cell, irregular positioning of pericyte processes, and intercellular space between the pericyte and endothelial cell (Shi, 2009). In the diabetic rat model, both iNOS and eNOS were upregulated in the cochlea, indicative of oxidative stress. BLB damage was evidenced by extravasation of Evans blue, associated with hearing loss (Liu et al., 2008). Noise exposure in the mouse knock out for manganese superoxide dismutase, an endogenous antioxidant, causes significantly more outer hair cell damage than normative (Tuerdi et al., 2017), and noise exposure induces nitrotyrosine production within the outer hair cells, associated with apoptosis of the outer hair cells (Han

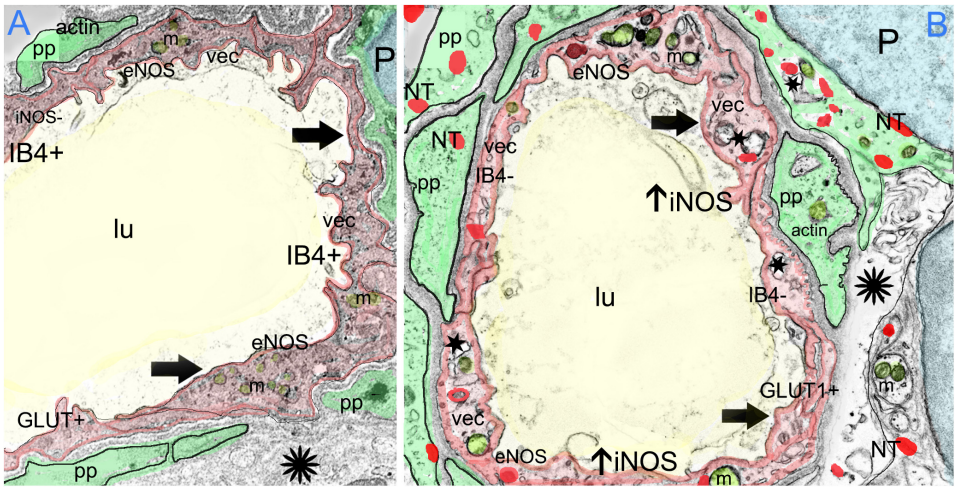

FIGURE 9 | The effect of oxidative stress in the BLB in Meniere's disease. Meniere's disease may be associated with a chronic inflammatory oxidative stress response within the microvasculature of the BLB as suggested by upregulation of oxidative stress markers iNOS and the presence of nitrotyrosine. The formation of ROS causes further cellular injury. Nitric oxide may also alter microvascular blood flow and VEC permeability causing loss of the integrity of the BLB through increased endothelial cell transcytosis, pericyte contraction and pericyte migration. VECs may become further damaged by reactive oxygen species and nitration of proteins, followed by increased permeability, allowing an extravasation of fluids and proteins, damaging the extracellular matrix and perivascular basement membranes, and causing associated stromal edema. **(A)** Depicts the normal BLB. **(B)** Depicts the effect of oxidative stress in the BLB in Meniere's disease.

et al., 2013). There may be a genetic susceptibility in patients with MD, with polymorphism in one gene involved in oxidative stress noted in higher expression in a Japanese population study (Teranishi et al., 2012).

There is evidence that strial BLB permeability change in noise exposure is mediated by a decreased expression of occludin, a tight junction associated protein (Shi and Nuttall, 2003; Zhang et al., 2013; Wu et al., 2014). The production of inflammatory mediators from the capillary VECs is hypothesized to trigger a cascade of subsequent events (Trune and Nguyen-Huynh, 2012). Pharmacological interventions targeting tight junction protein expression by pericytes are being developed for downregulation of oxidative stress proteins in stroke and cardiac arrest (Ronaldson and Davis, 2015). Further studies are indicated to evaluate the integrity of and expression of proteins in the tight junctions of the BLB of MD.

Pericytes may mediate a decreased capillary reflow due to oxidative-nitration mediated pericyte constriction (Yemisci et al., 2009). Thus, it is not clear whether the NO production is necessarily only detrimental, and indeed, the upregulation of NO production may be an attempt to vasodilate in response to hypoxia due to vasoconstriction. Further studies are indicated to evaluate for oxidative stress products, immunolocalization on a cellular level, to discover new potential targets for the treatment of intractable MD.

Summary of Oxidative Stress in the BLB of Meniere's Utricles

Figure 9A depicts the normal BLB, and **Figure 9B** depicts the changes due to oxidative stress in the BLB in MD that have been documented in the present study. We have shown that MD is associated with an upregulation of iNOS expression within the microvasculature of the BLB, along with constitutive expression of eNOS, the combination of which are likely associated with high levels of NO. The endothelial cell of the BLB exhibits nitrotyrosine expression, likely associated with increased microvascular permeability, VEC transcytosis into the subepithelial stromal utricular macula, pericyte migration and endothelial cell damage. The increased permeability of the BLB may be causative of the interstitial edema, stromal vacuolization, and damage to the basement membrane and extracellular matrix that our group has documented in prior studies (McCall et al., 2009; Ishiyama et al., 2017). The nitration of proteins may be also associated with neuroepithelial edema and damage to the sensory neuroepithelium as noted in this study with the presence of nitrotyrosine, within the neuroepithelium and stroma. A similar process may occur in the hearing system to cause hearing loss of MD.

CONCLUSION

The cellular and structural changes suggest that the VECs in the microvasculature of the BLB are damaged due to oxidative stress in MD. The VECs express iNOS and nitrotyrosine, exhibit degeneration, loss of organelles, loss of IB4 expression, and excessive transcytosis. Pericytes exhibit vacuolization and migration with loss of the encircling fingerlike projections. These degenerative changes of the BLB may be causative of the degeneration of the perivascular basement membrane and the extracellular matrix, as has been documented in our prior studies. These findings confirm with histopathology the MRI evidence for a loss of integrity of the BLB in MD and are strongly suggestive that oxidative stress plays a critical role in the pathophysiology of MD. Quantitative stereological studies at the transmission

electron microscopy level of the microvasculature are warranted to further understand the cellular and molecular biology of the BLB in normative and MD and such studies are integral for the development of therapeutic agents which may block the BLB inflammatory response.

AUTHOR CONTRIBUTIONS

GI development of the theory, designed the project, interpretation of histopathology and all studies, mentor and oversee the studies, interpretation of clinical data, experimental design, approve and work on final manuscript. JW performed immunofluorescence staining, interpretation of studies, writing first draft, approve and work on final manuscript. IL development of the theory, designed the project, participated and mentored in all aspects of the experiments, prepare the figures, approve and work on the final manuscript. LB-P performed gene expression array experiments and interpretation of its results. AI design of the project, collection of specimens, interpretation of clinical data, experimental design, approve and work on the final manuscript.

FUNDING

This work was supported by grants: Hearing Health Foundation grant 20180673 (GI), and National Institute on Deafness and Other Communication Disorders grant 1U24DC015910-01 (AI).

ACKNOWLEDGMENTS

We appreciate Dr. Matthew Schibler from the Advanced Microscopy Laboratory and Spectroscopy (AMLS) and Dr. Ivo Atasanov from the electron Imaging Center for NanoMachines (EICN) both of California Nanosystems Institute at UCLA (CNSI) for allowing the use of SP8 Leica laser confocal high-resolution microscope and the T12 Transmission electron microscope.

REFERENCES

Albrecht, E. W., Stegeman, C. A., Heerings, P., Henning, R. H., and van Goor, H. (2003). Protective role of endothelial nitric oxide synthase. *J. Pathol.* 199, 8–17. doi: 10.1002/path.1250

Arenberg, J. G., Komjathy, D. A., Seidman, M. D., and Quirk, W. S. (1997). Local effects of nitric oxide on vestibular blood flow in the *Mongolian gerbil*. *Eur. Arch. Otorhinolaryngol.* 254, 367–371. doi: 10.1007/BF01642552

Balaker, A. E., Ishiyama, P., Lopez, I. A., Ishiyama, G., and Ishiyama, A. (2013). Immunocytochemical localization of the translocase of the outer mitochondrial membrane (Tom20) in the human cochlea. *Anatom. Rec.* 296, 326–332. doi: 10.1002/ar.22622

Baloh, R. W. (2001). Prosper Meniere's and his disease. *Arch. Neurol.* 58, 1151–1156. doi: 10.1001/archneur.58.7.1151

Barath, K., Schuknecht, B., Monge, N. A., Schrepfer, T., Bockisch, C. J., and Hegemann, S. (2014). Detection and grading of endolymphatic hydrops in Meniere's disease using MR imaging. *AJNR Am. J. Neuroradiol.* 35, 1–6. doi: 10.3174/ajnr.A3856

Beckman, J. S., and Koppenol, W. H. (1996). Nitric oxide, superoxide, and peroxynitrite: the good, the bad, and ugly. *Am. J. Physiol.* 271, 1424–1437. doi: 10.1152/ajpcell.1996.271.5.C1424

Beltran-Parrazal, L., Acuna, D., Ngan, A. M., Kim, E., Ngan, A., Kawakami, K., et al. (2010). Neuroglobin, cryoglobulin, and transcriptional profiling of hypoxia-related genes in the rat cerebellum after prenatal chronic very mild carbon monoxide exposure (25 ppm). *Brain Res.* 1330, 61–71. doi: 10.1016/j.brainres.2010.03.005

Benton, R. L., Maddie, M. A., Minnillo, D. R., Hagg, T., and Whitemore, R. (2008). Griffonia simplicifolia isolectin B4 identifies a specific population of angiogenic blood vessels following contusive spiral cord injury in the adult mouse. *J Comp. Neurol.* 597, 1031–1052. doi: 10.1002/cne.21570

Brüne, B., von Knethen, A., and Sandau, K. B. (1999). Nitric oxide (NO): an effector of apoptosis. *Cell Death Differ* 6, 969–975. doi: 10.1038/sj.cdd.4400582

Calzada, A. P., Lopez, I. A., Beltran-Parrazal, L., Ishiyama, A., and Ishiyama, G. (2012a). Cochlin expression in vestibular endorgans obtained from patients with Meniere's disease. *Cell Tissue Res.* 350, 373–384. doi: 10.1007/s00441-012-1481-x

Calzada, A. P., Lopez, I. A., Ishiyama, G., and Ishiyama, A. (2012b). Otolithic membrane damage in patients with endolymphatic hydrops and drop attacks. *Otol. Neurotol.* 33, 1593–1598. doi: 10.1097/MAO.0b013e318271c48b

Capaccio, P., Pignataro, L., Gaini, L. M., Sigismund, P. E., Novembrino, C., De Giuseppe, R., et al. (2011). Unbalanced oxidative status in idiopathic sudden sensorineural hearing loss. *Eur. Arch. Otorhinolaryngol.* 269, 449–453. doi: 10.1007/s00405-011-1671-2

Chung, J. W., Fayad, J., Linthicum, F., Ishiyama, A., and Merchant, S. N. (2011). Histopathology after endolymphatic sac surgery for Meniere's syndrome. *Otol. Neurotol.* 32, 660–664. doi: 10.1097/MAO.0b013e31821553ce

Clementi, E., Brown, G. C., Feelisch, M., and Moncada, S. (1998). Persistent inhibition of cell respiration by nitric oxide: crucial role of S-nitrosylation of mitochondrial complex I and protective action of glutathione. *Proc. Natl. Acad. Sci. U.S.A.* 95, 7631–7636. doi: 10.1073/pnas.95.13.7631

Committee on Hearing and Equilibrium (1995). Meniere's disease: criteria for diagnosis and evaluation of therapy for reporting. *Otolaryngol. Head Neck Surg.* 113, 181–185. doi: 10.1016/S0194-5998(95)70102-8

Dai, M., and Shi, X. (2011). Fibro-vascular coupling in the control of cochlear blood flow. *PLoS One* 6:e20656.

Dore-Duffy, P. (2008). Pericytes: pluripotent cells of the blood brain barrier. *Curr. Pharm. Des.* 14, 1581–1593. doi: 10.2174/138161208784705469

Duijvestijn, A. M., van Goor, H., Klater, F., Majoor, G. D., van Bussel, E., and van Breda Vriesman, P. J. (1992). Antibodies defining rat endothelial cells. *RECA*-1, a pan-endothelial cell-specific monoclonal antibody. *Lab Invest* 66, 459–466.

Duncan, M. W. (2003). A review of approaches to the analysis of 3-nitrotyrosine. *Amino Acids.* 25, 351–361. doi: 10.1007/s00726-003-0022-z

Duong, T., Lopez, I. A., Ishiyama, A., and Ishiyama, G. (2011). Immunohistochemical distribution of WARP (von Willebrand A domain-related protein) in the inner ear. *Brain Res.* 1367, 50–61. doi: 10.1016/j.brainres.2010.10.056

Ernst, C., and Christie, B. R. (2006). Isolectin-IB4 as a vascular stain for the study of adult neurogenesis. *J. Neurosci. Methods* 150, 138–142. doi: 10.1016/j.jneumeth.2005.06.018

Farrell, C. L., and Pardridge, W. M. (1991). Blood-brain barrier glucose transporter is asymmetrically distributed on brain capillary endothelial luminal and abluminal membranes: an electron microscopic immunogold study. *Proc Natl Acad Sci. U.S.A.* 88, 5779–5783. doi: 10.1073/pnas.88.13.5779

Förstermann, U., and Li, H. (2011). Therapeutic effect of enhancing endothelial nitric oxide synthase (eNOS) expression and preventing eNOS uncoupling. *Br. J. Pharmacol.* 164, 213–223. doi: 10.1111/j.1476-5381.2010.01196.x

Garcia-Quintans, N., Sanchez-Ramos, C., Prieto, I., Tierrez, A., Arza, E., Alfranca, A., et al. (2016). Oxidative stress induces loss of pericyte coverage and vascular instability in PGC-1-alpha deficient mice. *Angiogenesis* 19, 217–228. doi: 10.1007/s10456-016-9502-0

Hainsworth, D. P., Katz, M. L., Sanders, D. A., Sanders, D. N., Wright, E. J., and Sturek, M. (2002). Retinal capillary basement membrane thickening in a porcine model of diabetes mellitus. *Comp. Med.* 52, 523–529.

Hallpike, C. S., and Cairns, H. (1938). Observations on the pathology of Ménière's syndrome. *J. Laryngol. Otol.* 53, 625–655. doi: 10.1017/S0022215100003947

Han, W. J., Shi, X. R., and Nuttall, A. (2013). Noise-induced nitrotyrosine increase and outer hair cell death in guinea pig cochlea. *Chin. Med. J.* 126, 2923–2927.

Heinrich, U. R., Selivanova, O., Feltens, R., Brieger, J., and Mann, W. (2005). Endothelial nitric oxide synthase upregulation in the guinea pig organ of Corti after acute noise trauma. *Brain Res.* 1047, 85–96. doi: 10.1016/j.brainres.2005.04.023

Heinrich, U. R., Selivanova, O., Feltens, R., Brieger, J., and Mann, W. (2006). Endothelial nitric oxide synthase upregulation in the cochlea of the guinea pig after intratympanic gentamicin injection. *European Arch Oto-Rhino-Laryn.* 263, 62–68. doi: 10.1007/s00405-005-0949-7

Hess, A., Bloch, W., Huverstuhl, J., Su, J., Stennert, E., Addicks, K., et al. (1999a). Expression of inducible nitric oxide synthase (iNOS/NOS II) in the cochlea of guinea pigs after intratympanical endotoxin-treatment. *Brain. Res.* 830, 113–122. doi: 10.1016/S0006-8993(99)01433-X

Hess, A., Bloch, W., Su, J., Stennert, E., Addicks, K., and Michel, O. (1999b). Expression of inducible nitric oxide-synthase in the vestibular system of hydropic guinea pigs. *Neurosci. Lett.* 264, 145–148. doi: 10.1016/S0304-3940(99)00195-0

Hirano, A., Kawanami, T., and Llena, J. F. (1994). Electron microscopy of the blood brain barrier in disease. *Microsc. Res. Technol.* 1194, 543–556. doi: 10.1002/jemt.1070270609

Hirose, K., Hartsock, J. J., Johnson, S., Santi, P., and Salt, A. N. (2014). Systemic lipopolysaccharide compromises the blood-labyrinthine barrier and increases entry of serum fluorescein into the perilymph. *J. Assoc. Res. Otolaryngol.* 15, 707–719. doi: 10.1007/s10162-014-0476-6

Hoshijima, H., Makimoto, K., Noi, O., Ohinata, Y., and Takenaka, H. (2002). Effects of nitric oxide synthase inhibitor on cochlear blood flow. *Hear. Res.* 171, 32–42. doi: 10.1016/S0378-5955(02)00328-3

Ishiyama, G., Ishiyama, A., Jacobson, K., and Baloh, R. W. (2001). Drop attacks in older patients secondary to an otologic cause. *Neurology* 57, 1103–1106. doi: 10.1212/WNL.57.6.1103

Ishiyama, G., Lopez, I. A., Beltran-Parrazal, L., and Ishiyama, A. (2010). Immunohistochemical localization and mRNA expression of aquaporins in the macula utricle of patients with Meniere's disease and acoustic neuroma. *Cell Tissue Res.* 340, 407–419. doi: 10.1007/s00441-010-0975-7

Ishiyama, G., Lopez, I. A., Ishiyama, P., Vinters, H. V., and Ishiyama, A. (2017). The blood labyrinthine barrier in the human normal and Meniere's disease macula utricle. *Sci. Rep.* 7:253. doi: 10.1038/s41598-017-00330-5

Ishiyama, G., Lopez, I. A., Sepahdari, A. R., and Ishiyama, A. (2015). Meniere's disease: histopathology, cytochemistry and imaging. *Ann. N.Y. Acad. Sci.* 1343, 49–57. doi: 10.1016/j.clinimag.2014.09.014

Jahnke, K. (1980). The blood-perilymph barrier. *Arch. Otorhinolaryngol.* 228, 29–34. doi: 10.1007/BF00455891

Juhn, S. K., Hunter, B. A., and Odland, R. M. (2001). Blood-labyrinth barrier and fluid dynamics of the inner ear. *Int. Tinnitus J.* 7, 72–83.

Juhn, S. K., Rybak, L. P., and Prado, S. (1981). Nature of blood – labyrinth barrier in experimental conditions. *Ann. Otol. Rhinol. Laryngol.* 90, 135–141. doi: 10.1177/000348948109000208

Kregel, K. C., and Zhang, H. J. (2007). An integrated view of oxidative stress in aging: basic mechanisms, functional effects, and pathological considerations. *Am. J. Physiol. Reg. Integr. Comp. Physiol.* 292, 18–36. doi: 10.1152/ajpregu.003227.2006

Krueger, M., Hartig, W., Reichengach, A., Bechmann, I., and Michalski, D. (2013). Blood brain barrier breakdown after embolic stroke in rats occurs without ultrastructural evidence for disrupting tight junctions. *PLoS One* 8:e56419. doi: 10.1371/journal.pone.0056419

Labbe, D., Teranishi, M. A., Hess, A., Bloch,W., and Michel, O. (2005). Activation of caspase-3 is associated with oxidative stress in the hydropic guinea pig cochlea. *Hear. Res.* 2005, 202, 21–27. doi: 10.1016/j.heares.2004.10.002

LeFloc'h, J., Tan, W., Telang, R. S., Vlajkovic, S. M., Nuttall, A., Rooney, W. D., et al. (2014). Markers of cochlear inflammation. *J. Magn. Reson. Imaging* 39, 150–161. doi: 10.1002/jmri.24144

Li. H., and Förstermann, U. (2013). Uncoupling of endothelial NO synthase in atherosclerosis and vascular disease. *Curr. Opin. Pharmacol.* 13, 161–167. doi: 10.1016/j.coph.2013.01.006

Liu, F., Xia, M., and Xu, A. (2008). Expression of VEGF, iNOS, and eNOS is increased in cochlear of diabetic rat. *Acta-Otolaryngol.* 128, 1178–1186. doi: 10.1080/00016480801901774

Liu, I. Y., Sepahdari, A. R., Ishiyama, G., and Ishiyama, A. (2016). High resolution MRI shows presence of endolymphatic hydrops in patients still symptomatic after endolymphatic shunt surgery. *Otol. Neurotol.* 37, 1128–1130. doi: 10.1097/MAO.0000000000001144

Liu, J. S. H., Zhao, M. L., Brosnan, C., and Lee, S. C. (2001). Expression of inducible nitric oxide synthase and nitrotyrosine in multiple sclerosis lesions. *Am. J. Pathol.* 158, 2057–2066.

Liu, S., Agalliu, D., Yu, C., and Fisher, M. (2012). The role of pericytes in blood–brain barrier function and stroke. *Curr. Pharm. Des.* 18, 3653–3662. doi: 10.2174/138161212802002706

Lopez, I. A., Ishiyama, G., Hosokawa, S., Hosokawa, K., Acuna, D., Linthicum, F. H., et al. (2016). Immunohistochemical techniques for the human inner ear. *Histochem. Cell Biol.* 146, 367–387. doi: 10.1007/s00418-016-1471-2

Lopez-Escamez, J. A., Carey, J., Chung, W.-H., Goebel, J. A., Magnusson, M., Mandala, M., et al. (2015). Diagnostic criteria for Meniere's disease. *J. Vestib. Res.* 25, 1–7.

McCall, A., Ishiyama, G., Lopez, I. A., Sunita, B., and Ishiyama, A. (2009). Histopathological and ultrastructural analysis of vestibular endorgans obtained from patients with Meniere's disease. *BMC Ear Nose Throat. Disord.* 2009;9:4. doi: 10.1186/1472-6815-9-4

Ménière's, P. (1861). Sur une forme de surdité grave dépendant d'une lésion de l'oreille interne. *Gaz Méd de Paris* 16:29.

Morizane, I., Hakuba, N., Hyodo, J., Shimizu, Y., Fujita, K., Yoshida, T., et al. (2005). Ischemic damage increases nitric oxide production via inducible nitric oxide synthase in the cochlea. *Neurosci. Lett.* 391, 62–67. doi: 10.1016/j.neulet.2005.08.038

Nag, S. (2003). Pathophysiology of blood-brain barrier breakdown. *Methods Mod Med.* 89, 97–119. doi: 10.1385/1-59259-419-0:97

Nag, S., Kapadia, N. A., and Stewart, D. J. (2011). Review: molecular pathogenesis of blood-brain barrier breakdown in acute brain injury. *Neuropathol. Appl. Neurobiol.* 37, 3–23. doi: 10.1111/j.1365-2990.2010.01138.x

Naganawa, S., and Nakashima, T. (2014). Visualization of endolymphatic hydrops with MR imaging in patients with Meniere's disease and related pathologies: current status of its methods and clinical significance. *Jpn. J. Radiol.* 32, 191–204. doi: 10.1007/s11604-014-0290-4

Nagata, M., Katz, M. L., and Robinson, W. G. Jr. (1986). Age related thickening of retinal capillary basement membrane. *Investigative Ophthalmol and Visual Sci* 27, 437–440.

Neng, L., Zhang, F., Kachelmeier, A., and Shi. X. (2013). Endothelial cell, pericytes, and perivascular macrophage-type melanocyte interactions regulate cochlear intrastrial fluid-blood barrier permeability. *JARO* 14,175–185. doi: 10.1007/s10162-012-0365-9

Pakdaman, M. N., Ishiyama, G., Ishiyama, A., Peng, K. A., Kim, H. J., Pope, W. B., et al. (2016). Blood-labyrinth barrier permeability in Meniere's disease and idiopathic sudden sensorineural hearing loss: findings on delayed contrast 3D-Flair MRI. *AJNR Am. J. Neuroradiol.* doi: 10.3174/ajnr.A48822 [Epub ahead of print].

Peluffo, G., and Radi, R. (2007). Biochemistry of protein tyrosine nitration in cardiovascular pathology. *Cardiovasc. Res.* 75, 291–302. doi: 10.1016/j.cardiores.2007.04.024

Popa, R., Anniko, M., Takumida, M., and Arnold, W. (2001). Localization of nitric oxide synthase isoform in the human cochlea. *Acta Otolaryngol.* 121, 454–459. doi: 10.1080/000164801300366570

Rapoport, S. I., Hori, M., and Klatzo, I. (1972). Testing of a hypothesis for osmotic opening of the blood-brain barrier. *Am. J. Physiol.* 223, 323–325. doi: 10.1152/ajplegacy.1972.223.2.323

Reese, T. S., and Karnovsky, M. J. (1967). Fine structural localization of a blood-brain barrier to exogenous peroxidase. *J. Cell. Biol.* 34, 207–217. doi: 10.1083/jcb.34.1.207

Ronaldson, P. T., and Davis, T. P. (2015). Targeting transporters: promoting blood-brain barrier repair in response to oxidative stress injury. *Brain Res.* 1623, 39–52. doi: 10.1016/j.brainres.2015.03.018

Schuknecht, H. F. (1993). *Pathology of the Ear*, 2nd Edn. Philadelphia, PA: Lea and Febiger.

Sepahdari, A. R., Ishiyama, G., Vorasubin, N., Peng, K. A., Linetsky, M., and Ishiyama, A. (2015). Delayed intravenous contrast-enhanced 3D FLAIR MRI in Meniere's disease: correlation of quantitative measures of endolymphatic hydrops with hearing. *Clin. Imaging* 39, 26–31. doi: 10.1016/j.clinimag.2014.09.014

Sepahdari, A. R., Vorasubin, N., Ishiyama, G., and Ishiyama, A. (2016). Endolymphatic hydrops reversal following acetazolamide therapy: demonstrated with delayed intravenous contrast-enhanced 3D-FLAIR MRI. *Am. J. Neuroradiol.* 37, 151–154. doi: 10.3174/ajnr.A4462

Shi, X. (2009). Cochlear pericyte responses to acoustic trauma and the involvement of hypoxia-inducible factor-1-alpha and vascular endothelial growth factor. *Am. J. Pathol.* 174, 1692–1704. doi: 10.2353/ajpath.2009.080739

Shi, X. (2010). Resident macrophages in the cochlear blood-labyrinth barrier and their renewal via migration of bone-marrow-derived cells. *Cell Tissue Res.* 342, 21–30. doi: 10.1007/s00441-010-1040-2

Shi, X. (2011). Physiopathology of the cochlear microcirculation. *Hear. Res.* 282, 10–24. doi: 10.1016/j.heares.2011.08.006

Shi, X. (2016). Pathophysiology of the cochlear intrastrial fluid-blood barrier (review) Hear. *Res.* 338, 52–63. doi: 10.1016/j.hearres.2016.01.010

Shi. X., Han, W., Yamamoto, H., Tang, W., Lin, X., Xiu, R., et al. (2008). The cochlear pericytes. *Microcirculation* 15, 515–529. doi: 10.1080/10739680802047445

Shi, X., and Nuttall, A. L. (2002). The demonstration of nitric oxide in cochlear blood vessels in vivo and in vitro: the role of endothelial nitric oxide in venular permeability. *Hear. Res.* 172, 73–80. doi: 10.1016/S0378-5955(02)00513-0

Shi, X., and Nuttall, A. L. (2003). Upregulated iNOS and oxidative damage to the cochlear stria vascularis due to noise stress. *Brain Res.* 967, 1–10. doi: 10.1016/S0006-8993(02)04090-8

Stokum, J. A., Gerzanich, V., and Simard, J. M. (2016). Molecular pathophysiology of cerebral edema. *J. Cereb. Blood Flow Metab.* 36, 513–538. doi: 10.1177/0271678x15617172

Suzuki, M., and Kaga, K. (1999). Development of blood-labyrinth barrier in the semicircular canal ampulla of the rat. *Hear. Res.* 129, 27–34. doi: 10.1016/S0378-5955(98)00214-7

Tagaya, M., Yamazaki, M., Teranishi, M., Suzuki, K., Iwano, S., Satake, H., et al. (2011). Endolymphatic hydrops and blood-labyrinthine barrier in Meniere's disease. *Acta Otolaryngol.* 131, 474–479. doi: 10.3109/00016489.2010.534114

Takumida, M., Akagi, N., and Anniko, M. (2008). A new animal mode for Meniere's disease. *Acta Otolaryngol.* 128, 263–271. doi: 10.1080/00016480701497436

Takumida, M., and Anniko, M. (1998a). Lipopolysaccharide-induced expression of nitric oxide synthase II in the guinea pig vestibular end organs. *Eur. Arch. Otorhinolaryngol.* 255, 184–188. doi: 10.1007/s004050050040

Takumida, M., and Anniko, M. (1998b). Localization of nitric oxide synthase isoforms (NOS I,II and III) in the vestibular end organs of the guinea pig. *ORL* 60, 67–72. doi: 10.1159/000027567

Takumida, M., and Anniko, M. (2001). Nitric oxide in guinea pig vestibular sensory cells following Gentamicin exposure in vitro. *Acta Otolaryngol.* 121, 346–350. doi: 10.1080/000164801300102734

Takumida, M., and Anniko, M. (2004). Functional significance of nitric oxide in the inner ear. *In vivo* 18, 345–350.

Teranishi, M., Uchida, Y., Nishio, N., Kato, K., Otake, H., Yoshida, T., et al. (2012). Polymorphisms in genes involved in oxidative stress response in patients with sudden sensorineural hearing loss and Ménière's disease in a japanese population. *DNA Cell Biol.* 31, 1555–1562. doi: 10.1089/dna.2012.1631

Trune, D. R., and Nguyen-Huynh, A. (2012). Vascular pathophysiology in hearing disorders. *Semin. Hear.* 33, 242–250. doi: 10.1055/s-0032-1315723

Tuerdi, A., Kinoshita, M., Kamogashira, T., Fujimoto, C., Iwasaki, S., Shimizu, T., et al. (2017). Manganese superoxide dismutase influences the extent of noise-induced hearing loss in mice. *Neurosci. Lett.* 642, 123–128. doi: 10.1016/j.neulet.2017.02.003

Vasquez-Vivar, J., Kalyanaraman, B., Martásek, P., Hogg, N., Masters, B. S. S., Karoui, H., et al. (1998). Superoxide generation by endothelial nitric oxide synthase: the influence of cofactors. *Proc. Natl. Acad. Sci. U.S.A.* 95, 9220–9225. doi: 10.1073/pnas.95.16.9220

Wackym, P. A. (1995). Histopathologic findings in Meniere's Disease. *Otol. Head & Neck Surg.* 112, 90–100. doi: 10.1016/S0194-5998(95)70307-1

Watanabe, K. I., Hess, A., Bloch, W., and Michel, O. (2000). Inhibition of inducible nitric oxide synthase lowers the cochlear damage by lipopolysaccharide in guinea pigs. *Free Radical Res.* 32, 363–370. doi: 10.1080/10715760000300361

Wu, Y. X., Zhu, G. X., Liu, X. Q., Sun, F., Zhou, K., Wang, S., et al. (2014). Noise alters guinea pig's blood labyrinth barrier ultrastructure and permeability along with a decrease of cochlear claudin-5 and occludin *BMC Neurosci.* 15:136. doi: 10.1186/s12868-014-0136-0

Yamakawa, K. (1938). Uber die pathologisch veranderung bei einem Ménière-kranken. *J. Otorhinolaryngol. Soc. Jpn.* 4, 2310–2312.

Yamazaki, M., Naganawa, M., Tagaya, M., Kawai, H., Ikeda, M., Sone, M., et al. (2012). Comparison of contrast effect on the cochlear perilymph after intratympanic and intravenous gadolinium injection. *AJNR* 33, 773–778. doi: 10.3174/ajnr.A2821

Ye, Y. Z., Strong, M., Huang, Z. Q., and Beckman, J. S. (1996). Antibodies that recognize nitrotyrosine. *Methods Enzymol.* 269, 201–209. doi: 10.1016/S0076-6879(96)69022-3

Yemisci, M., Gursoy-Ozdemir, Y., Vural, A., Can, A., Topalkara, K., and Dalkara, T. (2009). Pericyte contraction induced by oxidative-nitrative stress impair capillary reflow despite successful opening of an occluded cerebral artery. *Nat. Med.* 15, 1031–1037. doi: 10.1038/nm.2022

Zhang, F., Zhang, J., Neng, L., and Shi, X. (2013). Characterization and inflammatory response of perivascular macrophage-resident macrophage-like melanocytes in the vestibular system. *JARO* 14, 635–643. doi: 10.1007/s10162-013-0403-2

Zou, J., Pyykkö, I., Bjelke, B., Dastidar, P., and Toppila, E. (2005). Communication between the perilymphatic scalae and spiral ligament visualized by in vivo MRI. *Audiol. Neurotol.* 10, 145–152.

Conflict of Interest Statement: The authors declare that the research was conducted in the absence of any commercial or financial relationships that could be construed as a potential conflict of interest.

The handling Editor declared a shared affiliation, though she has no past or active collaboration with the authors prior to the editorial assignment.

frontiers in Physiology

SYSTEMATIC REVIEW
published: 17 December 2018
doi: 10.3389/fphys.2018.01799

Review on Chamber-Specific Differences in Right and Left Heart Reactive Oxygen Species Handling

Klaus-Dieter Schlüter, Hanna Sarah Kutsche, Christine Hirschhäuser, Rolf Schreckenberg and Rainer Schulz*

Department of Physiology, Justus-Liebig-University Giessen, Giessen, Germany

Reactive oxygen species (ROS) exert signaling character (redox signaling), or damaging character (oxidative stress) on cardiac tissue depending on their concentration and/or reactivity. The steady state of ROS concentration is determined by the interplay between its production (mitochondrial, cytosolic, and sarcolemmal enzymes) and ROS defense enzymes (mitochondria, cytosol). Recent studies suggest that ROS regulation is different in the left and right ventricle of the heart, specifically by a different activity of superoxide dismutase (SOD). Mitochondrial ROS defense seems to be lower in right ventricular tissue compared to left ventricular tissue. In this review we summarize the current evidence for heart chamber specific differences in ROS regulation that may play a major role in an observed inability of the right ventricle to compensate for cardiac stress such as pulmonary hypertension. Based on the current knowledge regimes to increase ROS defense in right ventricular tissue should be in the focus for the development of future therapies concerning right heart failure.

Keywords: cardiac remodeling, heart failure, oxidative stress, pulmonary hypertension, uncoupling protein, MAO

OPEN ACCESS

Edited by:
Thao P. Nguyen, UCLA David Geffen School of Medicine, United States

Reviewed by:
Marcos Lopez, University of Chicago, United States
Marlin Touma, UCLA David Geffen School of Medicine, United States

****Correspondence:***
Klaus-Dieter Schlüter
klaus-dieter.schlueter@physiologie.med.uni-giessen.de

Specialty section:
This article was submitted to Oxidant Physiology, a section of the journal Frontiers in Physiology

Received: *06 September 2018*
Accepted: *29 November 2018*
Published: *17 December 2018*

Citation:
Schlüter K-D, Kutsche HS, Hirschhäuser C, Schreckenberg R and Schulz R (2018) Review on Chamber-Specific Differences in Right and Left Heart Reactive Oxygen Species Handling. Front. Physiol. 9:1799. doi: 10.3389/fphys.2018.01799

INTRODUCTION

Oxidative stress is defined as a condition by which an imbalance occurs between the production of reactive oxygen species (ROS) and the antioxidant defense system. The term ROS includes molecules that have one or more unpaired electrons (i.e., superoxide and hydroxyl) and non-radicals that are able to generate free radicals (i.e., hydrogen peroxide). Intracellular sources of ROS are the electron transport chain of the mitochondria, monoamine oxidase (MAO), p66shc (for review, see Di Lisa et al., 2017), xanthine oxidase (XO), uncoupling proteins (UCP, depending on the mitochondrial membrane potential; for review see Cadenas, 2018), uncoupled nitric oxide (NO) synthase (NOS), sodium-potassium ATPase (NKA), and nicotinamide adenine dinucleotide phosphate (NADPH) oxidase (NOX) (for review, see Egea et al., 2017). The defense system contains enzymes such as superoxide dismutase (SOD), catalase, glutathione peroxidase, and coupled NOS. **Figures 1**, **2** give an overview about ROS sources and ROS defense systems in the heart. Whereas subtle changes in ROS act as intracellular signaling pathways (*redox signaling*) high levels of ROS can cause cell damage and dysfunction (*oxidative stress*) (for review, see Egea et al., 2017).

The following review article now summarizes our current understanding about similarities and differences in ROS handling between LV and RV. We searched the current literature (PubMed, MedLine data bank until July, 2018) using the terms "right heart and ROS," "pulmonary hypertension and ROS," "RV failure and ROS," "LV failure and ROS," "RV hypertrophy and ROS"

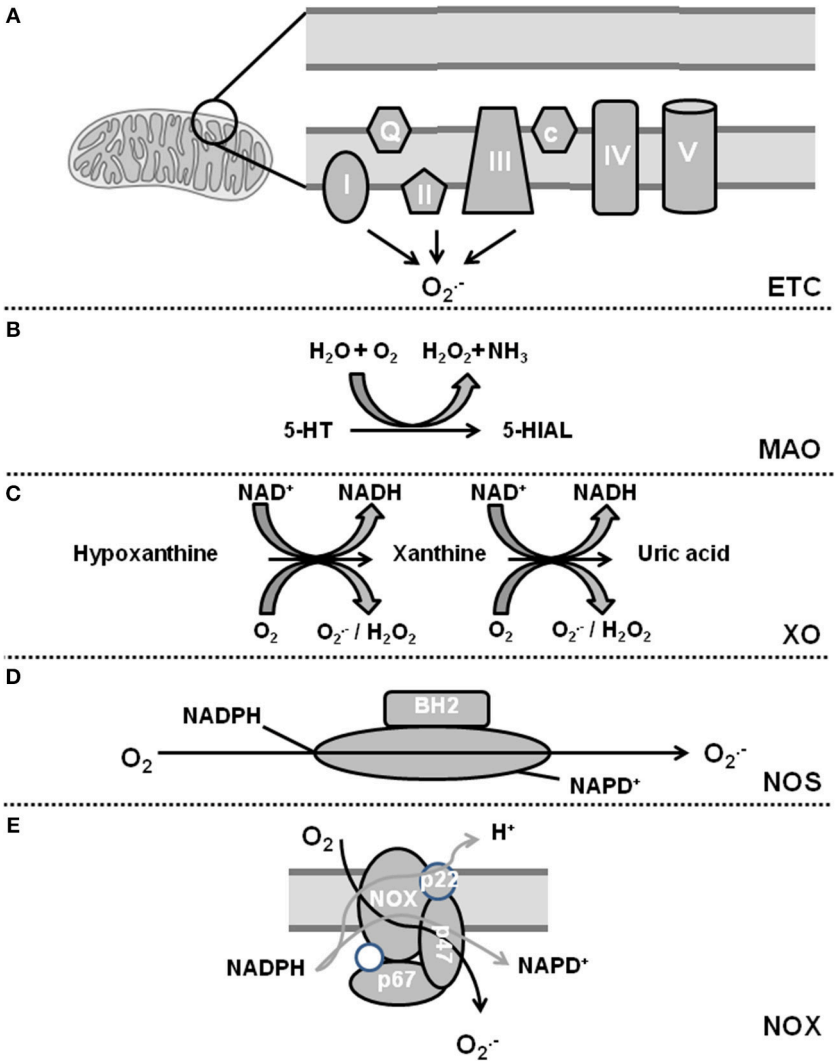

FIGURE 1 | Sources of reactive oxygen species in cardiomyocytes. **(A)** Complex I and III of the electron transport chain (ETC) constitutively release $O_2^{\cdot-}$ and complex II can be activated by NOX-dependent ROS. **(B)** Monoamine oxidase (MAO) generates H_2O_2. **(C)** Xanthine oxidase (XO) catalyzes a two-step reaction leading to additional release of H_2O_2. **(D)** Uncoupling of nitric oxide synthase (NOS) leads to generation of $O_2^{\cdot-}$. **(E)** NADPH oxidase (NOX) generates also $O_2^{\cdot-}$ upon activation.

and "LV hypertrophy and ROS." Most studies dealing with ROS and RV hypertrophy used models of pulmonary hypertension induced by banding, monocrotaline injection or chronic hypoxia. In these models ROS contribute to pulmonary hypertension and RV remodeling. In many studies, effects of ROS reduction on RV hypertrophy were secondary to reduced pulmonary pressure (reviewed by Wong et al., 2013). In the current review we therefore focus on studies directly assessing ROS and ROS-dependent effects in RV tissue and compare these results to established concepts generated from the LV.

OXIDATIVE STRESS IN THE HEART

Oxidative stress in cardiomyocytes occurs during chronic pressure or volume overload of the heart (Gladden et al., 2013; Hansen et al., 2016), cardiac ischemia/reperfusion (Riba et al., 2017), cardiomyopathy (Ishikawa et al., 2005), diabetes (Guido et al., 2017), chemotherapy-induced heart failure in the left (Mouli et al., 2015; Li et al., 2018), and right ventricle (Anghel et al., 2018), poison such as cigarette smoke (Talukder et al., 2011), chronic kidney disease (Duni et al., 2017), or aging (Chang et al., 2017), or as a response to congenital heart failure (Iacobazzi et al., 2016). Within the heart other sources of ROS are cells adjacent to cardiomyocytes such as inflammatory cells (Xu et al., 2011; Hernandez-Resendiz et al., 2018), endothelial cells (Burger et al., 2011), stem cells (Mandraffino et al., 2017), and cardiac fibroblasts (Ciulla et al., 2011). Redox signaling contributes to cardiac hypertrophy and even more important oxidative stress contributes to the transition of adaptive to maladaptive cardiac hypertrophy,

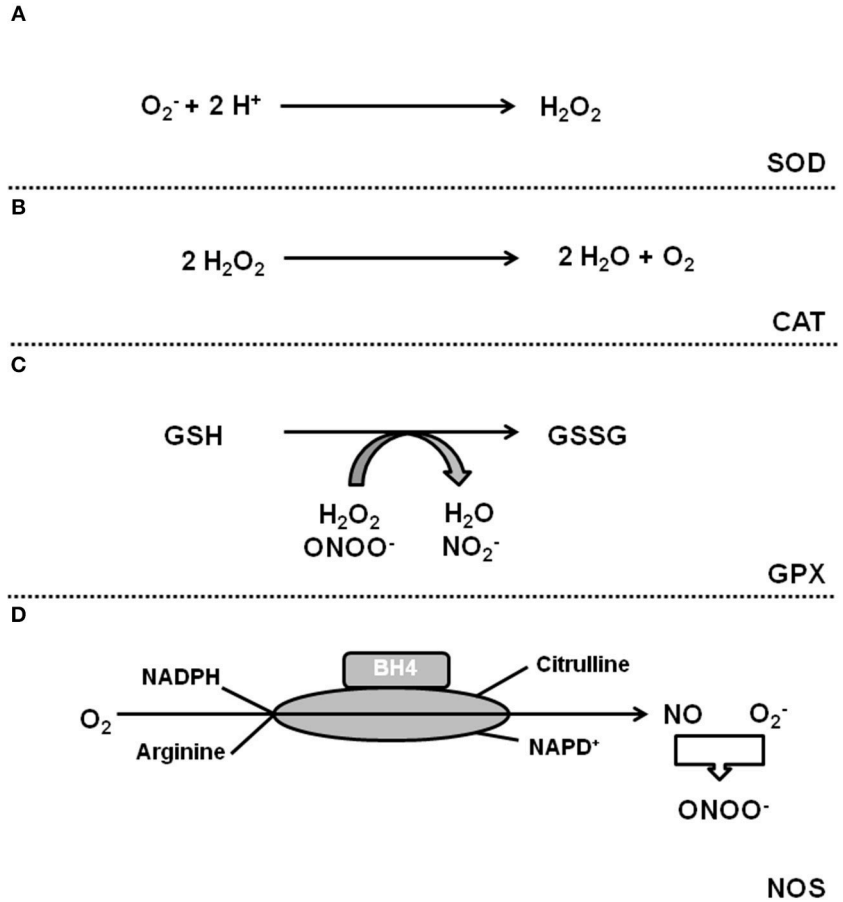

FIGURE 2 | ROS defense systems in cardiomyocytes. **(A)** Superoxide dismutases catalyze the formation of H_2O_2 that can be detoxificated by catalase **(B)**. **(C)** Gluatathione peroxidase (GPX) reduces H_2O_2. **(D)** Coupled NOS generates NO that neutralizes $O_2^{\cdot-}$.

named maladaptive remodeling. Oxidative stress can damage cells by growth factor-independent activation of cardiac growth regulation (Calamaras et al., 2015), can inactivate NO leading to loss of myocyte-specific NO function (Rassaf et al., 2006; Lüneburg et al., 2016), can directly reduce cardiomyocyte function by oxidative modification of sarcomere proteins such as tropomyosin (Heusch et al., 2010b; Canton et al., 2011) or sarcoplasmatic reticulum proteins (i.e., SERCA; Qin et al., 2017), can induce a calcium desensitization of myofibrils (Wang et al., 2008), can activate the Na-K-ATPase (Wang et al., 2017a), can damage mitochondrial function (Ide et al., 2001; Sverdlov et al., 2016), or can induce cell death (apoptosis, necrosis; Redza-Dutordoir and Averill-Bates, 2016). Therefore, ROS defense strategies of the cells are necessary for cell survival and functional stabilization in both ventricles.

DIFFERENCES BETWEEN RIGHT AND LEFT VENTRICLE

The different chambers of the heart are derived from different embryonic origin, namely the first (left ventricle, LV) and second heart field (right ventricle, RV). In rodent hearts, cardiomyocytes isolated from the LV or RV differ in size, number of mononucleated cells, cellular adaptation to culture conditions, and cell shortening (Schlüter, 2016; summarized in **Figure 3**). This gives raise to speculations that the LV and RV may differentially respond to cardiac stresses. Pressure overload is associated with adaptations performed on the transcriptional level. Many of them are similar between the RV and LV. However, some genes are upregulated in the pressure-overloaded RV only, including genes involved in Wnt signaling (Dickkopf 3, Sfrp2, and Wif1), annexin A7, clusterin/apolipoprotein J, neuroblastoma suppression of tumorigenicity 1 (Nbl1), formin-binding protein (Fnbp4), and the lectin-like oxidized low-density lipoprotein (oxLDL) receptor (LOX; Reddy and Bernstein, 2015). Differences occur also on the level of miRNA (Reddy and Bernstein, 2015). Considering the high impact of ROS for cardiac adaptation to pressure overload, it is also important to understand such differences with respect to ROS formation, ROS defense, and ROS-dependent cellular responses. Indeed, mitochondria isolated from the LV or RV of rat hearts generates different amounts of ROS (Schreckenberg et al., 2015; summarized in **Figure 3**). Treatment of isolated perfused rat hearts with serotonin, a substrate for MAO, results

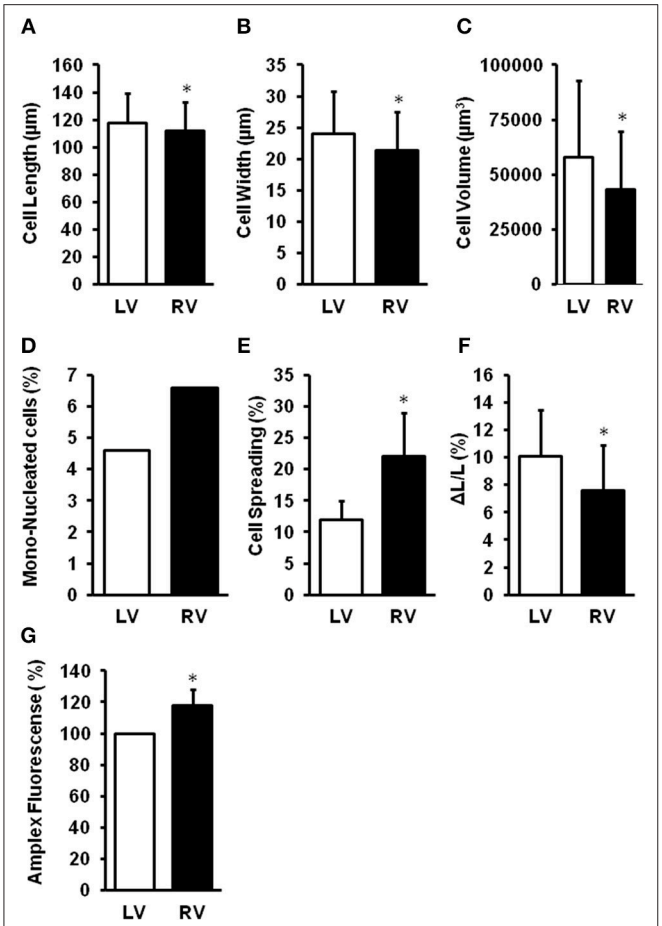

FIGURE 3 | Differences between right (RV) and left (LV) ventricular cardiomyocytes. LV cardiomyocytes are longer **(A)**, wider **(B)**, larger **(C)**, less mono-nucleated **(D)**, have a reduced cell spreading **(E)** as adaptation to culture conditions, and a stronger load-free cell shortening **(F)**. Furthermore, mitochondria from RV generate more ROS **(G)**. Data depicted from Schreckenberg et al. (2015) and Schlüter (2016). *$p < 0.05$ vs. LV.

in the promotion of protein carbonylation as evidenced by increased ROS formation, specifically in the RV but not the LV. Interestingly, no differences between RV and LV antioxidant enzymes and serotonin receptors/transporter are detected (Liu et al., 2008).

ROS IN RIGHT HEART HYPERTROPHY AND FAILURE: CYTOSOLIC ROS

Pressure overload induces the NOX subunit gp91 (Li et al., 2002; Byrne et al., 2003; Tanaka et al., 2005; Grieve et al., 2006; Liu et al., 2006, 2010; Guggilam et al., 2007; DeMarco et al., 2008; Nisbet et al., 2009; Chemaly et al., 2011; Xu et al., 2011; Ogura et al., 2013; Frazziano et al., 2014; Matsuda et al., 2015; Ma et al., 2016; Sirker et al., 2016; Zhu et al., 2017). In human right and left heart failure the p47phox subunit of NOX also translocates to the sarcrolemma (Nediani et al., 2007). Increased NOX expression is associated with increased formation of superoxide anions (Nediani et al., 2007; Ogura et al., 2013; Dos Santos Lacerda et al., 2017; Türck et al., 2018). Furthermore, hypoxia, leading to pulmonary hypertension, and RV hypertrophy, increases RV expression of NOX2/4 (Liu et al., 2014; Ye et al., 2016; Zhu et al., 2017). In the monocrotaline-induced pulmonary hypertension rat model, Nox4 expression is induced in cardiomyocytes but also in the intercellular area (mainly co-localizing with fibroblasts) (He et al., 2017). In the RV, NOX4 is also regulated by the α_{1A}-receptor (Cowley et al., 2017); stimulation of this receptor decreases NOX4 expression during pulmonary hypertension. NOX-dependent ROS modifies mitochondrial function by increased release of ROS from complex II of the mitochondria during the transition from RV hypertrophy to failure (Redout et al., 2007) (ROS induced ROS release). There are differences between the RV and LV ventricles in the primary source of ROS production. In the RV, NOX, and mitochondrial complex II activity both increase during the transition to heart failure, whereas, in the LV, NOX appears to be the primary source of ROS generation (Redout et al., 2010).

Xanthine oxidoreductase (XO) activity remains unaltered in the monocrotaline-induced RV hypertrophy model but its activity increases with the transition to RV failure. XO is mainly localized in $CD68^+$ inflammatory cells based on studies with an affinity-purified polyclonal antibody (de Jong et al., 2000). In another rat model of pulmonary hypertension-induced RV failure, metabolomics analysis revealed an increase in xanthine, and uric acid in the hypertrophied RV, suggesting the production of ROS by XO. Furthermore, the RV level of α-tocopherol nicotinate declined, consistent with oxidative stress decreasing antioxidants (Wang et al., 2017). XO also contributes to ROS formation in LV (Moris et al., 2017).

Uncoupled NOS is another protein involved in the generation of oxidative stress in the LV secondary to pressure overload (Takimoto et al., 2005). In the RV, uncoupled NOS contributes to ROS generation, too. In caveolin-1 (Cav-1) knockout mice subjected to chronic hypoxia the transition from RV hypertrophy to failure is accelerated compared to wild-type mice and caused by uncoupling of RV endothelial NOS and increased protein tyrosine nitration; all changes are prevented by re-expressing an endothelial-specific Cav-1 transgene (avoiding NOS uncoupling) or by NOS inhibition without modifying the extent of pulmonary hypertension (Cruz et al., 2012). Also, in a pharmacological model of hypertension chronic administration of L-NAME leads to uncoupling of NOS in RV (Schreckenberg et al., 2015).

Uncoupling of NOS can be caused by reduced substrate (arginine) for NOS. Reasons for substrate limitation can be an induction of arginase that leads to substrate limitation (Heusch et al., 2010; Schreckenberg et al., 2015), increased plasma concentrations of asymmetric dimethyl arginine (ADMA), a natural circulating inhibitor of NOS (Lüneburg et al., 2016), or depletion of NOS with tetrahydrobiopterin (BH_4, Shimizu et al., 2013).

ROS IN RIGHT HEART HYPERTROPHY AND FAILURE: MITOCHONDRIAL ROS

A proteomic analysis of the normal rabbit and porcine RV and LV free walls shows equivalent cellular aerobic capacity, volume

of mitochondria, mitochondrial enzyme content (cytochrome c oxidase, respiratory complexes 1 and 3–5, aconitase, SOD), and mitochondrial enzyme activities (Phillips et al., 2011). Interestingly, mitochondrial membrane potential, a surrogate of overall mitochondrial function, is lower in the resting RV compared to the LV (Nagendran et al., 2008), while—at least in rats—ROS formation in mitochondria isolated from the RV is slightly higher than in LV mitochondria (Schreckenberg et al., 2015). At last in part, the latter might be the consequence of a reduced ROS defense capacity (Borchi et al., 2010; Manni et al., 2016). Comparing mitochondria from hypertrophic RV with those of non-hypertrophic LV revealed differences in electrone transport chain activity and ATP generating enzyme expression Gupto et al., 2016.

While the mitochondrial protein profiles of the RV and LV are quite similar at rest, they diverge when subjected to an increased afterload (Phillips et al., 2011), and mitochondrial membrane potential increases with RV hypertrophy (Nagendran et al., 2008). This hyperpolarization of mitochondria, indicating reduced oxidative phosphorylation, is related to an activation of the nuclear factor of activated T cells (NFAT) pathway and is reversed by dichloroacetate, an inhibitor of pyruvate dehydrogenase kinases (PDK) (Nagendran et al., 2008). Thus, an increase in PDK activity in RV hypertrophy contributes to the decreased oxidation of pyruvate in mitochondria and an increased conversion of pyruvate to lactate in the cytosol. An increase in glycolytic hexokinase and lactate dehydrogenase activities occurs following monocrotaline-induced pulmonary hypertension at the stage of compensated RV hypertrophy (Balestra et al., 2015), further supporting the concept of a metabolic switch from mitochondrial oxidative phosphorylation to glycolysis in the compensated phase of RV hypertrophy (Paulin and Michelakis, 2014; Sutendra and Michelakis, 2014). Indeed, a decreased mitochondrial oxygen usage and an increased anaerobic glycolysis has been described in patients with pulmonary hypertension (Wong et al., 2011) (for a detailed review, see Freund-Michel et al., 2014), and the decrease in mitochondrial oxidative phosphorylation during the development of RV hypertrophy has been suggested to decrease mitochondrial ROS formation (for review, see Paulin and Michelakis, 2014).

The increase in glucose uptake and the mitochondrial hyperpolarization are lost with the progression of RV hypertrophy to failure (Nagendran et al., 2008). For the LV, ROS sensors revealed increased mitochondrial ROS in resting and contracting cardiomyocytes during the progression to heart failure. Pathway analysis of mitochondrial ROS-sensitive networks indicated that increased mitochondrial ROS in failing cardiomyocytes disrupts the normal coupling between cytosolic signals and nuclear gene programs driving mitochondrial function, calcium handling, action potential repolarization, and antioxidant enzymes (Dey et al., 2018). Indeed, in the RV, during the transition from RV hypertrophy to RV failure, mitochondrial ROS defense system (SOD-2) is down-regulated (Redout et al., 2007).

Another key regulator that is decreased during RV failure is the peroxisome proliferator-activated receptor gamma coactivator (PGC) 1α, leading to impaired fatty acid oxidation, decreased mitochondrial mass and number, and reduced oxidative capacity, potentially contributing to increased ROS production (Karamanlidis et al., 2011; Gomez-Arroyo et al., 2013). In an animal model of pulmonary hypertension-induced RV failure, fatty acid oxidation decreases secondary to the failure of palmitoylcarnitine to stimulate oxygen consumption. In humans with pulmonary hypertension, RV long-chain fatty acids and triglyceride contents are increased and ceramide, a mediator of lipotoxicity, accumulates (Brittain et al., 2016).

ROS DEFENSE SYSTEMS IN RV

In rats treated with monocrotaline to increase pulmonary artery pressure without inducing RV hypertrophy, RV hydrogen peroxide increases but SOD, catalase, and glutathione peroxidase activities are also enhanced (Siqueira et al., 2018).

During pressure overload–induced LV hypertrophy, antioxidant enzymes are activated in the compensated stage but their activity decreases during the onset of LV failure. In contrast, only the antioxidant enzyme catalase becomes activated in some (Ecarnot-Laubriet et al., 2003) but not all studies (Pichardo et al., 1999) while SOD and glutathione peroxidase are not activated at all in the compensated stage of RV hypertrophy secondary to pulmonary hypertension, predisposing the RV to ROS induced damage at an earlier stage than in the LV (Pichardo et al., 1999; Ecarnot-Laubriet et al., 2003; Schreckenberg et al., 2015). With a progression of from RV hypertrophy to failure, down-regulation of antioxidant enzymes, and increased ROS production occurs in a mice model of pulmonary hypertension (Aziz et al., 2015; Reddy and Bernstein, 2015), although in one model of monocrotaline-induced RV failure, glutathione peroxidase increases while catalase, and SOD activities are similar to sham animals (Türck et al., 2018).

Despite some controversial results the general view, however, remains that increased ROS formation and decreased ROS defense leads to increased oxidative stress driving the progression from RV hypertrophy to RV failure.

DOWNSTREAM SIGNALING

(Patho)physiological conditions known to activate p38 mitogen activated protein (MAP) kinase are often associated with increased ROS formation (Wenzel et al., 2001, 2006, 2007). Indeed, p38 MAP kinase is activated by oxidative stress (Redout et al., 2007). An activation of p38 MAP kinase pathways is linked to cardiac hypertrophy and dysfunction and in RV and LV of end-stage failing human hearts, p38 MAP kinase and extracellular-signal regulated kinase (ERK), but not c-Jun N-terminal kinases (JNK), are activated; a significant correlation between protein kinase activities is observed between LV and RV from the same heart (Nediani et al., 2007).

Increased ROS subsequently modifies tropomyosin, induces matrix metalloproteases (MMPs 2, 9, and 13), sensitizes β-adrenoceptors (via induction of protein kinase C-ε), and causes endothelial dysfunction in the right ventricle (Cheng et al., 2009; Lu et al., 2011; Cau et al., 2013; Schreckenberg et al., 2015).

In LV tissue, ROS is associated with an induction of $p90^{rsk}$ and the sodium-proton-exchanger (NHE) and furthermore, via ROS-dependent formation of lipid peroxidation-derived aldehydes (Cingolani et al., 2011). Furthermore, ROS activates the mammalian target of rapamycin (mTOR)-$p70^{s6k}$ pathway (Calamaras et al., 2015). Both pathways (NHE and mTOR-$p70^{s6k}$) are also involved in growth factor-dependent acceleration of protein synthesis (Simm et al., 1998; Schäfer et al., 2002). Commonly ROS and growth factors activate also the ERK pathway but the latter is not directly linked to the regulation of protein synthesis (Pönicke et al., 2001; Calamaras et al., 2015).

Apart from NOX, activation of the renin-angiotensin-system is apparent in the RV during pressure overload (for review, see Ameri et al., 2016). Compared to normal hearts, however, angiotensin II binding is diminished in the failing RV of pulmonary artery hypertension patients due to angiotensin II type 1 receptor down-regulation, despite RV myocardial angiotensin converting enzyme (ACE) activity being increased (Zisman et al., 1998). Interestingly, the ACE DD genotype, associated with an increased myocardial ACE activity, is more frequent in patients with pulmonary hypertension than in healthy individuals, but it is also associated with preserved RV function in pulmonary hypertension patients (Abraham et al., 2003).

A specific role for LOX-1 in RV hypertrophy and failure has been suggested. First, oxLDL receptors cross react with NOX (Ogura et al., 2013). Furthermore, ventricular expression of oxLDL receptors is induced under hypoxia leading to pulmonary hypertension and RV hypertrophy (Zhu et al., 2017). Cross-reactivity of oxLDL receptors with angiotensin II receptors type 1 has also been reported. In all these cases, NOX is subsequently activated favoring oxidative stress. It seems that this mechanism plays an important role in right heart failure.

THERAPEUTIC IMPLICATIONS

In general, attenuation of mitochondrial-derived oxidative stress is a reasonable therapeutic concept to attenuate RV hypertrophy and transition to RV failure (for review, see Maarman et al., 2017).

As expected from the findings that ROS is increased in RV hypertrophy and transition to RV failure, trapping molecules targeting mitochondrial ROS (mitoTEMPO), folic acid, EUK-134, a synthetic antioxidant mimicking the activity of SOD, attenuate RV hypertrophy (Redout et al., 2010; Qipshidze et al., 2012; Datta et al., 2015).

Regulation of SOD, in particular SOD-1 (located in the cytosol), and SOD-2 (located in mitochondria), has been proven to attenuate hypertrophy and even more important transition to heart failure. In a pharmacological rat model of hypertension (L-NAME induced hypertension) SOD-2 was induced in the LV but not in the RV (Schreckenberg et al., 2015). Up-regulation of SOD-2 in the LV was associated with less oxidative stress and preserved function in the presence of hypertrophy. Similarly, induction of SOD-2 activity has repeatedly reported to improve cardiac

TABLE 2 | Differences between LV and RV in ROS handling leading to hypertrophy and failure.

(A) ROS formation		
NOX gp91	LV ↑	RV ↑
NOX p47phox	LV ↑	RV ↑
NOX2/4		RV ↑
NOX-dependent ROS	LV ↑	
NOX-dependent Complex II		RV ↑
XO		RV ↑
NOS uncoupling	LV ↑	RV ↑
PDK		RV ↑
(B) ROS defense		
α-tocopherol nicotinate		RV ↓
Non-oxidative glucose metabolism		RV ↑
SOD-2	LV ↑	RV ↓
PGC-1α		RV ↓
Catalase	LV ↑	
Glutathione peroxidase	LV ↑	
(C) ROS-associated remodeling		
AT-1 receptor		RV ↓
ACE		RV ↑
LOX-1		RV↑

↑, *activated or induced during hypertrophy and/or transition to failure.*
↓, *deactivated or reduced during hypertrophy and/or transition to failure.*

TABLE 1 | Treatment of the angiotensin-NOX-ROS axis and effects on hypertrophy.

Drug	Species	Tissue	Target	Read-out	References
Isoflavone	Mice	LV	Ang-II-dependent	Hypertrophy	Chen et al., 2014
Taxofilin	Mice	LV	Ang-II-dependent	Hypertrophy	Guo et al., 2015
Spironolacton	Rats	LV	Renin-dependent	Hypertrophy	Habibi et al., 2011
Amlodipine/Atorvastatin	Rats	LV	Hypertension	Hypertrophy	Lu et al., 2009
Green Tea	Rats	LV	Ang-II-dependent	Hypertrophy	Papparella et al., 2008
AT1/ACE-I	Rats	LV	SHR	Hypertrophy	Tanaka et al., 2005
ACE inhibition	Rats	LV	Salt-induced BP	Cardiac function	Tsutsui et al., 2001
Atorvastatin	Rats	LV	Pressure overload	Hypertrophy	Li et al., 2013
Apocynin	Rats	LV	Pressure overload	Hypertrophy	Liu et al., 2010

function. Interestingly, at least for the LV multiple strategies to improve SOD activity work, such as the natural product Sheng-Mai-San (Chai et al., 2016), inhibition of the renin-angiotensin-system (Tanaka et al., 2005), calcium antagonists (Umemoto et al., 2004), or resveratrol (Danz et al., 2009). Whether any of these mechanisms is sufficient to increase SOD activity in RV remains unclear. As mentioned above, SOD is induced during hypertrophy in LV tissue (Date et al., 2002; Lu et al., 2010; Qiao et al., 2014; Aziz et al., 2015; Schreckenberg et al., 2015). Failure to increase SOD as an adaptive mechanism to rescue mitochondrial and cytosolic ROS is associated with heart failure (Redout et al., 2007; Koga et al., 2013). In a model of bronchopulmonary dysplasia, SOD-2 expression but not activity is induced leaving ROS formation unchanged. This underlines the importance of SOD-2 activity for protection against ROS-derived damage. Failure of the RV to up-regulate SOD-2 expression and activity might be a key step for right heart failure.

Other treatment using secoisolariciresinol diglucoside (Puukila et al., 2017), dehydroepiandrosterone (Alzoubi et al., 2013; Rawat et al., 2014), trimethoxystilbene (Liu et al., 2014), pterostilbene (Dos Santos Lacerda et al., 2017), trapidil (Türck et al., 2018), and α_{1A}-adrenoceptor stimulation with A61603 (Cowley et al., 2017) and finally fenofibrate (Galhotra et al., 2018) attenuate both RV hypertrophy and dysfunction and decreases RV ROS levels at the same time; however, a causality between changes in ROS and preservation of RV morphology and/or function could not be proven.

In contrast to the pharmacological approaches, neither the genetic deletion of sirtuin 3 (Waypa et al., 2013) nor the up-regulation of thioredoxin 2 (Adesina et al., 2017) affected RV hypertrophy during pulmonary hypertension. Sirtuin-3 is a nicotinamide adenine dinucleotide–dependent deacetylase that activates forkhead box O3a (FOXO3)-dependent up-regulation of SOD-2 (Sundaresan et al., 2009). Thioredoxin 2 is a mitochondrial located protein involved in ROS defense of the organelle (Dunn et al., 2010).

β-Blockers may also considered as a therapeutic option in right heart failure. β-Adrencoeptor signaling is sensitized by ROS. At least in the left ventricle carvedilol, a β-blocker with antioxidative properties, was able to attenuate the hypertrophic response to anthracylines (Arozal et al., 2011). In rats with monocrotaline-induced pulmonary hypertension bucindolol treatment decreases RV necrosis, fibrosis, and infiltration of inflammatory cells and improves RV systolic function. In addition, bucindolol promotes a decrease in the cardiac sympathovagal balance by reducing sympathetic drive and increasing parasympathetic drive (Lima-Seolin et al., 2017). Changes in ROS were not measured. In a model of hypertension (two-kidney one-clip), β-blockers attenuated ROS and MMP2, a ROS-dependent regulated MMP, independent of its antioxidative property suggesting that direct stimulation of β-adrenoceptors increases ROS in ventricular tissue (Rizzi et al., 2014).

There are multiple reports that treatment regimes affecting the angiotensin-NOX-ROS axis attenuate hypertrophy and heart failure, but also few examples showing no effects (**Table 1**).

CONCLUSION

A coupling between ROS, cardiac hypertrophy and heart failure has been established for the LV. Concerning the RV only few data are available that directly analyzes right heart hypertrophy in the context of ROS signaling. As it stands there is consensus that RV tissue has a reduced oxidative defense capacity thereby favoring oxidative stress especially during the transition from RV hypertrophy to failure. Whether ROS targets in the RV include those proteins that are directly linked to cardiac growth is unclear and questionable. In contrast, oxidative modification of proteins leading to failure seems to be similar between both ventricles. **Table 2** highlights the findings on ROS formation, defense, and targets in RV in comparison to LV.

AUTHOR CONTRIBUTIONS

K-DS and RaS wrote the manuscript, performed literature search, and work on the conception. HK and CH provided data to **Figure 3** and read and improved the manuscript. RoS read and added conceptional ideas and data to the chapter defense system.

FUNDING

K-DS and RaS received funding from the German Research Foundation (SFB/CRC 1213 B05).

ACKNOWLEDGMENT

We thank Claudia Lorenz (Alcedis GmbH) for proofreading of our manuscript.

REFERENCES

Abraham, W. T., Raynolds, M. V., Badesch, D. B., Wynne, K. M., Groves, B. M., Roden, R. L., et al. (2003). Angiotensin-converting enzyme DD genotype in patients with primary pulmonary hypertension: increased frequency and association with preserved haemodynamics. *J. Renin. Angiot. Aldoster. Syst*. 4, 27–30. doi: 10.3317/jraas.2003.003

Adesina, S. E., Wade, B. E., Bijli, K. M., Kang, B. Y., Williams, C. R., Ma, J., et al. (2017). Hypoxia inhibits expression and function of mitochondrial thioredoxin 2 to promote pulmonary hypertension. *Am. J. Physiol. Lung Cell. Mol. Physiol.* 312, L599–L608. doi: 10.1152/ajplung.00258.2016

Alzoubi, A., Toba, M., Abe, K., O'Neill, K. D., Rocic, P., Fagan, K. A., et al. (2013). Dehydroepiandrosterone restores right ventricular structure and function in rats with severe pulmonary arterial hypertension. *Am. J. Physiol. Heart Circ. Physiol.* 304, H1708–H1718. doi: 10.1152/ajpheart.00746.2012

Ameri, P., Bertero, E., Meliota, G., Cheli, M., Canepa, M., Brunelli, C., et al. (2016). Neurohormonal activation and pharmacological inhibition in pulmonary arterial hypertension and related right ventricular failure. *Heart Fail. Rev*. 21, 539–547. doi: 10.1007/s10741-016-9566-3

Anghel, N., Herman, H., Balta, C., Rosu, M., Stan, M. S., Nita, D., et al. (2018). Acute cardiotoxicity induced by doxorubicin in right ventricle is associated with increase of oxidative stress and apoptosis in rats. *Histol. Histopathol*. 33, 365–378. doi: 10.14670/HH-11-932

Arozal, W., Sari, F. R., Watanabe, K., Arumugam, S., Veeraveedu, P. T., Ma, M., et al. (2011). Carvedilol-afforded protection against daunorubicin-induced

cardiomyopathic rats *in vivo*: effects on cardiac fibrosis and hypertrophy. *ISRN Pharmacol.* 8:430549. doi: 10.5402/2011/430549

Aziz, A., Lee, A. M., Ufere, N. N., Damiano, R. J., Townsend, R. R., and Moon, M. R. (2015). Proteomic profiling of early chronic pulmonary hypertension: evidence for both adaptive and maladaptive pathology. *J. Pulm. Respir. Med.* 5:1000241. doi: 10.4172/2161-105X.1000241

Balestra, G. M., Mik, E. G., Eerbeek, O., Specht, P. A., van der Laarse, W. J., and Zuurbier, C. J. (2015). Increased *in vivo* mitochondrial oxygenation with right ventricular failure induced by pulmonary arterial hypertension: mitochondrial inhibition as driver of cardiac failure? *Respir. Res.* 16:6. doi: 10.1186/s12931-015-0178-6

Borchi, E., Bargelli, V., Stillitano, F., Giordano, C., Sebastiani, M., Nassi, P. A., et al. (2010). Enhanced ROS production by NADPH oxidase is correlated to changes in antioxidant enzyme activity in human heart failure. *Biochim. Biophys. Acta* 1802, 331–338. doi: 10.1016/j.bbadis.2009.10.014

Brittain, E. L., Talati, M., Fessel, J. P., Zhu, H., Penner, N., Calcutt, M. W., et al. (2016). Fatty acid metabolic defects and right ventricular lipotoxicity in human pulmonary arterial hypertension. *Circulation* 133, 1936–1944. doi: 10.1161/CIRCULATIONAHA.115.019351

Burger, D., Montezano, A. C., Nishgaki, N., He, Y., Carter, A., and Touyz, R. M. (2011). Endothelial microparticle formation by angiotensin II is mediated via Ang II receptor type I/NADPH oxidase/Rho kinase pathways targeted to lipid rafts. *Arterioscler. Thromb. Vasc. Biol.* 31, 1898–1907. doi: 10.1161/ATVBAHA.110.222703

Byrne, J. A., Grieve, D. J., Bendall, J. K., Li, J. M., Gove, C., Lambeth, J. D., et al. (2003). Contrasting roles of NADPH oxidase isoforms in pressure-overload versus angiotensin II–induced cardiac hypertrophy. *Circ. Res.* 93, 802–804. doi: 10.1161/01.RES.0000099504.30207.F5

Cadenas, S. (2018). Mitochondrial uncoupling, ROS generation and cardioprotection. *Biochim. Biophys. Acta* 1859, 940–950. doi: 10.1016/j.bbabio.2018.05.019

Calamaras, T. D., Lee, C., Lan, F., Ido, Y., Siwik, D. A., and Colucci, W. S. (2015). Lipid peroxidation product 4-hydroxy-trans-2-nonenal (HNE) causes protein synthesis in cardiac myocytes via activated mTORC1-P70S6K-RPS6 signaling. *Free Radic. Biol. Med.* 82, 137–146. doi: 10.1016/j.freeradbiomed.2015.01.007

Canton, M., Menazza, S., Sheeran, F. L., Polverino de Laureto, P., Di Lisa, F., Pepe, S., et al. (2011). Oxidation of myofibrillar proteins in human heart failure. *J. Am. Coll. Cardiol.* 57, 300–309. doi: 10.1016/j.jacc.2010.06.058

Cau, S. B., Barato, R. C., Celes, M. R., Muniz, J. J., Rossi, M. A., and Tanus-Santos, J. E. (2013). Doxycycline prevents acute pulmonary embolism-induced mortality and right ventricular deformation in rats. *Cardiovasc. Drugs Ther.* 27, 259–267. doi: 10.1007/s10557-013-6458-9

Chai, C. Z., Mo, W. L., Zhuang, X. F., Kou, J. P., Yan, Y. Q., and Yu, B. Y. (2016). Protective effects of Sheng-Mai-San on right ventricular dysfunction during chronic intermittent hypoxia in mice. *Evid. Based Complement. Alternat. Med.* 2016:4682786. doi: 10.1155/2016/4682786

Chang, Y. M., Chang, H. H., Lin, H. J., Tsai, C. C., Tsai, C. T., Chang, H. N., et al. (2017). Inhibition of cardiac hypertrophy effects in D-galactose-induced senescent hearts by alpinate oxyphyllae fructus treatment. *Evid. Based Complement. Alternat. Med.* 2017:2624384. doi: 10.1155/2017/2624384

Chemaly, E. R., Hadri, L., Zhang, S., Kim, M., Kohlbrenner, E., Sheng, J., et al. (2011). Long-term *in vivo* resistin overexpression induces myocardial dysfunction and remodeling in rats. *J. Mol. Cell. Cardiol.* 51, 144–155. doi: 10.1016/j.yjmcc.2011.04.006

Chen, G., Pam, S. Q., Chen, C., Pan, S. F., Zhang, X. M., and He, Q. Y. (2014). Puerarin inhibits angiotensin II-induced cardiac hypertrophy via the redox-sensitive ERK1/2, p38 and NF-κB pathways. *Acta Pharmacol. Sin.* 35, 463–475. doi: 10.1038/aps.2013.185

Cheng, Y. S., Dai, D. Z., and Dai, Y. (2009). Isoproterenol disperses distribution of NADPH oxidase, MMP-9, and pPKCε in the heart, which are mitigated by endothelin receptor antagonist CPU0213. *Acta Pharmacol. Sin.* 30, 1099–1106. doi: 10.1038/aps.2009.104

Cingolani, O. H., Pérez, N. G., Ennis, I. L., Alvarez, M. C., Mosca, S. M., Schinella, G. R., et al. (2011). *In vivo* key role of reactive oxygen species and NHE-1 activation in determining excessive cardiac hypertrophy. *Pflugers Arch. Eur. J. Physiol.* 462, 733–743. doi: 10.1007/s00424-011-1020-8

Ciulla, M. M., Paliotti, R., Carini, M., Magrini, F., and Aldini, G. (2011). Fibrosis, enzymatic and non-enzymatic cross-links in hypertensive heart disease. *Cardiovasc. Hematol. Disord. Drug Targets* 11, 61–73. doi: 10.2174/187152911798347025

Cowley, P. M., Wang, G., Joshi, S., Swigart, P. M., Lovett, D. H., Simpson, P. C., et al. (2017). α1A-Subtype adrenergic agonist therapy for the failing right ventricle. *Am. J. Physiol. Heart Circ. Physiol.* 313, H1109–H1118. doi: 10.1152/ajpheart.00153.2017

Cruz, J. A., Bauer, E. M., Rodriguez, A. I., Gangopadhyay, A., Zeineh, N. S., Wang, Y., et al. (2012). Chronic hypoxia induces right heart failure in caveolin-1-/- mice. *Am. J. Physiol. Heart Circ. Physiol.* 302, H2518–H2527. doi: 10.1152/ajpheart.01140.2011

Danz, E. D., Skramsted, J., Henry, N., Bennett, J. A., and Keller, R. S. (2009). Resveratrol prevents doxorubicin cardiotoxicity through mitochondrial stabilization and the Sirt1 pathway. *Free Radic. Biol. Med.* 46, 1589–1597. doi: 10.1016/j.freeradbiomed.2009.03.011

Date, M. O., Morita, T., Yamashita, N., Nishida, K., Yamaguchi, O., Higuchi, Y., et al. (2002). The antioxidant N-2-mercaptopropionyl glycine attenuates left ventricular hypertrophy in *in vivo* murine pressure-overload model. *J. Am. Coll. Cardiol.* 39, 907–912. doi: 10.1016/S0735-1097(01)01826-5

Datta, A., Kim, G. A., Taylor, J. M., Gugino, S. F., Farrow, K. N., Schumacker, P. T., et al. (2015). Mouse lung development and NOX1 induction during hyperoxia are developmentally regulated and mitochondrial ROS dependent. *Am. J. Physiol. Lung. Cell Mol. Physiol.* 309, L369–L377. doi: 10.1152/ajplung.00176.2014

de Jong, J. W., Schoemaker, R. G., de Jonge, R., Bernocchi, P., Keijzer, E., Harrison, R., et al. (2000). Enhanced expression and activity of xanthine oxidoreductase in the failing heart. *J. Mol. Cell. Cardiol.* 32, 2083–2089. doi: 10.1006/jmcc.2000.1240

DeMarco, V. G., Habibi, J., Whaley-Connell, A. T., Schneider, R. I., Heller, R. L., Bosanquet, J. P., et al. (2008). Oxidative stress contributes to pulmonary hypertension in the transgenic (mRen2)27 rat. *Am. J. Physiol. Heart Circ. Physiol.* 294, H2659–H2668. doi: 10.1152/ajpheart.00953.2007

Dey, S., DeMazumder, D., Sidor, A., Foster, D. B., and O'Rourke, B. (2018). Mitochondrial ROS drive sudden cardiac death and chronic proteome remodeling in heart failure. *Circ. Res.* 123, 356–371. doi: 10.1161/CIRCRESAHA.118.312708

Di Lisa, F., Giorgio, M., Ferdinandy, P., and Schulz, R. (2017). New aspects of p66Shc in ischaemia reperfusion injury and other cardiovascular diseases. *Br. J. Pharmacol.* 174, 1690–1703. doi: 10.1111/bph.13478

Dos Santos Lacerda, D., Türck, P., Gazzi de Lima-Seolin, B., Colombo, R., Duarte Ortiz, V., Poletto Bonetto, J. H., et al. (2017). Pterostilbene reduces oxidative stress, prevents hypertrophy and preserves systolic function of right ventricle in cor pulmonale model. *Br. J. Pharmacol.* 174, 3302–3314. doi: 10.1111/bph.13948

Duni, A., Liakopoulos, V., Rapsomanikis, K. P., and Dounousi, E. (2017). Chronic kidney disease and disproportionally increased cardiovascular damage: does oxidative stress explain the burden? *Oxidat. Med. Cell. Longevity.* 2017:9036450. doi: 10.1155/2017/9036450

Dunn, L. L., Buckle, A. M., Cooke, J. P., and Ng, M. K. (2010). The emerging role of the thioredoxin system in angiogenesis. *Arterioscler. Thromb. Vasc. Biol.* 30, 2089–2098. doi: 10.1161/ATVBAHA.110.209643

Ecarnot-Laubriet, A., Rochette, L., Vergely, C., Sicard, P., and Teyssier, J. R. (2003). The activation pattern of the antioxidant enzymes in the right ventricle of rat in response to pressure overload is of heart failure type. *Heart Dis.* 5, 308–312. doi: 10.1097/01.hdx.0000089836.03515.a9

Egea, J., Fabregat, I., Frapart, Y. M., Ghezzi, P., Görlach, A., Kietzmann, T., et al. (2017). European contribution to the study of ROS: a summary of the findings and prospects for the future from the COST action BM1203 (EU-ROS). *Redox Biol.* 13, 94–162. doi: 10.1016/j.redox.2017.05.007

Frazziano, G., Al Ghouleh, I., Baust, J., Shiva, S., Champion, H. C., and Pagano, P. J. (2014). Nox-derived ROS are acutely activated in pressure overload pulmonary hypertension: indications for a seminal role for mitochondrial Nox4. *Am. J. Physiol. Heart Circ. Physiol.* 306, H197–H205. doi: 10.1152/ajpheart.00977.2012

Freund-Michel, V., Khoyrattee, N., Savineau, J. P., Muller, B., and Guibert, C. (2014). Mitochondria: roles in pulmonary hypertension. *Int. J. Biochem. Cell Biol.* 55, 93–97. doi: 10.1016/j.biocel.2014.08.012

Galhotra, P., Prabhakar, P., Meghwani, H., Mohammed, S. A., Banerjee, S. K., Seth, S., et al. (2018). Beneficial effects of fenofibrate in pulmonary hypertension in rats. *Mol. Cell. Biochem.* 449, 185–194. doi: 10.1007/s11010-018-3355-3

Gladden, J. D., Zelickson, B. R., Guichard, J. L., Ahmed, M. I., Yancey, D. M., Ballinger, S., et al. (2013). Xanthine oxidase inhibition preserves left ventricular systolic but not diastolic function in cardiac volume overload. *Am. J. Physiol. Heart Circ. Physiol.* 305, H1440–H1450. doi: 10.1152/ajpheart.00007.2013

Gomez-Arroyo, J., Mizuno, S., Szczepanek, K., Van Tassell, B., Natarajan, R., dos Remedios, C. G., et al. (2013). Metabolic gene remodeling and mitochondrial dysfunction in failing right ventricular hypertrophy secondary to pulmonary arterial hypertension. *Circ. Heart Fail.* 6, 136–144. doi: 10.1161/CIRCHEARTFAILURE.111.966127

Grieve, D. J., Byrne, J. A., Siva, A., Layland, J., Johar, S., Cave, A. C., et al. (2006). Involvement of the nicotinamide adenosine dinucleotide phosphate oxidase isoform Nox2 in cardiac contractile dysfunction occurring in response to pressure overload. *J. Am. Coll. Cardiol.* 47, 817–826. doi: 10.1016/j.jacc.2005.09.051

Guggilam, A., Haque, M., Kerut, E. K., McIlwain, E., Lucchesi, P., Seghal, I., et al. (2007). TNF-α blockade decreases oxidative stress in the paraventricular nucleus and attenuates sympathoexcitation in heart failure rats. *Am. J. Physiol. Heart Circ. Physiol.* 293, H599–H609. doi: 10.1152/ajpheart.00286.2007

Guido, M. C., Marques, A. F., Tavares, E. R., Tavares de Melo, M. D., Salemi, V. M. C., and Maranhão, R. C. (2017). The effects of diabetes induction on the rat heart: differences in oxidative stress, inflammatory cells, and fibrosis between subendocardial and interstitial myocardial areas. *Oxidat. Med. Cell. Longevity* 2017:5343972. doi: 10.1155/2017/534397

Guo, H., Zhang, X., Cui, Y., Zhou, H., Xu, D., Shan, T., et al. (2015). Taxifolin protects against cardiac hypertrophy and fibrosis during biomechanical stress of pressure overload. *Toxicol. Appl. Pharmacol.* 287, 168–177. doi: 10.1016/j.taap.2015.06.002

Gupto, A. A., Cordero-Reyes, A. M., Youker, K. A., Matsunami, R. K., Engler, D. A., Li, S., et al. (2016). Differential mitochondrial function in remodeled right and nonremodeled left ventricles in pulmonary hypertension. *J. Card. Fail.* 22, 73–81. doi: 10.1016/j.cardfail.2015.09.001

Habibi, J., DeMarco, V. G., Ma, L., Pulakat, L., Rainey, W. E., Whaley-Connell, A. T., et al. (2011). Mineralocorticoid receptor blockade improves diastolic function independent of blood pressure reduction in a transgenic model of RAAS overexpression. *Am. J. Physiol. Heart Circ. Physiol.* 300, H1484–H1491. doi: 10.1210/endo-meetings.2011.PART4.P2.P3-440

Hansen, T., Galougahi, K. K., Celermajer, D., Rasko, N., Tang, O., Bubb, K. J., et al. (2016). Oxidative and nitrosative signalling in pulmonary arterial hypertension — implications for development of novel therapies. *Pharmacol. Therap.* 165, 50–62. doi: 10.1016/j.pharmthera.2016.05.005

He, J., Li, X., Luo, H., Li, T., Zhao, L., Qi, Q., et al. (2017). Galectin-3 mediates the pulmonary arterial hypertension-induced right ventricular remodeling through interacting with NADPH oxidase 4. *J. Am. Soc. Hypertens.* 11, 275–289.e2. doi: 10.1016/j.jash.2017.03.008

Hernandez-Resendiz, S., Chinda, K., Ong, S. B., Cabrera-Fuentes, H., Zazueta, C., and Hausenloy, D. J. (2018). The role of redox dysregulation in the inflammatory response to acute myocardial ischaemia-reperfusion injury - adding fuel to the fire. *Curr. Med. Chem.* 25, 1275–1293. doi: 10.2174/0929867324666170329100619

Heusch, P., Aker, S., Boengler, K., Deindl, E., van de Sand, A., Klein, K., et al. (2010). Increased inducible nitric oxide synthase and arginase II expression in heart failure: no net nitrite/nitrate production and protein S-nitrosylation. *Am. J. Physiol. Heart Circ. Physiol.* 299, H446–H453. doi: 10.1152/ajpheart.01034.2009

Heusch, P., Canton, M., Aker, S., van de Sand, A., Konietzka, I., Rassaf, T., et al. (2010b). The contribution of reactive oxygen species and p38 mitogen-activated protein kinase to myofilament oxidation and progression of heart failure in rabbits. *Br. J. Pharmacol.* 160, 1408–1416. doi: 10.1111/j.1476-5381.2010.00793.x

Iacobazzi, D., Suleiman, M. S., Ghorbel, M., George, S. J., Caputo, M., and Tulloh, R. M. (2016). Cellular and molecular basis of RV hypertrophy in congential heart disease. *Heart* 102, 12–17. doi: 10.1136/heartjnl-2015-308348

Ide, T., Tsutsui, H., Hayashidani, S., Kang, D., Suematsu, N., Nakamura, K., et al. (2001). Mitochondrial DNA damage and dysfunction associated with oxidative stress in failing hearts after myocardial Infarction. *Circ. Res.* 88, 529–535. doi: 10.1161/01.RES.88.5.529

Ishikawa, K., Kimura, S., Kobayashi, A., Sato, T., Matsumoto, H., Ujiie, Y., et al. (2005). Increased reactive oxygen species and anti-oxidative response in mitochondrial cardiomyopathy. *Circ. J.* 69, 617–620. doi: 10.1253/circj.69.617

Karamanlidis, G., Bautista-Hernandez, V., Fynn-Thompson, F., Del Nido, P., and Tian, R. (2011). Impaired mitochondrial biogenesis precedes heart failure in right ventricular hypertrophy in congenital heart disease. *Circ. Heart Fail.* 4, 707–713. doi: 10.1161/CIRCHEARTFAILURE.111.961474

Koga, K., Kenessey, A., and Ojamaa, K. (2013). Macrophage migration inhibitory factor antagonizes pressure overload-induced cardiac hypertrophy. *Am. J. Physiol. Heart Circ. Physiol.* 304, H282–H293. doi: 10.1152/ajpheart.00595.2012

Li, J. M., Gall, N. P., Grieve, D. J., Chen, M., and Shah, A. M. (2002). Activation of NADPH oxidase during progression of cardiac hypertrophy to failure. *Hypertension* 40, 477–484. doi: 10.1161/01.HYP.0000032031.30374.32

Li, M., Sala, V., De Santis, M. C., Cimino, J., Cappello, P., Pianca, N., et al. (2018). Phosphoinositide 3-kinase gamma inhibition protects from anthracycline cardiotoxicity and reduces tumor growth. *Circulation* 138, 696–711. doi: 10.1161/CIRCULATIONAHA.117.030352

Li, R., Fang, W., Cao, S., Li, Y., Wang, J., Xi, S., et al. (2013). Differential expression of NAD(P)H oxidase isoforms and the effect of atorvastatin on cardiac remodeling in two-kidney two-clip hypertensive rats. *Pharmazie* 68, 261–269. doi: 10.1691/ph.2013.2782

Lima-Seolin, B. G., Colombo, R., Bonetto, J. H. P., Teixeira, R. B., Donatti, L. M., Casali, K. R., et al. (2017). Bucindolol improves right ventricle function in rats with pulmonary arterial hypertension through the reversal of autonomic imbalance. *Eur. J. Pharmacol.* 798, 57–65. doi: 10.1016/j.ejphar.2016.12.028

Liu, B., Luo, X. J., Yang, Z. B., Zhang, J. J., Li, T. B., Zhang, X. J., et al. (2014). Inhibition of NOX/VPO1 pathway and inflammatory reaction by trimethoxystilbene in prevention of cardiovascular remodeling in hypoxia-induced pulmonary hypertensive rats. *J. Cardiovasc. Pharmacol.* 63, 567–576. doi: 10.1097/FJC.0000000000000082

Liu, J., Zhou, J., An, W., Lin, Y., Yang, Y., and Zang, W. (2010). Apocynin attenuates pressure overload-induced cardiac hypertrophy in rats by reducing levels of reactive oxygen species. *Can. J. Physiol.Pharmacol.* 88, 745–752. doi: 10.1139/Y10-063

Liu, J. Q., Zelko, I. N., Erbynn, E. M., Sham, J. S., and Folz, R. J. (2006). Hypoxic pulmonary hypertension: role of superoxide and NADPH oxidase (gp91phox). *Am. J. Physiol. Lung Cell. Mol. Physiol.* 290, L2–L10. doi: 10.1152/ajplung.00135.2005

Liu, L., Marcocci, L., Wong, C. M., Park, A. M., and Suzuki,Y. J. (2008). Serotonin-mediated protein carbonylation in the right heart. *Free Radic. Biol. Med.* 45, 847–854. doi: 10.1016/j.freeradbiomed.2008.06.008

Lu, J. C., Cui, W., Zhang, H. L., Liu, F., Han, M., Liu, D. M., et al. (2009). Additive beneficial effects of amilodipine and atorvastatin in reversing advanced cardiac hypertophy in elderly spontaneously hypertensive rats. *Clin. Exptl. Pharmacol. Physiol.* 36, 1110–1119. doi: 10.1111/j.1440-1681.2009.05198.x

Lu, X., Dang, C. Q., Guo, X., Molloi, S., Wassall, C. D., Kemple, M. D., et al. (2011). Elevated oxidative stress and endothelial dysfunction in right coronary artery of right ventricular hypertrophy. *J. Appl. Physiol.* 110, 1674–1681. doi: 10.1152/japplphysiol.00744.2009

Lu, Z., Xu, X., Hu, X., Fassett, J., Zhu, G., Tao, Y., et al. (2010). PGC-1a regulates expression of myocardial mitochondrial antioxidants and myocardial oxidative stress after chronic systolic overload. *Antiox. Redox. Signal.* 13, 1011–1022. doi: 10.1089/ars.2009.2940

Lüneburg, N., Siques, P., Brito, J., Arriaza, K., Pena, E., Klose, H., et al. (2016). Long-term chronic intermittent hypobaric hypoxia in rats causes an imbalance in the asymmetric dimethylarginine/nitric oxide pathway and ROS activity: a possible synergistic for altitude pulmonary hypertension? *Pulm. Med.* 2016:6578578. doi: 10.1155/2016/6578578

Ma, L., Ambalavanan, N., Liu, H., Sun, Y., Jhala, N., and Bradley, W. E. (2016). TLR4 regulates pulmonary vascular homeostasis and remodeling via redox signaling. *Front. Biosci.* 21, 397–409. doi: 10.2741/4396

Maarman, G. J., Schulz, R., Sliwa, K., Schermuly, R. T., and Lecour, S. (2017). Novel putative pharmacological therapies to protect the right ventricle in pulmonary hypertension: a review of current literature. *Br. J. Pharmacol.* 174, 497–511. doi: 10.1111/bph.13721

Mandraffino, G., Aragona, C. O., Cairo, V., Scuruchi, M., Lo Gullo, A., D'ascola, A., et al. (2017). Circulating progenitor cells in hypertensive subjects: effectiveness of a treatment with olmesartan in improving cell number and miR profile in addition to expected pharmacological effects. *PLoS ONE* 12:e0173030. doi: 10.1371/journal.pone.0173030

Manni, M. E., Rigacci, S., Borchi, E., Bargelli, V., Miceli, C., Giordano, C., et al. (2016). Monoamine oxidase is overactivated in left and right ventricles from ischemic hearts: an intriguing therapeutic target. *Oxidat. Med. Cell. Longevity* 2016:4375418. doi: 10.1155/2016/4375418

Matsuda, S., Umemoto, S., Yoshimura, K., Itoh, S., Murata, T., and Fukai, T. (2015). Angiotensin II activates MCP-1 and induces cardiac hypertrophy and dysfunction via Toll-like receptor 4. *Atheroscler. Thromb*. 26, 833–844. doi: 10.5551/jat.27292

Moris, D., Spartalis, M., Tzatzaki, E., Spartalis, E., Karachaliou, G. S., Triantafyllis, A. S., et al. (2017). The role of reactive oxygen species in myocardial redox signaling and regulation. *Ann. Transl. Med.* 5:324. doi: 10.21037/atm.2017.06.17

Mouli, S., Nanayakkara, G., AlAlasmari, A., Eldoumani, H., Fu, X., Berlin, A., et al. (2015). The role of frataxin in doxorubicin-mediated cardiac hypertrophy. *Am. J. Physiol. Heart Circ. Physiol.* 309, H844–H859. doi: 10.1152/ajpheart.00182.2015

Nagendran, J., Gurtu, V., Fu, D. Z., Dyck, J. R., Haromy, A., Ross, D. B., et al. (2008). A dynamic and chamber-specific mitochondrial remodeling in right ventricular hypertrophy can be therapeutically targeted. *J. Thorac. Cardiovasc. Surg*. 136, 168–178. doi: 10.1016/j.jtcvs.2008.01.040

Nediani, C., Borchi, E., Giordano, C., Baruzzo, S., Ponziani, V., Sebastiani, M., et al. (2007). NADPH oxidase-dependent redox signaling in human heart failure: relationship between the left and right ventricle. *J. Mol. Cell. Cardiol*. 42, 826–834. doi: 10.1016/j.yjmcc.2007.01.009

Nisbet, R. E., Graves, A. S., Kleinhenz, D. J., Rupnow, H. L., Reed, A. L., Fan, T. H., et al. (2009). The role of NADPH oxidase in chronic intermittent hypoxia-induced pulmonary hypertension in mice. *Am. J. Respir. Cell Mol. Biol*. 40, 601–609. doi: 10.1165/2008-0145OC

Ogura, S., Shimosawa, T., Mu, S., Sonobe, T., Kawakami-Mori, F., Wang, H., et al. (2013). Oxidative stress augments pulmonary hypertension in chronically hypoxic mice overexpressing the oxidized LDL receptor. *Am. J. Physiol. Heart Circ. Physiol*. 305, H155–H162. doi: 10.1152/ajpheart.00169.2012

Papparella, I., Ceolotto, G., Montemurro, D., Antonello, M., Garbisa, S., Rossi, G. P., et al. (2008). Green tea attenuates angiotensin II-induced cardiac hypertrophy in rats by modulating reactive oxygen species production and the Src/Epidermal growth factor receptor/Act signalling pathway. *J. Nutr*. 138, 1596–1601. doi: 10.1093/jn/138.9.1596

Paulin, R., and Michelakis, E. D. (2014). The metabolic theory of pulmonary arterial hypertension. *Circ Res*. 115, 148–164. doi: 10.1161/CIRCRESAHA.115.301130

Phillips, D., Aponte, A. M., Covian, R., Neufeld, E., Yu, Z. X., and Balaban, R. S. (2011). Homogenous protein programming in the mammalian left and right ventricle free walls. *Physiol. Genom.* 43, 1198–1206. doi: 10.1152/physiolgenomics.00121.2011

Pichardo, J., Palace, V., Farahmand, F., and Singal, P. K. (1999). Myocardial oxidative stress changes during compensated right heart failure in rats. *Mol. Cell. Biochem.* 196, 51–57. doi: 10.1023/a:1006914111957

Pönicke, K., Schlüter, K. D., Heinroth-Hoffmann, I., Seyfarth, T., Goldberg, M., Piper, H. M., et al. (2001). Naunyn Schmiedebergs. *Arch. Pharmacol*. 364, 444–453. doi: 10.1007/s002100100469

Puukila, S., Fernandes, R. O., Türck, P., Carraro, C. C., Bonetto, J. H. P., de Lima-Seolin, B. G., et al. (2017). Secoisolariciresinol diglucoside attenuates cardiac hypertrophy and oxidative stress in monocrotaline-induced right heart dysfunction. *Mol. Cell. Biochem*. 432, 33–39. doi: 10.1007/s11010-017-2995-z

Qiao, W., Zhang, W., Gai, Y., Zhao, L., and Fan, J. (2014). The histone acetyltransferase MOF overexpression blunts cardiac hypertrophy by targeting ROS in mice. *Biochem. Biophys. Res. Commun.* 448, 379–384. doi: 10.1016/j.bbrc.2014.04.112

Qin, F., Siwik, D. A., Pimentel, D. R., Morgan, R. J., Biolo, A., Tu, V. H., et al. (2017). Cytosolic H_2O_2 mediates hypertrophy, apoptosis, and decreased SERCA activity in mice with chronic hemodynamic overload. *Am. J. Physiol. Heart Circ. Physiol.* 306, H1453–H1463. doi: 10.1152/ajpheart.00084.2014

Qipshidze, N., Tyagi, N., Metreveli, N., Lominadze, D., and Tyagi, S. C. (2012). Autophagy mechanism of right ventricular remodeling in murine model of pulmonary artery constriction. *Am. J. Physiol. Heart Circ. Physiol*. 302, H688–H696. doi: 10.1152/ajpheart.00777.2011

Rassaf, T., Poll, L. W., Brouzos, P., Lauer, T., and Totzeck, M., Kleinbongard, P., et al. (2006). Positive effects of nitric oxide on left ventricular function in humans. *Eur. Heart J.* 27, 1699–1705. doi: 10.1093/eurheartj/ehl096

Rawat, D. K., Alzoubi, A., Gupte, R., Chettimada, S., Watanabe, M., Kahn, A. G., et al. (2014). Increased reactive oxygen species, metabolic maladaptation, and autophagy contribute to pulmonary arterial hypertension-induced ventricular hypertrophy and diastolic heart failure. *Hypertension* 64, 1266–1274. doi: 10.1161/HYPERTENSIONAHA.114.03261

Reddy, S., and Bernstein, D. (2015). Molecular mechanisms of right ventricular failure. *Circulation* 132, 1734–1742. doi: 10.1161/CIRCULATIONAHA.114.012975

Redout, E. M., van der Toorn, A., Zuidwijk, M. J., van de Kolk, C. W. A., van Echteld, C. J. A., Musters, R. J. P., et al. (2010). Antioxidant treatment attenuates pulmonary arterial hypertension-induced heart failure. *Am. J. Physiol. Heart Circ. Physiol*. 298, H1038–H1047. doi: 10.1152/ajpheart.00097.2009

Redout, E. M., Wagner, M. J., Zuidwijk, M. J., Boer, C., Musters, R. J. P., van Hardeveld, C., et al. (2007). Right-ventricular failure is associated with increased mitochondrial complex II activity and production of reactive oxygen species. *Cardiovasc. Res*. 75, 770–781. doi: 10.1016/j.cardiores.2007.05.012

Redza-Dutordoir, M., and Averill-Bates, D. A. (2016). Activation of apoptosis signalling pathways by reactive oxygen species. *Biochim. Biophys. Acta* 1863, 2977–2992. doi: 10.1016/j.bbamcr.2016.09.012

Riba, A., Deres, L., Sumegi, B., Toth, K., Szabados, E., and Halmosi, R. (2017). Cardioprotective effect of resveratrol in a postinfarction heart failure model. *Oxidative Med. Cell. Longevity* 2017:6819281. doi: 10.1155/2017/6819281

Rizzi, E., Guimaraes, D. A., Ceron, C. S., Prado, C. M., Pinheiro, L. C., Martins-Oliveira, A., et al. (2014). β1-Adrenergic blockers exert antioxidant effects, reduce matrix metalloproteinase activity, and improve renovascular hypertension-induced cardiac hypertrophy. *Free Radical. Biol. Med*. 73, 308–317. doi: 10.1016/j.freeradbiomed.2014.05.024

Schäfer, M., Schäfer, C., Piper, H. M., and Schlüter, K. D. (2002). Hypertrophic responsiveness of cardiomyocytes to α- and β-adrenoceptor stimulation requires sodium-proton-exchanger-1 (NHE-1) activation but not cellular alkalization. *Eur. J. Heart Fail*. 4, 249–254. doi: 10.1016/S1388-9842(02)00016-8

Schlüter, K. D. (ed.). (2016). "Ways to study the biology of cardiomyocytes," in *Cardiomyocytes – Active Players in Cardiac Disease* (Cham: Springer International Publishing), 3–23. doi: 10.1007/978-3-319-31251-4_1

Schreckenberg, R., Rebelo, M., Deten, A., Weber, M., Rohrbach, S., Pipicz, M., et al. (2015). Specific mechanisms underlying right heart failure: the missing upregulation of superoxide dismutase-2 and its decisive role in antioxidative defense. *Antioxdi. Redox Signal.* 23, 1220–1232. doi: 10.1089/ars.2014.6139

Shimizu, S., Ishibashi, M., Kumagai, S., Wajima, T., Hiroi, T., Kurihara, T., et al. (2013). Decreased cardiac mitochondrial tetrahydrobiopterin in a rat model of pressure overload. *Int. J. Mol. Med*. 31, 589–596. doi: 10.3892/ijmm.2013.1236

Simm, A., Schlüter, K. D., Diez, C., Piper, H. M., and Hoppe, J. (1998). Activation of p70S6 kinase by β-adrenoceptor agonists on adult cardiomyocytes. *J. Mol. Cell. Cardiol*. 30, 2059–2067. doi: 10.1006/jmcc.1998.0768

Siqueira, R., Colombo, R., Conzatti, A., de Castro, A. L., Carraro, C. C., Tavares, A. M. V., et al. (2018). Effects of ovariectomy on antioxidant defence systems in the right ventricle of female rats with pulmonary arterial hypertension induced by monocrotaline. *Can. J. Physiol. Pharmacol*. 96, 295–303. doi: 10.1139/cjpp-2016-0445

Sirker, A., Murdoch, C. E., Protti, A., Sawyer, G. J., Santos, C. X. C., Martin, D., et al. (2016). Cell-specific effects of Nox2 on the acute and chronic response to myocardial infarction. *J. Mol. Cell. Cardiol*. 98, 11–17. doi: 10.1016/j.yjmcc.2016.07.003

Sundaresan, N. R., Gupta, M., Kim, G., Rajamohan, S. B., Isbatan, A., and Gupta, M. P. (2009). Sirt3 blocks the cardiac hypertrophic response by augmenting Foxo3a-dependent antioxidant defense mechanisms in mice. *J. Clin. Invest*. 119, 2758–2771. doi: 10.1172/JCI39162

Sutendra, G., and Michelakis, E. D. (2014). The metabolic basis of pulmonary arterial hypertension. *Cell Metab*. 19, 558–573. doi: 10.1016/j.cmet.2014.01.004

Sverdlov, A. L., Elezaby, A., Qin, F., Behring, J. B., Luptak, I., Calamaras, T. D., et al. (2016). Mitochondrial reactive oxygen species mediate cardiac structural, functional, and mitochondrial consequences of diet-induced metabolic heart disease. *J. Am. Heart. Assoc*. 5:e002555. doi: 10.1161/JAHA.115.002555

Takimoto, E., Champion, H. C., Li, M., Ren, S., Rodriguez, E. R., Tavazzi, B., et al. (2005). Oxidant stress from nitric oxide synthase−3 uncoupling stimulates

cardiac pathologic remodeling from chronic pressure load. *J. Clin. Invest*. 115, 1221–1231. doi: 10.1172/JCI21968

Talukder, M. A., Johnson, W. M., Varadharaj, S., Lian, J., Kearns, P. N., El-Mahdy, M. A., et al. (2011). Chronic cigarette smoking causes hypertension, increased oxidative stress, impaired NO bioavailability, endothelial dysfunction, and cardiac remodeling in mice. *Am. J. Physiol. Heart Circ. Physiol*. 300, H388–H396. doi: 10.1152/ajpheart.00868.2010

Tanaka, M., Umemoto, S., Kawahara, S., Kubo, M., Itoh, S., Umeji, K., et al. (2005). Angiotensin II type 1 receptor antagonist and angiotensin-converting enzyme inhibitor altered the activation of Cu/Zn-containing superoxide dismutase in the heart of stroke-prone spontaneously hypertensive rats. *Hypertens. Res*. 28, 67–77. doi: 10.1291/hypres.28.67

Tsutsui, H., Ide, T., Hayashidami, S., Kinugawa, S., Suematsu, N., Utsumi, H., et al. (2001). Effects of ACE inhibition on left ventricular failure and oxidative stress in Dahl salt-sensitive rats. *J. Cardiovasc. Pharmacol*. 37, 725–733. doi: 10.1097/00005344-200106000-00010

Türck, P., Lacerda, D. S., Carraro, C. C., de Lima-Seolin, B. G., Teixeira, R. B., Poletto Bonetto, J. H., et al. (2018). Trapidil improves hemodynamic, echocardiographic and redox state parameters of right ventricle in monocrotaline-induced pulmonary arterial hypertension model. *Biomed. Pharmacother*. 103, 182–190. doi: 10.1016/j.biopha.2018.04.001

Umemoto, S., Tanaka, M., Kawahara, S., Kubo, M., Umeji, K., Hashimoto, R., et al. (2004). Calcium antagonist reduces oxidative stress by upregulating Cu/Zn superoxide dismutase in stroke-prone spontaneously hypertensive rats. *Hypertens. Res*. 27, 877–885. doi: 10.1291/hypres.27.877

Wang, L., Lopaschuk, G. D., and Clanachan, A. S. (2008). H_2O_2-induced left ventricular dysfunction in isolated working rat hearts is independent of calcium accumulation. *J. Mol. Cell. Cardiol*. 45, 787–795. doi: 10.1016/j.yjmcc.2008.08.010

Wang, X., Liu, J., Drummond, C. A., and Shapiro, J. I. (2017a). Sodium potassium adenosine triphosphatase (Na/K-ATPase) as a therapeutic target for uremic cardiomyopathy. *Exp. Opin. Ther. Targets* 21, 531–541. doi: 10.1080/14728222.2017.1311864

Wang, X., Shults, N. V., and Suzuki, Y. J. (2017). Oxidative profiling of the failing right heart in rats with pulmonary hypertension. *PLoS ONE* 12:e0176887. doi: 10.1371/journal.pone.0176887

Waypa, G. B., Osborne, S. W., Marks, J. D., Berkelhamer, S. K., Kondapalli, J., and Schumacker, P. T. (2013). Sirtuin 3 deficiency does not augment hypoxia-induced pulmonary hypertension. *Am. J. Respir. Cell Mol. Biol*. 49, 885–891. doi: 10.1165/rcmb.2013-0191OC

Wenzel, S., Abdallah, Y., Helmig, S., Schäfer, C., Piper, H. M., and Schlüter, K.-D. (2006). Contribution of PI 3-kinase isoforms to angiotzensin II- and α-adrenoceptor-mediated signaling pathways in cardiomyocytes. *Cardiovasc. Res*. 71, 352–362. doi: 10.1016/j.cardiores.2006.02.004

Wenzel, S., Rohde, C., Wingerning, S., Roth, J., Kojda, G., and Schlüter, K. D. (2007). Lack of endothelial nitric oxide synthase-derived nitric oxide formation favors hypertrophy in adult ventricular cardiomyocytes. *Hypertension* 49, 193–200. doi: 10.1161/01.HYP.0000250468.02084.ce

Wenzel, S., Taimor, G., Piper, H. M., and Schlüter, K. D. (2001). Redox-sensitive intermediates mediate angiotensin II-induced p38 MAP kinase activation, AP-1 binding activity, and TGF-β expression in adult ventricular cardiomyocytes. *FASEB J*. 15, 2291–2293. doi: 10.1096/fj.00-0827fje

Wong, C. M., Bansal, G., Pavlickova, L., Marocci, L., and Suzuki, Y. J. (2013). Reactive oxygen species and antioxidants in pulmonary hypertension. *Antioxid. Redox Signal*. 18, 1789–1796. doi: 10.1089/ars.2012.4568

Wong, Y. Y., Ruiter, G., Lubberink, M., Raijmakers, P. G., Knaapen, P., Marcus, J. T., et al. (2011). Right ventricular failure in idiopathic pulmonary arterial hypertension is associated with inefficient myocardial oxygen utilization. *Circ. Heart Fail*. 4, 700–706. doi: 10.1161/CIRCHEARTFAILURE.111.962381

Xu, Q., Dalic, A., Fang, L., Kiriazis, H., Ritchie, R. H., Sim, K., et al. (2011). Myocardial oxidative stress contributes to transgenic β_2-adrenoceptor activation induced cardiomyopathy and heart failure. *Br. J. Pharmacol*. 162, 1012–1028. doi: 10.1111/j.1476-5381.2010.01043.x

Ye, J. X., Wang, S. S., Ge, M., and Wang, D. J. (2016). Suppression of endothelial PGC-1α is associated with hypoxia-induced endothelial dysfunction and provides a new therapeutic target in pulmonary arterial hypertension. *Am. J. Physiol. Lung. Cell Mol. Physiol*. 310, L1233–L1242. doi: 10.1152/ajplung.00356.2015

Zhu, T. T., Zhang, W. F., Luo, P., Qian, Z. X., Li, F., Zhang, Z., et al. (2017). LOX-1 promotes right ventricular hypertrophy in hypoxia-exposed rats. *Life Sci*. 174, 35–42. doi: 10.1016/j.lfs.2017.02.016

Zisman, L. S., Asano, K., Dutcher, D. L., Ferdensi, A., Robertson, A. D., Jenkin, M., et al. (1998). Differential regulation of cardiac angiotensin converting enzyme binding sites and AT_1 receptor density in the failing human heart. *Circulation* 98,1735–1741. doi: 10.1161/01.CIR.98.17.1735

Conflict of Interest Statement: The authors declare that the research was conducted in the absence of any commercial or financial relationships that could be construed as a potential conflict of interest.

frontiers in Physiology

ORIGINAL RESEARCH
published: 21 May 2019
doi: 10.3389/fphys.2019.00624

The Effects of Bradykinin B1 Receptor Antagonism on the Myocardial and Vascular Consequences of Hypertension in SHR Rats

Laszlo Deres[1,2], Krisztian Eros[1,2], Orsolya Horvath[1,2], Noemi Bencze[1,2], Csongor Cseko[3], Sandor Farkas[3], Tamas Habon[4], Kalman Toth[2,4] and Robert Halmosi[2,4]**

[1] Medical School, University of Pécs, Pécs, Hungary, [2] Szentagothai Research Centre, University of Pécs, Pécs, Hungary, [3] Gedeon Richter Plc., Budapest, Hungary, [4] 1st Department of Medicine, Clinical Centre, University of Pécs, Pécs, Hungary

OPEN ACCESS

Edited by:
Thao P. Nguyen,
David Geffen School of Medicine at UCLA, United States

Reviewed by:
Arkady Rutkovskiy, University of Oslo, Norway
Andrea Sorrentino, Harvard Medical School, United States
Claudio de Lucia, Temple University, United States
Janos Paloczi, National Institutes of Health (NIH), United States

***Correspondence:**
Laszlo Deres
deres.laszlo@pte.hu
Robert Halmosi
halmosi.robert@pte.hu

Specialty section:
This article was submitted to Integrative Physiology, a section of the journal Frontiers in Physiology

Received: 30 September 2018
Accepted: 02 May 2019
Published: 21 May 2019

Citation:
Deres L, Eros K, Horvath O, Bencze N, Cseko C, Farkas S, Habon T, Toth K and Halmosi R (2019) The Effects of Bradykinin B1 Receptor Antagonism on the Myocardial and Vascular Consequences of Hypertension in SHR Rats. Front. Physiol. 10:624. doi: 10.3389/fphys.2019.00624

It is known that non-steroidal anti-inflammatory drugs increase cardiovascular (CV) morbidity and mortality. In this study, we examined whether a novel anti-inflammatory drug, bradykinin B1 receptor antagonist (FGY-1153) treatment could influence the development of hypertensive organ damages in spontaneously hypertensive rats (SHR). SHRs were treated with low (FGY-120) or high dose FGY-1153 (FGY-400) and with placebo (Control) for 26 weeks. Wistar–Kyoto rats were used as aged-matched, normotensive controls (WKY). Body weight, food consumption and blood pressure were measured regularly. Echocardiography was performed at the beginning and at the end of the study. Light and electron microscopic analysis of heart and great vessels were performed, and the extent of fibrotic areas was measured. The phosphorylation state of prosurvival Akt-1/glycogen synthase kinase (GSK)-3β pathway and the activation of signaling factors playing part in the fibrotic processes – mitogen activated protein kinases (MAPKs), and TGF-β/Smad2 – were monitored using Western-blot. Body weight and food consumption as well as the elevated blood pressure in SHRs was not influenced by FGY-1153 treatment. However, both doses of FGY-1153 treatment decreased left ventricular (LV) hypertrophy and diastolic dysfunction in hypertensive animals. Moreover systolic LV function was also preserved in FGY-120 group. Increased intima-media thickness and interstitial fibrosis were not significantly diminished in great vessels. FGY-1153 treatment inhibited the expression of TGFβ and the phosphorylation of SMAD2 in the heart. Our results suggest that the tested novel anti-inflammatory compound has no deleterious effect on CV system, moreover it exerts moderate protective effect against the development of hypertensive cardiopathy.

Keywords: hypertensive target organ damages, bradykinin B1 receptor antagonism, NSAIDs, cardiovascular remodeling, echocardiography, spontaneously hypertensive rats

INTRODUCTION

It is well known, that the worldwide most commonly prescribed pain relievers, the NSAIDs can significantly increase cardiovascular morbidity and mortality (Patrono and Baigent, 2014). Only the low dose aspirin treatment – without significant painkiller moiety – has positive effect on survival (Patrono et al., 2005). This unfavorable phenomenon is partly caused by the increase in atherothrombotic events (Garcia Rodriguez et al., 2008; McGettigan and Henry, 2011), however, the other major cause is the increase in mortality due to heart failure (Garcia Rodriguez and Hernandez-Diaz, 2003). Therefore there is an unmet medical need to develop novel and safer anti-inflammatory compounds.

The kallikrein–kinin system is one of the multiple systems which play a role in initiation, propagation and maintenance of inflammation and pain (Moreau et al., 2005). Kinins stimulate the synthesis and release of nitric oxide, cytokines, arachidonic acid, leukotrienes as well as chemotactic factors (Lerner et al., 1989; Tiffany and Burch, 1989; Sato et al., 1996). Primary kinins (e.g., bradykinin) act predominantly on constitutively expressed (brady)kinin B2 receptors, however, secondary kinins with longer half-life (e.g., des-arginin bradykinin) bind mainly to B1 receptors (Farkas and Eles, 2011). Bradykinin B1 receptors are expressed at a very low level in healthy tissues, but undergo massive induction due to tissue injury or inflammation. Therefore the inhibition of these receptors can be effective in the relief of chronic pain and inflammation. Moreover the pharmacological inhibition of bradykinin B1 receptors theoretically seems to be safe because of the previously mentioned features (Marceau and Bachvarov, 1998).

Actually in several works beneficial cardiac effects of bradykinin B1 receptor antagonism were showed. In KO animals and using pharmacological blockade of kinin B1 receptors, both *ex vivo* and *in vivo* the size of myocardial or cerebral infarct size decreased markedly (Lagneux et al., 2002; Yin et al., 2007; Austinat et al., 2009). An other workgroup proved, that in a diabetic cardiomyopathy model the systolic and diastolic left ventricular (LV) function was better in bradykinin B1 KO animals than in wild type ones (Westermann et al., 2009).

So far there is no data in the literature regarding the effect of kinin B1 receptor antagonism in chronic elevated blood pressure. Hypertension is one of the most important risk factor of cardio- and cerebrovascular diseases and based on population-attributable risk, hypertension has the greatest impact on the development of heart failure (Lloyd-Jones, 2001). SHR is a widely accepted and used animal model to examine the development of hypertension-induced target organ damages (Trippodo and Frohlich, 1981). According to the literature, the beginning of the hypertension is at the age of 6 to 8 weeks, which, by the age of 30 weeks leads to significant target organ damages (Kokubo et al., 2005).

In this work we aimed to evaluate the effects of a new type anti-inflammatory drug, a bradykinin B1 receptor antagonist (FGY-1153) on the development of hypertensive target organ damages in spontaneously hypertensive rats (SHR).

MATERIALS AND METHODS

Experimental Protocol

Forty-five male SHR (Charles River Laboratories, Budapest, Hungary) were used. The animals were 8 weeks old on arrival and weighed approximately 250–270 g. The study was started after an acclimatization period of 3 weeks. SHRs were randomly divided into three groups: Control group (n = 15), FGY120 group (n = 15) and FGY400 group (n = 15). The animals of FGY120 received test diet mixed with FGY-1153 at 120 ppm concentration (estimated to yield a dose level of approximately 6 mg/kg/day). The animals of FGY400 group received test diet mixed with FGY-1153 at 400 ppm concentration (estimated to a dose level of approximately 20 mg/kg/day). The special rat chow was purchased from Ssniff Spezialdiäten GmbH, Germany. The active ingredient (FGY1153) was developed by Richter Gedeon Plc., Hungary. The animals of the Control group received control diet (0 ppm concentration). The treatment with FGY-1153 started at the age of about 11-weeks. During the whole duration of the study (26 weeks) animals were treated orally, using standard rat chow containing FGY-1153 (in 120 or 400 ppm), or control rat diet. The rat chow was available to the animals *ad libitum*. SHR rats were observed daily, to achieve a description of normal activity, responsiveness to manipulation, weight, respiration, and general aspect (López et al., 2007).

Ten male Wistar-Kyoto age-matched rats (Harlan Laboratories S.r.l., San Pietro al Natisone, Italy) were used as a normotensive control group (WKY group). The animals of WKY group received control diet (0 ppm concentration). The animals were 32 weeks old on arrival and weighed approximately 380–420 g. After an acclimatization period of 2 weeks they were sacrificed.

Investigations and Measurements

Food Consumption and Body Weight

During the last 2 weeks of the acclimatization period, all animals received Control test diet (0 ppm concentration) for adaptation. The quantity of food consumed by each cage of animals was measured and recorded daily during the adaptation period. The quantity of food consumed by each cage of animals was measured and recorded once weekly during the treatment period (except for age-matched WKY group).

Body weights were measured and recorded once weekly during the acclimatization and treatment periods and on the day of necropsy (except for age-matched WKY group).

Measurement of Blood Pressure

Non-invasive blood pressure measurements were performed on each animal on three occasions at Weeks 0, 13, and 26 of the treatment period. Blood pressure measurements were performed by a non-invasive tail-cuff method as described earlier (Kubota et al., 2006; Magyar et al., 2014). Blood pressure was measured by Hatteras SC1000 Blood Pressure Analysis System with rat species platform (Panlab, Harvard Apparatus; LE5001; except for age-matched WKY group).

Echocardiographic Examinations

Transthoracic two dimensional echocardiography (n = 7 from each groups) under inhalation anesthesia was performed as described earlier (Bartha et al., 2009), at the beginning of the experiment and on the day of sacrifice. Rats were lightly anaesthetized with a mixture of 1.5% isoflurane (Forane) and 98.5% oxygen. The chests of the animals were shaved, acoustic coupling gel was applied, and warming pad was used to maintain normothermia. Rats were imaged in the left lateral decubitus position. Cardiac dimensions and functions were measured from short- and long-axis views at the mid-papillary level by a VEVO 770 high-resolution ultrasound imaging system (VisualSonics, Toronto, ON, Canada) – equipped with a 25 MHz transducer. LV ejection fraction (EF), LV end-diastolic volume (LVEDV), LV end-systolic volume (LVESV), LV inside dimensions (LVIDd and LVIDs), E/E' ratio and the thickness of septum and posterior wall (PW) were determined. EF (%) was calculated by: 100 × [(LVEDV – LVESV)/LVEDV]; relative wall thickness (RWT) was calculated by: (PW thickness + interventricular septal thickness)/LVIDd.

Investigation of Vascular and Cardiac Remodeling With Histology and Immunohistochemistry

Heart, carotid arteries and aortic segments excised for histological processing were fixed immediately after excision in buffered paraformaldehyde solution (4%) for 1 day. Five μm thick sections were cut. Slices were stained with Masson's trichrome staining to detect the interstitial fibrosis as described earlier (Deres et al., 2014; Magyar et al., 2014).

The intima-media thickness was measured on cross sections of histological preparations from great arteries with Mirax Viewer software (version: 1.12.22.0).

For assessment of cardiac fibrosis, five samples were taken from all cross-sectioned cardiac preparations at constant magnification from separate, continuous territories excluding perivascular, sub-endo- and sub-pericardial areas. Different stainings were discriminated by Color deconvolution plugin for ImageJ with built-in color vectors for Masson's trichrome. After autothresholding, the area fraction of aniline-blue staining was measured in each sample and ANOVA analysis was performed.

For evaluation of vascular fibrosis, five different areas (ROIs) from the territories of the tunica media layers of aorta and carotid arteries were selected, where measurements have been made. Different stainings were discriminated by Color deconvolution plugin for ImageJ with built-in color vectors for Masson's trichrome. After autothresholding, the area fraction of aniline-blue staining has been measured in each predefined ROIs. On carotis data Square root transformation has been made.

All histological samples were examined by an investigator in a blinded fashion.

Evaluation of Cardiac and Vascular Remodeling With Electron Microscopy

Electron microscopic examinations were performed on hearts and great vessels from the treated and control SHR animals. The fixative was supplemented with 1% glutaraldehyde. After washing, samples were stained with 1% OsO_4 in PB, dehydrated through ascending ethanol series and embedded in Durcupan ACM resin. Sections were cut, counterstained with Reynold's lead citrate, and examined and photographed in a JEOL 1200 EX electron microscope. All histological samples were examined by an investigator in a blinded fashion.

Western Blot Analysis on Heart and Great Vessels

Heart samples, carotid arteries and aortic segments were homogenized in ice-cold 50 mM Tris-buffer, pH 8.0 (containing Protease and Phosphatase Inhibitor Cocktail 1:1000, Sigma Aldrich – P88340, P5726 and 50 mM sodium vanadate) and harvested in 2× concentrated SDS-polyacrylamide gel electrophoresis sample buffer. Proteins were separated on 10 or 12% SDS-polyacrylamide electrophoresis gel and transferred to nitrocellulose membranes. After blocking (2 h with 3% non-fat milk in Tris-buffered saline), membranes were probed overnight at 4°C with antibodies recognizing the following antigens: anti-N-terminal domain of beta-actin (1:10,000; Cell Signaling Technology, 3700S), extracellular signal regulated kinase (ERK 1/2; 1:1000; Cell Signaling Technology, 9170S) and phospho-specific ERK 1/2 Thr^{202}/Tyr^{204} (1:1000; Cell Signaling Technology, 4370S), c-Jun N-terminal kinase (JNK; 1:1000; Cell Signaling Technology, 3708S) and phospho-specific JNK Thr^{183}/Tyr^{185} (1:1000; Cell Signaling Technology, 9255S), TGF-beta (1:1000; Cell Signaling Technology, 3711S), SMAD2 (1:000; Invitrogen, 436500) and phospho-specific SMAD2 $Ser^{465/467}$ (1:1000; Invitrogen, MA5-15122), p38 MAPK (1:000; Invitrogen, AOH1202) phospho-specific p38-MAPK Thr^{180}-Gly-Tyr^{182} (1:1000; Invitrogen, MA5-15177), Akt (1:1000; Cell Signaling Technology, 9272S) and phospho-specific Akt Ser^{473} (1:1000; Cell Signaling Technology, 9018S), GSK-3-beta (1:000; Signaling Technology, 9315S) and phospho-specific GSK-3-beta Ser^{9} (1:1000; Cell Signaling Technology, 9323S). Membranes were washed six times for 5 min in Tris-buffered saline (pH 7.5) containing 0.2% Tween (TBST) before addition of goat anti-rabbit horseradish peroxidase-conjugated secondary antibody (1:3000 dilution). The antibody–antigen complexes were visualized by means of enhanced chemiluminescence. After scanning, results were quantified by NIH Image J program.

Blood Sampling

To assess drug plasma exposures, blood samples were collected from the rats by direct cardiac puncture on the last day of the study just before necropsy between 08.20 am and 12.20 pm. The blood samples were drawn into either heparinized tubes or Lavender Vacutainer tubes containing EDTA. The blood samples were centrifuged at 1600 g for 15 min at 4°C to separate plasma. Supernatants were collected and kept at −70°C.

Statistical Analysis

All data are expressed as mean ± SEM. For comparison of WKY and Control groups, independent sample's t-test (2-tailed) was applied. Control and Treatment groups were analyzed

using one-way ANOVA (SPSS for Windows 20.0). For *post hoc* comparison Dunnett's test (2-tailed) was chosen. In cases of inhomogeneous group variances Welch correction was applied followed by Dunnett T3 *post hoc* test. On GCL cell number data Kruskal–Wallis test was conducted, due to extreme non-normal distribution of the FGY400 group. Values of $p < 0.05$ were considered statistically significant. All individual data are tabulated in the Appendix.

RESULTS

Effect of FGY-1153 on Body Weight and Food Consumption

Body weights were measured and recorded once weekly during the treatment period. There were no significant differences between the three hypertensive groups neither at the beginning nor at the end of treatment period (Control: 362.4 ± 4.4 g, FGY120: 366.8 ± 3.3 g, FGY400: 369.1 ± 5.8 g) (**Figure 1**). The quantity of food consumed by each cage of animals was measured and recorded once weekly during the treatment period. There were no overt differences between the food consumptions of the three groups throughout the study (**Figure 1** and **Supplementary Tables S1**–**S6**).

FGY-1153 Dose Calculation and Drug Plasma Concentrations Detected

The weekly calculated dose (calculation based upon: food consumption, FGY-1153 concentration in rat chow, body weight) of test substance was 6.32 ± 0.14 (ranged from 5.51 ± 0.47 to 7.76 ± 0.14) mg/kg/day in the FGY120 group and 20.9 ± 0.59 (ranged from 16.6 ± 0.4 to 28.0 ± 0.3) mg/kg/day in the FGY400 group (**Supplementary Tables S7**, **S8**, $n = 15$).

Plasma concentrations measured from the rats of the FGY120 and FGY400 groups are presented in **Supplementary Table S9**.

Effect of FGY-1153 on Blood Pressure

At the beginning of the study there was no significant difference between the systolic arterial blood pressure of the three hypertensive groups (Control: 178.73 ± 3.25 mmHg, FGY120 group: 172.47 ± 3.81 mmHg, FGY400 group: 174.53 ± 2.30 mmHg, $p = 0.374$). Systolic arterial blood pressure values did not differ significantly between the groups both at Week 13 (Control: 215.93 ± 6.11 mmHg, FGY120 group: 212.73 ± 5.68 mmHg, FGY400 group: 228.80 ± 4.48 mmHg, $p = 0.096$) and at Week 26 (Control: 256.36 ± 8.04 mmHg, FGY120 group: 256.80 ± 7.69 mmHg, FGY400 group: 275.33 ± 3.07 mmHg, $p = 0.078$; $n = 15$).

Nevertheless, a non-significant trend of higher blood pressure in the FGY400 group was apparent (**Supplementary Table S10**).

Effect of FGY-1153 on Echocardiographic Parameters

Compared to the parameters measured at the beginning of the study, the septum and PW thicknesses increased in all hypertensive groups during the treatment period ($p < 0.01$). However, treatment with both low dose and high dose FGY-1153 significantly attenuated the hypertrophy of septum and PW ($p < 0.01$ and $p < 0.05$, respectively vs. Control).

LVIDs and LVIDd were also increased in all SHR groups during the study, but the elevation of these parameters were significantly attenuated in the FGY120 group ($p < 0.05$), while not in the FGY400 group. Left ventricular systolic function – expressed as EF% – showed a decreasing tendency in both the Control group and the FGY400 group by the end of the study compared to the initial parameters (**Table 1**). In comparison with the Control group, these changes were significantly attenuated in the FGY120 group ($p < 0.05$ vs. Control), indicating that the low dose FGY-1153 treatment prevented the hypertension induced decrease in systolic left ventricular function. The E/E' ratio showed an increasing tendency during the study in the Control group, while this parameter was significantly decreased in both the FGY120 and FGY400 groups ($p < 0.05$ vs. Control) (**Table 1** and **Figure 2**).

Effect of FGY-1153 on the Interstitial Fibrosis of Heart and Great Vessels

Analysis of interstitial fibrosis in SHR heart samples revealed no statistically significant difference between Control and Treatment groups (FGY120 and 400). The collagen content in WKY hearts, however, was significantly lower ($p < 0.05$) compared to the Control group (Mean area fractions ± SEM: WKY: 0.390 ± 0.021; Control: 0.657 ± 0.069; FGY120: 0.636 ± 0.088; FGY400: 0.582 ± 0.041; $n = 4$) (**Figure 3**). In carotid arteries and aortas a statistically non-significant increase of vascular collagen could be observed in Control group compared to WKY. No significant differences could be found between Control, FGY120 and FGY400 groups (Mean area fractions ± SEM: Aorta: WKY: 1.084 ± 0.112 ($p = 0.536$ vs. Control); Control: 1.378 ± 0.414; FGY120: 1.239 ± 0.526; FGY400: 1.458 ± 0.324, ($p = 0.936$); $n = 4$). In carotid arteries a statistically non-significant decrease of vascular collagen could be observed in treated groups: WKY: 4.860 ± 0.532 ($p = 0.229$ vs. Control); Control: 5.994 ± 0.660; FGY120: 5.745 ± 1.465; FGY400: 5.158 ± 1.097; ($p = 0.866$), $n = 4$ data not shown).

Effect of FGY-1153 on the Intima-Media Thickness of Great Vessels

The IMT of carotid arteries was the lowest in the normotensive WKY group, (**Figures 4A,B,E**) ($p < 0.05$ vs. Control $n = 3$). Chronic hypertension caused a marked increase of IMT in the Control group. In comparison with the Control group (**Figure 3B**), the intima-media thickness of carotid vessels was slightly decreased in both the FGY120 and FGY400 groups (**Figures 4C,D**). However, the alterations were not statistically significant ($p = 0.149$, $n = 4$).

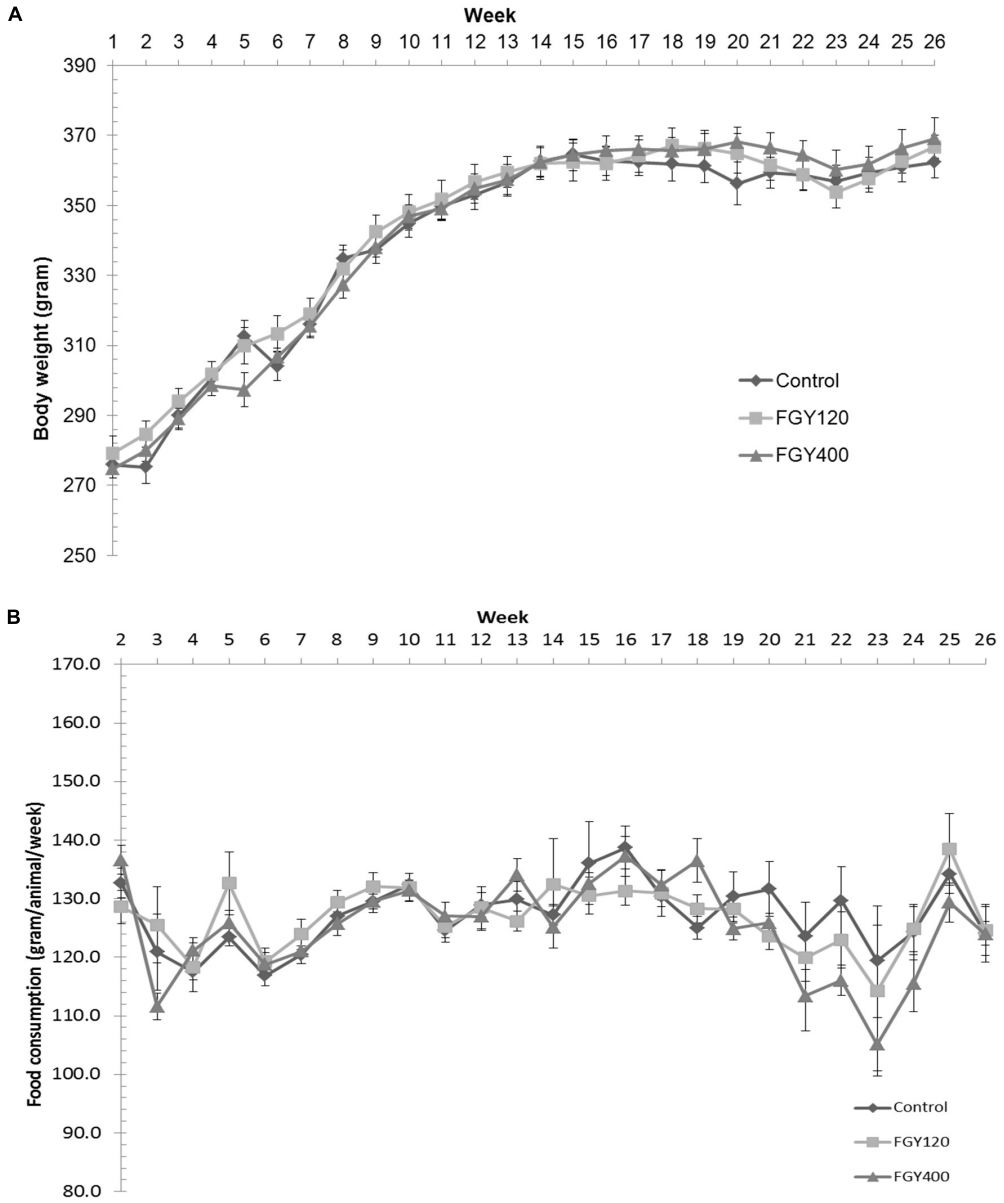

FIGURE 1 | Effect of FGY-1153 on body weight and food consumption during the treatment period. **(A)** Effect of FGY-1153 on body weight during the treatment period (n = 14 Control, n = 15 FGY120, n = 15 FGY400). Data are presented as mean ± S.E.M. One-way ANOVA analysis conducted for each week did not reveal statistically significant differences between groups. **(B)** Effect of FGY-1153 on food consumption during the treatment period (n = 7 Control, n = 7 FGY120, n = 7 FGY400). Data are presented as mean ± S.E.M. Data were analyzed with one-way ANOVA. No statistically significant differences were found at any time points between the groups.

Effect of FGY-1153 on the Ultrastructural Changes in the Myocardium and Great Vessels

Electron Microscopic Studies of the Myocardium

Transmission electron microscopic analysis of capillary endothelium in the myocardium (**Supplementary Figures S1**, **S2**) showed normal structure in all groups. The morphology of Eberth' lines (not shown) and sarcomere units was also normal in both the Control and FGY-1153 treated groups (**Supplementary Figures S1D–F**). The nuclei of cardiomyocytes in the Control rats predominantly display euchromatin with minor membrane-associated marginal heterochromatin (**Figure 5A**). In contrast, in the other two groups cell nuclei were pale and displayed higher amount of membrane-associated marginal chromatin suggesting differences in the activity of transcription (**Figures 5B,C**). In the cytoplasm glycogen (**Figure 5** and **Supplementary Figures S1**, **S2** arrow heads) and lipid droplets (not shown) could be seen in all groups, however, the amount of glycogen was

TABLE 1 | Evaluation of echocardiographic parameters.

	SHR week 0	Control week 26	FGY120 week 26	FGY400 week 26	WKY age-matched
Septum (mm)	1.66 ± 0.01	2.09 ± 0.04	1.90 ± 0.04**	1.88 ± 0.02**	1.67 ± 0.07**
Post. Wall (mm)	1.58 ± 0.02	1.94 ± 0.02	1.82 ± 0.01*	1.81 ± 0.04*	1.644 ± 0.11*
LVIDd	7.28 ± 0.07	8.28 ± 0.08	7.94 ± 0.09*	7.98 ± 0.11	8.00 ± 0.25
LVIDs	4.40 ± 0.07	5.38 ± 0.09	4.85 ± 0.08**	5.12 ± 0.14	4.52 ± 0.12**
LVEDV (ml)	280.49 ± 6.06	373.54 ± 8.11	340.79 ± 9.25*	344.72 ± 10.78	349.85 ± 24.66
LVESV (ml)	88.72 ± 3.33	141.56 ± 5.89	111.69 ± 4.15**	127.31 ± 8.66	97.07 ± 5.54**
EF (%)	68.48 ± 0.75	62.16 ± 1.24	67.10 ± 1.33*	63.36 ± 1.37	71.67 ± 0.87**
E/E'	35.16 ± 1.54	42.17 ± 5.26	30.05 ± 0.86*	26.50 ± 2.77*	30.00 ± 2.26
RWT	0.447 ± 0.004	0.485 ± 0.014	0.469 ± 0.007	0.464 ± 0.011	0.413 ± 0.01**

*Data of all animals are presented in the first column (SHR Week 0, N = 21) at the beginning of the study and data from the three groups (Control, FGY120, FGY400 Week 26; n = 7 in each groups) are indicated at the end of the treatment period. Last column represents the data of age-matched normotensive animals (WKY, n = 7). Values are expressed as mean ± S.E.M. Comparisons between WKY and Control groups were made by independent samples t-test. Data of Control and Treatment groups were analyzed with one-way ANOVA followed by Dunnett's post hoc test (*p < 0.05, **p < 0.01 vs. Control).*

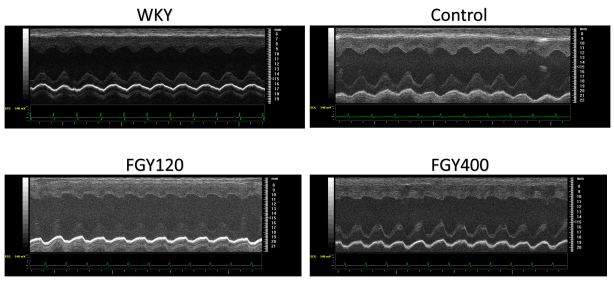

FIGURE 2 | Representative M-mode pictures of the left ventricle. M-mode pictures of each group: WKY, Control, FGY120, FGY400.

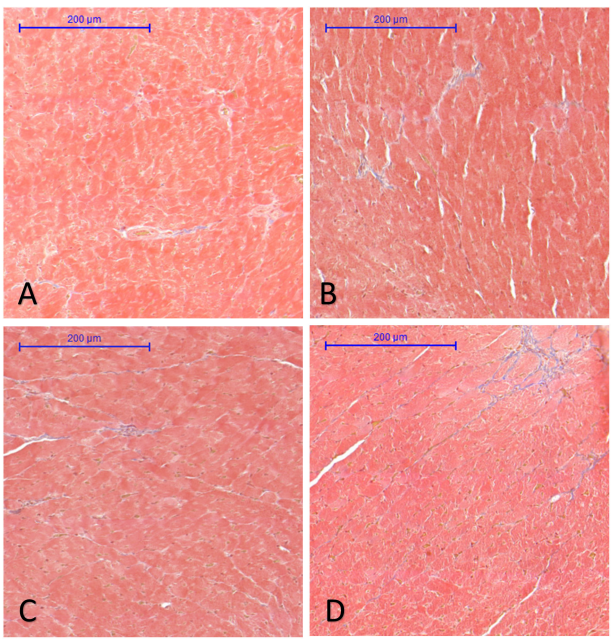

FIGURE 3 | Effect of FGY-1153 treatment on the interstitial cardiac fibrosis. Statistical analysis of Masson's trichrome stained sections revealed no significant difference between the Control **(B)**, FGY120 **(C)**, and FGY400 **(D)** groups. WKY group **(A)**, however, showed significantly lower collagen content relative to Control **(B)** group (WKY: 0.390 ± 0.021; Control: 0.657 ± 0.069; FGY120: 0.636 ± 0.088; FGY400: 0.582 ± 0.041; *n* = 4).

slightly increased and the number of lipid droplets was slightly decreased in the FGY120 group compared to the Control and FGY400 groups.

The mitochondria of SHR rats (**Figure 5**) differ from the normal mitochondria of healthy rats (**Supplementary Figure S2**). In the Control group (**Figure 5D**) extensive disruption of mitochondrial cristae and enlarged intracristal spaces could be observed. The mitochondrial population was characterized by morphological heterogeneity, their structure was polymorph, their shape was often elongated, and the mitochondrial matrix was very light.

The mitochondrial ultrastructure in the FGY120 group was similar to that of the healthy rats (**Figure 5E** and **Supplementary Figure S2**). The structure of the mitochondrial cristae was almost normal, dense matrix was seen and the mitochondria were less elongated. The ratio of mitochondria to myofibrils was higher, the elevated number of mitochondria was accompanied by increased amount of intracellular glycogen in comparison to the Control group. In the samples of FGY400 group (**Figure 5F**) the mitochondrial matrix was also dense, however, more morphological abnormalities, e.g., disorganized mitochondrial cristae could be revealed in comparison to the FGY120 group (n = 5 from each group, 3–5 block from each animal).

Electron Microscopic Studies of the Walls of Aortas and Carotid Arteries

The ultrastructure of the wall of normotensive aorta (not shown) and carotid arteries is characterized by endothelial cells lying almost directly on the internal elastic lamina (**Supplementary Figure S3**). The surface of the endothelial monolayer is smooth, the cells have very thin cytoplasm and an elongated nucleus which is oriented parallel to the internal elastic lamella. The subendothelial space is narrow, the internal elastic lamina is rarely interrupted. In the tunica

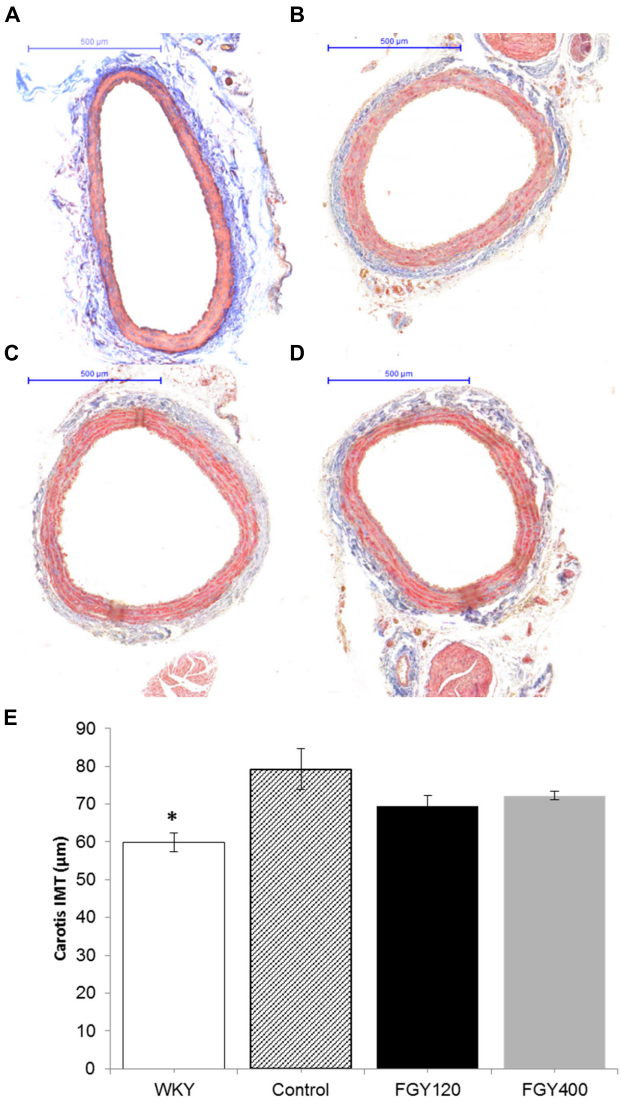

FIGURE 4 | Masson's trichrome staining of carotid vessels. IMT was the lowest in the WKY group **(A)**. In comparison with the Control group **(B)**, the intima-media thickness of carotid vessels was slightly decreased in both the FGY120 **(C)** and FGY400 groups **(D)**, (n = 4). The alterations were not significant. Effect of FGY-1153 treatment on intima-media thickness of carotid vessels **(E)**. IMT, intima-media thickness (*p < 0.05 vs. Control group (n = 3).

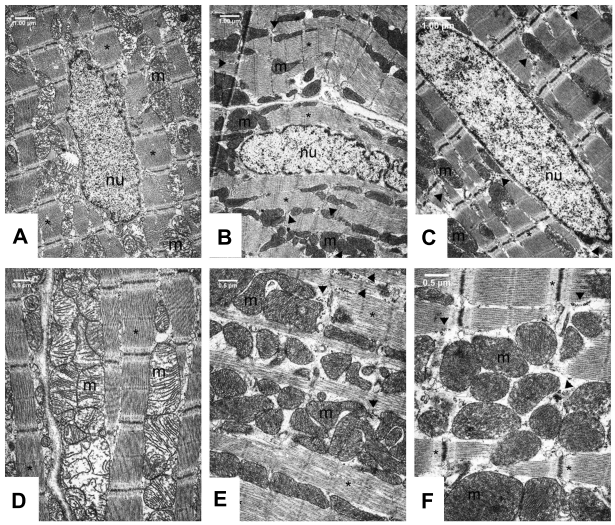

FIGURE 5 | Ultrastructural analysis of the cardiomyocytes in Control **(A,D)**, FGY120 **(B,E)**, and FGY400 **(C,F)** group. Sarcoplasm (sp), Muscle fibers (*), Mitochondria (m), Nuclei (nu), Glycogen (arrow heads), (n = 5 from each group, 3–5 block from each animal).

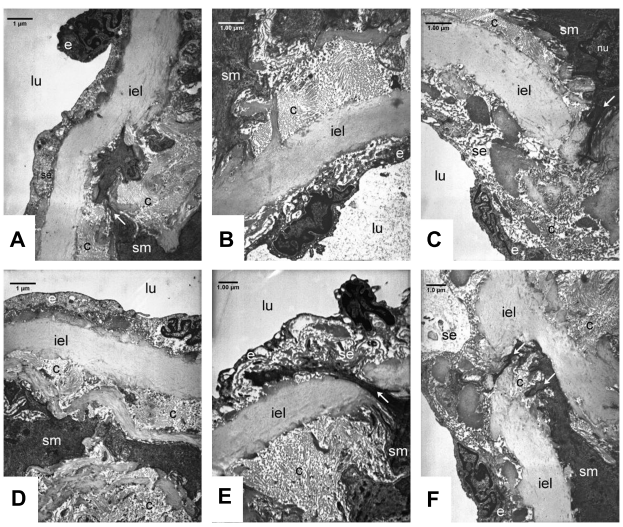

FIGURE 6 | Ultrastructural analysis of carotid walls in the Control **(A, D)**, FGY120 **(B, E)**, and FGY400 **(C, F)** groups. Lumen (lu), Endothelium (e), Subendothelium (se), Internal elastic lamina (iel), Smooth muscle cells (sm), Collagen fibers (c), Interruption of internal elastic lamella by the smooth muscle cells (arrows), (n = 5 from each group, 3–5 block from each animal).

intima the cellular elements (fibroblasts, smooth muscle cells) are arranged between the layers of internal elastic lamina (**Supplementary Figure S3**).

In the carotid arteries (**Figure 6**) and also in the aorta (data not shown) of the SHR groups the wall structure was pathologic. The nuclei of smooth muscle cells in the intimal layer were lobular and showed signs of activation. The activated smooth muscle cells are involved in the synthesis of the components of fibers, which was confirmed by the presence of collagen and elastic fibers around them (**Figure 6**). Expanding smooth muscle cells sporadically broke through the internal elastic lamina (**Figures 6C,E,F**), resulting in the appearance of collagen and cellular elements in the subendothelial space. Accumulation of connective tissue and cellular elements in the subendothelial space can exert tension to the endothelial monolayer, so the endothelial cells became distorted, their cytoplasm was lateralized and in some places became thinner. Presumably the endothelial permeability increased due to cell distortion,

which contributed to subendothelial space expansion and further endothelial erosion.

Additional sign of tension-distorted endothelial cells is the altered orientation of their nuclei, which became rounded and protruded into the lumen, so the surface of the endothelial monolayer became rough (**Figures 6A,B,E**).

Rearrangement of tunica media layers could be seen, as a consequence of hypertension-induced smooth muscle cell activation and collagen synthesis. In the walls of carotid arteries more intensive collagen synthesis was seen compared to aortic walls. We could not see any significant differences between the control group and the treated groups (FGY120 and FGY 400) (**Figure 6**) (n = 5 from each group, 3–5 block from each animal).

Effect of FGY-1153 on the TGFβ/SMAD2 Signaling Pathway in Heart and Great Vessels

Western Blot Analysis of Heart Samples

Western blot analysis showed that both TGFβ and SMAD2 phosphorylation levels were significantly lower in WKY animals compared to the Control group. FGY-1153 treatment inhibited the cardiac expression of TGFβ and the phosphorylation of the SMAD2 protein in the FGY120 group, however, the high dose treatment had no significant effect on the phosphorylation of SMAD2 in the FGY400 group. Actin is shown as loading control. Representative immunoblots from four experiments and densitometric evaluation are demonstrated (**Figure 7**).

Western Blot Analysis of Carotid Samples

Western blot analysis showed that both TGFβ expression and SMAD2 phosphorylation levels were significantly higher in Control group relative to WKY. Both low and high dose FGY-1153 treatment significantly inhibited the expression of TGFβ. The phosphorylation of the SMAD2 protein was significantly decreased in both the FGY120 and in FGY400 groups in carotid tissues. Actin is shown as loading control. Representative immunoblots from four experiments and densitometric evaluation are demonstrated (**Figure 8**).

Effect of FGY-1153 on the Phosphorylation of MAPK Signaling Cascade in Heart and Great Vessels

Western Blot Analysis of Heart Samples

Western blot analysis showed significantly lower ERK1/2 phosphorylation level in WKY, relative to the Control group (**Figure 9**). FGY-1153 treatment significantly inhibited ERK1/2 phosphorylation in both FGY120 and in FGY400 hearts. However, it had no statistically significant effect on the phosphorylation of p38-MAPK and JNK proteins (data not shown).

Western Blot Analysis of Carotid Samples

Phosphorylation level of JNK was significantly higher in the Control relative to the WKY group. Western blot analysis showed that low dose FGY-1153 treatment had no significant effect on phosphorylation of p38-MAPK and JNK proteins, but elevated the phosphorylation level of ERK1/2 protein. High

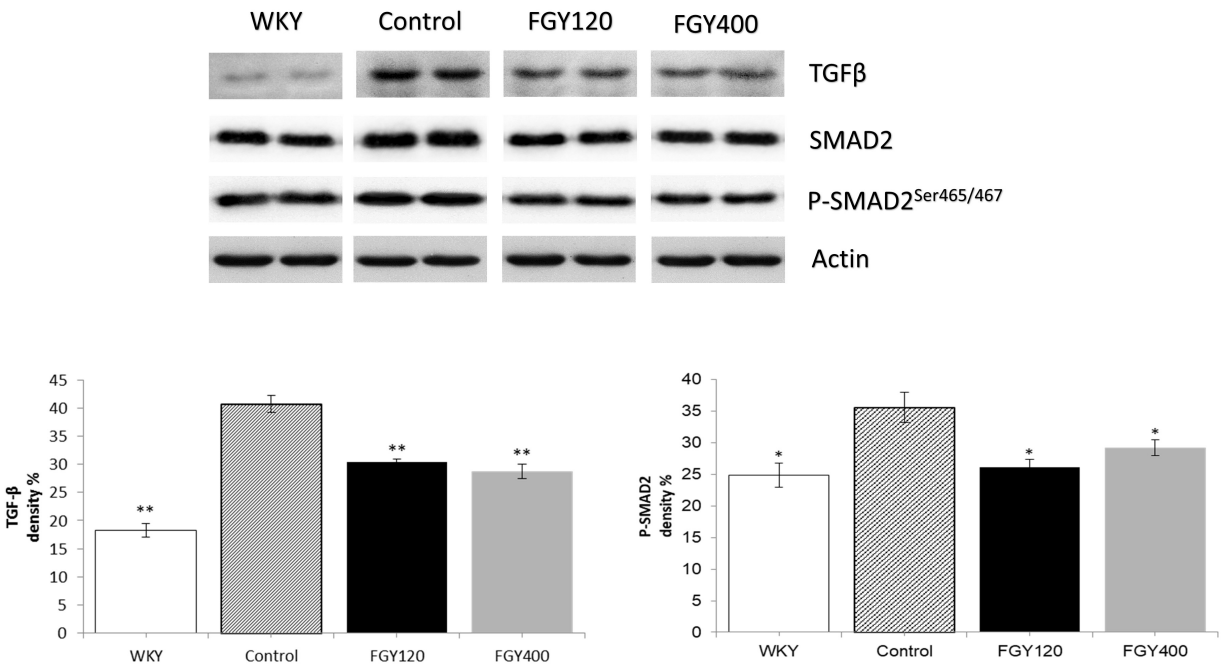

FIGURE 7 | The effect of FGY-1153 on the TGFβ/SMAD2 signaling pathway in heart samples. Data are presented as mean ± S.E.M. Data were analyzed by independent samples t-test between WKY and Control groups. Comparisons of Control and Treatment groups were made by one-way ANOVA followed by Dunnett's *post hoc* test. $^{*}p < 0.05$, $^{**}p < 0.01$ vs. Control, n = 4.

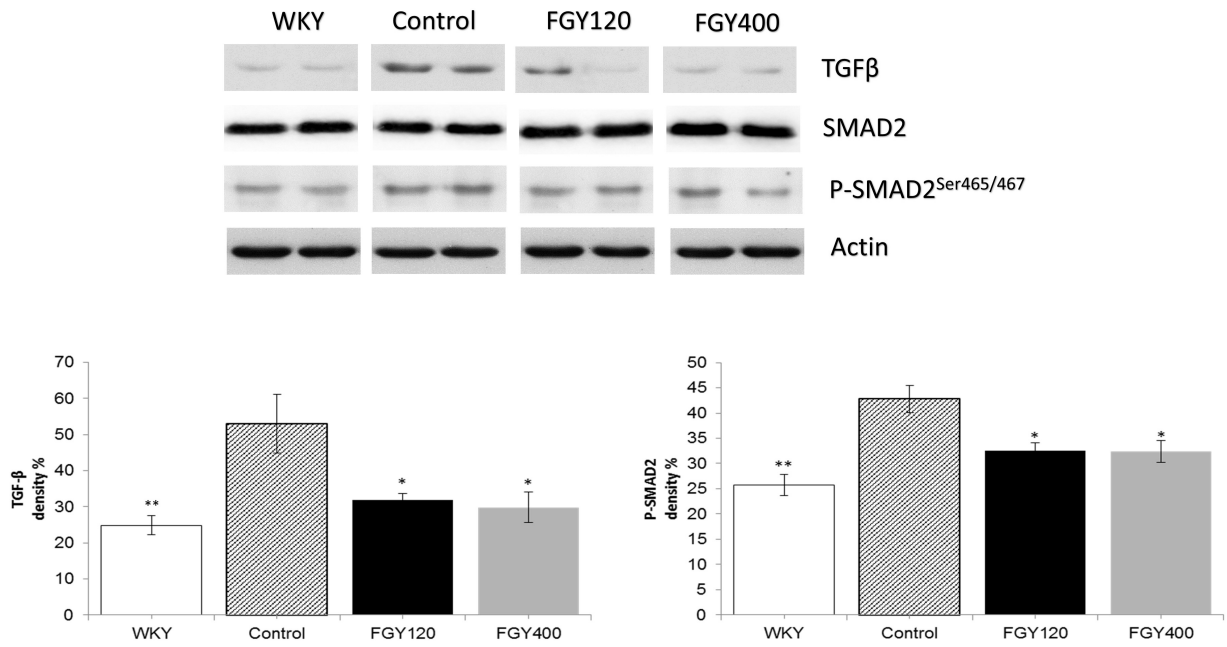

FIGURE 8 | The effect of FGY-1153 on the TGFβ/SMAD2 signaling pathway in the carotid arteries. Data are presented as mean ± S.E.M. Data were analyzed by independent samples *t*-test between WKY and Control groups. Comparisons of Control and Treatment groups were made by one-way ANOVA followed by Dunnett's *post hoc* test. $*p < 0.05$, $**p < 0.01$ vs. Control $n = 4$.

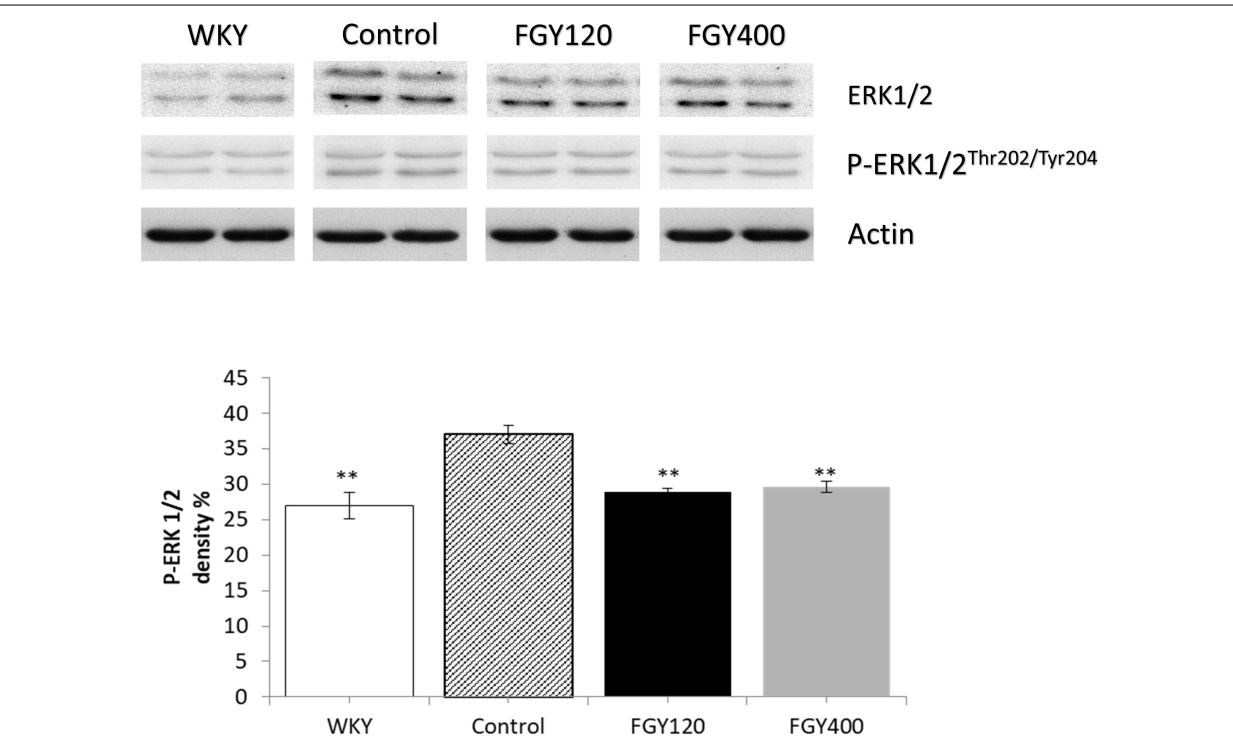

FIGURE 9 | The effect of FGY-1153 on the ERK 1/2 signaling in heart of SHR rats. Data are presented as mean ± S.E.M. Data were analyzed by independent samples *t*-test between WKY and Control groups. Comparisons of Control and Treatment groups were made by one-way ANOVA followed by Dunnett's *post hoc* test. $**p < 0.01$, $n = 4$.

dose treatment had no significant effect on the phosphorylation of MAPKs. Actin is shown as loading control. Representative immunoblots from four experiments and densitometric evaluation are demonstrated (**Figure 10**).

Effect of FGY-1153 on the Phosphorylation of Akt/GSK-3β Signaling Cascade in Heart and Great Vessels

Western Blot Analysis of Heart Samples

Western blot analysis showed GSK-3β phosphorylation to be significantly lower in WKY relative to Control group. High dose of FGY-1153 treatment significantly elevated phosphorylation of Akt protein, and both low dose and high dose treatment significantly attenuated the GSK-3β phosphorylation (data not shown).

Western Blot Analysis of Carotid Samples

Western blot analysis of Akt protein and GSK-3β phosphorylation showed no difference between the WKY and control SHR groups. FGY-1153 treatment significantly promoted the phosphorylation of Akt protein and GSK-3β in the carotid tissues of both FGY120 and FGY400 groups. However, the high dose treatment had milder effect on the GSK-3β phosphorylation in the FGY400 group. Actin is shown as loading control. Representative immunoblots from four experiments and densitometric evaluation are demonstrated (**Figure 11**).

DISCUSSION

The major finding of this study is that pharmacological inhibition of bradykinin B1 receptors do not cause elevation of blood pressure and do not cause worsening of hypertensive target organ damages in a chronic hypertensive animal model. Moreover, we have found that the administration of FGY-1153, an experimental bradykinin B1 receptor antagonist compound causes slight protective effect against cardiovascular remodeling. We used SHR which provide an animal model of high blood pressure that is similar to essential hypertension in humans (Ito et al., 2007).

Hypertension is a growing public health problem mainly in middle-aged and in elderly people. In hypertensive patients systolic blood pressure (SBP) and pulse pressure are the dominant prognostic markers. Plenty of studies showed that increasing levels of SBP were associated with a higher risk of cerebro- and cardiovascular events. Unfortunately, the rate of hypertension control only minimally improved over the last decades. One important factor in the background of the inadequate hypertension control is the drug interactions between

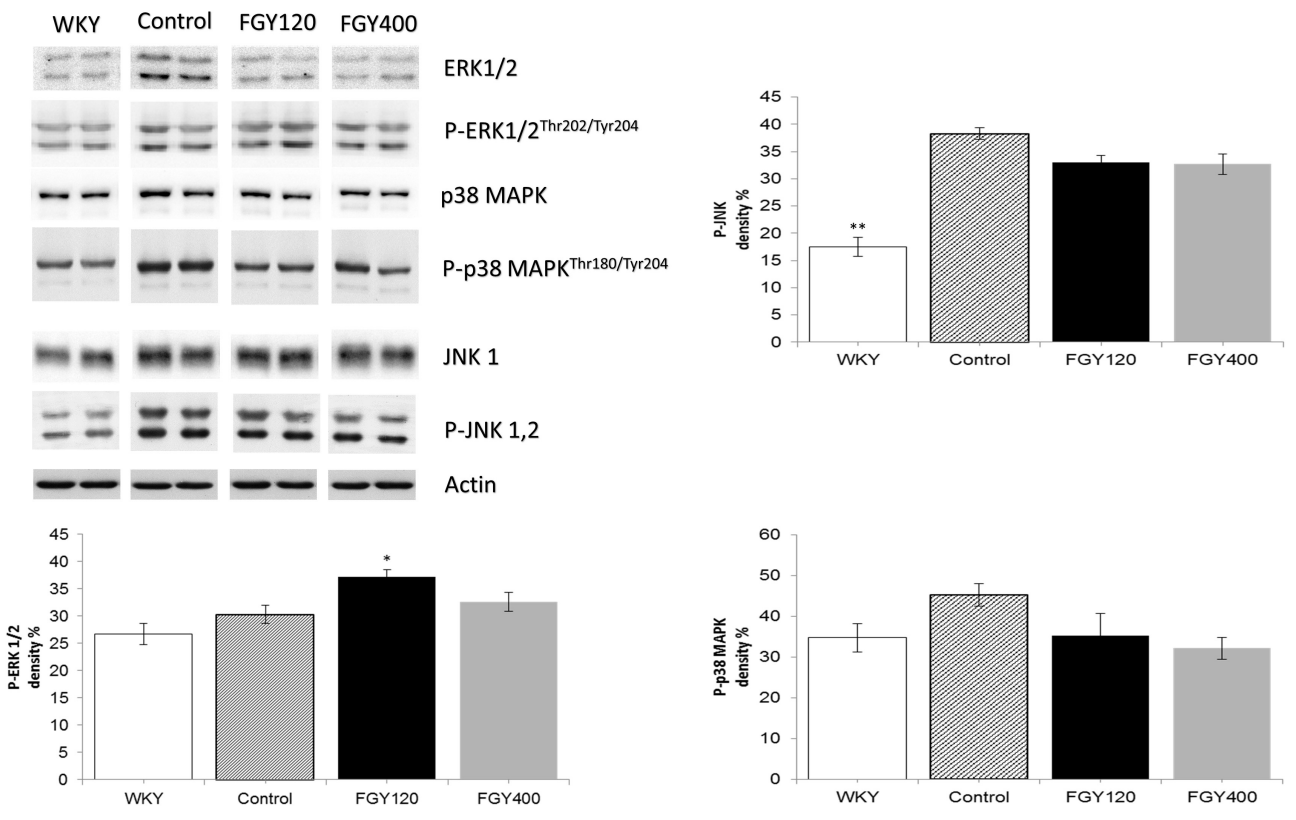

FIGURE 10 | The effect of FGY-1153 on the MAPK signaling factors in carotid vessels of SHR rats. Data are presented as mean ± S.E.M. Data were analyzed by independent samples *t*-test between WKY and Control groups. Comparisons of Control and Treatment groups were made by one-way ANOVA followed by Dunnett's *post hoc* test. $^{*}p < 0.05$, $^{**}p < 0.01$, $n = 4$.

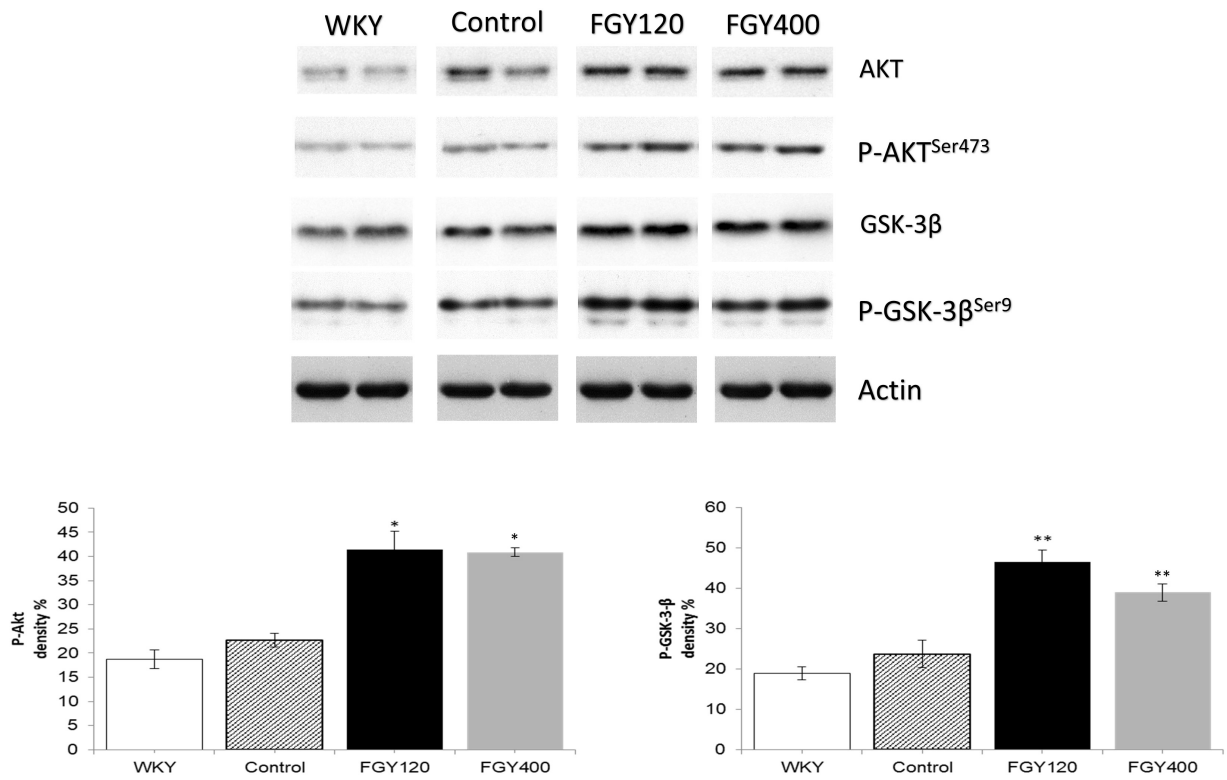

FIGURE 11 | The effect of FGY-1153 on the Akt/GSK-3β signaling cascade in carotis wall. Data are presented as mean ± S.E.M. Data were analyzed by independent samples *t*-test between WKY and Control groups. Comparisons of Control and Treatment groups on GSK-3β data were made by one-way ANOVA followed by Dunnett's *post hoc* test. On Akt data one-way ANOVA with Welch correction were conducted followed by Dunnett T3 *post hoc* test. $^{*}p < 0.05$, $^{**}p < 0.01$ vs. Control, $n = 4$.

antihypertensive agents and several non-cardiovascular drugs, e.g., NSAIDs (Pavlicević et al., 2008; Deedwania, 2011).

Moreover, it is also well-known, that the worldwide commonly prescribed pain relievers, the NSAIDs can significantly increase cardiovascular morbidity and mortality (Patrono and Baigent, 2014). This unfavorable phenomenon is partly caused by the increase in atherothrombotic events (Garcia Rodriguez et al., 2008; McGettigan and Henry, 2011), but the other major cause is the increase in mortality due to heart failure (Garcia Rodriguez and Hernandez-Diaz, 2003).

Because of the above mentioned causes there is an unmet medical need to develop novel and safer anti-inflammatory compounds.

Kinins are biologically active peptides that exert a broad spectrum of physiological effects, including vasodilation, smooth muscle contraction, inflammation, and pain induction (Tschöpe et al., 2000). The biological effects of kinins are mediated through the stimulation of bradykinin B1 and B2 receptors. The B2 receptor is constitutively expressed and is activated by intact kinins, bradykinin, and kallidin. This receptor is believed to play an important role in mediating the beneficial effects of ACE-inhibitors, but it is also involved in the acute phases of inflammation (Tschöpe et al., 2000; Leeb-Lundberg et al., 2005; Golias et al., 2007). However, the B1 receptor is activated by the carboxypeptidase metabolites of kinins, des-Arg9-BK and des-Arg10-kallidin. The B1 receptor is normally weakly expressed, but it is upregulated in the presence of cytokines, endotoxins or during tissue injury (Tschöpe et al., 2000; Leeb-Lundberg et al., 2005; Golias et al., 2007). The B1 receptor mediates chronic inflammation and pain (Leeb-Lundberg et al., 2005; Golias et al., 2007); thus, bradykinin B1 receptor antagonism can be a potential novel approach for treating these conditions without having deleterious cardiovascular effects.

On this basis, we examined the effect of FGY-1153, a bradykinin B1 receptor antagonist (administered in two concentrations) on the cardiovascular changes provoked by chronic hypertension.

FGY-1153 treatment did not have any effects on food consumption and on body weight. The mean daily doses of FGY-1153 in the 120 ppm and 400 ppm groups were approximately 6 mg/kg and 20 mg/kg, respectively.

Chronic onset of elevated blood pressure in hypertension leads to the development of hypertensive cardiopathy (Montezano et al., 2015). This pathology of heart is characterized morphologically by marked thickening of left ventricular walls, also known as left ventricular hypertrophy. Functionally these hearts show diastolic dysfunction and if the hypertension is not treated properly, finally the contractile function will also be

impaired (Nadruz, 2015). In our work there was no significant difference between the blood pressures in the three SHR groups, moreover, the high dose treatment (20 mg/kg/day) caused a non-significant increase in blood pressure. In spite of the unchanged or even slightly higher blood pressures, FGY-1153 had a mild but significant protective effect against the development of hypertension-induced left ventricular hypertrophy. The thickness of LV walls (septum and PW), as well as the RWT were lower in treated hypertensive groups. One of the best measures of diastolic function is the E/E' ratio (Sharifov et al., 2016). The higher the ratio, the worse the diastolic function. The highest ratios could be seen in the Control group and they were decreased in animals treated by the bradykinin B1 receptor antagonist compound. The EF is the best indicator of LV systolic function (Cameli et al., 2016). Chronic hypertension caused a significant decreased EF in the Control group compared to normotensive animals. Low dose FGY1153 treatment prevented the hypertension-induced decrease of EF, but there was only an improving tendency in EF in the high-dose group (FGY400).

In spite of the above mentioned positive effects, in our experimental model, the bradykinin B1 receptor antagonist treatment had only marginal, non-significant effect on hypertension-induced vascular wall thickening in great vessels characterized by IMT.

The increased thickness of left ventricle and vascular walls in hypertensive patients is determined by the hypertrophy of cardiomyocytes/vascular smooth muscle cells and by the amount of interstitial collagen accumulation (Montezano et al., 2015). The myocardial and vascular collagen content was examined by transmission electron microscopy and measured by Masson's trichrome staining. FGY-1153 treatment did not decrease significantly the extent of hypertension-induced myocardial and vascular fibrosis (it only caused an improving tendency) (Limas et al., 1980; Okruhlicová et al., 2008; Sandow et al., 2009).

In the background of the cardioprotective effect of pharmacological bradykinin B1 blockade the preservation of mitochondrial structure can be the main cause. In untreated hypertensive animals (Control group) mitochondrial structure was disorganized, the cristae were disrupted, the intracristal spaces were enlarged and the sizes of mitochondria were heterogeneous. FGY-1153 treatment – predominantly the lower dose – maintained the normal structure of mitochondria in spite of chronic elevated blood pressure. This is a very important effect of FGY-1153, because mitochondria are one of the most important sources of reactive oxygen species formation and oxidative stress plays a central role in the pathogenesis of hypertensive organ damages (Puddu et al., 2008; Cal et al., 2011). It is well known, that the prosurvival signaling pathway (PI3K/Akt-1/GSK-3β) exerts its protective effect via maintaining the mitochondrial structure and function (Yang et al., 2015). Measuring the activity of these factors, we could observe that FGY-1153 caused a marked phosphorylation of Akt-1 and GSK-3β signaling factors.

Damaged and disorganized mitochondria via oxidative stress can alter the activity of several signal transduction pathways that have an important role in the pathogenesis of vascular and cardiac remodeling.

Oxidative stress provoked activation of signal transduction pathways can promote remodeling. One of these signaling factors are the MAP kinases (MAPKs) (Tanaka et al., 2001). In the recent work hypertension caused an increased phosphorylation state of the various MAPKs (p38-MAPK, ERK, JNK). However, FGY-1153 treatment did not cause consistent and significant changes in the activation state of these signaling molecules. ERK1/2 activity decreased in heart samples and JNK activity was also decreased in carotid arterial samples compared to untreated ones. However, in other samples there were no differences between treated and untreated animals.

In the mediation of vascular remodeling, the TGF-β/Smad pathway also plays an important role (Ruiz-Ortega et al., 2007; Deres, 2014). In the recent work we proved that FGY-1153 caused a significant inhibition in hypertension-induced activation of TGF and Smad-2 pathways in both myocardium and vascular walls. Therefore in the background of the beneficial effects of FGY-1153 treatment (predominantly in lower dose) the modulation of this pathway can also be an important factor besides its mitochondrial protective effect (Ruiz-Ortega et al., 2007; Perrotta et al., 2011).

CONCLUSION

In conclusion, the bradykinin B1 receptor antagonist compound FGY-1153 did not have any deleterious effects in SHR rats administering in low dose nor in high dose. Moreover we could observe some protective effects against hypertensive cardiovascular remodeling despite the fact that FGY-1153 did not have any antihypertensive effect. Inhibition of the TGF-β/Smad-2 and activation of Akt-1/GSK-3β signaling may be the main underlying mechanisms in the background of its cardiovascular protective effect.

DISCLOSURE

CC and SF was employed by company Gedeon Richter Plc., Budapest, Hungary. All other authors declare no competing interests.

ETHICS STATEMENT

The investigation conforms to the Guide for the Care and Use of Laboratory Animals published by the U.S. National Institutes of Health and was approved by the Animal Research Review Committee of the University of Pécs, Medical School (BA02/2000-2/2010).

AUTHOR CONTRIBUTIONS

LD, RH, SF, CC, and KT designed the study. LD, KE, NB, OH, and RH performed the experiments. SF and CC provided compounds

and rats. LD, RH, TH, KE, and OH processed and analyzed the data. LD, RH, CC, KT, and SF wrote the manuscript. All the authors reviewed and finally approved the manuscript.

FUNDING

This work was supported by the New National Excellence Program of the Ministry of Human Capacities, ÚNKP-17-4-I-PTE-209 and by the Hungarian Science Research Fund GINOP-2.3.2-15-2016-00049, GINOP-2.3.2-15-2016-00048, and GINOP-2.3.2-15-2016-00048.

ACKNOWLEDGMENTS

We are grateful to Prof. Laszlo Seress for generous contribution to electron microscopic investigations. The manuscript is part of the first author's Ph.D. thesis.

SUPPLEMENTARY MATERIAL

The Supplementary Material for this article can be found online at: https://www.frontiersin.org/articles/10.3389/fphys.2019.00624/full#supplementary-material

REFERENCES

Austinat, M., Braeuninger, S., Pesquero, J. B., Brede, M., Bader, M., Stoll, G., et al. (2009). Blockade of bradykinin receptor B1 but not bradykinin receptor B2 provides protection from cerebral infarction and brain edema. *Stroke* 40, 285–293. doi: 10.1161/strokeaha.108.526673

Bartha, E., Solti, I., Kereskai, L., Lantos, J., Plozer, E., Magyar, K., et al. (2009). PARP inhibition delays transition of hypertensive cardiopathy to heart failure in spontaneously hypertensive rats. *Cardiovasc. Res.* 83, 501–510. doi: 10.1093/cvr/cvp144

Cal, L. A., Maso, L. D., Caielli, P., Pagnin, E., Fusaro, M., Davis, P. A., et al. (2011). Effect of olmesartan on oxidative stress in hypertensive patients: mechanistic support to clinical trials derived evidence. *Blood Press.* 20, 376–382. doi: 10.3109/08037051.2011.575570

Cameli, M., Mondillo, S., Solari, M., Righini, F. M., Andrei, V., Contaldi, C., et al. (2016). Echocardiographic assessment of left ventricular systolic function: from ejection fraction to torsion. *Heart Fail. Rev.* 21, 77–94. doi: 10.1007/s10741-015-9521-8

Deedwania, P. C. (2011). Blood pressure control in diabetes mellitus: is lower always better, and how low should it go? *Circulation* 123, 2776–2778. doi: 10.1161/circulationaha.111.033704

Deres, L. (2014). *Investigation of Potential Drug Targets in the Development and Progression of Hypertensive Organ Damages*. Ph. D thesis, Hungary, HU: Quinqueecclesiensis Universitas.

Deres, L., Bartha, E., Palfi, A., Eros, K., Riba, A., Lantos, J., et al. (2014). PARP-inhibitor treatment prevents hypertension induced cardiac remodeling by favorable modulation of heat shock proteins, Akt-1/GSK-3β and several PKC isoforms. *PLoS One* 9:e102148. doi: 10.1371/journal.pone.0102148

Farkas, S., and Eles, J. (2011). The therapeutic potential of bradykinin B1 inhibitors in chronic pain. *Drugs Fut.* 36:301. doi: 10.1358/dof.2011.036.04.1584114

Garcia Rodriguez, L. A., and Hernandez-Diaz, S. (2003). Nonsteroidal anti-inflammatory drugs as a trigger of clinical heart failure. *Epidemiology* 14, 240–246. doi: 10.1097/01.ede.0000034633.74133.c3

Garcia Rodriguez, L. A., Tacconelli, S., and Patrignani, P. (2008). Role of dose potency in the prediction of risk of myocardial infarction associated with nonsteroidal anti-inflammatory drugs in the general population. *J. Am. Coll. Cardiol.* 52, 1628–1636. doi: 10.1016/j.jacc.2008.08.041

Golias, C. H., Charalabopoulos, A., Stagikas, D., Charalabopoulos, K., and Batistatou, A. (2007). The kinin system–bradykinin: biological effects and clinical implications. multiple role of the kinin system–bradykinin. *Hippokratia* 11, 124–128.

Ito, N., Ohishi, M., Yamamoto, K., Tatara, Y., Shiota, A., Hayashi, N., et al. (2007). Renin-angiotensin inhibition reverses advanced cardiac remodeling in aging spontaneously hypertensive rats. *Am. J. Hypertens.* 20, 792–799. doi: 10.1016/j.amjhyper.2007.02.004

Kokubo, M., Uemura, A., Matsubara, T., and Murohara, T. (2005). Noninvasive evaluation of the time course of change in cardiac function in spontaneously hypertensive rats by echocardiography. *Hypertens. Res.* 7, 601–609. doi: 10.1291/hypres.28.601

Kubota, Y., Umegaki, K., Kagota, S., Tanaka, N., Nakamura, K., Kunitomo, M., et al. (2006). Evaluation of blood pressure measured by tail-cuff methods (without heating) in spontaneously hypertensive rats Biol. *Pharm. Bull.* 29, 1756–1758. doi: 10.1248/bpb.29.1756

Lagneux, C., Bader, M., Pesquero, J. B., Demenge, P., and Ribuot, C. (2002). Detrimental implication of B1 receptors in myocardial ischemia: evidence from pharmacological blockade and gene knockout mice. *Int. Immunopharmacol.* 2, 815–822. doi: 10.1016/s1567-5769(02)00022-x

Leeb-Lundberg, L. M., Marceau, F., Muller-Esterl, W., Pettibone, D. J., and Zuraw, B. L. (2005). International union of pharmacology. XLV. Classification of the kinin receptor family: from molecular mechanisms to pathophysiological consequences. *Pharmacol. Rev.* 57, 27–77. doi: 10.1124/pr.57.1.2

Lerner, U. H., Sahlberg, K., and Ljunggren, O. (1989). Thrombin and bradykinin enhance prostaglandin production in human peripheral blood monocytes. *J. Oral Pathol. Med.* 18, 246–250. doi: 10.1111/j.1600-0714.1989.tb00772.x

Limas, C., Westrum, B., and Limas, C. J. (1980). The evolution of vascular changes in the spontaneously hypertensive rat. *Am. J. Pathol.* 98, 357–384.

Lloyd-Jones, D. M. (2001). The risk of congestive heart failure: sobering lessons from the framingham heart study. *Curr. Cardiol. Rep.* 3, 184–190. doi: 10.1007/s11886-001-0021-1

López, N., Varo, N., Díez, J., and Fortuño, M. A. (2007). Loss of myocardial LIF receptor in experimental heart failure reduces cardiotrophin-1 cytoprotection. a role for neurohormonal agonists?. *Cardiovasc. Res.* 75, 536–545. doi: 10.1016/j.cardiores.2007.04.025

Magyar, K., Deres, L., Eros, K., Bruszt, K., Seress, L., Hamar, J., et al. (2014). A quinazoline-derivative compound with PARP inhibitory effect suppresses hypertension-induced vascular alterations in spontaneously hypertensive rats. *Biochim. Biophys. Acta* 1842, 935–944. doi: 10.1016/j.bbadis.2014.03.008

Marceau, F., and Bachvarov, D. R. (1998). Kinin receptors. *Clin. Rev. Allergy Immunol.* 16, 385–401.

McGettigan, P., and Henry, D. (2011). Cardiovascular risk with non-steroidal anti-inflammatory drugs: systematic review of population-based controlled observational studies. *PLoS Med.* 8:e1001098. doi: 10.1371/journal.pmed.1001098

Montezano, A. C., Tsiropoulou, S., Dulak-Lis, M., Harvey, A., Camargo Lde, L., and Touyz, R. M. (2015). Redox signaling, Nox 5 and vascular remodeling in hypertension. *Curr. Opin. Nephrol. Hypertens.* 24, 425–433. doi: 10.1097/MNH.0000000000000153

Moreau, M. E., Garbacki, N., Molinaro, G., Brown, N. J., Marceau, F., and Adam, A. (2005). The kallikrein-kinin system: current and future pharmacological targets. *J. Pharmacol. Sci.* 99, 6–38. doi: 10.1254/jphs.srj05001x

Nadruz, W. (2015). Myocardial remodeling in hypertension. *J. Hum. Hypertens.* 29, 1–6. doi: 10.1038/jhh.2014.36

Okruhlicová, L., Dlugosová, K., Mitasíková, M., and Bernátová, I. (2008). Ultrastructural characteristics of aortic endothelial cells in borderline hypertensive rats exposed to chronic social stress. *Physiol. Res.* 57(Suppl. 2), S31–S37.

Patrono, C., and Baigent, C. (2014). Nonsteroidal anti-inflammatory drugs and the heart. *Circulation* 129, 907–916.

Patrono, C., Garcia Rodriguez, L. A., Landolfi, R., and Baigent, C. (2005). Low-dose aspirin for the prevention of atherothrombosis. *N. Eng. J. Med.* 353, 2373–2383. doi: 10.1056/nejmra052717

Pavlicević, I., Kuzmanić, M., Rumboldt, M., and Rumboldt, Z. (2008). Interaction between antihypertensives and NSAIDs in primary care: a controlled trial. *Can. J. Clin. Pharmacol.* 15, 372–382.

Perrotta, I., Brunelli, E., Sciangula, A., Conforti, F., Perrotta, E., Tripepi, S., et al. (2011). iNOS induction and PARP-1 activation in human atherosclerotic lesions: an immunohistochemical and ultrastructural approach. *Cardiovasc. Pathol.* 20, 195–203. doi: 10.1016/j.carpath.2010.06.002

Puddu, P., Puddu, G. M., Cravero, E., Rosati, M., and Muscari, A. (2008). The molecular sources of reactive oxygen species in hypertension. *Blood Press.* 17, 70–77. doi: 10.1080/08037050802029954

Ruiz-Ortega, M., Rodríguez-Vita, J., Sanchez-Lopez, E., Carvajal, G., and Egido, J. (2007). TGF-β signaling in vascular fibrosis. *Cardiovasc. Res.* 74, 196–206. doi: 10.1016/j.cardiores.2007.02.008

Sandow, S. L., Gzik, D. J., and Lee, R. M. (2009). Arterial internal elastic lamina holes: relationship to function? *J. Anat.* 214, 258–266. doi: 10.1111/j.1469-7580.2008.01020.x

Sato, E., Koyama, S., Nomura, H., Kubo, K., and Sekiguchi, M. (1996). Bradykinin stimulates alveolar macrophages to release neutrophil, monocyte, and eosinophil chemotactic activity. *J. Immunol.* 157, 3122–3129.

Sharifov, O. F., Schiros, C. G., Aban, I., Denney, T. S., and Gupta, H. (2016). Diagnostic accuracy of tissue doppler index e/e' for evaluating left ventricular filling pressure and diastolic dysfunction/heart failure with preserved ejection fraction: a systematic review and meta-analysis. *J. Am. Heart Assoc.* 5, e002530. doi: 10.1161/JAHA.115.002530

Tanaka, K., Honda, M., and Takabatake, T. (2001). Redox regulation of MAPK pathways and cardiac hypertrophy in adult rat cardiac myocyte. *J. Am. Coll. Cardiol.* 37, 676–685. doi: 10.1016/s0735-1097(00)01123-2

Tiffany, C. W., and Burch, R. M. (1989). Bradykinin stimulates tumor necrosis factor and interleukin-1 release from macrophages. *FEBS Lett.* 247, 189–192. doi: 10.1016/0014-5793(89)81331-6

Trippodo, N. C., and Frohlich, E. D. (1981). Similarities of genetic (spontaneous) hypertension: man and rat. *Circ. Res.* 48, 309–319. doi: 10.1161/01.res.48.3.309

Tschöpe, C., Heringer-Walther, S., and Walther, T. (2000). Regulation of the kinin receptors after induction of myocardial infarction: a mini-review. *Braz. J. Med. Biol. Res.* 33, 701–708. doi: 10.1590/s0100-879x2000000600011

Westermann, D., Walther, T., Savvatis, K., Escher, F., Sobirey, M., Riad, A., et al. (2009). Gene deletion of the kinin receptor B1 attenuates cardiac inflammation and fibrosis during the development of experimental diabetic cardiomyopathy. *Diabetes* 58, 1373–1381. doi: 10.2337/db08-0329

Yang, S., Li, H., Tang, L., Ge, G., Ma, J., Qiao, Z., et al. (2015). Apelin-13 protects the heart against ischemia-reperfusion injury through the RISK-GSK-3β-mPTP pathway. *Arch. Med. Sci.* 11, 1065–1073. doi: 10.5114/aoms.2015.54863

Yin, H., Chao, J., Bader, M., and Chao, L. (2007). Differential role of kinin B1 and B2 receptors in ischemia-induced apoptosis and ventricular remodeling. *Peptides* 28, 1383–1389. doi: 10.1016/j.peptides.2007.05.010

Conflict of Interest Statement: The authors declare that the research was conducted in the absence of any commercial or financial relationships that could be construed as a potential conflict of interest.

frontiers in Physiology

ORIGINAL RESEARCH
published: 09 July 2019
doi: 10.3389/fphys.2019.00866

Trimethylamine N-Oxide Exacerbates Cardiac Fibrosis via Activating the NLRP3 Inflammasome

Xueling Li[1†], Jin Geng[2†], Jinxuan Zhao[3], Qianqian Ni[4], Chenze Zhao[1], Yaru Zheng[1], Xiaomin Chen[1] and Lihong Wang[1]*

[1] Department of Cardiology, Zhejiang Provincial People's Hospital, People's Hospital of Hangzhou Medical College, Hangzhou, China, [2] Department of Cardiology, Huai'an First People's Hospital, Nanjing Medical University, Huai'an, China, [3] Department of Cardiology, Drum Tower Hospital, Nanjing University Medical School, Nanjing, China, [4] Department of Medical Imaging, Jinling Hospital, Medical School of Nanjing University, Nanjing, China

Background/Aims: Gut microbiota has been reported to correlate with a higher mortality and worse prognosis of cardiovascular diseases. Trimethylamine N-oxide (TMAO) is a gut microbiota-dependent metabolite of specific dietary nutrients, which is linked to cardiac fibrosis. Recent reports have suggested that the activation of Nucleotide-binding oligomerization domain (NOD)-like receptor protein 3 (NLRP3) inflammasome contributed to cardiac fibrosis. However, whether TMAO mediates cardiac fibrosis via activating NLRP3 inflammasome remains unclear.

Methods and Results: To determine the role of TMAO–mediated cardiac fibrosis, we established mouse models of doxorubicin (DOX)-induced cardiac fibrosis with or without TMAO in drinking water. TMAO exacerbated DOX-induced cardiac dysfunction, heart weight and cardiac fibrosis manifested by enhanced collagen accumulation, higher profibrotic levels and elevated inflammatory factors as well as NLRP3 inflammasome activation. Using primary cultured mouse cardiac fibroblast, our results indicated that TMAO promoted proliferation, migration and collagen secretion in a dose-dependent manner by TGF-β/Smad3 signaling. Furthermore, TMAO treatment induced NLRP3 inflammasome activation including oxidative stress in cultured cardiac fibroblast. Importantly, the silencing of NLRP3 presented a protection effect against cardiac fibrosis including cellular proliferation, migration and collagen deposition *in vitro*.

Conclusion: Our data suggested that TMAO aggravated DOX-induced mouse cardiac fibrosis, at least in part, through activation of the NLRP3 inflammasome, providing a new potential target for preventing the progression of cardiac fibrosis.

Keywords: cardiac fibrosis, TMAO, NLRP3 inflammasome, cardiac fibroblast, doxorubicin

OPEN ACCESS

Edited by:
Mansoureh Eghbali, University of California, Los Angeles, United States

Reviewed by:
Xiaofeng Yang, Temple University, United States
Hanjun Wang, University of Nebraska Medical Center, United States

****Correspondence:***
Lihong Wang
zryxnk@163.com

† These authors have contributed equally to this work

Specialty section:
This article was submitted to Oxidant Physiology, a section of the journal Frontiers in Physiology

Received: *15 February 2019*
Accepted: *20 June 2019*
Published: *09 July 2019*

Citation:
Li X, Geng J, Zhao J, Ni Q, Zhao C, Zheng Y, Chen X and Wang L (2019) Trimethylamine N-Oxide Exacerbates Cardiac Fibrosis via Activating the NLRP3 Inflammasome. Front. Physiol. 10:866. doi: 10.3389/fphys.2019.00866

INTRODUCTION

Cardiac fibrosis is characterized by excessive proliferation of cardiac fibroblasts and accumulation of extracellular matrix (ECM), which ultimately leads to cardiac diastolic dysfunction and heart failure (Creemers and Pinto, 2011; Travers et al., 2016). Cardiac fibroblasts are the predominant cell type located within interstitial tissues, contributing to the secretion of ECM proteins and

influencing cardiac function in the presence of certain profibrotic stimuli (Lighthouse and Small, 2016; Xiang et al., 2017). Therefore, better strategies for regulating cardiac fibroblasts are essential for the development of effective anti-fibrosis intervention and delaying heart failure.

Trimethylamine N-oxide (TMAO) is a gut microbiota-dependent metabolite of specific dietary nutrients, including phosphatidylcholine, choline and carnitine (Wang et al., 2011). Previous studies have suggested that elevated plasma TMAO levels are associated with poor prognosis and increased mortality risk in cardiovascular disease, including heart failure (Tang et al., 2013; Heianza et al., 2017). Some clinical studies have reported TMAO levels to be higher with advanced left ventricular diastolic dysfunction in heart failure than in non-heart failure (Cannon and McMurray, 2014; Tang et al., 2014; Tang et al., 2015b). Several animal studies have suggested that elevated TMAO levels have a strong association with cardiac fibrosis and contribute to heart failure (Chen K. et al., 2017; Zhang et al., 2017; Li et al., 2018). However, the roles and mechanisms of TMAO-mediated cardiac fibrosis are not fully elucidated.

Nucleotide-binding oligomerization domain (NOD)-like receptor protein 3 (NLRP3), a member of the inflammasome family, could promote collagen production and cytokine interleukin (IL)-1β secretion, leading to fibrosis development in organs including the lung, liver and kidney (Song et al., 2016; Alegre et al., 2017; Wang et al., 2017). Recent evidence has shown that high glucose could promote NLRP3 inflammasome-mediated collagen synthesis, leading to caspase 1 activation and IL-1β secretion, which ultimately contribute to cardiac fibrosis in diabetic cardiomyopathy (Zhang et al., 2018). However, the role of the NLRP3 inflammasome in TMAO-mediated cardiac fibrosis remains unclear.

In the present study, we first examined the role of TMAO in doxorubicin (DOX)-induced cardiac fibrosis. Investigating the effects and exploring the underlying mechanisms of TMAO in primary cultured cardiac fibroblasts could provide novel therapeutic strategies based on NLRP3 inflammasome activation.

MATERIALS AND METHODS

Animals and Treatments

C57BL-6J wild-type mice (6–8 weeks old males) were obtained from the Model Animal Research Center of Nanjing University (Nanjing, China). All mouse protocols were approved by the Institutional Ethics Committee of Nanjing Drum Tower Hospital and carried out according to the guidelines of the United States Department of Health (NIH Publication No. 85-23, revised 1996) for the use and care of laboratory animals. TMAO was purchased from Sigma (MO, United States). All mice were assigned to four groups (n = 10 per group): Control, TMAO, doxorubicin (DOX) or DOX+TMAO. To investigate the effects of TMAO on DOX-induced cardiac fibrosis, mice were intraperitoneally injected with four doses of DOX (6 mg/kg) or PBS every 3 days in accordance with a previous study (Rasanen et al., 2016). Moreover, all mice were treated with or without TMAO (120 mg/kg, 1.60 mmol/l) in drinking water as described previously (Makrecka-Kuka et al., 2017; Zhang et al., 2017). At 8 weeks after treatment, a mouse ultrasonic cardiogram was performed, and parameters including left ventricular end-systolic diameter (LVESD), left ventricular end-diastolic diameter (LVEDD), fractional shortening (FS) and ejection fraction (EF) were measured and analyzed with a Vevo2100 High-Resolution Micro-Ultrasound System (Visual Sonics, Toronto, Canada) (Li et al., 2017). Subsequently, the animals were sacrificed, and hearts and blood samples were collected.

Histological Analysis

Heart tissues were fixed in 4% paraformaldehyde embedded in paraffin and sectioned at 5 μm intervals. Masson's trichrome and immunohistochemical staining of collagen type I, NLRP3 and caspase 1 (1:200, Abcam, United States) were performed to analyze cardiac fibrosis using standard procedures as previously described (Yuan et al., 2017). Moreover, heart weight/body weight (HW/BW) and heart weight/tibia length (HW/TL) were also measured.

Primary Mouse Cardiac Fibroblast Cultures and Treatments

Newborn ICR mice (1–2 days old) were anesthetized and sacrificed. Hearts were removed, and the ventricles were quickly and finely minced and digested with Trypsin-EDTA 0.125% (Invitrogen) and collagenase (Invitrogen, 1 mg/ml in DMEM) as we have described (Li et al., 2017). Subsequent supernatants were collected and centrifuged at 200 × g for 5 min and cultured in DMEM containing 4.5 g/L glucose plus 10% fetal bovine serum (FBS) and 1% penicillin/streptomycin (GIBCO) at 37°C. After 1.5 h, non-adherent and weakly attached cells were considered cardiac fibroblasts and cultured in new culture flasks. Cardiac fibroblasts after 2–3 passages were used in experiments (Piccoli et al., 2017; Liang et al., 2018). To evaluate the effect of TMAO on cultured cardiac fibroblasts, cardiac fibroblasts were treated with TMAO at different concentrations (10, 50, 100 μmol/l). The control groups were administered PBS alone.

Small Interfering RNA Transfection and Treatments

SiRNA targeting mouse NLRP3 (5′-CAGCCAGAGTGGAATGACACGTGTA-3′) and control siRNA (5′-UUCUCCGAACGUGUCACG-3′) were synthesized by Genepharm Biotech (Shanghai, China). The second generation of cardiac fibroblasts was transfected with Lipofectamine 2000 (Invitrogen, Germany) according to the manufacturer's instructions. At 48 h after transfection, cardiac fibroblasts were treated with AngII (100 nmol/l, Sigma, United States) or TMAO (100 μmol/l) or PBS as a control. The siRNA efficacy data was shown in **Supplementary Figure S1** in **Supplementary Materials**.

Western Blotting

Collected hearts and cardiac fibroblasts were lysed using RIPA protein extraction reagent with protease inhibitors (Beyotime, Shanghai, China). Then, equal amounts of proteins were run on

8–15% gels and blotted onto PVDF membranes. Subsequently, membranes were blocked with 5% non-fat dried milk in TBST and incubated with primary antibodies overnight at 4°C. The primary antibodies were Col III, Col I, MMP-2, TLR4, TGF-β (1:1000, Abcam, United States), Smad3, p-Smad3 (1:1000, Cell Signaling Technology, Inc.) and GAPDH (1:5000, Bioworld Technology, Inc.), as a loading control. After washing twice, membranes were incubated with appropriate HRP-conjugated secondary antibodies for 2 h at room temperature. Signals were detected using an ECL chromogenic substrate and quantified with densitometry by Quantity One software (Bio-Rad, Berkeley, CA, United States).

Cell Viability Assays

Cell viability was measured using a Cell Counting Kit-8 (CCK8; Dojindo, WTS, Japan) to detect cell proliferation as described previously (Sun et al., 2017). Cells were seeded in 96-well plates at 5×10^3 cells/well (100 μl). Cells were treated with different TMAO concentrations for 24 h, and then CCK8 (10 μl) was added to each well immediately for a 2 h incubation at 37°C. The absorbance was read at 570 nm (A570) using a microplate spectrophotometer.

Immunofluorescence and Edu Staining

Cardiac fibroblasts were fixed in 4% paraformaldehyde, permeabilized with 0.2% Triton X-100 and then blocked with 10% TBST with goat serum. Subsequently, cells were incubated with α-SMA antibody (1:200, Abcam, United States) overnight in the dark. After washing twice, the cells were incubated with Cy3-labeled goat anti-rabbit lgG (H+L) (1:200, Abcam, United States) at room temperature in the dark for 2 h. DAPI was used for nuclear staining.

Edu staining was also performed to evaluate cell proliferation using Edu-Apollo®567 (RiboBio, Guangzhou, China) according to the manufacturer's instructions. Briefly, after treatment with NLRP3 siRNA, Edu labeling solution was added to cardiac fibroblasts and incubated for 2 h. Subsequently, cardiac fibroblasts were fixed with 4% paraformaldehyde and 2 mg/ml glycine solution. After washing twice with PBS, cardiac fibroblasts were incubated with 1× Hoechst 3342 solution to label the cell nuclei. Finally, images were acquired using a Lecia fluorescence microscope (Leica, Germany).

Cell Migration and Apoptosis Assays

Cell migration assays were assessed using a cell scratch assay and Transwell chambers (8-μm, Corning, United States) (Liu et al., 2018). Cardiac fibroblasts cultured in 6-well plates were treated with different TMAO concentrations and then subjected to a cell scratch assay with a 200 μl micropipette tip for 24 h following a protocol described previously (Liang et al., 2007). The width of the wound was measured by microscopy at 0 and 24 h. Cells were stained with 0.1% crystal violet at 24 h to better measure the width. Then, the migration rates (scratch width at 24 h/ scratch width at 0 h × 100%) were calculated from at least three separate experiments.

After treatment, the lower chamber was placed into a 24-well plate with medium containing 10% FBS. Then, 1×10^5 cardiac fibroblasts suspended in serum-free DMEM were seeded into the upper chamber. After 24 h, cells that crossed the membrane were stained with 0.1% crystal violet. Finally, cells were counted from five random images of each chamber under a microscope.

Cell apoptosis was assessed with an Annexin Apoptosis Detection Kit APC (eBioscience, Inc.). Following double staining with 5 μl allophycocyanin (APC)-Annexin V and 10 μl propidium iodide (PI) for 10 min at room temperature in the dark, cells were examined by a FACScan (BD Biosciences, CA, United States) equipped with Cell Quest software (BD Biosciences).

Oxidative Stress Assay

Intracellular oxidative stress was determined using dihydroethidium (DHE) according to the manufacturer's instructions as indicated previously (Qin et al., 2018). After treatment, cardiac fibroblasts were incubated with 10 μM DHE (Beyotime, Shanghai, China) for 30 min at 37°C in the dark. The cells were observed under a fluorescence microscope and quantified using ImageJ software.

Quantitative Real-Time PCR

Total RNA from mouse hearts was collected using TRIzol reagent (Invitrogen, Life Technology, United States). Total RNA was quantified using a NanoDrop 2000 spectrophotometer (NanoDrop, Wilmington, DE, United States), and 1 μg of total RNA from each sample was reverse transcribed into cDNA using HiScript II Q RT SuperMIx for qPCR (Vazyme, Nanjing, China). Quantitative real-time PCR (qRT-PCR) was performed in a Stepone plus Real-Time PCR system (Applied Biosystems) at 95°C for 30 s, followed by 45 cycles of 95°C for 10 s and 60°C for 30 s. The qRT-PCR data were normalized to the average levels of the housekeeping gene GAPDH. Relative mRNA expression levels were described as the 2-ΔΔCt value. The sequences of the primers used for PCR are as follows: Forward: 5′-AGCTTCAGGCAGGCAGTATC-3′, Reverse: 5′-TCATCTCGGAGCCTGTAGTG -3′ (Mouse IL-1β); Forward: 5′- AACTCCAGGCGGTGCCTATG -3′, Reverse: 5′- TCCAGCTGCTCCTCCACTTG -3′ (Mouse TNF-α); and Forward: 5′- GAGAAACCTGCCAAGTATGATGAC-3′, Reverse: 5′- AGAGTGGGAGTTGCTGTTGAAG -3′ (Mouse GAPDH).

Caspase 1 Activity Assay

Caspase-1 activity was measured by using colorimetric assay (Beyotime, China) according to the manufacturer's instructions (Luo et al., 2014; Qiu et al., 2017). This assay was based on the ability of caspase-1 to change acetyl-Tyr-Val-Ala-Asp p-nitroaniline (Ac-YVAD-pNA) into the yellow formazan product p-nitroaniline (pNA). 50 ug of total proteins from mouse hearts were incubated in a 96-well microtiter plate with 20 nmol Ac-YVAD-pNA overnight at 37°C. The absorbance was read at 405 nm (OD405) using a microplate spectrophotometer. Then the level of caspase-1 activation can be assessed by measuring the production of pNA in tested sample using a standard curve of pNA at 405 nm.

Statistical Analysis

Data are presented as the mean ± SD of at least three independent experiments. The differences in data were analyzed by unpaired, two-tailed Student's *t*-test for two groups or one-way analysis of variance (ANOVA) for multiple comparisons. SPSS 22.0 (IBM SPSS, Armonk, NY, United States) was used for statistical analyses, and statistical significance was indicated by $P < 0.05$.

RESULTS

TMAO Exacerbated DOX-Induced Cardiac Dysfunction

To analyze the effects of TMAO on cardiac fibrosis, we administered intraperitoneal injections of DOX to establish a murine cardiac fibrosis model. Then, the mice were given drinking water with or without TMAO for 8 weeks (**Figure 1A**). The mice treated with DOX showed significantly reduced relative heart weight, including HW/BW and HW/TL, which could be further reduced by additional treatment with TMAO (**Figures 1B,C**). An ultrasonic cardiogram was used to evaluate cardiac function in mice. After DOX treatment, all mice exhibited significant functional impairment in the left ventricular EF and FS. Importantly, poor cardiac function was completely deteriorated by TMAO (**Figures 1D,E**). However, no significant differences were seen in heart weight and cardiac parameters, including EF and FS, between control- and TMAO-treated normal mice, most likely due to the short-term effect and relatively low levels of TMAO. In addition, the similar results also were found in the other cardiac parameters including LVESD and LVEDD (**Supplementary Figure S2**) in **Supplementary Materials**.

TMAO Aggravated DOX-Induced Cardiac Fibrosis

Animals subjected to DOX treatment showed poor cardiac function and apparent cardiac fibrosis (Deng et al., 2007; Hang et al., 2017). Consistent with previous reports, we confirmed that DOX resulted in marked fibrosis and collagen deposition in mouse hearts by Masson and collagen type (Col) III staining (**Figures 2A,B,D,E**). These alterations were also observed in TMAO-treated mice, though to a lesser extent than those in the DOX-treated animals. Importantly, co-administration of TMAO and DOX resulted in more pronounced cardiac fibrosis than the administration of either alone in mice. Cardiac sections were stained for α-SMA, which is a common marker of cardiac fibroblasts. The proportion of α-SMA-positive cells in DOX-treated mouse hearts was markedly higher than that in control hearts and was further increased in combination with TMAO (**Figures 2C,F**). In addition, the expression levels of profibrotic factors were also detected by western blotting in all animals. DOX-treated animals showed increased expression levels of α-SMA, collagen type I, and collagen type III in the heart compared to untreated animals (**Figures 2G,H**). In agreement with these findings, TMAO was also able to slightly upregulate the levels of profibrotic factors; however, no significant differences were observed in normal TMAO-treated mouse hearts, although these factors were significantly upregulated by TMAO in DOX-treated mouse hearts.

TMAO Induced Cardiac Fibroblast Proliferation, Migration, and Collagen Deposition

To investigate the effects of TMAO on cardiac fibroblasts, we cultured cardiac fibroblasts with TMAO at several indicated concentrations for 24 h. TGF-β/Smad3 signaling plays a critical role in the development of fibrotic diseases. Therefore, we detected these profibrotic factor levels in TGF-β signaling by western blotting. Similar to the results from mouse hearts, TMAO increased the expression levels of profibrotic factors, including TGF-β and p-Smad3, in cultured cardiac fibroblasts in a dose-dependent manner (**Figures 3A,C**). A trend was also observed in collagen deposition-related protein expression, including Col I, Col III and MMP-2 levels (**Figures 3B,D**). Moreover, we performed scratch tests to detect the migration of cardiac fibroblasts in response to different doses of TMAO. The ratio of the migration area decreased in a dose-dependent manner, indicating that TMAO facilitated dose-dependent migration of cultured cardiac fibroblasts (**Figures 3E,F**). Furthermore, TMAO was also able to promote cardiac fibroblast proliferation in a dose-dependent manner as assessed by a CCK8 assay (**Figure 3G**). Interestingly, TMAO failed to induce cardiac fibroblast apoptosis, perhaps due to more proliferating cells and fewer apoptotic cells (**Figure 3H**). Overall, our results show that TMAO promotes cardiac fibroblast proliferation, migration and collagen secretion in a dose-dependent manner, indicating that TMAO contributes to cardiac fibrosis via regulating the function of cardiac fibroblasts.

TMAO Induced NLRP3 Inflammasome Activation *in vivo* and *in vitro*

The NLRP3 inflammasome has been described as a key player in the development of cardiovascular disease. Previous investigations have revealed that TMAO could activate the NLRP3 inflammasome to mediate endothelial dysfunction and vascular inflammation (Boini et al., 2017; Chen M.L. et al., 2017). To explore the relationship between TMAO and the NLRP3 inflammasome in cardiac fibrosis, we detected the protein levels of the NLRP3 inflammasome complex, including NLRP3, caspase 1 and interleukin-1β (IL-1β), by western blotting. The levels of NLRP3 and IL-1β/pro- IL-1β were significantly increased in the DOX-treated groups compared to those in the control- and TMAO-treated groups, which were the highest in the TMAO+DOX group (**Figures 4A,B**). The ratio of cleaved caspase 1/caspase 1 was also higher in the TMAO+DOX-treated groups than either the TMAO- or DOX- treated group (**Figures 4A,B**). In addition, we detected the expression levels of NLRP3 and caspase 1 in mouse hearts by immunohistochemistry. Our results demonstrated that the expression of NLRP3 and caspase 1 could be observed in TMAO-treated hearts and that co-administration of TMAO and DOX further induced higher levels than either treatment alone (**Figures 4C–F**). Moreover, we also detect the

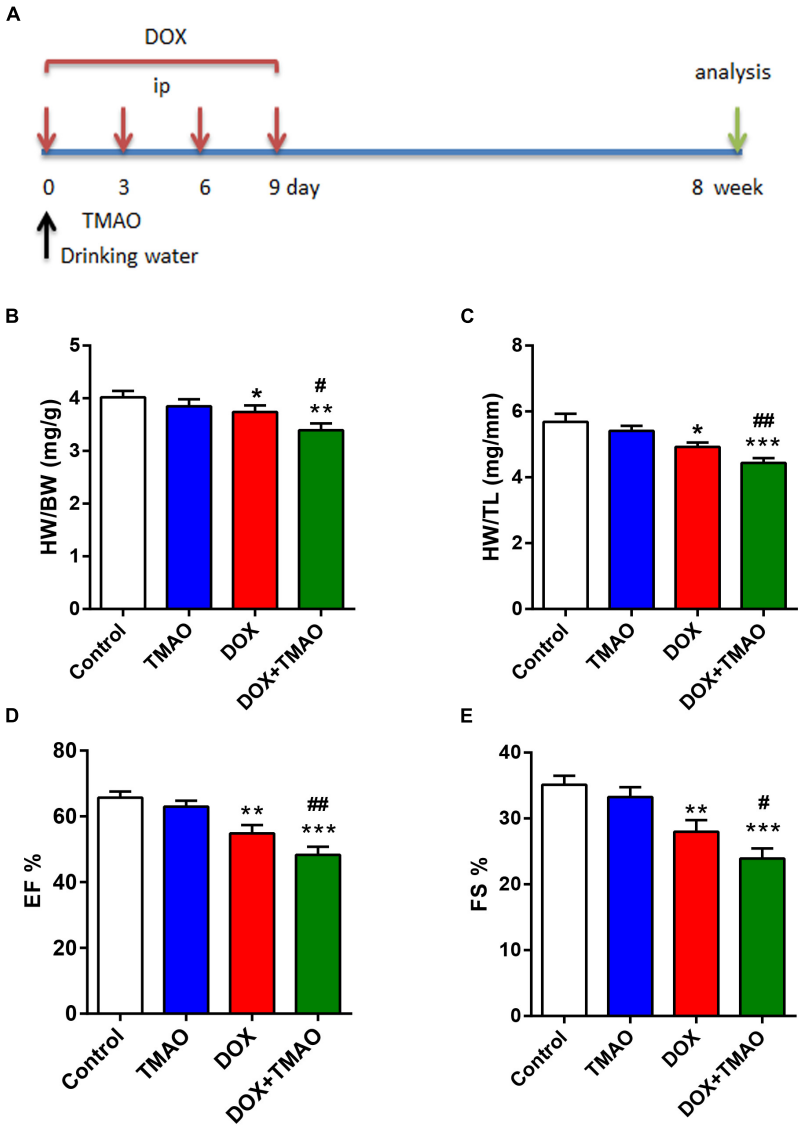

FIGURE 1 | TMAO exacerbated doxorubicin (DOX)-induced cardiac dysfunction. **(A)** Schedule of the 8-week experiment. The mice received four doses of DOX (6 mg/kg) or PBS every 3 days by intraperitoneal injection (i.p.). Moreover, all mice were treated with or without TMAO (120 mg/kg, 1.60 mmol/l) in drinking water. **(B)** Heart weight/body weight (HW/BW) and **(C)** heart weight/tibial length (HW/TL) were analyzed. **(D)** EF and **(E)** FS of the mice were measured at 8 weeks. All data were analyzed at least three times. Mean ± SD. $^{*}P < 0.05$, $^{**}P < 0.01$, $^{***}P < 0.001$ (vs. Control). $^{\#}P < 0.05$, $^{\#\#}P < 0.01$ (vs. DOX).

activation levels of caspase 1 in mouse hearts by caspase1 activity assay kit. Consistent with the above results, the caspase 1 activity was significantly increased in in the DOX-treated groups compared to those in the control- and TMAO-treated groups but lower than TMAO+DOX group (**Figure 4G**). NLRP3 activation is involved in inflammation; thus, we analyzed the expression of inflammatory genes by quantitative real-time PCR. The data revealed that TMAO administration increased the expression of TNF-α and IL-1β but had no significant statistical difference (**Figure 4H**). Similarly, TMAO promoted a significant increase in inflammatory factor expression following DOX treatment (**Figure 4H**). The data supported that TMAO induced NLRP3 inflammasome activation in mouse hearts.

We also evaluated the effect of TMAO on the NLRP3 inflammasome in cardiac fibroblasts using western blotting. To investigate the effects of TMAO on cardiac fibroblasts, we selected Ang II-treated cells as positive control. The results shown in **Figures 5A–E** indicated that the expression of NLRP3, cleaved caspase 1, pro-IL-1β, IL-1β and apoptosis-associated speck-like protein (ASC) significantly increased in the TMAO-treated cardiac fibroblasts, consistent with the observed increase in the AngII-treated group. In addition, TMAO also increased the expression of TLR4, which has been recognized as an important upstream molecule that regulates NLRP3 signaling (Gaidt et al., 2016; **Figures 5B,D**). Furthermore, oxidative stress was reported to be vital to NLRP3 inflammasome-mediated

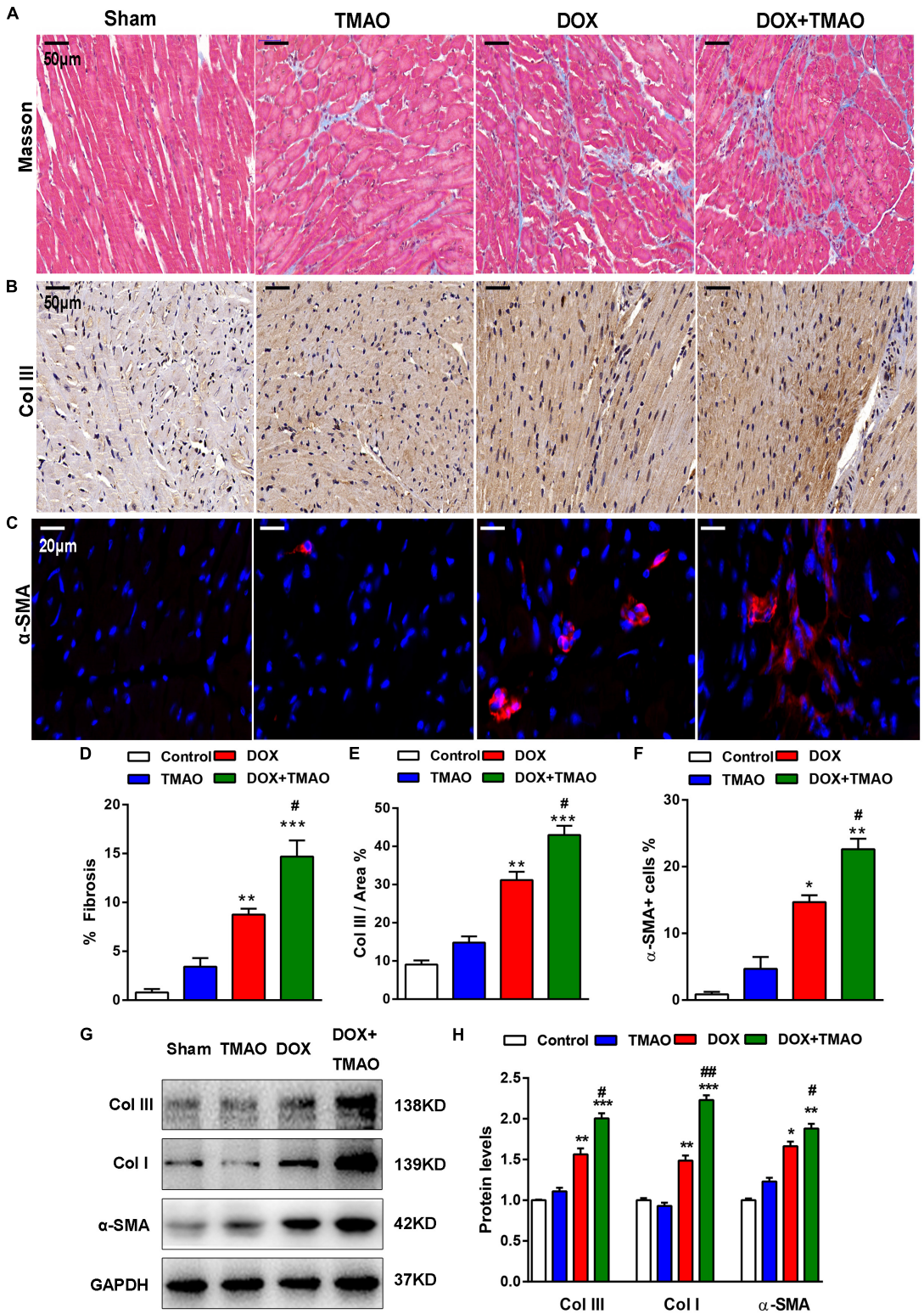

FIGURE 2 | TMAO aggravated doxorubicin-induced cardiac fibrosis in mice. **(A)** Representative images of Masson's staining and immunohistochemical staining for collagen type III (Col III) **(B)** and immunofluorescence staining for α-SMA (red) and DAPI (blue) in cardiac sections **(C)**. Scale bar = 50 μm. **(D)** Quantification of the percentage of fibrosis, Col III area **(E)** and α-SMA-positive cells **(F)**. **(G,H)** Collagen I (Col I), Col III, and α-SMA protein expression levels were analyzed by western blotting and quantified according to immunoblotting (the ratio of protein pixel density/GAPDH pixel density). All data were analyzed at least three times. Mean ± SD. $^{*}P < 0.05$, $^{**}P < 0.01$, $^{***}P < 0.001$ (vs. Control). $^{\#}P < 0.05$, $^{\#\#}P < 0.01$ (vs. DOX).

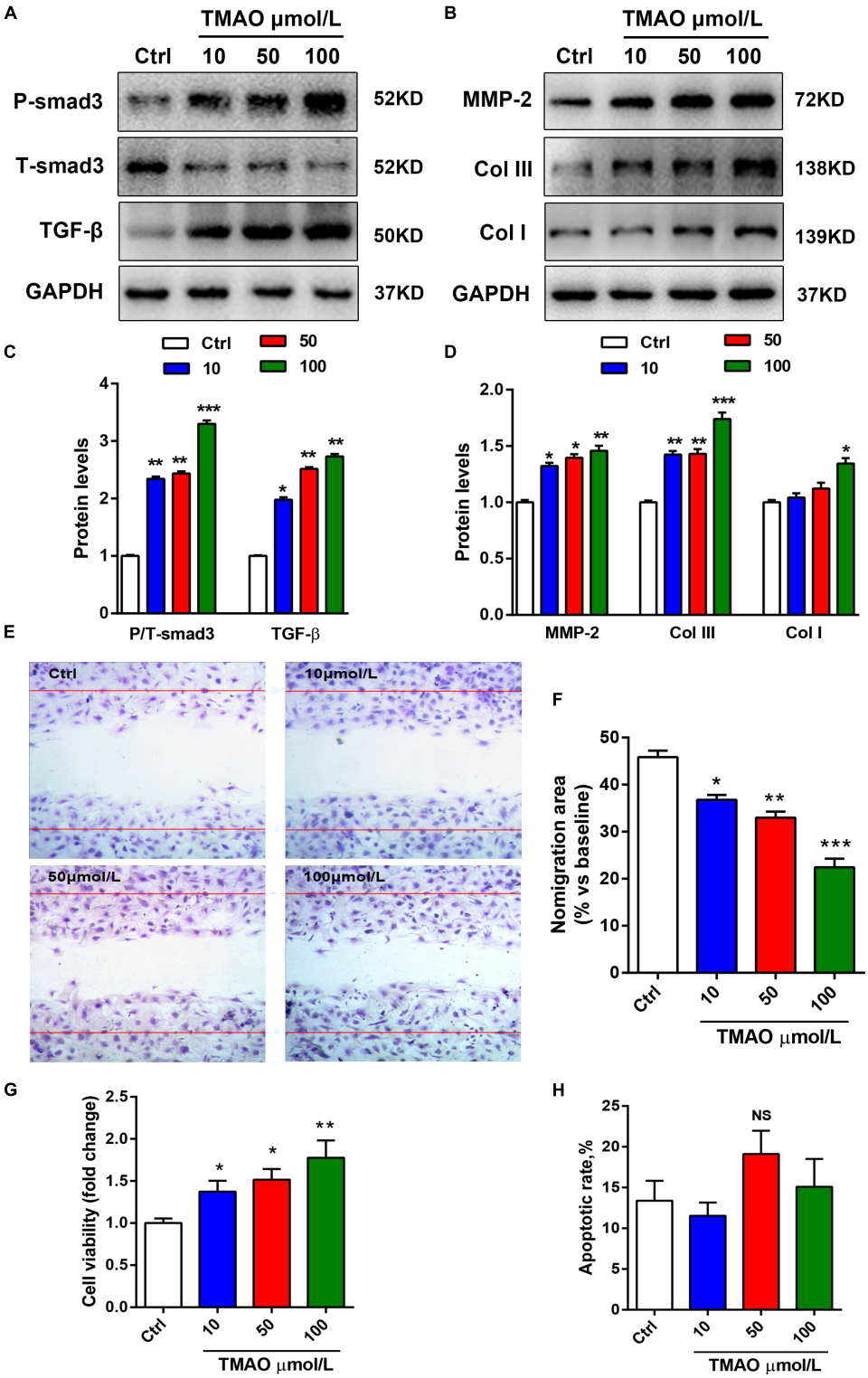

FIGURE 3 | TMAO induced cardiac fibroblast proliferation, migration and collagen deposition in a dose-dependent manner. **(A)** P-Smad3, T-Smad3, TGF-β, MMP-2, Col I, and Col III **(B)** protein expression was analyzed by western blotting and quantified **(C,D)** according to immunoblotting (the ratio of protein pixel density/GAPDH pixel density) following different doses of TMAO exposure. **(E)** Scratch assays showing the migration ability of cardiac fibroblasts for 24 h under 200× magnification. **(F)** Quantification of the percentage of the migration area. **(G)** CCK-8 assay showing the proliferation of cardiac fibroblasts subjected to TMAO at different doses. **(H)** Quantification of the apoptotic rate of cardiac fibroblasts by an Annexin Apoptosis Detection Kit APC assays. All data were analyzed at least three times. Mean ± SD. $^{*}P < 0.05$, $^{**}P < 0.01$, $^{***}P < 0.001$ (vs. Control).

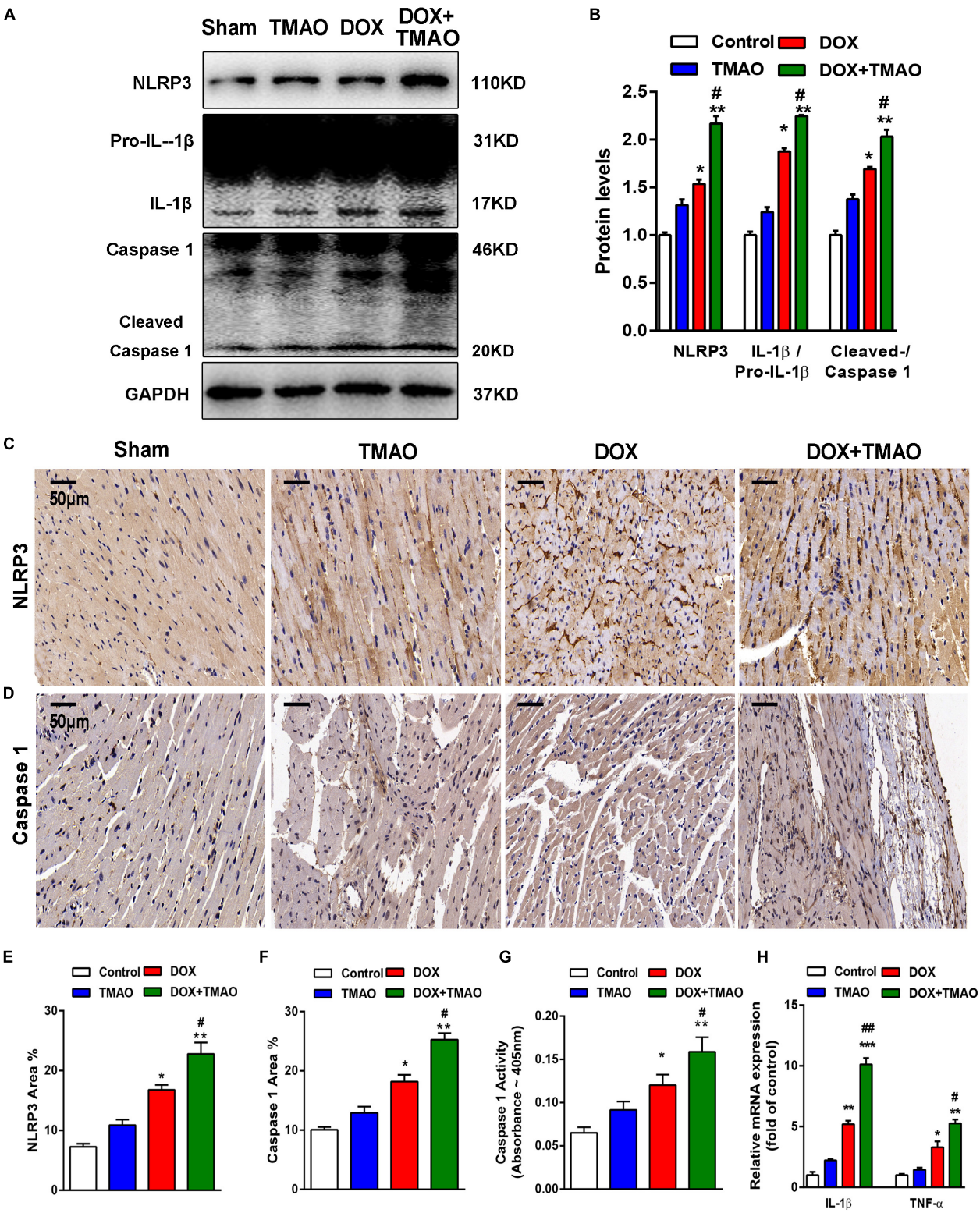

FIGURE 4 | TMAO induced NLRP3 inflammasome activation *in vivo*. **(A)** NLRP3, pro-IL-1β, IL-1β, caspase 1 and cleaved caspase 1 protein expression was analyzed by western blotting and quantified **(B)** according to immunoblotting (the ratio of protein pixel density/GAPDH pixel density) after 8 weeks. **(C)** Representative images of immunohistochemical staining for NLRP3 and caspase 1 **(D)** in cardiac sections. Scale bar = 50 μm. **(E)** Quantification of the percentage of NLRP3- and caspase 1-positive areas **(F)**. **(G)** Caspase-1 activity was determined by caspase-1 activity assay. **(H)** QRT-PCR analysis of TNF-α and IL-1β mRNA expression levels in heart tissues. All data were analyzed at least three times. Mean ± SD. $^{*}P < 0.05$, $^{**}P < 0.01$, $^{***}P < 0.001$ (vs. Control). $^{\#}P < 0.05$, $^{\#\#}P < 0.01$ (vs. DOX).

inflammation, so we detected reactive oxygen species (ROS) in cardiac fibroblasts by DHE staining. We found that TMAO increased the levels of ROS consistent with AngII treatment in cultural cardiac fibroblasts (**Figures 5E,F**). These results indicated that TMAO could activate the NLRP3 inflammasome and oxidative stress.

TMAO Induced Cardiac Fibrosis via NLRP3 Activation

Considerable evidence has suggested that the NLRP3 inflammasome contributes to fibrosis in various diseases. TMAO activated NLRP3 inflammasome-initiated inflammation signaling, which led us to hypothesize that inhibition of NLRP3 with siRNA may protect against cardiac fibrosis induced by TMAO. Importantly, NLRP3 knockdown blunted the fibrotic effects of TMAO, including the attenuation of profibrotic factor levels and a reduction in the migration of cardiac fibroblasts. In our study, NLRP3 silencing abolished the increase in NLRP3, IL-1β/pro- IL-1β, Col I, TGF-β, and Col III levels induced by TMAO in cardiac fibroblasts (**Figures 6A,B**). Furthermore, TMAO increased the number of α-SMA-positive cells significantly compared with the control, and this effect was attenuated by NLRP3 silencing (**Figures 6C,D**). The Edu assay showed that TMAO increased cardiac fibroblast proliferation compared with the control condition and that this effect was significantly inhibited after NLRP3 silencing (**Figures 6E,F**). By counting migratory cardiac fibroblasts with a transwell assay, we found that TMAO increased the migration rate of cardiac fibroblasts, which was decreased by NLRP3 knockdown (**Figures 6G,H**). The above data demonstrated that NLRP3 inflammasome might be a possible mechanism in the development of cardiac fibrosis promoted by TMAO.

DISCUSSION

The present study aimed to explore the contributions of the role and physiological mechanism of NLRP3 inflammasome activation to cardiac fibrosis. Here, we observed that TMAO aggravated DOX-induced murine cardiac fibrosis and cardiac dysfunction. In addition, we found that TMAO induced cardiac fibroblast proliferation, migration and collagen synthesis. Furthermore, we showed that TMAO could activate the NLRP3 inflammasome as well as ROS production *in vivo* and *in vitro*. Finally, our study suggested that TMAO worsen cardiac fibrosis via NLRP3 inflammasome activation in DOX-treated mice.

In recent years, accumulating evidence has revealed that the gut microbiome plays a pivotal role in the onset and development of cardiovascular diseases (Crothers and Bry, 2018; Peng et al., 2018). TMAO, a major metabolite of the gut microbiome from nutrients, has been shown to be a risk factor that correlates with a higher mortality and worse prognosis of cardiovascular diseases, including atherosclerosis, atrial fibrillation and heart failure, in many clinical studies (Tang et al., 2014; Randrianarisoa et al., 2016; Yu et al., 2018). A growing body of research has demonstrated a strong association between TMAO and myocardial fibrosis. Therefore, inhibition of gut microbes or generation of TMAO may become a potential target for the prevention and treatment of cardiac fibrosis. In the present study, our results from heart weight, echocardiography, immunohistochemistry and western blotting revealed that TMAO might have no significant effect on heart weight and cardiac function, while it could induce mild cardiac fibrosis in normal mouse hearts. Indeed, a previous report has shown that dietary TMAO induced increased fibrosis in the kidney (Tang et al., 2015a). Cardiac fibrosis and collagen deposition were also observed in mice given water with supplemental TMAO, consistent with previous research (Organ et al., 2016). In addition, we demonstrated that TMAO exacerbated DOX-induced cardiac dysfunction and fibrosis in mouse hearts. Consistently, a recent study has reported that elevated circulating TMAO levels contribute to cardiac fibrosis and inflammation in Western diet-induced murine obesity (Chen K. et al., 2017). However, Huc et al. (2018) have found that increased dietary TMAO seems to reduce diastolic dysfunction and heart fibrosis in hypertensive rats. The discrepancy between Huc et al. (2018) and our findings may result from several factors, such as low doses and long-term treatment with TMAO in Huc's study. Collectedly, these findings clarified that TMAO induced myocardial fibrosis and worsening cardiac function in DOX-treated mice.

Cardiac fibroblasts are known to play a vital role in heart fibrosis, which leads to cardiac dysfunction (Frangogiannis, 2018). Thus, we performed *in vitro* experiments to explore the effect of TMAO on cardiac fibroblasts, including proliferation, apoptosis, migration and collagen synthesis. We found that TMAO was able to induce the proliferation, migration and collagen secretion of cardiac fibroblasts in a dose-dependent manner but had no effect on apoptosis. Perhaps because TMAO induced proliferating cardiac fibroblasts to a greater extent than it does apoptotic cells, no significant increase in apoptosis rates was observed. These data demonstrated that treatment with TMAO contributed to cardiac dysfunction in mice by modulating the functions of cardiac fibroblasts, which are associated with increased proliferation, migration and collagen secretion. However, TMAO had no significant effect on normal mouse hearts, most likely due to the low doses, smaller number of animals and short-term treatment, which is consistent with the results of previous studies (Chang et al., 2015; Chen K. et al., 2017).

The NLRP3 inflammasome, a multiprotein complex including NLRP3, caspase-1, IL-1β and ASC, has been widely shown to be an essential step in cardiovascular disease and is linked to atrial fibrillation, atherosclerosis, diabetic cardiomyopathy and cardiac remodeling (Suetomi et al., 2018; Yao et al., 2018; Zhang et al., 2018). When activated by diverse stimuli, including ROS, pathogen-associated molecular patterns (PAMPs) and calcium influx, NLRP3 forms a protein complex with the adapter molecule ASC and the effector protein caspase-1, regulating the activation of the protease caspase-1 and cytokine IL-1β. Moreover, NLRP3 activated by Ca^{2+} may trigger mitochondrial damage, leading to an increase in ROS production (Pavillard et al., 2018; Yang et al., 2018). In some vivo studies, siRNA-mediated knockdown or genetic deletion of

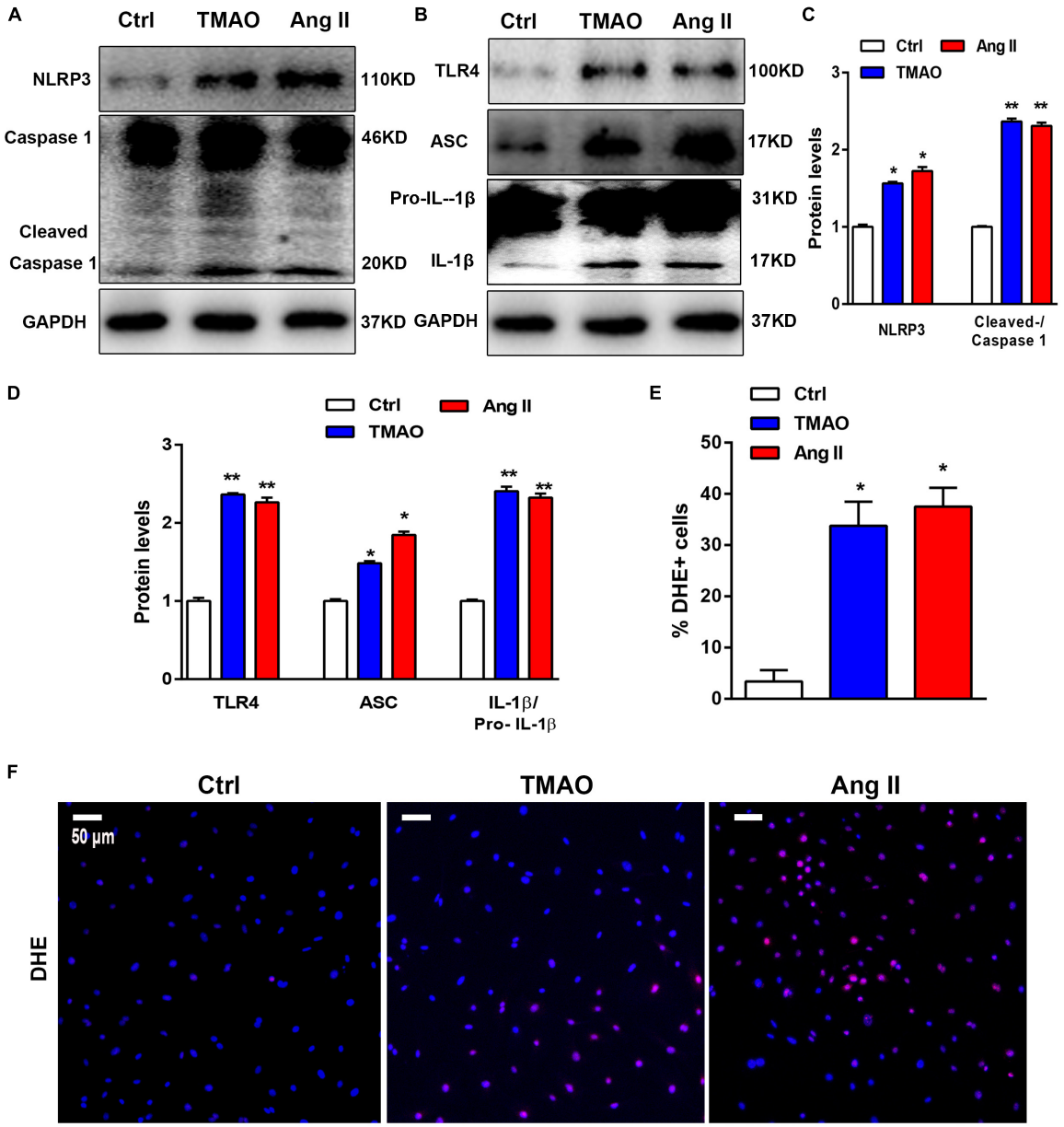

FIGURE 5 | TMAO induced NLRP3 inflammasome activation *in vitro*. **(A,B)** NLRP3, pro-IL-1β,IL-1β, caspase-1, cleaved caspase-1, TLR4, and ASC protein expression levels were analyzed by western blotting and quantified **(C,D)** according to immunoblotting (the ratio of protein pixel density/GAPDH pixel density) after TMAO or Ang II treatment for 24 h. **(E,F)** Representative images and quantification of DHE staining (red) and DAPI (blue). Scale bar = 50 μm. All data were analyzed at least three times. Mean ± SD. $^{*}P < 0.05$, $^{**}P < 0.01$, $^{***}P < 0.001$ (vs. Control).

NLRP3 experiments prevented pathological cardiac remodeling and decreased ischemic damage and cardiac fibrosis under cardiac injury conditions (Sandanger et al., 2013; Zhang et al., 2014; Bugyei-Twum et al., 2016). In accord with these findings, we also showed that TMAO activated NLRP3 inflammasome signaling in cultured cardiac fibroblasts, which was consistent with the increase in fibrotic factor levels induced by TMAO. Additionally, the levels of ROS in cardiac fibroblasts were found to be elevated after TMAO or AngII treatment. Furthermore, we blocked the expression of NLRP3 by siRNA to explore the association between NLRP3 and fibrosis under TMAO treatment. Importantly, TGF-β/Smad3 signaling has been implicated as a principal mediator of the fibrotic response associated with inflammation and tissue injury and could be regulated by NLRP3 in fibrotic disease as described in previous studies (Khalil et al., 2017; Tian et al., 2017). Moreover, TLR4, which is upstream of NLRP3 and TGF-β signaling, plays a role in the fibrotic response. Under the pathological conditions, inactive NLRP3 was generated in the cytoplasm by TLR4 in response to pathogen-associated molecular patterns or danger-associated

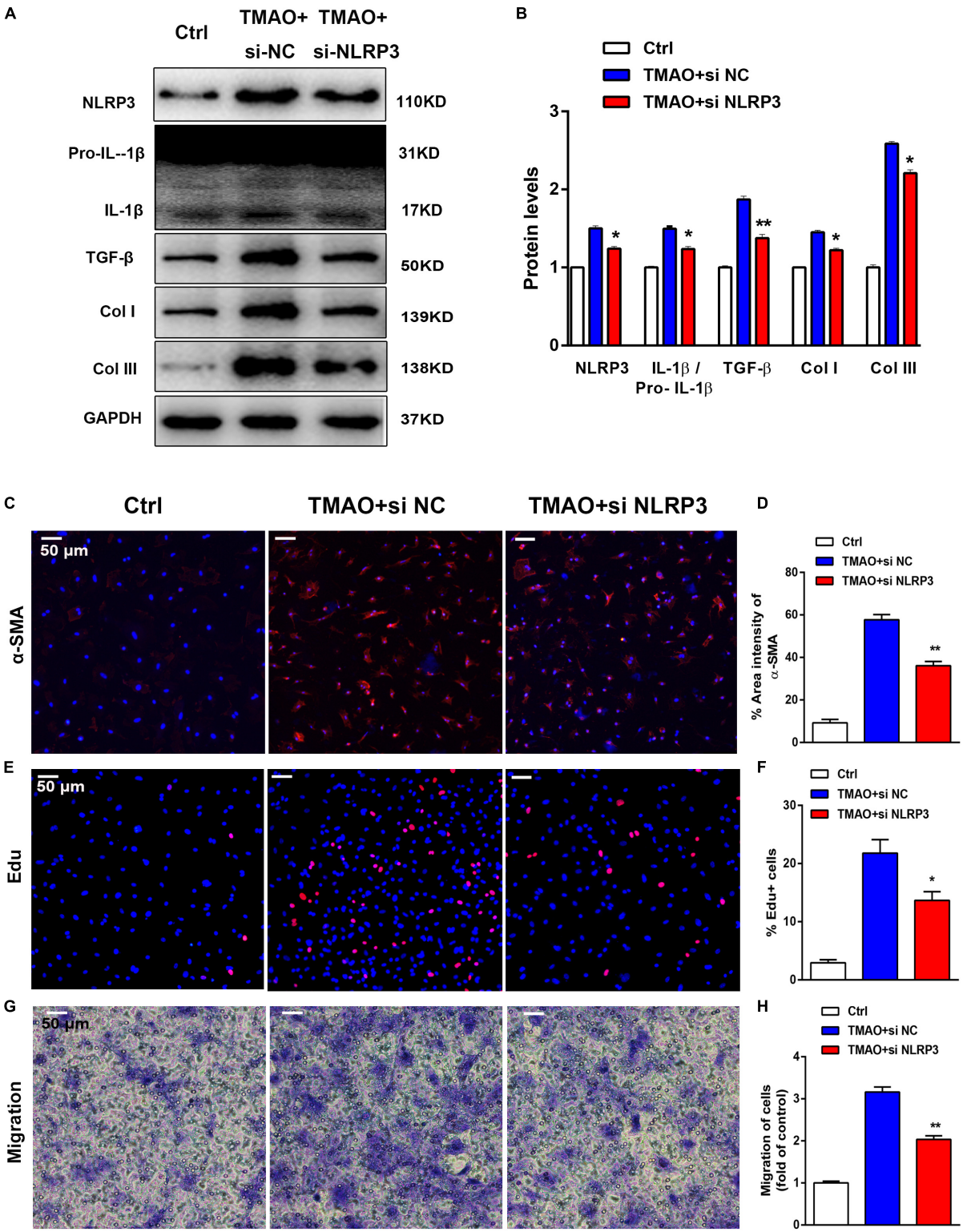

FIGURE 6 | TMAO induced cardiac fibrosis via NLRP3 activation. Knockdown of NLRP3 with siRNA could reverse the effect of TMAO on cardiac fibroblasts. **(A)** NLRP3, pro-IL-1β, IL-1β, TGF-β, Col I and Col III protein expression levels were analyzed by western blotting and quantified **(B)** according to immunoblotting (the ratio of protein pixel density/GAPDH pixel density). **(C)** Representative images and quantification **(D)** of immunofluorescence staining for α-SMA (red) and DAPI (blue) in cardiac sections. **(E)** Edu staining showing cardiac fibroblast proliferation after 24 h of treatment, and quantification **(F)** of the percentage of Edu-positive cells (red). **(G)** Transwell assay showing the stained migrated cardiac fibroblasts after 24 h and calculation **(H)**. All scale bars = 50 μm. All data were analyzed at least three times. Mean ± SD. $^{*}P < 0.05$, $^{**}P < 0.01$, $^{***}P < 0.001$ (vs. TMAO+si NC).

molecular patterns (DAMPs). Thus, we speculated that TMAO might induce heart tissue injury and produce DAMPs, and then activate the TLR4-NLRP3-TGF-β signaling pathway, which is associated with an increase in ROS production, inflammatory cytokines and collagen deposition, finally leading to severe cardiac fibrosis and cardiac dysfunction, providing a potential novel therapy approach.

At present, some mechanisms of the effect of TMAO in cardiovascular diseases have been proposed. In the pathological process of atherosclerosis, TMAO accelerated endothelial dysfunction through the activation of PKC/NF-κB/VCAM-1 (Ma et al., 2017). TMAO has also been found to reverse GFP-PDS-mediated endoplasmic reticulum perturbation, contributing to endoplasmic reticulum balance (Shepshelovich et al., 2005). Previous studies revealed that TMAO may exacerbate cardiac fibrosis and inflammation induced by high glucose levels via upregulating the proinflammatory cytokines TNF-α and IL-1β (Chen K. et al., 2017). Li et al. (2018) showed that gut microbe-derived metabolite TMAO induced transverse aortic constriction (TAC)-induced cardiac hypertrophy and fibrosis involving Smad3 signaling. The NLRP3 inflammasome has been implicated in cardiac inflammation and fibrosis. However, the biological role of the NLRP3 inflammasome in TMAO-induced cardiac fibrosis is still unclear. Our results indicated for the first time that TMAO induced cardiac fibrosis through the activation of the NLRP3 inflammasome *in vivo* and *in vitro*, suggesting that the NLRP3 inflammasome plays an important role in cardiac fibrosis after TMAO treatment. In addition, we showed that inhibition of NLRP3 could reverse TMAO-mediated cardiac fibrosis, indicating a potential target for the treatment of cardiac fibrosis.

Some limitations of this study should be pointed out. Gut microbiota analysis was not performed, and we could not analyze the gut microbiota composition and circulating TMAO levels in our animal models. Previous reports have shown that additional dietary TMAO could increase circulating TMAO levels in mouse plasma (Organ et al., 2016; Chen K. et al., 2017). Thus, further studies including gut microbiota analysis are needed. In addition, TMAO has been implicated in inflammation, including myocardial infarction, atherosclerosis, and diabetes mellitus (Janeiro et al., 2018; Kasselman et al., 2018). Apart from the NLRP3 inflammasome and ROS in our study, more inflammatory processes, such as NF-κB, STAT3, and MAPK signaling, could be further verified. Finally, the mechanism underlying the NLRP3 inflammasome and TGF-β-mediated fibrosis in cardiac fibroblasts has not yet been identified. Thus, more studies are needed.

In conclusion, our findings showed that TMAO could aggravate cardiac dysfunction and heart weight in DOX-treated mice. In addition, we showed that TMAO promoted myocardial fibrosis via TGF-β signaling *in vitro* and *in vivo* and that the activation of the NLRP3 inflammasome played a crucial role in TMAO-induced cardiac fibrosis. Therefore, our results for the first time help to clarify the association between TMAO and the NLRP3 inflammasome, suggesting a new potential target for preventing the progression of cardiac fibrosis.

DATA AVAILABILITY

The raw data supporting the conclusion of this manuscript will be made available by the authors, without undue reservation, to any qualified researcher.

ETHICS STATEMENT

All mouse protocols were approved by the Institutional Ethics Committee of the Nanjing Drum Tower Hospital and carried out according to the guidelines of the United States Department of Health (NIH Publication No. 85-23, revised 1996) for the use and care of laboratory animals.

AUTHOR CONTRIBUTIONS

XL and JG conceived and designed the experiments. All authors performed the experiments, analyzed the data, and wrote the manuscript.

FUNDING

This work was supported by grants from the Medical and Health Science and Technology Project of Zhejiang Province – Youth Talent Project (2019RC018 and 2019330974), the National Natural Science Foundation of China (81670447 and LY15H020006), and the National Natural Science Foundation of China – Youth Fund Project (81600312).

ACKNOWLEDGMENTS

We thank the Nanjing Drum Tower Hospital and Zhejiang Provincial People's Hospital for providing its SPF-class animal laboratory and completing the animal and cellular experiments.

SUPPLEMENTARY MATERIAL

The Supplementary Material for this article can be found online at: https://www.frontiersin.org/articles/10.3389/fphys.2019.00866/full#supplementary-material

REFERENCES

Alegre, F., Pelegrin, P., and Feldstein, A. E. (2017). Inflammasomes in liver fibrosis. *Semin. Liver Dis.* 37, 119–127. doi: 10.1055/s-0037-1601350

Boini, K. M., Hussain, T., Li, P. L., and Koka, S. S. (2017). Trimethylamine-N-oxide instigates NLRP3 inflammasome activation and endothelial dysfunction. *Cell. Physiol. Biochem.* 44, 152–162. doi: 10.1159/000484623

Bugyei-Twum, A., Abadeh, A., Thai, K., Zhang, Y., Mitchell, M., Kabir, G., et al. (2016). Suppression of NLRP3 inflammasome activation ameliorates chronic

kidney disease-induced cardiac fibrosis and diastolic dysfunction. *Sci. Rep.* 6:39551. doi: 10.1038/srep39551

Cannon, J. A., and McMurray, J. J. (2014). Gut feelings about heart failure. *J. Am. Coll. Cardiol.* 64, 1915–1916. doi: 10.1016/j.jacc.2014.04.088

Chang, C. J., Lin, C. S., Lu, C. C., Martel, J., Ko, Y. F., Ojcius, D. M., et al. (2015). Ganoderma lucidum reduces obesity in mice by modulating the composition of the gut microbiota. *Nat. Commun.* 6:7489. doi: 10.1038/ncomms8489

Chen, K., Zheng, X., Feng, M., Li, D., and Zhang, H. (2017). Gut microbiota-dependent metabolite trimethylamine N-oxide contributes to cardiac dysfunction in western diet-induced obese mice. *Front. Physiol.* 8:139. doi: 10.3389/fphys.2017.00139

Chen, M. L., Zhu, X. H., Ran, L., Lang, H. D., Yi, L., and Mi, M. T. (2017). Trimethylamine-N-oxide induces vascular inflammation by activating the NLRP3 inflammasome through the SIRT3-SOD2-mtROS signaling pathway. *J. Am. Heart Assoc.* 6:e006347. doi: 10.1161/JAHA.117.006347

Creemers, E. E., and Pinto, Y. M. (2011). Molecular mechanisms that control interstitial fibrosis in the pressure-overloaded heart. *Cardiovasc. Res.* 89, 265–272. doi: 10.1093/cvr/cvq308

Crothers, J., and Bry, L. (2018). Gutting TMA to save the heart. *Cell Host Microbe* 24, 470–471. doi: 10.1016/j.chom.2018.09.014

Deng, S., Kulle, B., Hosseini, M., Schluter, G., Hasenfuss, G., Wojnowski, L., et al. (2007). Dystrophin-deficiency increases the susceptibility to doxorubicin-induced cardiotoxicity. *Eur. J. Heart Fail.* 9, 986–994. doi: 10.1016/j.ejheart.2007.07.016

Frangogiannis, N. G. (2018). Cardiac fibrosis: cell biological mechanisms, molecular pathways and therapeutic opportunities. *Mol. Aspects Med.* 65, 70–99. doi: 10.1016/j.mam.2018.07.001

Gaidt, M. M., Ebert, T. S., Chauhan, D., Schmidt, T., Schmid-Burgk, J. L., Rapino, F., et al. (2016). Human monocytes engage an alternative inflammasome pathway. *Immunity* 44, 833–846. doi: 10.1016/j.immuni.2016.01.012

Hang, P., Zhao, J., Sun, L., Li, M., Han, Y., Du, Z., et al. (2017). Brain-derived neurotrophic factor attenuates doxorubicin-induced cardiac dysfunction through activating Akt signalling in rats. *J. Cell Mol. Med.* 21, 685–696. doi: 10.1111/jcmm.13012

Heianza, Y., Ma, W., Manson, J. E., Rexrode, K. M., and Qi, L. (2017). Gut microbiota metabolites and risk of major adverse cardiovascular disease events and death: a systematic review and meta-analysis of prospective studies. *J. Am. Heart Assoc.* 6:e004947. doi: 10.1161/jaha.116.004947

Huc, T., Drapala, A., Gawrys, M., Konop, M., Bielinska, K., Zaorska, E., et al. (2018). Chronic, low-dose tmao treatment reduces diastolic dysfunction and heart fibrosis in hypertensive rats. *Am. J. Physiol. Heart Circ. Physiol.* 315, H1805–H1820. doi: 10.1152/ajpheart.00536.2018

Janeiro, M. H., Ramirez, M. J., Milagro, F. I., Martinez, J. A., and Solas, M. (2018). Implication of trimethylamine N-oxide (TMAO) in disease: potential biomarker or new therapeutic target. *Nutrients* 10:E1398. doi: 10.3390/nu10101398

Kasselman, L. J., Vernice, N. A., DeLeon, J., and Reiss, A. B. (2018). The gut microbiome and elevated cardiovascular risk in obesity and autoimmunity. *Atherosclerosis* 271, 203–213. doi: 10.1016/j.atherosclerosis.2018.02.036

Khalil, H., Kanisicak, O., Prasad, V., Correll, R. N., Fu, X., Schips, T., et al. (2017). Fibroblast-specific TGF-beta-Smad2/3 signaling underlies cardiac fibrosis. *J. Clin. Invest.* 127, 3770–3783. doi: 10.1172/JCI94753

Li, X., Geng, J., Chen, Y., Chen, F., Liu, C., Xu, Q., et al. (2017). Exposure to particulate matter induces cardiomyocytes apoptosis after myocardial infarction through NFkappaB activation. *Biochem. Biophys. Res. Commun.* 488, 224–231. doi: 10.1016/j.bbrc.2017.05.047

Li, Z., Wu, Z., Yan, J., Liu, H., Liu, Q., Deng, Y., et al. (2018). Gut microbe-derived metabolite trimethylamine N-oxide induces cardiac hypertrophy and fibrosis. *Lab. Invest.* 99, 346–357. doi: 10.1038/s41374-018-0091-y

Liang, C. C., Park, A. Y., and Guan, J. L. (2007). In vitro scratch assay: a convenient and inexpensive method for analysis of cell migration in vitro. *Nat. Protoc.* 2, 329–333. doi: 10.1038/nprot.2007.30

Liang, H., Pan, Z., Zhao, X., Liu, L., Sun, J., Su, X., et al. (2018). LncRNA PFL contributes to cardiac fibrosis by acting as a competing endogenous RNA of let-7d. *Theranostics* 8, 1180–1194. doi: 10.7150/thno.20846

Lighthouse, J. K., and Small, E. M. (2016). Transcriptional control of cardiac fibroblast plasticity. *J. Mol. Cell Cardiol.* 91, 52–60. doi: 10.1016/j.yjmcc.2015.12.016

Liu, X., Xu, Y., Deng, Y., and Li, H. (2018). MicroRNA-223 regulates cardiac fibrosis after myocardial infarction by targeting RASA1. *Cell. Physiol. Biochem.* 46, 1439–1454. doi: 10.1159/000489185

Luo, B., Li, B., Wang, W., Liu, X., Xia, Y., Zhang, C., et al. (2014). NLRP3 gene silencing ameliorates diabetic cardiomyopathy in a type 2 diabetes rat model. *PLoS One* 9:e104771. doi: 10.1371/journal.pone.0104771

Ma, G., Pan, B., Chen, Y., Guo, C., Zhao, M., Zheng, L., et al. (2017). Trimethylamine N-oxide in atherogenesis: impairing endothelial self-repair capacity and enhancing monocyte adhesion. *Biosci. Rep.* 37:BSR20160244. doi: 10.1042/BSR20160244

Makrecka-Kuka, M., Volska, K., Antone, U., Vilskersts, R., Grinberga, S., Bandere, D., et al. (2017). Trimethylamine N-oxide impairs pyruvate and fatty acid oxidation in cardiac mitochondria. *Toxicol. Lett.* 267, 32–38. doi: 10.1016/j.toxlet.2016.12.017

Organ, C. L., Otsuka, H., Bhushan, S., Wang, Z., Bradley, J., Trivedi, R., et al. (2016). Choline diet and its gut microbe-derived metabolite, trimethylamine N-oxide, exacerbate pressure overload-induced heart failure. *Circ. Heart Fail.* 9:e002314. doi: 10.1161/CIRCHEARTFAILURE.115.002314

Pavillard, L. E., Marin-Aguilar, F., Bullon, P., and Cordero, M. D. (2018). Cardiovascular diseases, NLRP3 inflammasome, and western dietary patterns. *Pharmacol. Res.* 131, 44–50. doi: 10.1016/j.phrs.2018.03.018

Peng, J., Xiao, X., Hu, M., and Zhang, X. (2018). Interaction between gut microbiome and cardiovascular disease. *Life Sci.* 214, 153–157. doi: 10.1016/j.lfs.2018.10.063

Piccoli, M. T., Gupta, S., Viereck, J., Foinquinos, A., Samolovac, S., Kramer, F., et al. (2017). Inhibition of the cardiac fibroblast-enriched lncRNA Meg3 prevents cardiac fibrosis and diastolic dysfunction. *Circ. Res.* 121, 575–583. doi: 10.1161/CIRCRESAHA.117.310624

Qin, G., Xia, J., Zhang, Y., Guo, L., Chen, R., and Sang, N. (2018). Ambient fine particulate matter exposure induces reversible cardiac dysfunction and fibrosis in juvenile and older female mice. *Part. Fibre Toxicol.* 15:27. doi: 10.1186/s12989-018-0264-2

Qiu, Z., Lei, S., Zhao, B., Wu, Y., Su, W., Liu, M., et al. (2017). NLRP3 inflammasome activation-mediated pyroptosis aggravates myocardial ischemia/reperfusion injury in diabetic rats. *Oxid. Med. Cell. Longev.* 2017:9743280. doi: 10.1155/2017/9743280

Randrianarisoa, E., Lehn-Stefan, A., Wang, X., Hoene, M., Peter, A., Heinzmann, S. S., et al. (2016). Relationship of serum trimethylamine N-oxide (TMAO) levels with early atherosclerosis in humans. *Sci. Rep.* 6:26745. doi: 10.1038/srep26745

Rasanen, M., Degerman, J., Nissinen, T. A., Miinalainen, I., Kerkela, R., Siltanen, A., et al. (2016). VEGF-B gene therapy inhibits doxorubicin-induced cardiotoxicity by endothelial protection. *Proc. Natl. Acad. Sci. U.S.A.* 113, 13144–13149. doi: 10.1073/pnas.1616168113

Sandanger, O., Ranheim, T., Vinge, L. E., Bliksoen, M., Alfsnes, K., Finsen, A. V., et al. (2013). The NLRP3 inflammasome is up-regulated in cardiac fibroblasts and mediates myocardial ischaemia-reperfusion injury. *Cardiovasc. Res.* 99, 164–174. doi: 10.1093/cvr/cvt091

Shepshelovich, J., Goldstein-Magal, L., Globerson, A., Yen, P. M., Rotman-Pikielny, P., and Hirschberg, K. (2005). Protein synthesis inhibitors and the chemical chaperone TMAO reverse endoplasmic reticulum perturbation induced by overexpression of the iodide transporter pendrin. *J. Cell. Sci.* 118(Pt 8), 1577–1586. doi: 10.1242/jcs.02294

Song, C., He, L., Zhang, J., Ma, H., Yuan, X., Hu, G., et al. (2016). Fluorofenidone attenuates pulmonary inflammation and fibrosis via inhibiting the activation of NALP3 inflammasome and IL-1beta/IL-1R1/MyD88/NF-kappaB pathway. *J. Cell. Mol. Med.* 20, 2064–2077. doi: 10.1111/jcmm.12898

Suetomi, T., Willeford, A., Brand, C. S., Cho, Y., Ross, R. S., Miyamoto, S., et al. (2018). Inflammation and NLRP3 inflammasome activation initiated in response to pressure overload by Ca(2+)/calmodulin-dependent protein kinase II delta signaling in cardiomyocytes are essential for adverse cardiac remodeling. *Circulation* 138, 2530–2544. doi: 10.1161/CIRCULATIONAHA.118.034621

Sun, Z., Nie, X., Sun, S., Dong, S., Yuan, C., Li, Y., et al. (2017). Long non-coding RNA MEG3 downregulation triggers human pulmonary artery smooth muscle cell proliferation and migration via the p53 signaling pathway. *Cell. Physiol. Biochem.* 42, 2569–2581. doi: 10.1159/000480218

Tang, W. H., Wang, Z., Fan, Y., Levison, B., Hazen, J. E., Donahue, L. M., et al. (2014). Prognostic value of elevated levels of intestinal microbe-generated metabolite trimethylamine-N-oxide in patients with heart failure: refining the gut hypothesis. *J. Am. Coll. Cardiol.* 64, 1908–1914. doi: 10.1016/j.jacc.2014.02.617

Tang, W. H., Wang, Z., Kennedy, D. J., Wu, Y., Buffa, J. A., Agatisa-Boyle, B., et al. (2015a). Gut microbiota-dependent trimethylamine N-oxide (TMAO) pathway contributes to both development of renal insufficiency and mortality risk in chronic kidney disease. *Circ. Res.* 116, 448–455. doi: 10.1161/CIRCRESAHA.116.305360

Tang, W. H., Wang, Z., Shrestha, K., Borowski, A. G., Wu, Y., Troughton, R. W., et al. (2015b). Intestinal microbiota-dependent phosphatidylcholine metabolites, diastolic dysfunction, and adverse clinical outcomes in chronic systolic heart failure. *J. Card. Fail.* 21, 91–96. doi: 10.1016/j.cardfail.2014.11.006

Tang, W. H., Wang, Z., Levison, B. S., Koeth, R. A., Britt, E. B., Fu, X., et al. (2013). Intestinal microbial metabolism of phosphatidylcholine and cardiovascular risk. *N. Engl. J. Med.* 368, 1575–1584. doi: 10.1056/NEJMoa1109400

Tian, R., Zhu, Y., Yao, J., Meng, X., Wang, J., Xie, H., et al. (2017). NLRP3 participates in the regulation of EMT in bleomycin-induced pulmonary fibrosis. *Exp. Cell. Res.* 357, 328–334. doi: 10.1016/j.yexcr.2017.05.028

Travers, J. G., Kamal, F. A., Robbins, J., Yutzey, K. E., and Blaxall, B. C. (2016). Cardiac fibrosis: the fibroblast awakens. *Circ. Res.* 118, 1021–1040. doi: 10.1161/CIRCRESAHA.115.306565

Wang, S., Li, Y., Fan, J., Zhang, X., Luan, J., Bian, Q., et al. (2017). Interleukin-22 ameliorated renal injury and fibrosis in diabetic nephropathy through inhibition of NLRP3 inflammasome activation. *Cell. Death Dis.* 8:e2937. doi: 10.1038/cddis.2017.292

Wang, Z., Klipfell, E., Bennett, B. J., Koeth, R., Levison, B. S., Dugar, B., et al. (2011). Gut flora metabolism of phosphatidylcholine promotes cardiovascular disease. *Nature* 472, 57–63. doi: 10.1038/nature09922

Xiang, F. L., Fang, M., and Yutzey, K. E. (2017). Loss of beta-catenin in resident cardiac fibroblasts attenuates fibrosis induced by pressure overload in mice. *Nat. Commun.* 8:712. doi: 10.1038/s41467-017-00840-w

Yang, L., Zhang, H., and Chen, P. (2018). Sulfur dioxide attenuates sepsis-induced cardiac dysfunction via inhibition of NLRP3 inflammasome activation in rats. *Nitric Oxide* 81, 11–20. doi: 10.1016/j.niox.2018.09.005

Yao, C., Veleva, T., Scott, L. Jr., Cao, S., Li, L., Chen, G., et al. (2018). Enhanced cardiomyocyte NLRP3 inflammasome signaling promotes atrial fibrillation. *Circulation* 138, 2227–2242. doi: 10.1161/CIRCULATIONAHA.118.035202

Yu, L., Meng, G., Huang, B., Zhou, X., Stavrakis, S., Wang, M., et al. (2018). A potential relationship between gut microbes and atrial fibrillation: trimethylamine N-oxide, a gut microbe-derived metabolite, facilitates the progression of atrial fibrillation. *Int. J. Cardiol.* 255, 92–98. doi: 10.1016/j.ijcard.2017.11.071

Yuan, J., Chen, H., Ge, D., Xu, Y., Xu, H., Yang, Y., et al. (2017). Mir-21 promotes cardiac fibrosis after myocardial infarction via targeting smad7. *Cell. Physiol. Biochem.* 42, 2207–2219. doi: 10.1159/000479995

Zhang, H., Meng, J., and Yu, H. (2017). Trimethylamine N-oxide supplementation abolishes the cardioprotective effects of voluntary exercise in mice fed a western diet. *Front. Physiol.* 8:944. doi: 10.3389/fphys.2017.00944

Zhang, W., Xu, X., Kao, R., Mele, T., Kvietys, P., Martin, C. M., et al. (2014). Cardiac fibroblasts contribute to myocardial dysfunction in mice with sepsis: the role of NLRP3 inflammasome activation. *PLoS One* 9:e107639. doi: 10.1371/journal.pone.0107639

Zhang, X., Fu, Y., Li, H., Shen, L., Chang, Q., Pan, L., et al. (2018). H3 relaxin inhibits the collagen synthesis via ROS- and P2X7R-mediated NLRP3 inflammasome activation in cardiac fibroblasts under high glucose. *J. Cell. Mol. Med.* 22, 1816–1825. doi: 10.1111/jcmm.13464

Conflict of Interest Statement: The authors declare that the research was conducted in the absence of any commercial or financial relationships that could be construed as a potential conflict of interest.

frontiers in Physiology

BRIEF RESEARCH REPORT
published: 20 September 2019
doi: 10.3389/fphys.2019.01186

Experimental Pulmonary Hypertension Is Associated With Neuroinflammation in the Spinal Cord

*Mylene Vaillancourt, Pamela Chia, Lejla Medzikovic, Nancy Cao, Gregoire Ruffenach, David Younessi and Soban Umar**

Department of Anesthesiology and Perioperative Medicine, University of California, Los Angeles, Los Angeles, CA, United States

Rationale: Pulmonary hypertension (PH) is a rare but fatal disease characterized by elevated pulmonary pressures and vascular remodeling, leading to right ventricular failure and death. Recently, neuroinflammation has been suggested to be involved in the sympathetic activation in experimental PH. Whether PH is associated with neuroinflammation in the spinal cord has never been investigated.

Methods/Results: PH was well-established in adult male Wistar rats 3-week after pulmonary endothelial toxin Monocrotaline (MCT) injection. Using the thoracic segments of the spinal cord, we found a 5-fold increase for the glial fibrillary acidic protein (GFAP) in PH rats compared to controls ($p < 0.05$). To further determine the region of the spinal cord where GFAP was expressed, we performed immunofluorescence and found a 3 to 3.5-fold increase of GFAP marker in the gray matter, and a 2 to 3-fold increase in the white matter in the spinal cord of PH rats compared to controls. This increase was due to PH (MCT vs. Control; $p < 0.01$), and there was no difference between the dorsal versus ventral region. PH rats also had an increase in the pro-inflammatory marker chemokine (C-C motif) ligand 3 (CCL3) protein expression (~ 3-fold) and (2.8 to 4-fold, $p < 0.01$) in the white matter. Finally, angiogenesis was increased in PH rat spinal cords assessed by the adhesion molecule CD31 expression (1.5 to 2.3-fold, $p < 0.01$).

Conclusion: We report for the first time evidence for neuroinflammation in the thoracic spinal cord of pulmonary hypertensive rats. The impact of spinal cord inflammation on cardiopulmonary function in PH remains elusive.

Keywords: pulmonary hypertension, Monocrotaline, neuroinflammation, spinal cord, oxidative stress, sympathetic nervous system, sympathetic activation

OPEN ACCESS

Edited by:
Thao P. Nguyen, UCLA David Geffen School of Medicine, United States

Reviewed by:
Sreekumar Ramachandran, Johns Hopkins Medicine, United States
Xiaofeng Yang, Temple University, United States
Lin Wang, Stanford Health Care, United States

***Correspondence:**
Soban Umar
sumar@mednet.ucla.edu

Specialty section:
This article was submitted to Oxidant Physiology, a section of the journal Frontiers in Physiology

Received: *16 December 2018*
Accepted: *02 September 2019*
Published: *20 September 2019*

Citation:
Vaillancourt M, Chia P, Medzikovic L, Cao N, Ruffenach G, Younessi D and Umar S (2019) Experimental Pulmonary Hypertension Is Associated With Neuroinflammation in the Spinal Cord. Front. Physiol. 10:1186. doi: 10.3389/fphys.2019.01186

INTRODUCTION

Pulmonary arterial hypertension (PAH) is a rare but fatal disease characterized by elevated pulmonary vascular pressure and pulmonary arterial remodeling, leading to right ventricular failure and patient's death. The pathogenesis of PAH is very complex and multifactorial, including inflammation and dysregulation of the autonomic nervous response (Huertas et al., 2014; Vaillancourt et al., 2017). Several studies described an activation of the sympathetic nervous system in PAH patients, which was

associated with clinical worsening and poor outcome (Velez-Roa et al., 2004; Dimopoulos et al., 2009; Wensel et al., 2009; Ciarka et al., 2010; Mak et al., 2012; Witte et al., 2016). Recently, neuroinflammation has been suggested to be involved in this sympathetic activation in experimental PH (Hilzendeger et al., 2014; Sharma et al., 2018). According to Sharma et al. (2018), inflammation in the paraventricular nucleus, which contains nerves projecting directly to the right ventricle (RV), may lead to right heart hypertrophy and failure. Therefore, it may be appealing to directly target neuroinflammation response in the brain to protect against PH. However, in clinical setting, pharmacological treatments of the central nervous system can be challenging due to physical and biochemical obstacles created by the blood-brain barrier (Bhowmik et al., 2015; Pulicherla and Verma, 2015). Furthermore, studies comparing neuroinflammation following identical traumas in the brain and spinal cord concluded for a greater inflammatory response in the spinal cord than in the brain (Schnell et al., 1999; Zhang and Gensel, 2014). Whether PH is associated with neuroinflammation in the spinal cord has never been investigated.

Astrocytes are the most abundant cells in the nervous tissue and play a controversial role in neuroinflammation (Colombo and Farina, 2016). Oxidative stress induces activation of astrocytes in dose and time-dependent manner as evident by increased expression of GFAP (Daverey and Agrawal, 2016). In acute inflammation, they secrete anti-inflammatory cytokines to limit inflammation, form glia scar in injured tissue and promote neuronal survival and myelin regeneration. On the other hand, astrogliosis may lead to detrimental effects by upregulating nuclear factor kappa B (NFkB), thus promoting secretion of pro-inflammatory chemokines such as chemokine (C-C motif) ligand (CCL) 2 and CCL-3 (Choi et al., 2014; Gowrisankar and Clark, 2016). Microglia, resident immune cells in the central nervous tissue, also are key regulators of neuroinflammation. After activation by nervous tissue injury, microglia proliferate and help scavenging altered myelin during demyelination and myelin regeneration (Carlson et al., 1998; Watanabe et al., 1999). However, as for astrocytes, overactivated microglia may become harmful to the tissue by expressing several pro-inflammatory components, including CCL3 (Murphy et al., 1995; Boutej et al., 2017), TNF-α (Kuno et al., 2005; Guadagno et al., 2013), glutamate (Takaki et al., 2012), and superoxide (Chao et al., 1992; Mead et al., 2012). Pro-inflammatory mediators, in addition to activating glial cells, affect the blood-spinal cord barrier (BSCB) by activating endothelial cells and increasing the recruitment and trans-endothelial migration of inflammatory cells into the tissue (Takeshita and Ransohoff, 2012). Here we report for the first time evidences for the presence of activated astrocytes, increased production of pro-inflammatory chemokines, as well as impaired BSCB in MCT-induced PH rat model.

MATERIALS AND METHODS

Protocols received UCLA animal research committee approval. Please refer to **Supplementary Materials** for details on methods.

Animal Experiment

Male Wistar rats were injected s.c. with either 60 mg/kg of crotaline (MCT, $n = 4$) or PBS (Ctrl, $n = 4$) (**Figure 1A**). After 21 days, animals were anesthetized and right ventricular systolic pressure (RVSP) was measured. Lungs and spinal cords were collected.

Western Blot Analysis

Western blots were performed on thoracic segments of the spinal cord. Blots were incubated with primary antibody against GFAP.

Immunofluorescence Staining

Thoracic spinal cord sections were stained for GFAP, CCL3, CD31, and MAP2. Images were acquired with a confocal microscope (Nikon) and analyzed.

Enzyme-Linked Immunosorbent Assay (ELISA)

CCL3 concentration was measured on thoracic segments of the spinal cord using a rat-specific CCL3 ELISA kit according to manufacturer's instructions.

Statistical Analysis

Values were expressed in fold changes or mean ± SEM. Mann-Whitney *U* test was used for comparisons between two groups. 2-way ANOVA, with factors of treatment (MCT vs. Ctrl) and region (gray vs. white matter and dorsal vs. ventral), was performed when comparing the different regions of the spinal cord. Probability values <0.05 were considered statistically significant.

RESULTS

Astrogliosis Is Present in the Spinal Cord of Pulmonary Hypertensive Rats

Pulmonary hypertension in MCT-treated rats was confirmed by increased RV pressure and pulmonary vascular remodeling (**Figures 1B,C**). To assess the presence of astrogliosis in PH, we performed a Western blot for GFAP, a marker for astrocyte activation. GFAP expression was significantly increased by 5-fold in MCT-induced PH rats compared to controls ($p < 0.05$) (**Figure 1D**). To further determine in which region of the spinal cord GFAP was expressed, we performed immunofluorescence of thoracic spinal cord tissue sections in combination with the microtubule-associated protein 2 (MAP2) marker to distinguish between the gray and the white matter. We found a 3 to 3.5-fold increase of GFAP marker in the gray matter, and a 2 to 3-fold increase in the white matter in the spinal cord of our PH rats compared to controls (**Figures 1E,F**). There was no impact of the region of the spinal cord (dorsal vs. ventral and gray vs. white matter) on this increase of GFAP. However, there was a significant effect ($p < 0.01$) of PH development (MCT vs. Control) on GFAP expression in the spinal cord tissue (**Figure 1F**). Interestingly, we observed an accumulation of activated astrocytes around the outer laminae of the dorsal horn (**Figure 1G**), which receives terminals of primary afferent

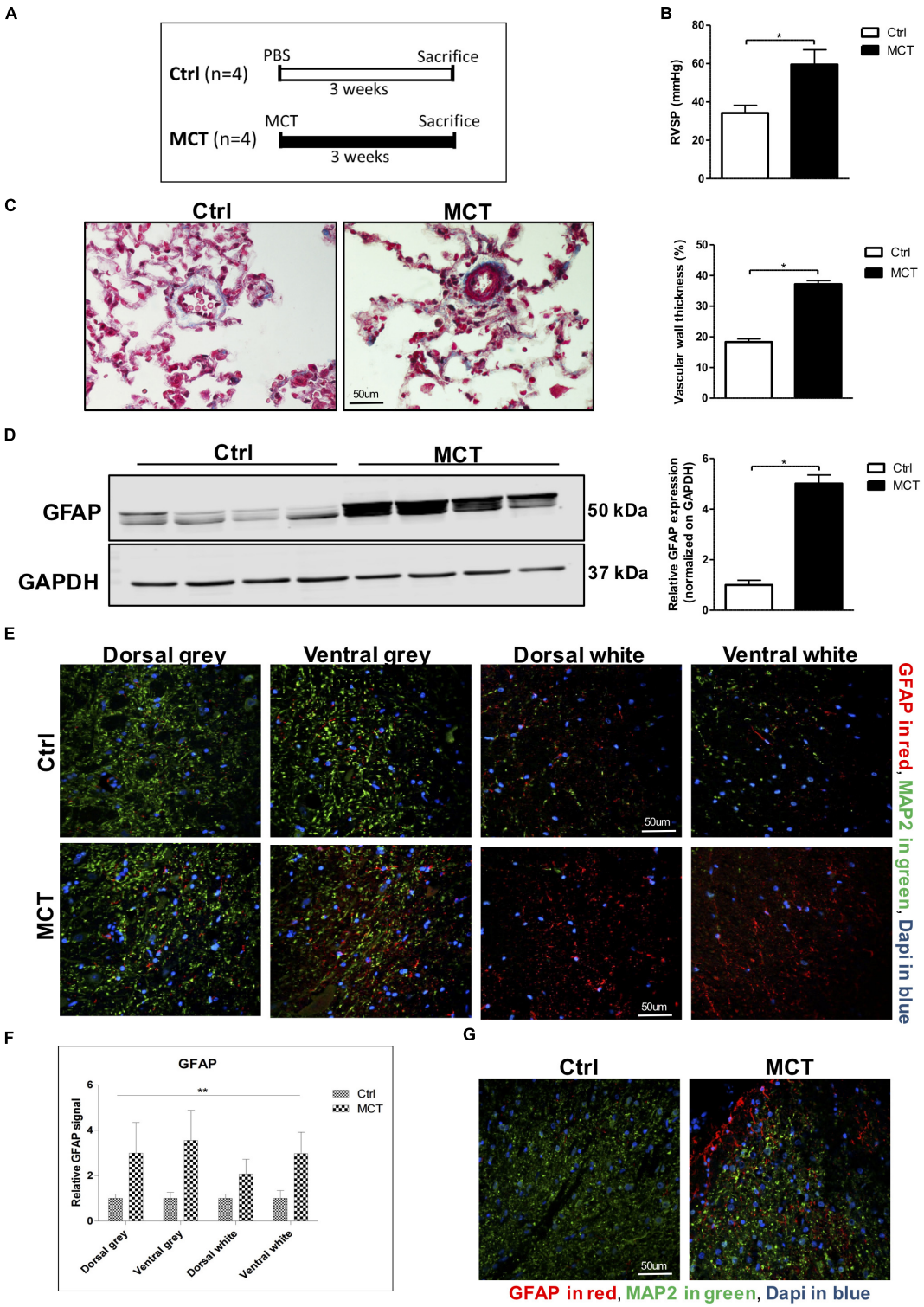

FIGURE 1 | Astrogliosis is present in the spinal cord of pulmonary hypertensive rats. **(A)** Male Wistar rats received a subcutaneous injection of either MCT (60 mg/kg) or PBS for 21 days. **(B)** MCT-treated rats developed PH assessed by an increased RVSP. **(C)** Trichrome staining and quantification for pulmonary vascular remodeling. **(D)** Western blot for GFAP expression in the spinal cord. **(E)** Representative immunofluorescence for GFAP shown in red, MAP2 in green and nuclei (Dapi) in blue. **(F)** Quantification of GFAP staining in the different regions of the spinal cord. 2-way ANOVA, with factors of treatment (MCT vs. Ctrl) and region (gray vs. white matter and dorsal vs. ventral), revealed a main effect of MCT treatment, shown by (**$p < 0.01$), with no significant main effect of the region or interaction. **(G)** Immunofluorescence showing a concentration of GFAP positive glial cells around the dorsal horn in MCT-induced PH rats. Mann-Whitney *U* test was used for comparisons between two groups. *$p < 0.05$, **$p < 0.01$, ***$p < 0.001$.

and sensory neurons, in opposition to the ventral horn which contains efferent and motor neurons.

Pro-inflammatory Chemokine CCL3 Is Increased in Spinal Neuronal Tissue From PH Rats

Detrimental astroglial activation is characterized by the release of pro-inflammatory cytokines and chemokines, which may lead to other glial cell activation and leukocyte recruitment in neuronal tissue. We looked for the presence of CCL3, one of these chemokines, in the spinal cord and found a -2.5 to 4-fold increase in CCL3 staining in the white matter of PH rats compared to controls. This increase was due to the development of PH ($p < 0.01$) and the expression increased in dorsal and ventral white parts but was not different between the dorsal and the ventral gray parts of the thoracic spinal cord (**Figures 2A–C**). Furthermore, CCL3 expression in the thoracic section of the spinal cord was also increased ∼ 3-fold in rats treated with MCT compared to controls, as measured by ELISA (**Figure 2D**).

Experimental PH Is Associated With Spinal Neurovascular Endothelial Activation

CD31 is an adhesion molecule member of the immunoglobulin superfamily highly expressed by endothelial cells. CD31, in addition of being an endothelial marker, is a key regulator of leukocyte trans-endothelial migration and angiogenesis (Woodfin et al., 2007) and was increased after spinal cord injury (Schnell et al., 1999). We then looked for possible changes in CD31 expression in the spinal cord of PH rats. By immunofluorescence, we found a 1.5 to 1.7-fold increase of the CD31 adhesion molecule in the gray matter, as well as a 1.7 to 2.3-fold increase in the white matter in the spinal cord of PH rats compared to controls (**Figures 2B–E**). Once again, this increase was significantly impacted by PH development ($p < 0.01$), but not dependent on the region (dorsal vs. ventral and gray vs. white matter).

DISCUSSION

Taken together, the presence of astrogliosis, increased production of pro-inflammatory mediators like CCL3, as well as the increased expression of the adhesion molecule CD31 are the first evidences ever-published suggesting neuroinflammation in the spinal cord of MCT-induced PH rats. Sensory neurons ending in the dorsal horn play a prominent role in the transmission and modulation of pain signals. After peripheral sensitization of sensory neurons in response to local tissue injury or inflammation, these sensory neurons release increased amounts of neurotransmitters such as substance P and calcitonin gene-related peptide (Iyengar et al., 2017). The increased release of these neurotransmitters in the dorsal horn by sensory neurons may have caused sustained astrocyte activation and neuroinflammation in the thoracic spinal cord of the PH rats in our study.

CCL3 is a pro-inflammatory chemokine poorly expressed in resting glial cells. However, activated astrocytes and microglia begin expressing CCL3 upon stimulation with TNF-α, IL1-β (Choi et al., 2014), two cytokines known to be highly increased in the plasma of PAH patients (Humbert et al., 1995; Soon et al., 2010). Recently, increased levels of chemokines such as CCL1, CCL2, and CCL3 were also found in the lungs of mice and humans with PH (Florentin et al., 2018). As for astrocytes, persistent microglial activation tends to sustain inflammation rather than resolving it. In a mouse model of retinal degeneration, microglia expressing CCL3 were shown to exacerbate inflammation and retinal degeneration, which were attenuated in CCL3 knock-out mice (Kohno et al., 2014). After stimulation with TNF-α, human brain microvascular endothelial cells increased the secretion and presentation of CCL3 on their apical surface along with a decreased expression of tight junction proteins and an upregulation of adhesion molecules (Chui and Dorovini-Zis, 2010; De Laere et al., 2017). Therefore, it is possible to extrapolate a similar role for CCL3 on the BSCB integrity during neuroinflammation.

The BSCB integrity is essential for preventing inflammatory immune cell infiltration in the tissue and its disruption precedes the post-traumatic inflammatory response in spinal cord injury (Schnell et al., 1999). Moreover, the microvascular endothelium in the spinal cord is vulnerable to demyelinating inflammatory diseases, supported by observations of increased BSCB permeability related to the severity of disease in models of multiple sclerosis (Kirk and Karlik, 2003; Roscoe et al., 2009). Increased angiogenesis was shown in demyelinated lesions of a multiple sclerosis model and was persistent with chronic inflammation, perivascular infiltration and severity of the disease (Kirk and Karlik, 2003; Roscoe et al., 2009; Holley et al., 2010). In the same manner, the increased expression of CD31 in the spinal cord of our PH rats may promote recruitment and migration of leukocytes in the spinal cord of PH rats, thus sustaining neuroinflammation.

Our study suggests the presence of neuroinflammation in the spinal cord in experimental PH. Whether this neuroinflammation has direct or indirect impact on pulmonary artery pressures or right heart deterioration still needs to be investigated. It has recently been suggested that microglial activation in the CNS was playing a role in PH development (Sharma et al., 2018). Local inhibition of microglial activation in the paraventricular nucleus of PH rats prevented sympathetic activation compared to sham-treated rats, assessed by decreased plasma level of norepinephrine and restored the autonomic balance. This was associated with improvement of pulmonary pressures, vascular remodeling, and right ventricular function (Sharma et al., 2018). The upper thoracic segments of the spinal cord contain preganglionic sympathetic neurons innervating the heart and lungs, thus controlling their autonomic activity. Hence, it is possible to think that oxidative stress and neuroinflammation in this location may also increase the sympathetic activity in the heart and the pulmonary circulation promoting PH and RV dysfunction. On the other hand, Quilez et al. (2011) showed that rats mechanically ventilated with a high tidal volume developed lung injury and inflammation, leading to neuronal

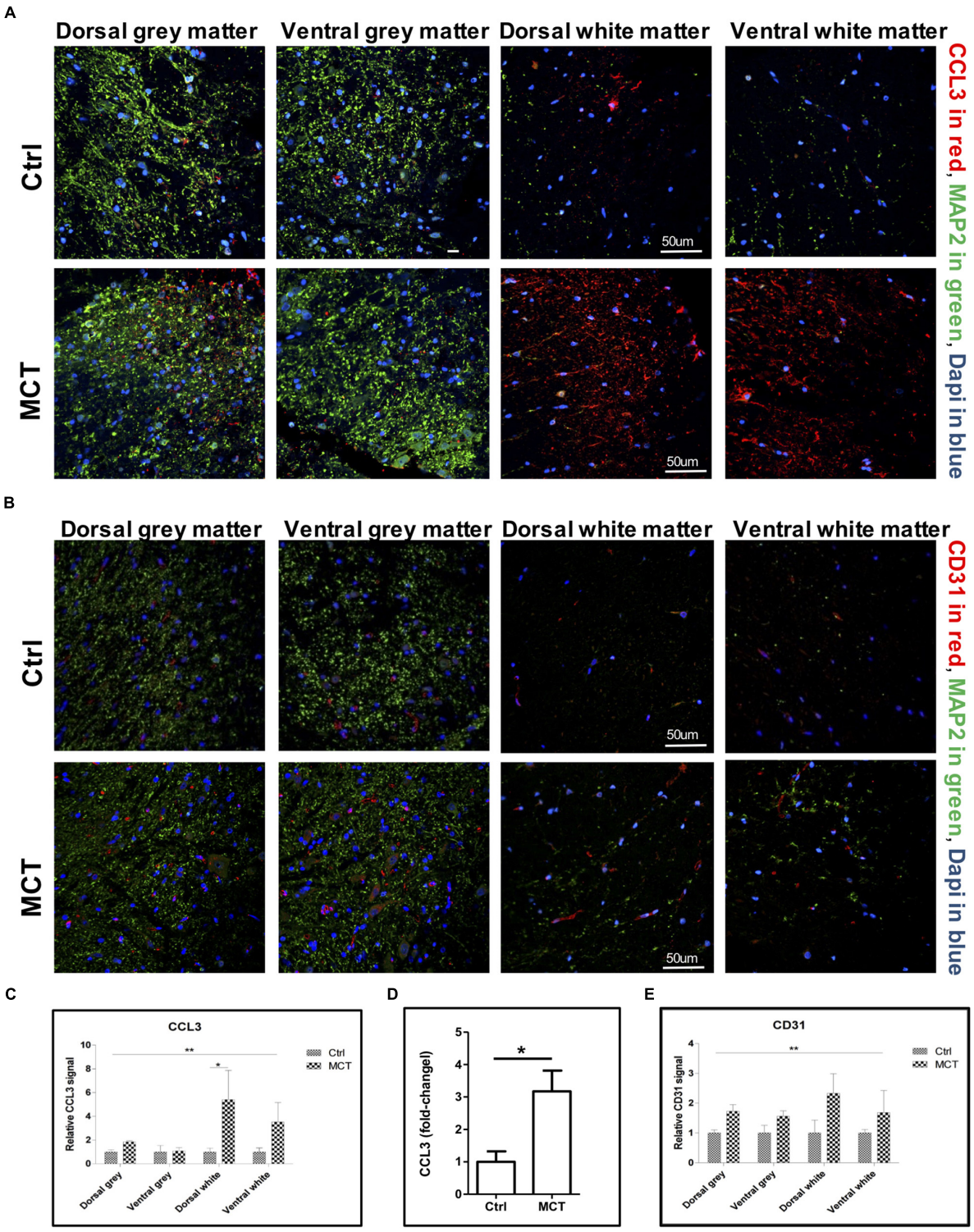

FIGURE 2 | Pulmonary hypertension is associated with increased pro-inflammatory markers and angiogenesis. **(A)** Representative immunofluorescence showing CCL3 in red, MAP2 in green and nuclei (Dapi) in blue. **(B)** Representative immunofluorescence showing the adhesion molecule CD31 expression in red, MAP2 in green and nuclei (Dapi) in blue. **(C)** Quantification of CCL3 expression using a 2-way ANOVA, with factors of treatment (MCT vs. Ctrl) and region (gray vs. white matter and dorsal vs. ventral), revealing an effect of MCT treatment shown by (**$p < 0.01$), with no significant main effect of the region or interaction except for dorsal white (*$p < 0.05$). **(D)** Quantification of CCL3 expression in the thoracic section of the spinal cords using ELISA (*$p < 0.05$). **(E)** Quantification of CD31 expression using a 2-way ANOVA, with factors of treatment (MCT vs. Ctrl) and region (gray vs. white matter and dorsal vs. ventral), revealing a main effect of MCT treatment shown by (**$p < 0.01$), with no significant main effect of the region or interaction. Mann-Whitney *U* test was used for comparisons two groups.

activation in different regions of the brain, including the paraventricular nucleus. Finally, several studies showed that chronic heart dysfunction following acute myocardial infarction induces microglial activation and chronic neuroinflammation in the periventricular nucleus (Rana et al., 2010; Dworak et al., 2014; Du et al., 2015). Microglial activation, as well as the following sympatho-excitatory response, were inhibited by the administration of minocycline (Dworak et al., 2014). These studies highlight the interplay between the lung, heart, and brain. Therefore, it is possible to hypothesize a possible role for lung inflammation and RV dysfunction in triggering and/or sustaining the neuroinflammation seen in the thoracic spinal cord of our rats with PH.

In conclusion, we report for the first time evidence for the presence of neuroinflammation in the thoracic spinal cord of pulmonary hypertensive rats. Whether this neuroinflammation is triggered and/or sustained by lung inflammation and RV dysfunction, as well as its potential impact on cardiopulmonary function remains elusive.

AUTHOR CONTRIBUTIONS

MV, PC, LM, NC, GR, DY, and SU were responsible for collecting, analyzing, and interpreting the data. MV and SU wrote the manuscript. SU supervised the study.

FUNDING

SU was supported by a Mentored Research Training Grant from the Foundation for Anesthesia Education and Research (FAER) and NIH K08 Grant (1K08 HL141995 01A1).

SUPPLEMENTARY MATERIAL

The Supplementary Material for this article can be found online at: https://www.frontiersin.org/articles/10.3389/fphys.2019.01186/full#supplementary-material

REFERENCES

Bhowmik, A., Khan, R., and Ghosh, M. K. (2015). Blood brain barrier: a challenge for effectual therapy of brain tumors. *Biomed. Res. Int.* 2015:320941. doi: 10.1155/2015/320941

Boutej, H., Rahimian, R., Thammisetty, S. S., Béland, L.-C., Lalancette-Hébert, M., and Kriz, J. (2017). Diverging mRNA and protein networks in activated microglia reveal SRSF3 suppresses translation of highly upregulated innate immune transcripts. *Cell Rep.* 21, 3220–3233. doi: 10.1016/j.celrep.2017.11.058

Carlson, S. L., Parrish, M. E., Springer, J. E., Doty, K., and Dossett, L. (1998). Acute inflammatory response in spinal cord following impact injury. *Exp. Neurol.* 151, 77–88. doi: 10.1006/exnr.1998.6785

Chao, C. C., Hu, S., Molitor, T. W., Shaskan, E. G., and Peterson, P. K. (1992). Activated microglia mediate neuronal cell injury via a nitric oxide mechanism. *J. Immunol.* 149, 2736–2741.

Choi, S. S., Lee, H. J., Lim, I., Satoh, J., and Kim, S. U. (2014). Human astrocytes: secretome profiles of cytokines and chemokines. *PLoS One* 9:e92325. doi: 10.1371/journal.pone.0092325

Chui, R., and Dorovini-Zis, K. (2010). Regulation of CCL2 and CCL3 expression in human brain endothelial cells by cytokines and lipopolysaccharide. *J. Neuroinflamm.* 7:1. doi: 10.1186/1742-2094-7-1

Ciarka, A., Doan, V., Velez-Roa, S., Naeije, R., and van de Borne, P. (2010). Prognostic significance of sympathetic nervous system activation in pulmonary arterial hypertension. *Am. J. Respir. Crit. Care Med.* 181, 1269–1275. doi: 10.1164/rccm.200912-1856OC

Colombo, E., and Farina, C. (2016). Astrocytes: key regulators of neuroinflammation. *Trends Immunol.* 37, 608–620. doi: 10.1016/j.it.2016.06.006

Daverey, A., and Agrawal, S. K. (2016). Curcumin alleviates oxidative stress and mitochondrial dysfunction in astrocytes. *Neuroscience* 333, 92–103. doi: 10.1016/j.neuroscience.2016.07.012

De Laere, M., Sousa, C., Meena, M., Buckinx, R., Timmermans, J.-P., Berneman, Z., et al. (2017). Increased transendothelial transport of CCL3 Is insufficient to drive immune cell transmigration through the blood–brain barrier under inflammatory conditions in vitro. *Mediat. Inflamm.* 2017:6752756. doi: 10.1155/2017/6752756

Dimopoulos, S., Anastasiou-Nana, M., Katsaros, F., Papazachou, O., Tzanis, G., Gerovasili, V., et al. (2009). Impairment of autonomic nervous system activity in patients with pulmonary arterial hypertension: a case control study. *J. Card. Fail.* 15, 882–889. doi: 10.1016/j.cardfail.2009.06.001

Du, D., Jiang, M., Liu, M., Wang, J., Xia, C., Guan, R., et al. (2015). Microglial P2X7 receptor in the hypothalamic paraventricular nuclei contributes to sympathoexcitatory responses in acute myocardial infarction rat. *Neurosci. Lett.* 587, 22–28. doi: 10.1016/j.neulet.2014.12.026

Dworak, M., Stebbing, M., Kompa, A. R., Rana, I., Krum, H., and Badoer, E. (2014). Attenuation of microglial and neuronal activation in the brain by ICV minocycline following myocardial infarction. *Auton. Neurosci.* 185, 43–50. doi: 10.1016/j.autneu.2014.03.007

Florentin, J., Coppin, E., Vasamsetti, S. B., Zhao, J., Tai, Y. Y., Tang, Y., et al. (2018). Inflammatory macrophage expansion in pulmonary hypertension depends upon mobilization of blood-borne monocytes. *J. Immunol.* 200, 3612–3625. doi: 10.4049/jimmunol.1701287

Gowrisankar, Y. V., and Clark, M. A. (2016). Angiotensin II induces interleukin-6 expression in astrocytes: role of reactive oxygen species and NF-κB. *Mol. Cell Endocrinol.* 437, 130–141. doi: 10.1016/j.mce.2016.08.013

Guadagno, J., Xu, X., Karajgikar, M., Brown, A., and Cregan, S. P. (2013). Microglia-derived TNFα induces apoptosis in neural precursor cells via transcriptional activation of the Bcl-2 family member Puma. *Cell Death Dis.* 4:e538. doi: 10.1038/cddis.2013.59

Hilzendeger, A. M., Shenoy, V., Raizada, M. K., and Katovich, M. J. (2014). Neuroinflammation in pulmonary hypertension: concept, facts, and relevance. *Curr. Hypertens. Rep.* 16:469. doi: 10.1007/s11906-014-0469-1

Holley, J. E., Newcombe, J., Whatmore, J. L., and Gutowski, N. J. (2010). Increased blood vessel density and endothelial cell proliferation in multiple sclerosis cerebral white matter. *Neurosci. Lett.* 470, 65–70. doi: 10.1016/j.neulet.2009.12.059

Huertas, A., Perros, F., Tu, L., Cohen-Kaminsky, S., Montani, D., Dorfmüller, P., et al. (2014). Immune dysregulation and endothelial dysfunction in pulmonary arterial hypertension: a complex interplay. *Circulation* 129, 1332–1340. doi: 10.1161/circulationaha.113.004555

Humbert, M., Monti, G., Brenot, F., Sitbon, O., Portier, A., Grangeot-Keros, L., et al. (1995). Increased interleukin-1 and interleukin-6 serum concentrations in severe primary pulmonary hypertension. *Am. J. Respir. Crit. Care Med.* 151, 1628–1631. doi: 10.1164/ajrccm.151.5.7735624

Iyengar, S., Ossipov, M. H., and Johnson, K. W. (2017). The role of calcitonin gene-related peptide in peripheral and central pain mechanisms including migraine. *Pain* 158, 543–559. doi: 10.1097/j.pain.0000000000000831

Kirk, S. L., and Karlik, S. J. (2003). VEGF and vascular changes in chronic neuroinflammation. *J. Autoimmun.* 21, 353–363. doi: 10.1016/s0896-8411(03)00139-2

Kohno, H., Maeda, T., Perusek, L., Pearlman, E., and Maeda, A. (2014). CCL3 production by microglial cells modulates disease severity in murine models of retinal degeneration. *J. Immunol.* 192, 3816–3827. doi: 10.4049/jimmunol.1301738

Kuno, R., Wang, J., Kawanokuchi, J., Takeuchi, H., Mizuno, T., and Suzumura, A. (2005). Autocrine activation of microglia by tumor necrosis factor-α. *J. Neuroimmunol.* 162, 89–96. doi: 10.1016/j.jneuroim.2005.01.015

Mak, S., Witte, K. K., Al-Hesayen, A., Granton, J. J., and Parker, J. D. (2012). Cardiac sympathetic activation in patients with pulmonary arterial hypertension. *Am. J. Physiol. Regul. Integrat. Comp. Physiol.* 302, R1153–R1157. doi: 10.1152/ajpregu.00652.2011

Mead, E. L., Mosley, A., Eaton, S., Dobson, L., Heales, S. J., and Pocock, J. M. (2012). Microglial neurotransmitter receptors trigger superoxide production in microglia; consequences for microglial–neuronal interactions. *J. Neurochem.* 121, 287–301. doi: 10.1111/j.1471-4159.2012.07659.x

Murphy, G., Jia, X.-C., Song, Y., Ong, E., Shrivastava, R., Bocchini, V., et al. (1995). Macrophage inflammatory protein 1-α mRNA expression in an immortalized microglial cell line and cortical astrocyte cultures. *J. Neurosci. Res.* 40, 755–763. doi: 10.1002/jnr.490400607

Pulicherla, K. K., and Verma, M. K. (2015). Targeting therapeutics across the blood brain barrier (BBB), prerequisite towards thrombolytic therapy for cerebrovascular disorders—an overview and advancements. *AAPS Pharm. Sci. Tech.* 16, 223–233. doi: 10.1208/s12249-015-0287-z

Quilez, M. E., Fuster, G., Villar, J., Flores, C., Martí-Sistac, O., Blanch, L., et al. (2011). Injurious mechanical ventilation affects neuronal activation in ventilated rats. *Crit. Care* 15:R124. doi: 10.1186/cc10230

Rana, I., Stebbing, M., Kompa, A., Kelly, D. J., Krum, H., and Badoer, E. (2010). Microglia activation in the hypothalamic PVN following myocardial infarction. *Brain Res.* 1326, 96–104. doi: 10.1016/j.brainres.2010.02.028

Roscoe, W. A., Welsh, M. E., Carter, D. E., and Karlik, S. J. (2009). VEGF and angiogenesis in acute and chronic MOG((35-55)) peptide induced EAE. *J. Neuroimmunol.* 209, 6–15. doi: 10.1016/j.jneuroim.2009.01.009

Schnell, L., Fearn, S., Klassen, H., Schwab, M. E., and Perry, V. H. (1999). Acute inflammatory responses to mechanical lesions in the CNS: differences between brain and spinal cord. *Eur. J. Neurosci.* 11, 3648–3658. doi: 10.1046/j.1460-9568.1999.00792.x

Sharma, R. K., Oliveira, A. C., Kim, S., Rigatto, K., Zubcevic, J., Rathinasabapathy, A., et al. (2018). Involvement of neuroinflammation in the pathogenesis of monocrotaline-induced pulmonary hypertension. *Hypertension* 71, 1156–1163. doi: 10.1161/HYPERTENSIONAHA.118.10934

Soon, E., Holmes, A. M., Treacy, C. M., Doughty, N. J., Southgate, L., Machado, R. D., et al. (2010). Elevated levels of inflammatory cytokines predict survival in idiopathic and familial pulmonary arterial hypertension. *Circulation* 122, 920–927. doi: 10.1161/CIRCULATIONAHA.109.933762

Takaki, J., Fujimori, K., Miura, M., Suzuki, T., Sekino, Y., and Sato, K. (2012). L-glutamate released from activated microglia downregulates astrocytic L-glutamate transporter expression in neuroinflammation: the 'collusion' hypothesis for increased extracellular L-glutamate concentration in neuroinflammation. *J. Neuroinflamm.* 9:275.

Takeshita, Y., and Ransohoff, R. M. (2012). Inflammatory cell trafficking across the blood-brain barrier (BBB): chemokine regulation and in vitro models. *Immunol. Rev.* 248, 228–239. doi: 10.1111/j.1600-065X.2012.01127.x

Vaillancourt, M., Chia, P., Sarji, S., Nguyen, J., Hoftman, N., Ruffenach, G., et al. (2017). Autonomic nervous system involvement in pulmonary arterial hypertension. *Respir. Res.* 18:201. doi: 10.1186/s12931-017-0679-6

Velez-Roa, S., Ciarka, A., Najem, B., Vachiery, J.-L., Naeije, R., and van de Borne, P. (2004). Increased sympathetic nerve activity in pulmonary artery hypertension. *Circulation* 110, 1308–1312. doi: 10.1161/01.cir.0000140724.90898.d3

Watanabe, T., Yamamoto, T., Abe, Y., Saito, N., Kumagai, T., and Kayama, H. (1999). Differential activation of microglia after experimental spinal cord injury. *J. Neurotrauma* 16, 255–265. doi: 10.1089/neu.1999.16.255

Wensel, R., Jilek, C., Dörr, M., Francis, D. P., Stadler, H., Lange, T., et al. (2009). Impaired cardiac autonomic control relates to disease severity in pulmonary hypertension. *Eur. Respir. J.* 34, 895–901. doi: 10.1183/09031936.00145708

Witte, C., Meyer-Arend, J. U. M., Zur, H., Genannt Andrié, R., Schrickel, J. W., Hammerstingl, C., et al. (2016). "Heart rate variability and arrhythmic burden in pulmonary hypertension," in *Pulmonary Dysfunction and Disease*, ed. M. Pokorski (Cham: Springer), 9–22. doi: 10.1007/5584_2016_18

Woodfin, A., Reichel, C. A., Khandoga, A., Corada, M., Voisin, M.-B., Scheiermann, C., et al. (2007). JAM-A mediates neutrophil transmigration in a stimulus-specific manner in vivo: evidence for sequential roles for JAM-A and PECAM-1 in neutrophil transmigration. *Blood* 110, 1848–1856. doi: 10.1182/blood-2006-09-047431

Zhang, B., and Gensel, J. C. (2014). Is neuroinflammation in the injured spinal cord different than in the brain? Examining intrinsic differences between the brain and spinal cord. *Exp. Neurol.* 258, 112–120. doi: 10.1016/j.expneurol.2014.04.007 doi: 10.1016/j.expneurol.2014.04.007

Conflict of Interest Statement: The authors declare that the research was conducted in the absence of any commercial or financial relationships that could be construed as a potential conflict of interest.

The handling Editor declared a shared affiliation, though no other collaboration, with the authors at the time of the review.

frontiers in Physiology

REVIEW
published: 24 September 2019
doi: 10.3389/fphys.2019.01233

Oxidative Stress and Its Implications in the Right Ventricular Remodeling Secondary to Pulmonary Hypertension

*Matthew Mikhael†, Christian Makar†, Amir Wissa†, Trixie Le, Mansoureh Eghbali and Soban Umar**

Division of Molecular Medicine, Department of Anesthesiology and Perioperative Medicine, David Geffen School of Medicine, UCLA, Los Angeles, CA, United States

OPEN ACCESS

Edited by:
Feng Chen,
Augusta University, United States

Reviewed by:
Saurabh Aggarwal,
The University of Alabama at Birmingham, United States
Deepesh Pandey,
Johns Hopkins University, United States

***Correspondence:**
Soban Umar
sumar@mednet.ucla.edu

† These authors have contributed equally to this work as co-first authors

Specialty section:
This article was submitted to Oxidant Physiology, a section of the journal Frontiers in Physiology

Received: *28 February 2019*
Accepted: *09 September 2019*
Published: *24 September 2019*

Citation:
Mikhael M, Makar C, Wissa A, Le T, Eghbali M and Umar S (2019) Oxidative Stress and Its Implications in the Right Ventricular Remodeling Secondary to Pulmonary Hypertension. Front. Physiol. 10:1233. doi: 10.3389/fphys.2019.01233

Pulmonary hypertension (PH) is a pulmonary vascular disease characterized by increased pulmonary artery pressures. Long standing pulmonary arterial pressure overload leads to right ventricular (RV) hypertrophy, RV failure, and death. RV failure is a major determinant of survival in PH. Oxidative stress has been associated with the development of RV failure secondary to PH. Here we summarize the structural and functional changes in the RV in response to sustained pulmonary arterial pressure overload. Furthermore, we review the pre-clinical and clinical studies highlighting the association of oxidative stress with pulmonary vasculature and RV remodeling in chronic PH. Targeting oxidative stress promises to be an effective therapeutic strategy for the treatment of RV failure.

Keywords: oxidative stress, right ventricle, pulmonary hypertension, remodeling, RV failure

PULMONARY HYPERTENSION AND ITS EFFECTS ON THE RIGHT VENTRICLE

Pulmonary hypertension (PH) is characterized by an average mean pulmonary artery pressure of 25 mmHg or greater at rest. Long standing right ventricular (RV) pressure overload in PH leads to RV hypertrophy and eventually RV failure and death (Grosse et al., 2017). Early detection of PH can lead to a better prognosis and increase in the average survival rate (McLaughlin, 2013).

Considering healthy pulmonary circulation maintains low pressure compared to the systemic circulation, the RV walls are thinner and less resilient than the left ventricular (LV) walls (Badano et al., 2010). In response to chronic pressure overload due to PH, the RV undergoes adaptations including myocardial hypertrophy, followed by contractile impairment, and activation of myocardial renin-angiotensin-aldosterone system. Despite all these adaptations, RV may still exhibit dysfunction due to afterload mismatch. This RV dysfunction can be attributed to a reduced cardiac output, and functional tricuspid regurgitation. As hypertrophy and dilation continue to affect the RV, the RV becomes more spherical and its cross-sectional area enlarges, and the interventricular septum flattens; ultimately causing LV dysfunction (Badano et al., 2010; **Figure 1**).

PULMONARY HYPERTENSION-INDUCED RIGHT VENTRICULAR HYPERTROPHY

Right ventricular hypertrophy (RVH) is an adaptive transformation in the RV tissue that is usually triggered by chronic pressure overload. This pressure overload can result from stenotic valvular heart diseases or more commonly, pulmonary vascular disease associated with PH (Ikeda et al., 2014; Avazmohammadi et al., 2017). Pressure overload induces different responses in the LV and the RV due to their differing embryonic formations. Both chambers typically start developing at a 3.5 mm thickness prenatally but will grow at different rates after birth. The RV will grow to a 4 mm thickness while the LV quadruples in size to about 11 mm (Ryan and Archer, 2014). Thus in order to accommodate for the higher chronic pulmonary arterial pressures that accompany the different types of PH, these two relative thicknesses will change.

Right ventricular cardiac output depends on the synchronization between the force of contractile myocytes and the resistance to the blood flow through the pulmonary system. Normally, the RV can accommodate large but acute changes in volume loading during high levels of physical exercise, for example. However, there is a limited contractile reserve to keep the ejection fraction at homeostatic levels. In clinical cases and pre-clinical studies of animal models, the dilation of the RV is proportional to the severity of the adjacent vascular pressures (Watts et al., 2010). Hence, as afterload increases, the RV must significantly increase in size in order to maintain a suitable stroke volume. As a result, the naturally low pressure and elastic RV becomes large and inelastic, pushing on the interventricular septum to subsequently decrease the size of the LV (see **Figure 1**).

Some patients can live for years with adaptive RV hypertrophy by overcoming the high pressures, but when the RV becomes maladaptive, the complications follow soon afterward. Despite numerous studies highlighting the structural and functional changes of the RV secondary to PH, the transcriptomic profile, and molecular pathways that regulate these changes in the RV are not well studied (Lahm et al., 2018). For example, regulators such as extracellular ubiquitin, STAT3, Nrf2, and Ang-2/Tie-2 have all been identified as angiogenic regulators that contribute to LV morphological change, but it is not known whether these same pathways are regulating the RV as well (Lahm et al., 2018).

RIGHT VENTRICULAR FAILURE SECONDARY TO CHRONIC PULMONARY HYPERTENSION

Right ventricular function is the leading prognostic determinant of survival in PH patients. For example, 5-year survival in patients with pulmonary arterial hypertension (PAH) is strongly correlated with RV ejection fraction (RVEF) compared to pulmonary artery pressures or pulmonary vascular resistance (van de Veerdonk et al., 2011). However, there is no true definition for right ventricular failure (RVF) as it clinically varies from case to case and the therapeutic options for RVF are very limited. Recently, the American Thoracic Society defined RVF as "*a complex clinical syndrome characterized by insufficient delivery of blood from the RV in the setting of elevated systemic venous pressure at rest or exercise.*" This widespread phenomenon (affecting nearly 70 million in the United States alone) is a direct result of RV hypertrophy as the overworked myocytes experience increased afterload and lose their contractility (van de Veerdonk et al., 2011). While RV hypertrophy is just the initial compensatory mechanism for high pulmonary vascular pressures, RVF takes effect once the hypertrophy becomes maladaptive.

ROLE OF OXIDATIVE STRESS IN THE LUNGS AND PULMONARY VASCULATURE IN PULMONARY HYPERTENSION

Oxidative stress occurs when the number of reactive oxygen species (ROS) exceeds that which the biological system can combat and neutralize. ROS are oxygen containing molecules with an odd number of electrons, termed free radicals. These free radicals can oxidize molecules, such as lipids and DNA, causing a multitude of harmful effects. The pulmonary vasculature undergoes morphological changes in PH that can be mediated by oxidative stress. Past research has shown the expression of various oxidative stress markers changes in the lungs and pulmonary vasculature of animals and humans with PH.

In animal studies, Xu et al. (2011) found that increased oxidative stress contributes to the PH development in rodents. In normal conditions, extracellular superoxide dismutase (SOD3) is expressed in high concentrations in the lungs and is responsible for removing extracellular superoxide anions, a type of free radical contributing to oxidative stress. The absence of SOD3 resulted in significantly worse PH in hypoxic SOD3 knockout mice and MCT rats with a SOD3 loss-of-function gene mutation (Xu et al., 2011). In another study, Wang L. et al. (2017) examined the effects of 17β-estradiol and 2-methoxyestradiol on the oxidative stress-hypoxia inducible factor-1 (OS-HIF-1) pathway in rats with hypoxia-induced PH. Hypoxic rats had a significant increase in oxidative stress levels as indicated by increased serum ROS levels, decreased serum SOD, and decreased manganese SOD (MnSOD) levels. Furthermore, MnSOD mRNA and protein levels were decreased in the lung tissue (Wang L. et al., 2017).

Bertoli et al. (2018) investigated the effects of chronic iron-overload on the resistance pulmonary arteries in rats. They found that rats treated with a high dose of iron dextran demonstrated increased vasoconstriction and vascular hyper-reactivity and reduced NO which were reversed by antioxidant therapy (Bertoli et al., 2018). Hoshikawa et al. (2001) found that the free radical phosphatidylcholine hydroperoxide (PCOOH) increased within 7 days following hypoxic exposure in rat lungs, and treating the rats with antioxidant N-acetylcysteine resulted in suppression of lung PCOOH levels. The activity of xanthine oxidase (XO), an enzyme that generates ROS, was also increased in rat lung

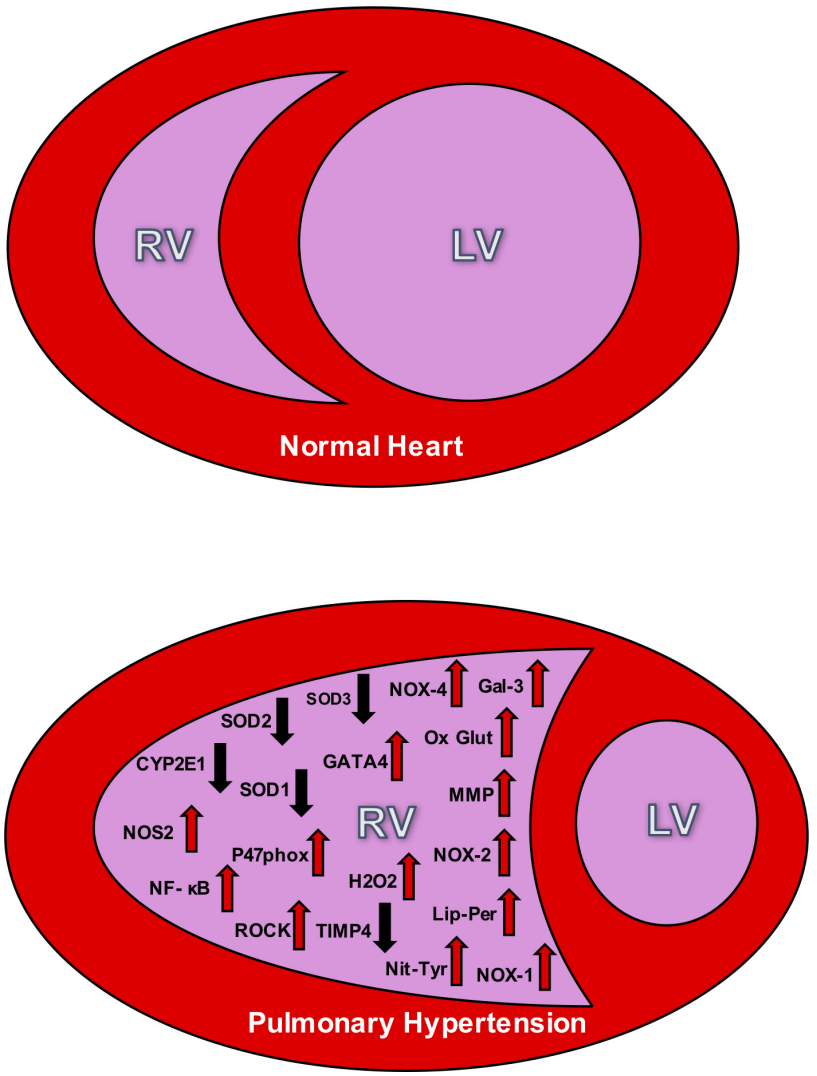

FIGURE 1 | The **top** panel depicts the relative size difference between the right ventricle (RV) and the left ventricle (LV) in a normal heart. The **bottom** panel shows the effect of RV hypertrophy and the change in structure that accompanies PH. This **bottom** figure also illustrates the oxidative stress markers seen in the RV during PH. The up arrows signify increases in the markers during PH, and down arrows signify decreases. NOX, NADPH oxidase; SOD, superoxide dismutase; NOS, nitric oxide synthase; Ox Glut, oxidized glutathiones; TIMP, tissue inhibitor of metalloproteinase; MMP, matrix metalloproteinase; ROCK, Rho kinase; H_2O_2, peroxide; Lip-Per, lipid peroxidation; Nit-Tyr, nitrotyrosine. Sources: Gal 3 (He), NOX-4 (He, Cowley, Li), SOD3 (Zelko), SOD2 (Maron), SOD 1 (Cowley), GATA4 (Park and Suzuki), CYP2EI (Potus), NOS2 (Dunlop), NF- κB (Boehm), oxidized glutathiones (Wang, Türck), nitrotyrosine (Qipshidze, Demarco), TIMP4 (Qipshidze), MMP (Qipshidze), NOX-2 (Ikeda,Li), p47phox (Ikeda), Rho kinase (Ikeda, Alzoubi), NOX-1 (Galhotra, Meghwani, Türck), hydrogen peroxide (Brandes), and lipid peroxidation (Puukila).

tissue over time from day 1 through day 21 of hypoxia. Treating rats with the XO inhibitor allopurinol significantly inhibited the hypoxia-induced PH and resulted in decreased lung PCOOH levels (Hoshikawa et al., 2001).

Shi et al. (2018) used Baicalein, a flavonoid with known anti-proliferative and anti-inflammatory effects, to reduce oxidative stress in the lungs in an attempt to ameliorate hemodynamic and pulmonary vascular changes associated with MCT-induced PH in rats. Baicalein treatment inhibited inflammatory biomarkers (such as IL-6, TNF-α, and IL-1β) and reduced the Bax/Bcl-2 ratio and levels of cleaved caspase-3 which led to an increase in SOD production resulting in lowered ROS and inhibition of the NF-κB pathway (Shi et al., 2018).

On review of human studies, Bowers et al. (2004) demonstrated that histological lung sections from patients with severe PH exhibited increased oxidative stress than healthy controls, and chronic prostacyclin infusion, a commonly prescribed therapy for PH, exerted an anti-inflammatory effect.

Preterm infants with persistent pulmonary hypertension of the newborn (PPHN) present distinct challenges due to their lack of antioxidant defense mechanisms. Wedgwood et al. (2019) argued that oxidant stress in PPHN results from free radical generation from underlying lung disease or from free radicals generated by supplemental oxygen. These free radicals in turn act on the NO pathway resulting in decreased cGMP levels and pulmonary vasoconstriction (Wedgwood et al., 2019).

Kikuchi et al. (2018) recently demonstrated that Selenoprotein P (SeP), an extracellular protein responsible for maintaining cellular metabolism, exhibits a 32-fold increase in human PAH-PASMCs compared with control PASMCs. They reported that SeP promoted PASMC proliferation and resistance to apoptosis through increased oxidative stress and mitochondrial dysfunction associated with dysregulated glutathione metabolism. In addition, SeP-knockout mice ($SeP^{-/-}$) exposed to chronic hypoxia demonstrated significantly reduced PH and pulmonary vascular remodeling (Kikuchi et al., 2018).

Krüppel-like factor 4 (KLF4) plays an important role in the protection of endothelial cells (ECs) by regulating vasodilation, inflammation, coagulation, and oxidative stress. In a recent study, Ban et al. (2019) demonstrated that KLF4 undergoes S-nitrosation in response to nitrosative stress in the human umbilical vein ECs, which is mediated by endothelin-1 and is inhibited by endothelin receptor antagonist Bosentan. Furthermore, they demonstrated that S-nitrosated KLF4 was significantly increased in lung tissues, along with decreased nuclear localization of KLF4 in rats with hypoxia-induced PH (Ban et al., 2019). In another study, Masri et al. (2008) hypothesized that ROS consumption of NO may contribute to low NO levels and development of PH in human lungs. They found that antioxidants, glutathione peroxidase and SOD activities were decreased in IPAH lungs compared to controls, while catalase and glutathione activities were similar among the groups (Masri et al., 2008).

In summary, there is growing evidence implicating oxidative stress in the pathogenesis of PH in pre-clinical and clinical studies. It is important to identify the expression and function of oxidative stress markers in specific cell types in the lungs and pulmonary vasculature in order to help devise novel targeted therapies.

CONTRIBUTION OF OXIDATIVE STRESS TO RV REMODELING IN PH

Oxidative stress plays a key role in pulmonary vascular remodeling, which in turn increases the RV after-load leading to RV hypertrophy and eventual RV failure (Bello-Klein et al., 2018). Additionally, it has been shown that the RV is more vulnerable to oxidative stress than the LV (Reddy and Bernstein, 2015), potentially because the RV cannot upregulate manganese superoxide dismutase expression, an enzyme that combats ROS (Shults et al., 2018).

Formation of ROS in many animal models of PH are derived from NADP oxidase activity, xanthine oxidase, and endothelial NOS. As PH progresses, circulating monocytes accumulate in the pulmonary arterioles and start to generate ROS to induce cell proliferation and fibrosis in the RV and small pulmonary arteries (Demarco et al., 2010). In an experimental model of PH induced by MCT in rats, high fat diet resulted in high levels of free radical formation in the dilated RV (Khoo et al., 2012). In Sugen-hypoxia model of PH in rats, a significant increase in oxidative stress caused cardiomyocyte deterioration. Furthermore, oxidative stress promoted perivascular fibrosis, leading to RV remodeling (Woo et al., 2017). In a rat model of angio-proliferative PH, although RV pressures were similar between males and females, males had worse RV hypertrophy, fibrosis, dysfunction, and survival compared to females. The reduced RV fibrosis in females was likely due to protection against oxidative stress as it correlated with increased caveolin-1 and decreased endothelial nitric oxide (NO) synthase-derived superoxide (Rafikova et al., 2015).

A decrease in SOD3 causes an imbalance between oxidants and antioxidants, and may therefore lead to vascular remodeling and PH. In SOD3 knockout mouse model with silica-induced PH, RV pressures were significantly higher compared to the wild type control mice (Zelko et al., 2018). The isoform SOD2 stabilizes the superoxide anion to hydrogen peroxide, which is less likely to damage the RV vasculature (Maron and Abman, 2017). Hence, the commonly used animal models of PH demonstrate association of oxidative stress markers with the changes accompanying RV remodeling.

MOLECULAR PATHWAYS ASSOCIATED WITH RV OXIDATIVE STRESS IN PULMONARY HYPERTENSION

There are several proposed pathways leading to RV oxidative stress in PH. PH creates ROS, which in turn causes carbonylation of annexin A1 protein that results in its degradation by proteasomes in the RV. Annexin A1 is an inhibitor of CBF/NF-Y, a transcription factor that functions to activate the GATA4 gene. The GATA4 gene is a regulator of hypertrophy in the RV. In animal models of PH, increased GATA4 expression in the RV has been observed (Park et al., 2010; Suzuki and Shults, 2017). In an RV transcriptomic analysis of MCT-induced PH in Sprague-Dawley rats, Annexin A1 was identified to be dysregulated. Furthermore, the transcriptomic analysis of the RV showed that CYP2El, a gene that combats oxidative stress, is downregulated in PH (Potus et al., 2018).

When the RV experiences pressure overload, it uses NO to decrease the afterload by promoting pulmonary vasodilation. NO synthase 2 (NOS2) is induced in cardiac fibroblasts under RV pressure overload. Induction of NOS2 has been associated with collagen formation, which causes fibrosis in the RV and impaired function. Oxidative stress and cytokines which are elevated in PH, result in increased NF-κB expression. The NOS2 promotor has a NF-κB binding site that promotes transcription of NOS2. This creates oxidative stress, ROS formation, and eventual collagen deposition, which leads to fibrotic formation in the RV (Boehm et al., 2018).

Galectin-3 (Gal-3), a biomarker for LV remodeling, has been shown to interact with NOX4-derived oxidative stress promoting cardiac fibrosis in the RV in PH patients (He et al., 2017). Budas et al. (2018) studied the effects of inhibition of redox-sensitive apical MAPK and apoptosis signal-regulating kinase 1 (ASK1) on RV remodeling in rats with PH. Inhibiting ASK1 reduced remodeling of the pulmonary vasculature and the RV. ASK1 inhibitor, GS-444217 was shown to improve cardiac function and reduce fibrosis. GS-444217 decreased phosphorylation of

p38 and JNK (c-Jun N-terminal kinase), and reduced cardiac fibroblast activation. Fibrosis formation causes a further increase in the severity of symptoms in PH patients. In a study by Wang X. et al. (2017) rats with Sugen-induced PH developed RV hypertrophy with increased levels of oxidized glutathiones, xanthine, and uric acid in the RV, which suggested higher production of ROS by xanthine oxidase. Also, there was a 30-fold lower level of antioxidant α-tocopherol nicotinate in the RV (Wang X. et al., 2017).

Glucose-6-phosphate (G6P) dehydrogenase is a major source of NADP which is a substrate for NADP oxidase in the RV. If G6P is inhibited, it reduces hypertrophy in the RV. One possible inhibitor of G6P is a 17-ketosteroid called Dehydroepiandrosterone, which was also shown to improve LV diastolic function (Rawat et al., 2014).

Oxidative stress generates nitrotyrosine residues in tissue inhibitor of metalloproteinase (TIMPs) which frees active martix metalloproteinase (MMP). It was hypothesized that the imbalance in MMP to TIMP causes fibrosis and ultimately RVF. It was found that folic acid did increase TIMP-4 and decreased different isoforms of MMPs. In pulmonary arterial constriction models, this was the opposite where TIMP-4 was decreased and MMP was increased. As a result, folic acid decreased levels of ROS in the RV wall, interstitial fibrosis, and RV pressures affirming the correlation between the oxidative stress and the RVF through the MMP to TIMP ratio (Qipshidze et al., 2012).

Ikeda et al. (2014) measured expression levels of oxidative stress related genes in the RV 24 h after pulmonary arterial constriction. Oxidative stress genes, such as p47phox and NOX2, were upregulated in the RV. Rho kinase (ROCK2) was rapidly induced after pulmonary arterial constriction in the RV free wall. In dominant negative Rho kinase mice, there was no presence of oxidative species. The timing between these steps are significant because it illustrates a correlation between Rho kinase, high pressures in the RV, and oxidative species (Ikeda et al., 2014). A possible treatment for Rho kinase overexpression is dehydroepiandrosterone (DHEA), a steroid, which has been shown to decrease NADPH levels in the RV. DHEA reduced the activity of Rho kinase, which in turn resulted in reduction of active forms of STAT3 and NFATc3 leading to rescue of RV remodeling. Overall the antioxidant activity of DHEA preserved contractility and slightly reduced high RVSP resulting from PH (Alzoubi et al., 2013).

A study by Dunlop et al. (2014) previously found that extended exposure to inhaled NO and chronic hypoxia causes a complete RV systolic dysfunction. A follow up study was done using therapeutic hypercapnia (10% CO2) in order to block the Interleukin (IL)-1α pathway which in turn inhibits NOS-2. This causes a complete normalization of RV hypertrophy (Dunlop et al., 2014). Chovanec et al. (2009) theorized another mechanism of hypercapnia, in which the release of oxygen radicals and NO are directly inhibited while in a hypoxic environment. In summary, there are multiple pathways leading to generation of oxidative stress in the RV secondary to pressure overload (see **Table 1** for summary of pathways).

TARGETING OXIDATIVE STRESS IN RV REMODELING ASSOCIATED WITH PULMONARY HYPERTENSION

Pharmacological Treatments

A number of therapeutic strategies have been tested to alleviate the effects of oxidative stress in PH. Antioxidants are the primary agents that inhibit oxidation of biomolecules by ROS. However, oxidative stress regulation in the RV can be controlled by epigenetics, and a diverse group of protein interactions. Therefore solely administering antioxidants in bulk amounts is unlikely to be effective (Suzuki and Shults, 2017).

Many new therapies have been tested that simultaneously ameliorate the effects of both oxidative stress and PH. Dihydroartemisinin (DHA), an agent that has anti-inflammatory, anti-malaria, and anti-tumor effects has been shown to reduce the symptoms of MCT-induced PH. DHA inhibits pulmonary arterial EC proliferation and reduces oxidative stress by increasing SOD expression and reducing ROS (Yu et al., 2018). PPARα agonist fenofibrate (FF) is another discovered therapy against oxidative stress and PH. In MCT-induced PH rats, FF was orally administered to the rats 3-days post MCT. FF reduced RV hypertrophy, oxidative stress, ROS, NADPH Oxidase (NOX-1) expression, and increased the Bcl2/Bax ratio in the RV that was caused by PH (Galhotra et al., 2018). Trapidil, a vasodilator, has also been shown to mitigate the effects of oxidative stress and PH. Increased lipid and glutathione peroxidation as well as an increase in RV diameter has been reported in MCT model of PH in Wistar rats. Trapidil reduced NOX-1 activity, reduced glutathione oxidation in the RV, and reduced the diameter of the RV (Türck et al., 2018). Rats treated with high doses of iron caused pathological remodeling in the RV. The oxidative stress that causes the hypertrophy was mediated by Angiotensin II Type 1 receptor (AT1). An AT1 antagonist was administered orally and was shown to restore vascular function (Bertoli et al., 2018). It has been shown that α1-adrenergic receptor (α1-AR) antagonist A61603 improves left ventricular failure. In the bleomycin model of RV failure, A61603 increased cellular SOD1 and decreased NOX4, myocyte necrosis, and fibrosis in the RV (Cowley et al., 2017). Pterostilbene (PTS), a phytophenol, paired with hydroxypropyl-β-cyclodextrin (HPβCD) at high doses completely prevents RV failure and hypertrophy caused by PH, while protecting systolic function by reducing NADPH oxidase-dependent superoxide anions (Dos Santos Lacerda et al., 2017).

According to a study by Zimmer et al. (2017) it was initially believed that aerobic exercise would increase RV function in MCT-induced PH rats. However, they found no change in oxidative stress due to stable levels of eNOS activity (Zimmer et al., 2017). Contrary to the findings from Zimmer et al. (2017) aerobic exercise has been shown to promote hydrogen peroxide and vascular endothelial growth factor which ultimately improve RV function, in spite of ROS created by hydrogen peroxide. However, it is not specified if other antioxidant markers are associated with aerobic exercise (Colombo et al., 2016). In addition, aerobic exercise at early stages of PH decreases mitochondrial oxidative stress, demonstrating cardioprotective

TABLE 1 | Mechanistic pathways for the regulatory oxidative markers found in the right ventricle (RV) of pulmonary hypertension (PH) models.

Oxidative stress marker	PH induction method	Pathways in the right ventricle	Source
↑Nit-Tyr, ↑MMP, and ↓TIMP-4	Pulmonary artery constriction	RV-pressure overload by pulmonary arterial constriction → Increased ROSs → Oxidative stress generates nitrotyrosine residues in TIMPs → Increase in MMP, decrease in TIMP-4 → Mitophagy → RVF	Qipshidze et al., 2012
↑GATA4	Chronic hypoxia	PH → Pressure overload → ROS → Carbonylation of Annexin A1 → Annexin A1 degraded by proteasome → Annexin A1 no longer inhibits CBF/NFY → GATA4 activated → RV hypertrophy	Park et al., 2010; Suzuki and Shults, 2017
↑p47phox, ↑NOX-2, and ↑ROCK	Pulmonary artery constriction	Pulmonary arterial constriction → Upregulation of p47phox, NOX-2, and ROCK → ROCK leads to RV dysfunction	Ikeda et al., 2014
↑Gal-3 and ↑NOX4	MCT	Gal-3, NOX4, and NOX4 derived oxidative stress significantly elevated in PH → Gal-3 interacts with NOX4 and NOX4 derived oxidative stress and mediates TGF-β1-induced cardiac fibrosis → RV remodeling	He et al., 2017
↑NOS2 and ↑NF-κβ	Pulmonary artery banding	Pressure overloaded RV → NF-κβ regulates NOS2 transcription → NOS2 induction → ROS formation → collagen deposition from fibroblasts → RV hypertrophy and dilation	Boehm et al., 2018
↑Ox Glut	Sugen5416 + ovalbumin immunization	↑Pulmonary arterial pressure from Sugen5416 injection and ovalbumin immunization → increase in RV oxidized glutathione, xanthine and uric acid → ROS production by xanthine oxidase → RV failure	Wang X. et al., 2017
↑Lip-Per	MCT	→Pulmonary arterial pressure from MCT → Increase in ROS → Lipid Peroxidation and RV hypertrophy	Puukila et al., 2017
↑NOX-1, ↑Ox-Glut, and ↑Lip-Per	MCT	MCT induced PH → Increase in NOX-1, Ox Glut, and Lip-Per → Increased diameter of RV with impaired contractile function	Türck et al., 2018

Nit-Tyr, nitrotyrosine; MMP, matrix metalloproteinase; TIMP, tissue inhibitor of metalloproteinase; NOX, NADPH oxidase; ROCK, Rho kinase; NOS, nitric oxide synthase; Ox Glut, oxidized glutathiones; Lip-Per, lipid peroxidation.

effects (Moreira-Gonçalves et al., 2015). Each study focused on a different oxidative stress marker, which led them to different conclusions on the effect of exercise on oxidative damage. However, all three studies have shown that RV hypertrophy is unaffected by aerobic exercise.

EUK-134, a known antioxidant, reduced cardiomyocyte hypertrophy and decreased end systolic volume in MCT-induced PH rats (Redout et al., 2010). Thus, this was one of the first studies that demonstrated the importance of ROS in contractile dysfunction due to PH and how antioxidants such as EUK-134 can be used for PH treatment.

Herbal Treatments

Many of the novel therapies used to target oxidative stress and PH simultaneously, are derived from natural herbs and plants. One such therapy that showed similar effects to FF is ocimum sanctum (OS), a plant predominantly found in India. Similar to FF treatment, OS has shown a decrease in both RV hypertrophy and NOX-1 expression and an increase in Bcl2/Bax ratio in the RV tissue (Meghwani et al., 2018). The stem bark of a plant called Terminalia arjuna and Carvacrol, an oil in oregano and thyme, was also used to increase the Bcl2/Bax ratio in the pulmonary artery SMC (Zhang et al., 2016; Meghwani et al., 2017). Similar to the previously mentioned therapies, Copaiba oil has also been shown to decrease RV hypertrophy, and reduce oxidation of proteins and lipids in the RV of the MCT group (Campos-Carraro et al., 2018). In hypoxia-induced PH rats, Trimethoxystilbene (a novel polypehnol found in grapes and red wine with known anti-inflammatory effects) treatment prevented RVH by inhibiting the NOX/VPO1 pathway that mediates oxidative stress (Liu et al., 2014). NOX and VPO1 work together to cause higher levels of peroxide, which leads to smooth muscle cell proliferation (Brandes, 2011).

Grape seed procyanidin extract (GSPE) has been shown to prevent hypoxia-induced PH through antioxidant properties resulting in decreased RVSP and RV dilation. GSPE increased SOD and decreased NOX4 mRNA levels simultaneously, which decreased ROS production in pulmonary arterial SMC (Jin et al., 2016). Sesamin, an extract from sesame seeds, was used to inhibit NOX2 and NOX4 in the pulmonary vessels. This consequentially lowered RVSP and RV hypertrophy index (Li et al., 2015). The decrease of NOX4 and increase of SOD1 balances the antioxidant imbalance caused by PH. Secoisolariciresinol diglucoside (SDG), derived from flaxseed, was given to MCT rats with RV hypertrophy and increased lipid peroxidation. It did not decrease RV hypertrophy, however, it decreased ROS levels and SOD activity in the RV. When rats were pretreated with SDG, it was more effective in decreasing RV dysfunction (Puukila et al., 2017). When MCT rats were treated with Withania somnifera, a clinical antioxidant, oxidative markers such as levels of ROS were decreased in the lungs, which led to decreased RVSP (Kaur et al., 2015). The therapeutic effects of protandim, which enables Nrf2 to upregulate the expression of genes that code for antioxidants, were examined in Su/Hx model in rats. Protandim was found only to protect against RV failure, without affecting other PH symptoms like angio-obliteration caused by PH (Voelkel et al., 2013). This is important because a well-functioning RV is an important prognostic indicator of survival in PH patients.

In summary, there is a growing body of evidence demonstrating the association of oxidative stress to the

development of RV remodeling in PH. Investigators have tested novel therapies targeting oxidative stress markers and molecular pathways to treat experimental RV failure. Further pre-clinical and clinical research is needed to validate the efficacy of these experimental therapies for targeting RV oxidative stress in PH.

PAST FAILURES OF ANTIOXIDANT PH THERAPIES IN THE RV AND LUNGS

A variety of antioxidant therapies have been tested for the treatment of pre-clinical PH. Some studies have focused on targeting oxidative stress in the lungs, whereas others have focused more on the effects of antioxidant therapies in the RV. RV failure is the primary cause of death in PH patients, and although treatment of patients with vasodilator antioxidants may reduce pulmonary vascular resistance, this effect may not be accompanied by improvements in the RV (Drake et al., 2013).

Antioxidant therapies targeting the lungs and RV in PH have shown prior failures. NO can modulate cellular and physiological processes to limit oxidative stress. Saugstad (2000) argued that NO can act as an antioxidant and pro-oxidant depending on the dose of NO administered and the presence of other oxidants. Previous rat studies found that NO in high concentrations induces free radical mediated injury in rat lungs. Oxidative stress was only partially treated in the hyperoxic condition, which in itself, helped exacerbate the disease (Saugstad, 2000). L-arginine, a substrate needed to produce endogenous NO was studied to see whether it prevents RV and pulmonary vascular hypertrophy in hypoxic rats. Long term oral L-arginine failed to prevent RV and pulmonary vascular hypertrophy in the rats with hypoxia-induced PH (Laursen et al., 2008). Horstman et al. (1998) used a direct administration of low concentrations of inhaled NO and found that inhaled NO attenuates RV hypertrophy and vascular remodeling secondary to hypoxia, but has no such effects in MCT-induced PH. This shows that the effectiveness of inhaled NO in attenuating remodeling in PH is dependent on the mechanism by which PH was induced. Another group also found mechanism-dependent results when they looked to make a determination between vasodilator doses of inhaled NO and the prevention of progression of PH in MCT rats. In MCT-induced PH, there was a decrease in pulmonary artery pressure. However, in chronic hypoxic conditions inhaled NO did not prevent development of PH with no changes in the RV (Maruyama et al., 1997).

The use of continuous inhalation of NO as a treatment was also used in a study of rats exposed to chronic hypoxia followed by normoxia, but there was no effect on alleviating pulmonary vascular remodeling in the PH lungs (Jiang et al., 2004). Prior studies on the umbilical vein endothelial cells led to the belief that NO can decrease malignant ET-1 overexpression which in theory should minimize the effects of oxidative stress. However, in a group of rats with hypoxia induced PH, investigators found that NO had no impact on the increased ET-1 expression in rat lungs with PH induced by hypoxic conditions (Earley et al., 2002).

A novel attempt at using the administration of chronic oxygen, instead of NO, was used as a possible antioxidant therapy for PH. However, results showed that the high influx of oxygen resulted in increased RV inflammation, pulmonary arterial hypertrophy, and SOD activity. Rats that received MCT and oxygen therapy recruited leukocytes that promoted RV inflammation and failure. And despite increases in SOD activity, antioxidants were not able to sufficiently counteract the oxidative stress caused by the combination of MCT and chronic oxygen therapy (Fujita et al., 2018).

As discussed earlier in this review, protandim which upregulates the expression of genes encoding antioxidants such as SOD and heme oxygenase-1 (HO-1), was found only to protect against RV failure, without affecting pulmonary vascular angioobliterative lesions caused by PH. The authors argued that antioxidants may affect pulmonary vascular remodeling when administered early during the development of the pulmonary vascular lesions while antioxidants may impact RV failure even late in the disease process (Voelkel et al., 2013).

Several studies have demonstrated the efficacy of statins in experimental models of PH, by reducing oxidative stress and inflammation, inhibiting PASMC proliferation, and inducing PASMC/PAEC apoptosis and vasodilatation (Nishimura et al., 2002, 2003; Taraseviciene-Stewart et al., 2006; Girgis et al., 2007). These results were also supported by observational studies in PH patients (Kao, 2005; King and Day, 2011). However, a phase-II randomized clinical trial of aspirin and simvastatin for PAH (ASA-STAT) failed to demonstrate a significant effect on the six-minute walk distance between simvastatin and placebo groups (Kawut et al., 2011).

To summarize, although antioxidants have shown promise in the treatment of experimental PH and RV failure, there have been reports of failure of some of these therapies. Understanding the precise role of oxidative stress in the pathogenesis and progression of PH and RV failure will help in developing targeted and effective antioxidant therapies.

CONCLUSION

Long standing PH leads to RV hypertrophy and RV failure. Accumulating evidence suggests involvement of oxidative stress in the development and progression of RV remodeling associated with PH. Targeting RV oxidative stress associated with PH may lead to the development of novel therapies for RV failure secondary to PH.

AUTHOR CONTRIBUTIONS

MM, CM, AW, TL, and ME contributed in drafting and revising the manuscript. SU contributed in drafting and revising the manuscript, and provided the supervision.

FUNDING

SU was supported by a Mentored Research Training Grant from the Foundation of Anesthesia Education and Research (FAER) and a K08 Grant (1K08 HL141995 01A1) from the NIH (NHLBI).

REFERENCES

Alzoubi, A., Toba, M., Abe, K., O'Neill, K. D., Rocic, P., Fagan, K. A., et al. (2013). Dehydroepiandrosterone restores right ventricular structure and function in rats with severe pulmonary arterial hypertension. *Am. J. Physiol. Heart Circ. Physiol.* 304, H1708–H1718. doi: 10.1152/ajpheart.00746.2012

Avazmohammadi, R., Hill, M., Simon, M., and Sacks, M. (2017). Transmural remodeling of right ventricular myocardium in response to pulmonary arterial hypertension. *APL Bioeng.* 1:016105. doi: 10.1063/1.5011639

Badano, L. P., Ginghina, C., Easaw, J., Muraru, D., Grillo, M. T., Lancellotti, P., et al. (2010). Right ventricle in pulmonary arterial hypertension: haemodynamics, structural changes, imaging, and proposal of a study protocol aimed to assess remodelling and treatment effects. *Eur. J. Echocardiogr.* 11, 27–37. doi: 10.1093/ejechocard/jep152

Ban, Y., Liu, Y., Li, Y., Zhang, Y., Xiao, L., Gu, Y., et al. (2019). S-nitrosation impairs KLF4 activity and instigates endothelial dysfunction in pulmonary arterial hypertension. *Redox Biol.* 21:101099. doi: 10.1016/j.redox.2019.101099

Bello-Klein, A., Mancardi, D., Araujo, A. S., Schenkel, P. C., Turck, P., and de Lima Seolin, B. G. (2018). Role of redox homeostasis and inflammation in the pathogenesis of pulmonary arterial hypertension. *Curr. Med. Chem.* 25, 1340–1351. doi: 10.2174/0929867325666171226114838

Bertoli, S. R., Marques, V. B., Rossi, E. M., Krause, M., Carneiro, M. T. W. D., Simões, M. R., et al. (2018). Chronic iron overload induces vascular dysfunction in resistance pulmonary arteries associated with right ventricular remodeling in rats. *Toxicol. Lett.* 295, 296–306. doi: 10.1016/j.toxlet.2018.07.010

Boehm, M., Novoyatleva, T., Kojonazarov, B., Veit, F., Weissmann, N., Ghofrani, H. A., et al. (2018). Nitric oxide synthase 2 induction promotes right ventricular fibrosis. *Am. J. Respir. Cell Mol. Biol.* 60, 346–356. doi: 10.1165/rcmb.2018-0069OC

Bowers, R., Cool, C., Murphy, R. C., Tuder, R. M., Hopken, M. W., Flores, S. C., et al. (2004). Oxidative stress in severe pulmonary hypertension. *Am. J. Respir. Crit. Care Med.* 169, 764–769. doi: 10.1164/rccm.200301-147OC

Brandes, R. P. (2011). Vascular peroxidase 1/peroxidasin: a complex protein with a simple function? *Cardiovasc. Res.* 91, 1–2. doi: 10.1093/cvr/cvr120

Budas, G. R., Boehm, M., Kojonazarov, B., Viswanathan, G., Tian, X., Veeroju, S., et al. (2018). ASK1 inhibition halts disease progression in preclinical models of pulmonary arterial hypertension. *Am. J. Respir. Crit. Care Med.* 197, 373–385. doi: 10.1164/rccm.201703-0502OC

Campos-Carraro, C., Turck, P., de Lima-Seolin, B. G., Tavares, A. M. V., Dos Santos Lacerda, D., Corssac, G. B., et al. (2018). Copaiba oil attenuates right ventricular remodeling by decreasing myocardial apoptotic signaling in monocrotaline-induced rats. *J. Cardiovasc. Pharmacol.* 72, 214–221.

Chovanec, M., Novotná, J., Wilhelm, J., Hampl, V., Vízek, M., and Herget, J. (2009). Hypercapnia attenuates hypoxic pulmonary hypertension by inhibiting lung radical injury. *Physiol. Res.* 58(Suppl. 2), S79–S85.

Colombo, R., Siqueira, R., Conzatti, A., de Lima Seolin, B. G., Fernandes, T. R. G., Godoy, A. E. G., et al. (2016). Exercise training contributes to H2O2/VEGF signaling in the lung of rats with monocrotaline-induced pulmonary hypertension. *Vascul. Pharmacol.* 87, 49–59. doi: 10.1016/j.vph.2016.06.006

Cowley, P. M., Wang, G., Joshi, S., Swigart, P. M., Lovett, D. H., Simpson, P. C., et al. (2017). α1A-Subtype adrenergic agonist therapy for the failing right ventricle. *Am. J. Physiol. Heart Circ. Physiol.* 313, H1109–H1118. doi: 10.1152/ajpheart.00153.2017

Demarco, V. G., Whaley-Connell, A. T., Sowers, J. R., Habibi, J., and Dellsperger, K. C. (2010). Contribution of oxidative stress to pulmonary arterial hypertension. *World J. Cardiol.* 2, 316–324. doi: 10.4330/wjc.v2.i10.316

Dos Santos Lacerda, D., Türck, P., Gazzi de Lima-Seolin, B., Colombo, R., Duarte Ortiz, V., Poletto Bonetto, J. H., et al. (2017). Pterostilbene reduces oxidative stress, prevents hypertrophy and preserves systolic function of right ventricle in cor pulmonale model. *Br. J. Pharmacol.* 174, 3302–3314. doi: 10.1111/bph.13948

Drake, J. I., Gomez-Arroyo, J., Dumur, C. I., Kraskauskas, D., Natarajan, R., Bogaard, H. J., et al. (2013). Chronic carvedilol treatment partially reverses the right ventricular failure transcriptional profile in experimental pulmonary hypertension. *Physiol. Genomics* 45, 449–461. doi: 10.1152/physiolgenomics.00166.2012

Dunlop, K., Gosal, K., Kantores, C., Ivanovska, J., Dhaliwal, R., Desjardins, J.-F., et al. (2014). Therapeutic hypercapnia prevents inhaled nitric oxide-induced right-ventricular systolic dysfunction in juvenile rats. *Free Radic. Biol. Med.* 69, 35–49. doi: 10.1016/j.freeradbiomed.2014.01.008

Earley, S., Nelin, L. D., Chicoine, L. G., and Walker, B. R. (2002). Hypoxia-induced pulmonary endothelin-1 expression is unaltered by nitric oxide. *J. Appl. Physiol.* 92, 1152–1158. doi: 10.1152/japplphysiol.00829.2001

Fujita, N., Yamasaki, N., Eto, K., Asaeda, M., Kuwahara, W., and Imagita, H. (2018). Oxygen therapy may worsen the survival rate in rats with monocrotaline-induced pulmonary arterial hypertension. *PLoS One* 13:e0204254. doi: 10.1371/journal.pone.0204254

Galhotra, P., Prabhakar, P., Meghwani, H., Mohammed, S. A., Banerjee, S. K., Seth, S., et al. (2018). Beneficial effects of fenofibrate in pulmonary hypertension in rats. *Mol. Cell. Biochem.* 449, 185–194. doi: 10.1007/s11010-018-3355-3

Girgis, R. E., Mozammel, S., Champion, H. C., Li, D., Peng, X., Shimoda, L., et al. (2007). Regression of chronic hypoxic pulmonary hypertension by simvastatin. *Am. J. Physiol. Lung. Cell Mol. Physiol.* 292, L1105–L1110.

Grosse, A., Grosse, C., and Lang, I. M. (2017). Distinguishing chronic thromboembolic pulmonary hypertension from other causes of pulmonary hypertension using CT. *Am. J. Roentgenol.* 209, 1228–1238. doi: 10.2214/AJR.17.17871

He, J., Li, X., Luo, H., Li, T., Zhao, L., Qi, Q., et al. (2017). Galectin-3 mediates the pulmonary arterial hypertension-induced right ventricular remodeling through interacting with NADPH oxidase 4. *J. Am. Soc. Hypertens.* 11, 275–289.e2. doi: 10.1016/j.jash.2017.03.008

Horstman, D. J., Frank, D. U., and Rich, G. F. (1998). Prolonged inhaled NO attenuates hypoxic, but not monocrotaline-induced, pulmonary vascular remodeling in rats. *Anesth. Analg.* 86, 74–81. doi: 10.1097/00000539-199801000-00015

Hoshikawa, Y., Ono, S., Suzuki, S., Tanita, T., Chida, M., Song, C., et al. (2001). Generation of oxidative stress contributes to the development of pulmonary hypertension induced by hypoxia. *J. Appl. Physiol.* 90, 1299–1306. doi: 10.1152/jappl.2001.90.4.1299

Ikeda, S., Satoh, K., Kikuchi, N., Miyata, S., Suzuki, K., Omura, J., et al. (2014). Crucial role of rho-kinase in pressure overload-induced right ventricular hypertrophy and dysfunction in mice. *Arterioscler. Thromb. Vasc. Biol.* 34, 1260–1271. doi: 10.1161/ATVBAHA.114.303320

Jiang, B. H., Maruyama, J., Yokochi, A., Iwasaki, M., Amano, H., Mitani, Y., et al. (2004). Prolonged nitric oxide inhalation fails to regress hypoxic vascular remodeling in rat lung. *Chest* 125, 2247–2252. doi: 10.1378/chest.125.6.2247

Jin, H., Liu, M., Zhang, X., Pan, J., Han, J., Wang, Y., et al. (2016). Grape seed procyanidin extract attenuates hypoxic pulmonary hypertension by inhibiting oxidative stress and pulmonary arterial smooth muscle cells proliferation. *J. Nutr. Biochem.* 36, 81–88. doi: 10.1016/j.jnutbio.2016.07.006

Kao, P. N. (2005). Simvastatin treatment of pulmonary hypertension: an observational case series. *Chest* 127, 1446–1452. doi: 10.1016/s0012-3692(15)34501-3

Kaur, G., Singh, N., Samuel, S. S., Bora, H. K., Sharma, S., Pachauri, S. D., et al. (2015). Withania somnifera shows a protective effect in monocrotaline-induced pulmonary hypertension. *Pharm. Biol.* 53, 147–157. doi: 10.3109/13880209.2014.912240

Kawut, S. M., Bagiella, E., Lederer, D. J., Shimbo, D., Horn, E. M., Roberts, K. E., et al. (2011). Randomized clinical trial of aspirin and simvastatin for pulmonary arterial hypertension: ASA-STAT. *Circulation* 123, 2985–2993. doi: 10.1161/CIRCULATIONAHA.110.015693

Khoo, N. K. H., Cantu-Medellin, N., Devlin, J. E., St Croix, C. M., Watkins, S. C., Fleming, A. M., et al. (2012). Obesity-induced tissue free radical generation: an *in vivo* immuno-spin trapping study. *Free Radic. Biol. Med.* 52, 2312–2319. doi: 10.1016/j.freeradbiomed.2012.04.011

Kikuchi, N., Satoh, K., Kurosawa, R., Yaoita, N., Elias-Al-Mamun, M., Siddique, M. A. H., et al. (2018). Selenoprotein P promotes the development of pulmonary arterial hypertension. *Circulation* 138, 600–623. doi: 10.1161/CIRCULATIONAHA.117.033113

King, W. T., and Day, R. W. (2011). Treatment of pediatric pulmonary hypertension with simvastatin: an observational study. *Pediatr. Pulmonol.* 46, 261–265. doi: 10.1002/ppul.21361

Lahm, T., Douglas, I. S., Archer, S. L., Bogaard, H. J., Chesler, N. C., Haddad, F., et al. (2018). Assessment of right ventricular function in the research setting: knowledge gaps and pathways forward. An official American thoracic society research statement. *Am. J. Respir. Crit. Care Med.* 198, e15–e43. doi: 10.1164/rccm.201806-1160ST

Laursen, B. E., Dam, M. Y., Mulvany, M. J., and Simonsen, U. (2008). Hypoxia-induced pulmonary vascular remodeling and right ventricular hypertrophy is unaltered by long-term oral L-arginine administration. *Vascul. Pharmacol.* 49, 71–76. doi: 10.1016/j.vph.2008.03.001

Li, X., Gao, Y., Li, S., and Yang, J. (2015). [Effect of sesamin on pulmonary vascular remodeling in rats with monocrotaline-induced pulmonary hypertension]. *China J. Chin. Mater. Medica* 40, 1355–1361.

Liu, B., Luo, X.-J., Yang, Z.-B., Zhang, J.-J., Li, T.-B., Zhang, X.-J., et al. (2014). Inhibition of NOX/VPO1 pathway and inflammatory reaction by trimethoxystilbene in prevention of cardiovascular remodeling in hypoxia-induced pulmonary hypertensive rats. *J. Cardiovasc. Pharmacol.* 63, 567–576. doi: 10.1097/FJC.0000000000000082

Maron, B. A., and Abman, S. H. (2017). Translational advances in the field of pulmonary hypertension. Focusing on developmental origins and disease inception for the prevention of pulmonary hypertension. *Am. J. Respir. Crit. Care Med.* 195, 292–301. doi: 10.1164/rccm.201604-0882PP

Maruyama, J., Maruyama, K., Mitani, Y., Kitabatake, M., Yamauchi, T., and Miyasaka, K. (1997). Continuous low-dose NO inhalation does not prevent monocrotaline-induced pulmonary hypertension in rats. *Am. J. Physiol.* 272, H517–H524. doi: 10.1152/ajpheart.1997.272.1.H517

Masri, F. A., Comhair, S. A., Dostanic-Larson, I., Kaneko, F. T., Dweik, R. A., Arroliga, A. C., et al. (2008). Deficiency of lung antioxidants in idiopathic pulmonary arterial hypertension. *Clin. Transl. Sci.* 1, 99–106.

McLaughlin, V. (2013). Managing pulmonary arterial hypertension and optimizing treatment options: prognosis of pulmonary artery hypertension. *Am. J. Cardiol.* 111, 10C–15C. doi: 10.1016/j.amjcard.2013.01.319

Meghwani, H., Prabhakar, P., Mohammed, S. A., Dua, P., Seth, S., Hote, M. P., et al. (2018). Beneficial effect of *Ocimum sanctum* (Linn) against monocrotaline-induced pulmonary hypertension in rats. *Medicines* 5:E34. doi: 10.3390/medicines5020034

Meghwani, H., Prabhakar, P., Mohammed, S. A., Seth, S., Hote, M. P., Banerjee, S. K., et al. (2017). Beneficial effects of aqueous extract of stem bark of *Terminalia arjuna* (Roxb.), An ayurvedic drug in experimental pulmonary hypertension. *J. Ethnopharmacol.* 197, 184–194. doi: 10.1016/j.jep.2016.07.029

Moreira-Gonçalves, D., Ferreira, R., Fonseca, H., Padrão, A. I., Moreno, N., Silva, A. F., et al. (2015). Cardioprotective effects of early and late aerobic exercise training in experimental pulmonary arterial hypertension. *Basic Res. Cardiol.* 110:57. doi: 10.1007/s00395-015-0514-5

Nishimura, T., Faul, J. L., Berry, G. J., Vaszar, L. T., Qiu, D., Pearl, R. G., et al. (2002). Simvastatin attenuates smooth muscle neointimal proliferation and pulmonary hypertension in rats. *Am. J. Respir. Crit. Care Med.* 166, 1403–1408. doi: 10.1164/rccm.200203-268oc

Nishimura, T., Vaszar, L. T., Faul, J. L., Zhao, G., Berry, G. J., Shi, L., et al. (2003). Simvastatin rescues rats from fatal pulmonary hypertension by inducing apoptosis of neointimal smooth muscle cells. *Circulation* 108, 1640–1645. doi: 10.1161/01.cir.0000087592.47401.37

Park, A.-M., Wong, C.-M., Jelinkova, L., Liu, L., Nagase, H., and Suzuki, Y. J. (2010). Pulmonary hypertension-induced GATA4 activation in the right ventricle. *Hypertens* 56, 1145–1151. doi: 10.1161/HYPERTENSIONAHA.110.160515

Potus, F., Hindmarch, C. C. T., Dunham-Snary, K. J., Stafford, J., and Archer, S. L. (2018). Transcriptomic signature of right ventricular failure in experimental pulmonary arterial hypertension: deep sequencing demonstrates mitochondrial, fibrotic, inflammatory and angiogenic abnormalities. *Int. J. Mol. Sci.* 19:E2730. doi: 10.3390/ijms19092730

Puukila, S., Fernandes, R. O., Türck, P., Carraro, C. C., Bonetto, J. H. P., de Lima-Seolin, B. G., et al. (2017). Secoisolariciresinol diglucoside attenuates cardiac hypertrophy and oxidative stress in monocrotaline-induced right heart dysfunction. *Mol. Cell. Biochem.* 432, 33–39. doi: 10.1007/s11010-017-2995-z

Qipshidze, N., Tyagi, N., Metreveli, N., Lominadze, D., and Tyagi, S. C. (2012). Autophagy mechanism of right ventricular remodeling in murine model of pulmonary artery constriction. *Am. J. Physiol. Heart Circ. Physiol.* 302, H688–H696. doi: 10.1152/ajpheart.00777.2011

Rafikova, O., Rafikov, R., Meadows, M. L., Kangath, A., Jonigk, D., and Black, S. M. (2015). The sexual dimorphism associated with pulmonary hypertension corresponds to a fibrotic phenotype. *Pulm. Circ.* 5, 184–197. doi: 10.1086/679724

Rawat, D. K., Alzoubi, A., Gupte, R., Chettimada, S., Watanabe, M., Kahn, A. G., et al. (2014). Increased reactive oxygen species, metabolic maladaptation, and autophagy contribute to pulmonary arterial hypertension-induced ventricular hypertrophy and diastolic heart failure. *Hypertens* 64, 1266–1274. doi: 10.1161/HYPERTENSIONAHA.114.03261

Reddy, S., and Bernstein, D. (2015). Molecular mechanisms of right ventricular failure. *Circulation* 132, 1734–1742. doi: 10.1161/CIRCULATIONAHA.114.012975

Redout, E. M., van der Toorn, A., Zuidwijk, M. J., van de Kolk, C. W. A., van Echteld, C. J. A., Musters, R. J. P., et al. (2010). Antioxidant treatment attenuates pulmonary arterial hypertension-induced heart failure. *Am. J. Physiol. Heart Circ. Physiol.* 298, H1038–H1047. doi: 10.1152/ajpheart.00097.2009

Ryan, J. J., and Archer, S. L. (2014). The right ventricle in pulmonary arterial hypertension: disorders of metabolism, angiogenesis and adrenergic signaling in right ventricular failure. *Circ. Res.* 115, 176–188. doi: 10.1161/CIRCRESAHA.113.301129

Saugstad, O. D. (2000). Does nitric oxide prevent oxidative mediated lung injury? *Acta Paediatr. Oslo Nor.* 1992, 905–907. doi: 10.1111/j.1651-2227.2000.tb00405.x

Shi, R., Wei, Z., Zhu, D., Fu, N., Wang, C., Yin, S., et al. (2018). Baicalein attenuates monocrotaline-induced pulmonary arterial hypertension by inhibiting vascular remodeling in rats. *Pulm. Pharmacol. Ther.* 48, 124–135. doi: 10.1016/j.pupt.2017.11.003

Shults, N. V., Melnyk, O., Suzuki, D. I., and Suzuki, Y. J. (2018). Redox biology of right-sided heart failure. *Antioxidants* 7:106. doi: 10.3390/antiox7080106

Suzuki, Y. J., and Shults, N. V. (2017). Redox signaling in the right ventricle. *Adv. Exp. Med. Biol.* 967, 315–323. doi: 10.1007/978-3-319-63245-2_19

Taraseviciene-Stewart, L., Scerbavicius, R., Choe, K. H., Cool, C., Wood, K., Tuder, R. M., et al. (2006). Simvastatin causes endothelial cell apoptosis and attenuates severe pulmonary hypertension. *Am. J. Physiol. Lung. Cell. Mol. Physiol.* 291, L668–L676.

Türck, P., Lacerda, D. S., Carraro, C. C., de Lima-Seolin, B. G., Teixeira, R. B., Poletto Bonetto, J. H., et al. (2018). Trapidil improves hemodynamic, echocardiographic and redox state parameters of right ventricle in monocrotaline-induced pulmonary arterial hypertension model. *Biomed. Pharmacother.* 103, 182–190. doi: 10.1016/j.biopha.2018.04.001

van de Veerdonk, M. C., Kind, T., Marcus, J. T., Mauritz, G.-J., Heymans, M. W., Bogaard, H.-J., et al. (2011). Progressive right ventricular dysfunction in patients with pulmonary arterial hypertension responding to therapy. *J. Am. Coll. Cardiol.* 58, 2511–2519. doi: 10.1016/j.jacc.2011.06.068

Voelkel, N. F., Bogaard, H. J., Al Husseini, A., Farkas, L., Gomez-Arroyo, J., and Natarajan, R. (2013). Antioxidants for the treatment of patients with severe angioproliferative pulmonary hypertension? *Antioxid. Redox Signal.* 18, 1810–1817. doi: 10.1089/ars.2012.4828

Wang, L., Zheng, Q., Yuan, Y., Li, Y., and Gong, X. (2017). Effects of 17β-estradiol and 2-methoxyestradiol on the oxidative stress-hypoxia inducible factor-1 pathway in hypoxic pulmonary hypertensive rats. *Exp. Ther. Med.* 13, 2537–2543. doi: 10.3892/etm.2017.4243

Wang, X., Shults, N. V., and Suzuki, Y. J. (2017). Oxidative profiling of the failing right heart in rats with pulmonary hypertension. *PLoS One* 12:e0176887. doi: 10.1371/journal.pone.0176887

Watts, J. A., Marchick, M. R., and Kline, J. A. (2010). Right ventricular heart failure from pulmonary embolism: key distinctions from chronic pulmonary hypertension. *J. Card. Fail.* 16, 250–259. doi: 10.1016/j.cardfail.2009.11.008

Wedgwood, S., Steinhorn, R. H., and Lakshminrusimha, S. (2019). Optimal oxygenation and role of free radicals in PPHN. *Free Radic. Biol. Med.* doi: 10.1016/j.freeradbiomed.2019.04.001 [Epub ahead of print].

Woo, E., Kato, R., Imano, H., Fujiwara, Y., Ijiri, Y., Okada, Y., et al. (2017). Capillary degeneration and right ventricular remodeling due to hypoxic stress with Sugen5416. *Curr. Vasc. Pharmacol.* 15, 589–598. doi: 10.2174/1570161115666170427154217

Xu, D., Guo, H., Xu, X., Lu, Z., Fassett, J., Hu, X., et al. (2011). Exacerbated pulmonary arterial hypertension and right ventricular hypertrophy in animals with loss of function of extracellular superoxide dismutase. *Hypertens* 58, 303–309. doi: 10.1161/HYPERTENSIONAHA.110.166819

Yu, H., Liu, J., Dong, Y., Xu, M., Xu, L., Guan, H., et al. (2018). Anti-hypoxic effect of dihydroartemisinin on pulmonary artery endothelial cells. *Biochem. Biophys. Res. Commun.* 506, 840–846. doi: 10.1016/j.bbrc.2018.10.176

Zelko, I. N., Zhu, J., and Roman, J. (2018). Role of SOD3 in silica-related lung fibrosis and pulmonary vascular remodeling. *Respir. Res.* 19:221. doi: 10.1186/s12931-018-0933-6

Zhang, Q., Fan, K., Wang, P., Yu, J., Liu, R., Qi, H., et al. (2016). Carvacrol induces the apoptosis of pulmonary artery smooth muscle cells under hypoxia. *Eur. J. Pharmacol.* 770, 134–146. doi: 10.1016/j.ejphar.2015.11.037

Zimmer, A., Teixeira, R. B., Bonetto, J. H. P., Siqueira, R., Carraro, C. C., Donatti, L. M., et al. (2017). Effects of aerobic exercise training on metabolism of nitric oxide and endothelin-1 in lung parenchyma of rats with pulmonary arterial hypertension. *Mol. Cell. Biochem.* 429, 73–89. doi: 10.1007/s11010-016-2937-1 doi: 10.1007/s11010-016-2937-1

Conflict of Interest: The authors declare that the research was conducted in the absence of any commercial or financial relationships that could be construed as a potential conflict of interest.

frontiers in Physiology

ORIGINAL RESEARCH
published: 24 October 2019
doi: 10.3389/fphys.2019.01269

A Novel Model of Mixed Vascular Dementia Incorporating Hypertension in a Rat Model of Alzheimer's Disease

*Paul Denver[1], Heather D'Adamo[1,2,3], Shuxin Hu[1,2,4], Xiaohong Zuo[1,2,4], Cansheng Zhu[1,2], Chihiro Okuma[1,2], Peter Kim[1,2,4], Daniel Castro[1,2], Mychica R. Jones[1,2], Carmen Leal[1,2,4], Marisa Mekkittikul[1,2,4], Elham Ghadishah[1,2,3], Bruce Teter[1,4], Harry V. Vinters[1,2], Gregory Michael Cole[1,2,3,4] and Sally A. Frautschy[1,2,3,4]**

[1] Department of Neurology, David Geffen School of Medicine, University of California, Los Angeles, Los Angeles, CA, United States, [2] Veterans Affairs Greater Los Angeles Healthcare System, Los Angeles, CA, United States, [3] Department of Medicine, David Geffen School of Medicine, University of California, Los Angeles, Los Angeles, CA, United States, [4] Geriatric Research Education and Clinical Center, Greater Los Angeles Veterans Affairs Healthcare System, Los Angeles, CA, United States

OPEN ACCESS

Edited by:
Francine Marques, Monash University, Australia

Reviewed by:
Vicente Lahera, Complutense University of Madrid, Spain
Stefanie Schreiber, Universitätsklinikum Magdeburg, Germany

***Correspondence:**
Sally A. Frautschy
sfrautschy@mednet.ucla.edu

Specialty section:
This article was submitted to Integrative Physiology, a section of the journal Frontiers in Physiology

Received: *02 April 2019*
Accepted: *19 September 2019*
Published: *24 October 2019*

Citation:
Denver P, D'Adamo H, Hu S, Zuo X, Zhu C, Okuma C, Kim P, Castro D, Jones MR, Leal C, Mekkittikul M, Ghadishah E, Teter B, Vinters HV, Cole GM and Frautschy SA (2019) A Novel Model of Mixed Vascular Dementia Incorporating Hypertension in a Rat Model of Alzheimer's Disease. Front. Physiol. 10:1269. doi: 10.3389/fphys.2019.01269

Alzheimer's disease (AD) and mixed dementia (MxD) comprise the majority of dementia cases in the growing global aging population. MxD describes the coexistence of AD pathology with vascular pathology, including cerebral small vessel disease (SVD). Cardiovascular disease increases risk for AD and MxD, but mechanistic synergisms between the coexisting pathologies affecting dementia risk, progression and the ultimate clinical manifestations remain elusive. To explore the additive or synergistic interactions between AD and chronic hypertension, we developed a rat model of MxD, produced by breeding APPswe/PS1ΔE9 transgenes into the stroke-prone spontaneously hypertensive rat (SHRSP) background, resulting in the SHRSP/FAD model and three control groups (FAD, SHRSP and non-hypertensive WKY rats, n = 8–11, both sexes, 16–18 months of age). After behavioral testing, rats were euthanized, and tissue assessed for vascular, neuroinflammatory and AD pathology. Hypertension was preserved in the SHRSP/FAD cross. Results showed that SHRSP increased FAD-dependent neuroinflammation (microglia and astrocytes) and tau pathology, but plaque pathology changes were subtle, including fewer plaques with compact cores and slightly reduced plaque burden. Evidence for vascular pathology included a change in the distribution of astrocytic end-foot protein aquaporin-4, normally distributed in microvessels, but in SHRSP/FAD rats largely dissociated from vessels, appearing disorganized or redistributed into neuropil. Other evidence of SVD-like pathology included increased collagen IV staining in cerebral vessels and PECAM1 levels. We identified a plasma biomarker in SHRSP/FAD rats that was the only group to show increased Aqp-4 in plasma exosomes. Evidence of neuron damage in SHRSP/FAD rats included increased caspase-cleaved actin, loss of myelin and reduced calbindin staining in neurons. Further, there were mitochondrial deficits specific to SHRSP/FAD, notably the loss of complex II, accompanying FAD-dependent loss of mitochondrial complex I. Cognitive deficits exhibited by FAD rats were not exacerbated by the introduction of the SHRSP phenotype, nor was

the hyperactivity phenotype associated with SHRSP altered by the FAD transgene. This novel rat model of MxD, encompassing an amyloidogenic transgene with a hypertensive phenotype, exhibits several features associated with human vascular or "mixed" dementia and may be a useful tool in delineating the pathophysiology of MxD and development of therapeutics.

Keywords: cerebrovascular integrity, tau pathogenesis, Alzheimer disease, vascular dementia, rat model

INTRODUCTION

The Continuum Between Alzheimer's Disease, Vascular and Mixed Dementia

The number of people living with dementia globally is projected to reach 81 million by 2040 (Ferri et al., 2005), while cases of Alzheimer's disease (AD), estimated to be the most prevalent dementia type, are predicted to exceed 13.8 million by 2050 in the United States (Hebert et al., 2013) and 81 million globally (Rizzi et al., 2014; Baumgart et al., 2015), translating to an economic burden associated with dementia of over $800 billion (Wimo et al., 2013, 2017). Despite reports that AD is the most common dementia with an incidence of 50–64%, pure AD is rare as shown in the Religious Orders Study, with a prevalence of only 10%. One reason for this discrepancy is that 60–90% of those diagnosed with Alzheimer's dementia are found at autopsy to have coexisting cerebrovascular disease (CBVD) and may or may not be diagnosed with mixed dementia (MxD). CBVD pathologies include white matter lesions, microvascular degeneration, microinfarcts and vascular amyloid (Kalaria et al., 2012). Mixed dementia (MxD) refers to the coexistence of vascular pathology with dementia, and the diagnosis depends on the severity of vascular pathology and diagnostic criteria. There may be cortical or subcortical tissue loss, but in all cases of MxD, cerebral small vessel disease (SVD) is evident (Khan et al., 2016; Vinters et al., 2018). Due to the varied criteria for classifying dementia cases as MxD, the incidence is debatable, as reports range widely from 2 to 58%, averaging around 20 to 22% (Jellinger and Attems, 2007; Custodio et al., 2017). Incidence rates at the lower end of this range are usually reported by studies with younger subjects (less prone to MxD) or more rigorous criteria, such as different cutoffs for minimum infarct volume and exclusion of cases with cerebral amyloid angiopathy (CAA) from the criteria.

Critical gaps in knowledge include a paucity of understanding the potential synergism between tau, amyloid and vascular pathology and how this may increase vulnerability to central nervous system (CNS) damage. Vascular pathology in the clinically normal elderly is associated with impaired episodic memory independent of medial temporal atrophy (Wennberg et al., 2019). Furthermore, data from the Honolulu-Asian Aging cohort suggest that the dementia frequency in cognitively normal men more than doubles with increased cerebrovascular lesions accompanied by augmented tau pathology and surprisingly fewer neuritic plaques (Petrovitch et al., 2005), but the manner in which subclinical levels of AD and vascular pathology impacts dementia risk is unclear.

Cardiovascular Disease Increases Risk for Alzheimer's Disease and Vascular Dementia

Elevated blood pressure is strongly associated with AD, and mid-life hypertension correlates with greater subsequent cognitive decline (Launer et al., 2000; Petrovitch et al., 2000; Gottesman et al., 2014). Cognitively normal subjects with uncontrolled hypertension show increased amyloid and dementia incidence, particularly in ApoE4 carriers (Rodrigue et al., 2013; Yasar et al., 2013; Oberlin et al., 2015; Walker et al., 2017). Treatment of vascular risk factors may slow decline in AD (Valenti et al., 2014), as suggested by the multi-domain trial in Finnish patients with AD and high CBVD risk (Ngandu et al., 2015). Together these data suggest a meaningful association between cardiovascular health, CBVD, AD and dementia.

Efficacy of drugs directed at pure AD may be attenuated or contraindicated by the presence of CBVD. For example, AD subjects with vascular pathology, such as acute or sub-acute micro-hemorrhage or superficial siderosis, may experience more adverse effects with amyloid-clearing drugs such as anti-amyloid vaccination and may therefore be excluded from clinical trials (Sevigny et al., 2016). Further, a meta-analysis showed memantine to be beneficial after 6 months in moderate to severe AD, but not in patients with mild to moderate vascular dementia (VaD) (Areosa et al., 2005). For these reasons, many AD drug trials deliberately exclude patients with neuroimaging indices of vascular pathology while drug development generally neglects the assessment of efficacy in models of MxD, a major real world patient population.

Vascular Pathologies and Mechanisms in Mixed Dementia

The molecular mechanisms underlying VaD affect pathogenesis in MxD are unknown. For example, VaD may accelerate AD pathogenesis, including tau and amyloid pathology, by interrupting normal clearance of these proteins from the brain and impeding blood and interstitial fluid flow as a result of vasomotor tone dysregulation (Di Marco et al., 2015; Iadecola, 2016). Alternatively, AD may exacerbate CBVD by contributing to vasoconstriction leading to hypoxia and infarct (Marfany et al., 2018). Some studies suggest that deficient vessel integrity from chronic hypertension decreases cerebral blood flow, leading to hypoperfusion of the brain, protein misfolding and reduced clearance of Aβ and other toxins (de la Torre, 2012). Chronically elevated arterial pressure also leads to thickening of

cerebral vessel walls with increased collagen deposition (Zhou et al., 2015), reduced elasticity and narrowing of the lumen (Heagerty et al., 2010). This is especially apparent in small vessels (Feihl et al., 2008; Heagerty et al., 2010), particularly those of the cerebrovasculature (Grinberg and Thal, 2010). The brains of AD patients contain smaller blood vessels, exhibiting reduced density, length and diameter, effects that are especially evident in the vicinity of senile plaques (Bouras et al., 2006; Kitaguchi et al., 2007). Pathologies associated with CBVD include microvascular degeneration, periventricular venous collagenosis and increased vessel tortuosity (Moody et al., 1995; Farkas et al., 2000). Synergistic versus additive effects of CBVD on AD pathogenesis and cognitive decline are not fully understood (Attems and Jellinger, 2014).

Distinguishing Alzheimer's Disease From Mixed Dementia

There is no consensus on the neuropsychological parameters that differentiate AD from MxD (Planton et al., 2017; Ramirez-Gomez et al., 2017), although subjects with subcortical ischemic vascular disease, including small vessel disease, commonly show increased difficulty in executive function, but may respond better than AD subjects to cues, suggesting improved preservation of recognition memory, as opposed to AD subjects that have difficulty in coding or storage of memory (Mendez and Ashla-Mendez, 1991; Lafosse et al., 1997; Looi and Sachdev, 1999; Lukatela et al., 2000; Traykov et al., 2002). In addition to impaired executive function, reduced attention, processing speed, and memory retrieval have been reported in MxD (Baker et al., 2012).

Neuroimaging findings can be included in the classification of MxD, but may not necessarily detect mild white matter intensities (WMI) or SVD, another reason the prevalence of MxD may be underestimated (Baker et al., 2012). Additionally, there is no clear consensus on the amount of vascular pathology identified by neuroimaging required to be clinically significant (Dey et al., 2016). Alternatively, the SVD score (0–4), based on white matter hyperintensities, lacunae, microbleeds, and enlarged perivascular spaces detected by magnetic resonance imaging (MRI) is sometimes used to define MxD (Staals et al., 2015).

Although there are NINDS-AIREN and ADDTC criteria for diagnosing MxD, the former including neuropathology and the latter requiring both clinical and neuroimaging abnormalities, there is no clear consensus and no CERAD criteria to define MxD (Jellinger and Attems, 2007). The pathologies of AD and VaD often overlap in subcortical regions (basal ganglia, thalamus, hippocampus and white matter). MxD patients often exhibit multi-infarcts so one definition of MxD requires that patients must meet the criteria for AD and have larger and hemispheral infarcts, reaching 30–50 ml of infarcted volume (Khan et al., 2016), which may indicate synergism between the two pathologies and not just two coexisting pathways. Other groups also include more severe vascular pathology such as territorial infarcts, lobar hematomas, cortical microbleeds or even CAA (De Reuck et al., 2018). It is presumed that in MxD the thresholds for developing dementia may be lowered due to subclinical levels of both pathologies, or that the presence of vascular pathology can unmask AD pathology and trigger dementia (Fischer et al., 1991; Kalaria et al., 2012).

Models of Cerebrovascular Disease

Models of dementia associated with cerebrovascular insufficiency have typically involved surgical manipulation of the arteries that supply the brain, to invoke transient or chronic hypertensive events (Galisova et al., 2014; Kwon et al., 2014; Wang, 2014; Venkat et al., 2017; Khoshnam et al., 2018; Liu et al., 2018; Yu et al., 2018). Such invasive procedures invariably introduce a multitude of potentially confounding factors and inadequately model the clinical scenario of chronic hypertension. As such, animal models that accurately recreate the clinical scenario of MxD are lacking. Induction of hypertension in a pig model and in 3xTg mice causes shrinkage of hippocampal dendritic arbors, microglial activation, blood brain barrier (BBB) leakage and impaired learning and memory, in addition to elevated amyloid burden (Shih et al., 2018). This suggests that hypertension leads to AD-like brain pathologies in a naïve animal model, while induction of hypertension in an amyloidogenic model can exacerbate pathology further. Hypertension in APP/PS1 mice accelerates progression of AD-like pathologies, including cognitive dysfunction and amyloid pathology, in addition to reduced density of microvessels and cerebrovascular dysfunction (Cifuentes et al., 2015). In naïve APP/PS1 mice, Aβ accumulation in cerebral blood vessel walls has been demonstrated (Klakotskaia et al., 2018). Others have observed microangiopathies and aneurysms throughout the microvessels of the liver, kidneys and the brain of APP/PS1 mice (Kelly et al., 2015, 2017), suggesting a causal relationship between amyloidogenesis and systemic vascular dysfunction, at least in the APP/PS1 mouse. Hypertension in rats results in BBB dysfunction, cognitive impairments and white matter lesions, along with fibrinoid necrosis, hyalinosis and vascular remodeling of small vessels in the brain (Fan et al., 2015). Downregulation of tight junction proteins and disturbed tight junction ultrastructure are apparent in hypertensive rats (Fan et al., 2015; Meissner et al., 2017), and have also been observed in AD and other inflammatory disorders of the brain (Coisne and Engelhardt, 2011; Grammas et al., 2011). Hypertensive cardiovascular disease involves a significant inflammatory component (Harrison et al., 2011), and mounting evidence suggests that inflammation-driven endothelial cell damage leads to BBB breakdown and SVD, an important risk factor in VaD (Wardlaw et al., 2013).

The selectively inbred spontaneous hypertensive rat (SHR) was developed in 1963 at Kyoto University and exhibits elevated systolic blood pressure, cortical and striatal infarcts, along with white matter damage, BBB dysfunction and gliosis that progressively worsens (Tayebati et al., 2012; Kaiser et al., 2014; Venkat et al., 2015). This model also shows evidence of reduced BBB proteins and enhanced permeability within paraventricular and brain stem regions (Biancardi et al., 2014; Meissner et al., 2017) along with progressive elevations of oxidative stress markers in brain and plasma (Takemori et al., 2013). It is widely appreciated that the SHR rat represents an excellent model of essential hypertension leading to cerebral SVD, stroke

and VaD (Hainsworth and Markus, 2008; Bailey et al., 2009; Hainsworth et al., 2012; Kaiser et al., 2014). By 6 months of age SHRs develop SVD along with cognitive deficits, hippocampal neurodegeneration and white matter loss (Jalal et al., 2012), detectable by MRI (Koundal et al., 2019). The stroke-prone SHR (SHRSP) was created in 1974, as a sub-strain of the SHR with a high incidence of stroke and hypertension (220–240 mmHg) (Okamoto and Aoki, 1963; Nabika et al., 2012). By 3–4 months of age these rats develop hypertension, which causes elevated plasma levels of pro-inflammatory cytokines (Sicard et al., 2008), and cerebral SVD (Schreiber et al., 2014). In addition to thickened cerebral small vessel walls, these rats also develop cognitive dysfunction, including spatial learning deficits, effects that were ameliorated by COX-2 inhibition (Tang et al., 2015) as well as demyelination and oligodendrocyte apoptosis (Jalal et al., 2012; Weaver et al., 2014), suggesting an association between vascular injury and demyelination, that may be mediated by inflammation.

The SHRSP rats have been reported to have AD like pathology with small but significant increases in hyperphosphorylated tau and Aβ, most notably vascular Aβ associated with the progressive vessel wall damage, thrombotic occlusions and reductions of cerebral blood flow in SHRSP (Bueche et al., 2014; Schreiber et al., 2014; Held et al., 2017; Pirici et al., 2017; Jandke et al., 2018). However, to date there are no animal models of dementia with widespread abundant neuritic plaque pathology and detergent insoluble ptau that incorporate clinically relevant hypertension, making it difficult to investigate the interplay between cerebrovascular damage and ptau and amyloid accumulation.

Purpose of the Study

This study addresses the need for an adequate model of MxD. Rat models have advantages over mice due to improved cognitive ability and larger volumes of brain, cerebrospinal fluid and plasma, which can expedite development of diagnostic and surrogate imaging and fluid biomarkers. The TgF344-AD rat model, developed by Cohen and colleagues (Cohen et al., 2013), expresses human APP_{swe} and PS1ΔE9 mutations and develops age-dependent cerebral amyloidosis, gliosis and phospho-tau pathology (Cohen et al., 2013). TgF344-AD rats also exhibit pronounced cognitive and neuropsychiatric behavioral abnormalities by 15 months of age, along with dysregulated neural network activity (Munoz-Moreno et al., 2018; Stoiljkovic et al., 2018), as well as age-dependent deterioration of hippocampal synaptic function in this model (Smith and McMahon, 2018). Mouse models harboring amyloidogenic transgenes show hyperphosphorylated tau, but not robust detergent insoluble tau and tangles (tauopathy), neurodegeneration but not robust neuron loss. Introduction of human tau or frontotemporal tau dementia mutations can lead to development of neurofibrillary tangles, but those models do not precisely recapitulate pathogenesis in AD, in part because AD patients do not have tau mutations driving tauopathy (Sydow et al., 2011; Sayed et al., 2018). Here we hypothesized that the introduction of a hypertensive phenotype in an AD rat model could exacerbate Aβ and/or tau pathology, gliosis, vascular pathology and cognitive dysfunction and serve as a new model of MxD for future studies of mechanism, biomarkers and therapeutics.

MATERIALS AND METHODS

Animals

The SHRSP/FAD rat model was developed at the UCLA Division of Laboratory Animal Medicine vivarium, and the colony is now maintained at the Veterans Affairs Greater Los Angeles Health Care System. All experimentation was approved by the UCLA Chancellor's Animal Research Committee and the Veteran Administration Institutional Animal Care and Use Committee and carried out in compliance with National Institutes of Health guide for the care and use of Laboratory animals (NIH Publications No. 8023, revised 1978). Rats were bred and housed in groups of least two under a 12-h light-dark cycle and had access to standard chow and water *ad libitum*. Four strains were used (16–18 month old, females and males): (i) non-hypertensive WKY ($n = 8$), (ii) TgF344-AD (FAD) ($n = 11$), (iii) hypertensive SHRSP ($n = 10$) and (iv) SHRSP/FAD ($n = 9$) rats. The hypertensive rats in this study were 75:25% SHRSP:F344, and the non-hypertensive rats had 75%:25% WKY:F344 backgrounds, and the methods for breeding them described below.

Stroke-Prone Spontaneously Hypertensive Rats With (SHRSP/FAD) or Without (SHRSP) the FAD Transgene

The founder hypertensive rats (SHRSP) were obtained from Charles River Laboratories and the original FAD rats, created at NIH by Dr. Robert Cohen, were obtained directly from his laboratory at Emory as well as purchased from the Rat Resource & Research Center, University of Missouri. The FAD female offspring of the first mating were again crossed with 100% SHRSP males, which produced the SHRSP/FAD litters used in this study. The SHRSP sub-strain of the SHR, created in 1974, is considered a robust model of hypertension and stroke. Although the precise loci are debated, SHRSP genetic susceptibility for hypertension and cerebral lesions is autosomal dominantly inherited (Gratton et al., 1998), allowing us to cross with the TgF344-AD (FAD) rat, producing a novel rat, expressing autosomal dominant familial AD genes, on the SHRSP background (SHRSP/FAD).

The founder FAD rats were derived from the FAD rat on an F344 background, which express human mutant variants of APP (Swedish) and PS1 (ΔE9) and develop age-dependent amyloid pathology, hyperphosphorylation of tau, gliosis and cognitive dysfunction (Cohen et al., 2013). The current hypertensive FAD is 98:2% SHRSP:F344 background.

Non-hypertensive Rats With (FAD) or Without (WKY) FAD Transgene

There were two types of non-hypertensive rats (WKY or WKY/FAD). Since the background strain of the SHRSP and FAD rats is WKY and F344, respectively, we bred WKY, the original background of the SHRSP, into the FAD model. Specifically, male WKY rats were paired with female FAD rats. The resulting

background was 50:50% WKY/F344, and rats with the FAD transgene were again paired with 100% WKY animals, creating the F2 generation with 75:25% WKY:F344, and the two non-hypertensive groups (FAD and WKY) that were used for the study. The current non-hypertensive FAD colony has a 98% WKY background. The non-hypertensive, non-transgenic control rats are henceforth described as WKY, while the non-hypertensive, transgenic controls are described as FAD rats.

Blood Pressure Measurement

Arterial blood pressure was measured in the caudal tail artery of rats using the CODA^{TM} Non-invasive Blood Pressure System (Kent Scientific, Torrington, CT, United States). Rats were handled and acclimatized to the apparatus for 15 min daily for 3 days prior to blood pressure measurements. On the fourth day, rats were allowed to enter the holder freely with as little force as possible and allowed to remain in place for 15 min. Then an occlusion cuff was passed over the animal's tail to the base and inflated to impede blood flow to the tail. The occlusion cuff was slowly deflated, while a second tail cuff that incorporates a volume pressure recording (VPR) sensor was secured to the tail, distal to the occlusion cuff. The tail of the animal was kept in contact with a heated platform, while the VPR sensor measured physiological characteristics of the returning blood flow. As blood returned to the tail, the VPR sensor cuff measured the swelling of the tail that results from arterial pulsations from the blood flow. Systolic blood pressure was automatically measured at the first appearance of tail swelling. Diastolic blood pressure is automatically measured when the increasing rate of swelling ceases in the tail.

Behavioral Testing

Behavioral testing took place in a quiet, dimly lit room and the testing apparatus was isolated using divider panels. The apparatus was cleaned with 70% isopropanol between trials to avoid the accumulation of olfactory cues. Animals were handled in the testing room for 1 week prior to beginning the experiments, by the experimenter that performed the testing.

Open Field Task

Locomotor activity and anxiety were assessed in the open field task (OFT), during which rats were placed into a black box 27.5 inches in width, 27.5 inches in length and with walls 15.5 inches in height. The arena was dimly lit from above, and rats were allowed to explore freely for 8 min. The animals' movements were tracked with an overhead camera and recorded on Anymaze^{TM} software (Stoelting, Wood Dale, IL, United States). Path length and speed were calculated automatically. An independent investigator, blinded to the identity of the animals, manually counted defecation, rearing and grooming events.

Novel Object Recognition Task

The OFT was considered the first habituation day for the novel object recognition task (NOR). The second day of habituation took place 24 h following the OFT. Rats were returned to the same box along with two identical objects, secured to the floor, spaced evenly apart and equidistant from the walls, and allowed to explore freely for 10 min. The objects were either pipette tip boxes or filled cell culture flasks and these were alternated between rats in order to mitigate the effects of preference for or aversion to either object. Twenty-four hours later, rats were again placed into the box with the same identical objects and allowed to explore for 10 min. Rats were then returned to their cage for an interval of 1 h before being placed, once again, into the box with two objects. This time one of the objects was replaced with a previously un-encountered object, either a tip box or a flask, and the rat was, again, allowed to explore freely for 10 min. The time spent exploring each object was measured and recognition indices calculated for each object, which were then compared to determine whether or not the animal showed a significant preference for the novel object, an innate behavior in healthy rats. A discrimination index (DI) was also calculated for each mouse in the test phase with the equation $(tN - tF)/(tN + tF)$, where tN equals time spent exploring the novel object and tF equals time spent exploring the familiar object. Another measurement of preference was, the recognition index (RI) calculated by $tN/(tN+tF)$.

Y Maze

The Y maze consisted of three arms and walls 12 inches in height. Testing took place another day following completion of the NOR task. The rat was placed into the bottom arm of the Y maze, designated A and allowed to explore the rest of the maze freely. The animals' movements were tracked with an overhead camera and recorded on Anymaze software, measuring entries into each arm (A, B, and C). We then calculated corrected arm entries as those into a "novel" subsequent arm (e.g., A > B > C or B > C > A or C > B > A). Errors were measured as entries into a directly previous arm (e.g., A > B > A or C > B > C or B > A > B). Spontaneous alternation was calculated with the equation $C / (T-1) \times 100$, where C equals correct arm entries and T equals total arm entries.

Euthanasia, Plasma and Brain Collection for Biochemistry and Histology

At the end of the experiment, rats were injected with a lethal dose of pentobarbital (100 mg/kg i.p.) and upon deep anesthesia, the chest cavity was opened and rats were perfused intracardially with a physiologically isotonic buffer containing 10 mM HEPES, 137 mM NaCl, 4.6 mM KCL, 1.1 mM KH2PO4, 0.6 MgSO4, 1.1 mM EDTA, and protease inhibitors (5 mg/ml of leupeptin and aprotinin and 2 mg/ml pepstatin A, pH 7.4). The brain was bisected and the hippocampus and cortex were dissected from the left hemisphere, snap frozen in liquid nitrogen and stored at −80°C until use for biochemistry, while the right hemisphere was immersion-fixed in 4% formalin, sucrose cryopreserved and frozen at −80°C until cryosectioning.

Histology

Immunohistochemistry

Coronal sections of frozen rat hemi-brains were cryosectioned at 12 μm thick, mounted on slides and stored at −20°C. For immunohistochemistry (IHC), slides were warmed to room temperature for 1 h and then steamed for 20 min using

a citric acid base antigen-unmasking solution (Vector Labs, Burlingame, CA, United States). Sections were quenched with hydrogen peroxide (H_2O_2) in methanol for 30 min at room temperature, then washed three times with tris buffered saline (TBS) (pH 7.4) (for staining of Aβ, Tau pS422, collagen-4) or treated with 0.3% Triton X-100 in 0.1 M TBS (pH 7.4) for 10 min at room temperature (for staining of Aqp-4, GFAP, Tau pS422, collagen-IV). For Aβ staining, sections were pretreated with 70% formic acid for 10 min at room temperature. For all IHC, sections were treated with a blocking solution, consisting of 1.5–5% normal serum and 3% bovine serum albumin (BSA) in TBS for 1 h at 37°C, followed by incubation with primary antibodies for 1 h at 37°C, then overnight at 4°C. Amyloid-β (Aβ) deposits were labeled with 6E10 (1:500, anti-Aβ) recognizing residues 1-16 (Biolegend, San Diego, CA, United States). Astrocytic endfeet associated with capillaries were labeled with anti-Aqp-4 polyclonal (1:200, NOVUS Biologicals, Littleton, CO, United States) and processes with anti-GFAP monoclonal (1:5000; Sigma-Aldrich St. Louis, MO, United States). Anti-calbindin D 28K rabbit polyclonal antibody (1:800; Thermo Fisher, Asheville, NC, United States) was used as a neuronal marker. Microglia were labeled with an anti-Iba1 rabbit polyclonal (1:200; Wako, Richmond, VA, United States) antibody raised against a synthetic peptide corresponding to the C-terminus of Iba1. Levels of Tau phosphorylated at serine 422 (pS422) were detected using a rabbit polyclonal antibody against MAPT/Tau pS422-Aff-purified (1:800, Acris, San Diego, CA, United States). Blood vessels were labeled with anti-collagen IV mouse monoclonal antibody (Invitrogen, Waltham, MA, United States). Sections were then incubated with secondary antibodies diluted in normal serum and 3% BSA for 1 h at 37°C followed by avidin-biotin complex (ABC; Vector Labs, Burlingame, CA, United States) reagent for 1 h 20 min at 37°C. After ABC incubation, metal-enhanced peroxidase diaminobenzidine (DAB; Pierce, Rockford, IL, United States) was used for detection of positive staining.

Luxol Fast Blue Myelin Staining

The Kluver-Barrera Luxol Fast Blue Method was used to stain myelin using cryostat sections. Briefly, sections were rinsed in 95% alcohol, then incubated overnight at 60°C with a 0.1% solution of Luxol Fast Blue (Solvent Blue 38 Sigma) dissolved in 95% alcohol, 0.5% and ∼10% glacial Acetic Acid, then filtered. Sections were washed with 95% ethanol, rinsed with distilled water, then differentiated by quick immersion in 0.05% lithium carbonate solution, followed by several changes in 70% ethanol and then rinsed with distilled water. Then sections are incubated for 6 min with 60°C filtered 0.1% Cresyl Echt Violet solution in distilled water with 15 drops of 15% glacial acetic acid added. Sections were differentiated and acidified (drops of 5N HCL) in 95% alcohol then cleared in CitriSolv™ Solvent and Clearing Agent (VWR) prior to cover slipping with Thermo Scientific™ DPX Mounting Media. Evaluation of differences in Luxol Blue staining patterns was performed by an experimenter blinded to transgenic animal. Four consecutive coronal sections were evaluated per rat at Bregma at −4.0.

Western Blot

Brain tissue was weighed before starting protein extraction. Frozen brain tissues were added to TBS (10 × volume of brain wet weight) containing complete protease inhibitor (PI) and phosphatase inhibitor (PPI) cocktail (Roche, Mannheim, DE, United States) and sonicated for 10 s × 3 times on ice to disrupt cell membranes. The sonication conditions were kept the same in all the following steps. After sonication, samples were centrifuged at 132,000 × *g* for 20 min at 4°C to produce TBS supernatant used to measure soluble proteins. The pellet was further extracted in modified RIPA lysis buffer with PI and PPI to obtain detergent-soluble membrane fractions and lysis-insoluble pellets for insoluble tau aggregates. Lysis pellets were then re-suspended in sample buffer. All the samples were stored at −80°C and protein assayed prior to use. The protein concentration was measured according to Bio-Rad protocol (Bio-Rad, Hercules, CA, United States). For western blotting, 15–30 mg of protein was electrophoresed on a 7.5–12% acrylamide gradient gel, and then transferred to polyvinylidene fluoride membrane. After blocking in 10% non-fat milk, blots were incubated with primary antibodies against Aqp-4 (NOVUS Biologicals, Littleton, CO, United States), GFAP (Sigma-Aldrich, St. Louis, MO, United States), tau pS202 (CP13; gift from Peter Davies, Albert Einstein College, New York), caspase-cleaved actin (fractin from author Greg Cole, Yang et al., 1998), platelet-endothelial cell adhesion molecule-1 (PECAM-1), Synaptosome Associated Protein 25 (SNAP25), synaptophysin, drebrin and *N*-methyl D-aspartate receptor subtype 2B (NMDAR2B or NR2B), NR2B (Santa Cruz Biotechnology) then incubated with horseradish peroxidase-conjugated secondary antibodies. SuperSignal West Femto Substrate (Pierce, Rockford, IL, United States) was exposed on x-ray film below saturation, and bands were scanned and quantified using a UVP bio-imaging system (UVP, Upland, CA, United States).

Mitochondrial Complexes

Mitochondrial enzymes were measured by western blot, using the premixed cocktail of primary monoclonal antibodies provided in the OxPhos Panel kit (Abcam, previously MitoSciences) ab110413) against Complex I subunit NDUFB8 (ab110242), CII complex II-30kDa (ab14714), Complex III-Core protein 2 (ab14745) Complex IV subunit I (ab14705) and Complex 5V alpha subunit (ab14748). The lysis fraction from the hippocampal extract was used, and samples loaded as described above.

Plasma Exosomes

Plasma was collected at euthanasia, prior to perfusion and stored at −80°C. Plasma exosomes were isolated according to the method of exosome precipitation (Fiandaca et al., 2015). Briefly, 250 μl of plasma was spun at 3000 × *g* for 15 min then the supernatant with added protease inhibitor cocktail (Roche Applied Sciences, Inc.) was incubated with 100 μl thromboplastin-D (Thermo Scientific, Inc.) at room temperature for 60 min. After spinning at 13,500 rpm for 5 min, the supernatant with added protease inhibitor cocktail was mixed

with 63 µl of ExoQuick^{TM}-TC exosome precipitation solution (System Biosciences, Inc.) and incubated at 4°C for 60 min. The samples were again spun at 1500 × *g* for 30 min, were then removed and the supernatant was spun again for 5 min. The pellets were re-suspended in 1 × PBS with H_2O/protein inhibitor. Then the isolated exosomes were purified by Exo-spin^{TM} column (Cell Guidance Systems, Inc.) according to the manufacturer's instructions. After purification, exosomes were run on reduced 6–15% Tris-Glycine/SDS gel and western blot was run using an anti-Aqp-4 (Novus Biologicals, Littleton, CO, United States) antibody.

Statistical Analysis

Western and Mitochondrial Analysis

Statistical analysis was performed using SPSS V.22 (IBM, Inc). Two way ANOVA [SHR (WKY or SHRSP) × FAD (Tg- or Tg+)] was performed to determine differences in protein levels, and where applicable, Multivariate Analysis (MANOVA) was performed. Log or square root transformation for data with unequal variances. Two-way ANOVA followed by *post hoc* LSD or *t*-tests was used to analyze behavioral data. *P*-values lower than 0.05 were considered statistically significant. *P*-values between 0.1 and 0.05 were considered trends.

Immunohistochemical Analysis

Data for immunohistochemistry analysis were collected from microscopic images acquired using a Macintosh computer with a digital MC170 5 MPixel Leica camera on an Olympus Vannox-T (AHBT) microscope. Images were then analyzed using the public domain software Image J, http://rsbweb.nih.gov/ij/. Immunohistochemical data were analyzed quantitatively using two-way ANOVA (FAD × SHRSP × brain region), and differences between strains were determined by Fisher's least significant difference (LSD) *post hoc* analysis. Sex was included in the model only if initial analysis showed significant effects ($p < 0.05$). A sex effect was identified only for Aqp-4 western blot, as females showed the highest Aqp-4 increases in SHRSP/FAD. Four consecutive sections and the bregma specific for the region of interest were assessed per rat. Density thresholding was used with Image J macros to evaluate integrative density, size of individual cells number of cells per area, and percentage area stained.

RESULTS

SHRSP/FAD Rats Show Hypertension and Preservation of the SHRSP Phenotype

Blood pressure readings were acquired from the caudal tail arteries of the four strains (**Figure 1**). Data were analyzed via MANOVA [variables (diastolic and systolic) × SHRSP × FAD × sex], and log transformation of data was needed to establish equal variance. The multivariate main effect was only significant for SHRSP [Pillai's Trace = 0.719, $F(4,50)$, $p < 0.0001$] as was the univariate main effect for SHRSP, on diastolic and systolic pressure [$F(2,33) = 11.565$, $p < 0.0001$ and $F(2,33) = 21.044$, $p < 0.0001$, respectively]. Although univariate tests revealed a main effect of FAD, *post hoc* analysis showed only incremental (5%) non-significant increases in blood pressure in FAD rats, compared to WKY. In contrast, *post hoc* analysis showed that both systolic and diastolic pressures were higher in SHRSP and SHRSP/FAD rats, compared to FAD and WKY rats ($p < 0.001$), consistent with preservation of the SHRSP hypertensive phenotype in this new SHRSP/FAD model.

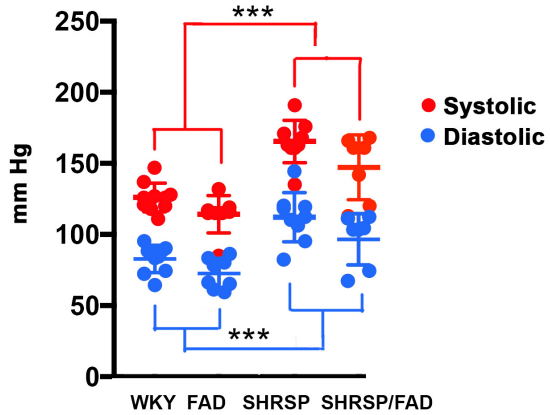

FIGURE 1 | Systolic and diastolic blood pressure is elevated in SHRSP and SHRSP/FAD rats. Shown are systolic (red) and diastolic (blue) blood pressure measurements in FAD ($n = 11$), SHRSP ($n = 10$), and SHRSP/FAD ($n = 9$) rats, as well as non-transgenic WKY controls ($n = 8$), as measured in the rats' caudal tail artery. The multivariate analysis showed a significant effect of SHRSP only ($p < 0.0001$), indicating that SHRSP but not sex or FAD transgene influenced blood pressure. Similarly the univariate *F* tests showed significant main effects of SHRSP on both diastolic and systolic pressure ($p < 0.0001$ and $p < 0.0001$, respectively). The univariate effect of FAD on diastolic and systolic pressure was significant ($p < 0.019$, respectively), but *post hoc* analysis showed that the trend for slightly higher pressure in SHRSP/FAD rats was marginal and not significant. *Post hoc* analysis showed that both systolic and diastolic pressure were higher in SHRSP and SHRSP/FAD rats than in WKY and FAD ($p < 0.001$), consistent with preservation of the SHRSP hypertensive phenotype in the SHRSP/FAD rat. Data represent means ± SEM. ***$p < 0.001$; MANOVA with Pillai's Trace. Log transformation of data was performed to establish homogeneity of variance.

Amyloid and Tau Pathology in the Hippocampus

Amyloid-β Plaque Burden in SHRSP/FAD Is Slightly Reduced and Plaques Have More Diffuse Morphology Than in FAD Rats

Micrographs in **Figure 2** depict Aβ deposition (6E10) in the hippocampus of FAD and SHRSP/FAD rats, while no plaques were observed in WKY rats. Quantitative analysis of plaque number and percentage area stained was assessed in three brain regions, the hilus (highest density of plaques), perirhinal and entorhinal cortices (moderate plaque burden). Two-way ANOVA was performed (strain × region) and log transformation was used to obtain equal variances for percentage area stained. The

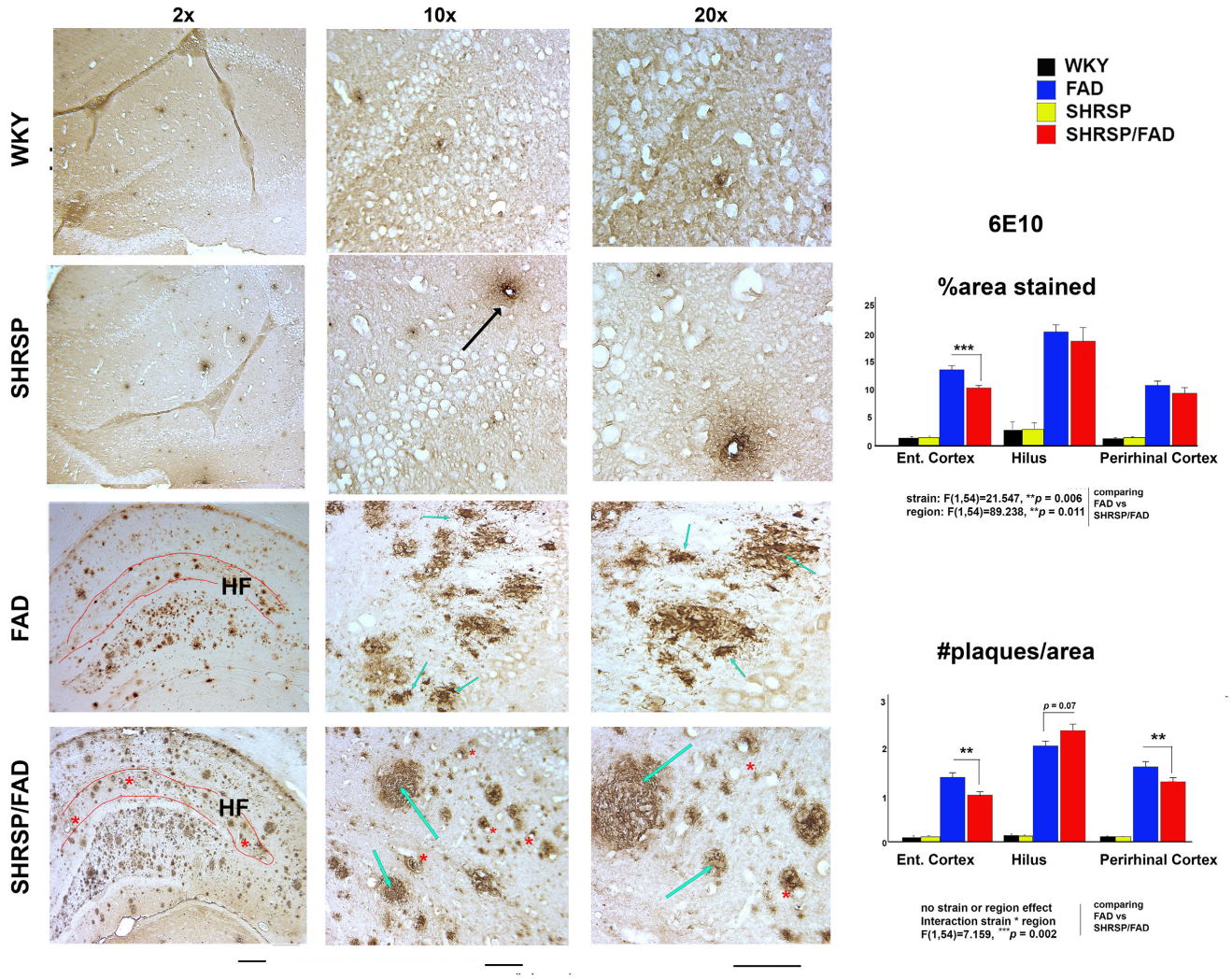

FIGURE 2 | Neuritic Amyloid-β plaques in FAD rats become more diffuse with hypertension. Micrographs depicting Aβ (6E10) immunohistochemical staining of brain sections (hippocampus) from FAD (n = 11) and SHRSP/FAD (n = 9) rats are shown. No plaques were observed in WKY rats, while there was sparse vascular staining in the SHRSP rat (black arrow), unlike advance plaque pathology in the FAD and SHRSP/FAD groups. With the low magnification micrographs, more compact, neuritic plaques (black arrows) were observed in FAD rats, whereas plaques in the hippocampus of SHRSP/FAD rats rarely had compact cores and were more diffuse (blue arrows) and frequently associated with vessels (red asterisks). The highly vascularized hippocampal fissure is outlined in red. Although there was moderate staining for Aβ in the HF of FAD rats, the SHRSP/FAD rats showed extensive staining of plaques and vessels (red asterisks). Since there was negligible staining in the SHRSP and WKY groups, quantitative analysis was performed in the plaque-rich hilus, measuring Aβ plaque number and average percentage area only in the FAD and SHRSP/FAD groups. Two-way ANOVA (region × strain) of percent area and count, showed significant region effects, which *post hoc* analysis revealed was due to higher plaque burden and count in the hilus. For percent area, there was also a significant main effect of strain and *post hoc* analysis showed that this was due to a reduction in plaques in the entorhinal cortex of SHRSP rats. For plaque count, two-way ANOVA showed an interaction between strain and region. *Post hoc* analysis showed significant reductions in plaque number in both the entorhinal and perirhinal cortices of SHRSP rats. Data represent means ± SEM. $^{*}p < 0.05$, $^{**}p < 0.01$; two-way ANOVA. Log transformation of data for percent area was also performed to establish homogeneity of variance.

main effects for strain and region were significant (p = 0.006 and p = 0.011, respectively) and while there was no interaction between strain and region, *post hoc* analysis revealed a reduction in plaque numbers in the entorhinal cortex of SHRSP/FAD rats compared to FAD in (p = 0.001). Two-way ANOVA of plaque number showed that the effects of strain or region were non-significant, but there was a significant interaction between strain and region (p = 0.002).

Post hoc analysis revealed that Aβ plaque number was significantly reduced in the entorhinal and perirhinal cortices of SHRSP/FAD rats ($p < 0.05$), whereas plaque number was increased, albeit non-significantly (p = 0.07), in the hilus of SHRSP/FAD rats, compared with FAD. Furthermore, plaques in the SHRSP/FAD rats were more diffuse, when compared with those in FAD rats, which were of coarser texture, typical of neuritic plaques.

Tau (pS422) Staining of Neurites and Cell Bodies and Insoluble Tau (CP13) Levels Are Increased in SHRSP/FAD Rats

In **Figure 3**, micrographs depict Tau pS422 staining in the hippocampal hilus of the four strains. Unlike WKY, SHRSP and FAD rats, which showed light staining of their hilar neurons, SHRSP/FAD rats showed intense staining of occasional neurons with pre-tangle morphology, similar to globose neurofibrillary tangles, and a few displaying tortuous neurites. Two-way ANOVA analysis of both percentage area stained and cell size, showed significant main effects of SHRSP ($p = 0.001$ and $p = 0.006$), FAD ($p < 0.0001$ and $p < 0.0001$) and SHRSP × FAD interactions ($p = 0.025$ and $p = 0.034$). For percentage area stained, the SHRSP/FAD rats showed two-fold increases in levels above all other strains ($p < 0.0001$), which contributed to the interaction between SHRSP and FAD. Despite the significant main effect of FAD on percentage area of tau pS422 staining and incremental increases in FAD and SHRSP rats, compared to WKY, these differences were not significant with *post hoc* analysis. In contrast, *post hoc* analysis showed that tau pS422-positive cell size was significantly elevated in FAD rats, compared to WKY ($p < 0.01$) and in SHRSP/FAD rats, compared to FAD ($p < 0.001$) and SHRSP rats ($p < 0.001$). Together, this suggests that tau pS422 staining is robustly increased in the hilus of SHRSP/FAD rats, compared to FAD or SHRSP alone.

The lower right panel of **Figure 3** shows representative lanes from western blot experiments measuring tau protein (CP13 antibody) in the detergent lysis buffer insoluble pellets extracted with SDS from hippocampi from the four rat strains. Two-way ANOVA showed significant main effects for FAD effects and the FAD × SHRSP interaction. *Post hoc* analysis showed a non-significant trend for increased detergent insoluble CP13 levels in FAD, compared to WKY rats. Whereas levels of CP13 in the hippocampus were significantly elevated in SHRSP/FAD rats, compared to WKY ($p < 0.001$), FAD ($p < 0.05$), and SHRSP rats ($p < 0.001$). These data suggest that the small increase of insoluble tau levels in the hippocampus of FAD rats is robustly increased in the SHRSP/FAD rat.

Neuroinflammation

Iba1

Illustrated in **Figure 4** are micrographs showing microglial staining in the hilus of the hippocampus of the four strains. Brains of WKY, FAD and SHRSP rats displayed microglia with reactive ramified processes and well-defined, darkly stained oval soma, which was most pronounced in SHRSP rats (red asterisks). In contrast, in the SHRSP/FAD group, microglia were hyper-ramified with thickened bushy processes (red dashed arrows) and narrowed soma, some with occasional rod morphology (black arrows). Total percentage area stained, cell size (soma and branches) and cells per unit area were evaluated using two-way ANOVA (FAD × SHRSP). There were no significant FAD effects on Iba1-positive cell size or count, but there was a main FAD effect ($p < 0.0001$) on percentage area stained and a significant SHRSP × FAD interaction ($p = 0.001$). *Post hoc* analysis showed that the significant SHRSP × FAD interaction was related to an elevation of percentage area of Iba1 staining in the hippocampus of SHRSP/FAD rats, compared to all the other groups ($p < 0.001$). In fact, this significant interaction was also seen with cell count and size, which *post hoc* analysis revealed was similarly due to changes in the SHRSP/FAD rats but not the FAD group. *Post hoc* analysis also demonstrated a small FAD effect associated with increased microglia in FAD rats ($p < 0.05$), but in SHRSP/FAD rats, the FAD effect was associated with fewer microglia ($p < 0.001$), despite increased percentage area stained.

Hypertrophic Astrocytes and Disorganized Aquaporin-4+ End-Feet in SHRSP/FAD Rats

Figure 5 shows immunostaining of brain sections for the astrocytic antigen GFAP. In Tg- WKY control rats, soma generally extended thick primary branches, from which multiple secondary and tertiary processes diverged. There are many star-shaped soma typical of quiescent astrocytes. The most noticeable difference between strains was increased GFAP staining throughout the hilus and other regions of the brain (not shown) in SHRSP/FAD rats. These SHRSP/FAD rats manifested hypertrophied soma size, and extended thickened and dense processes with fewer thin, secondary and tertiary processes, consistent with immune activation. There was also a similar but more modest effect in FAD rats as well as an SHRSP effect. Specifically, astrocytes in the SHRSP rats had fewer processes but more cells than WKY, consistent with SHRSP-dependent proliferation. Data collected from image analysis were analyzed by two-way ANOVA (region × SHRSP × FAD), which revealed significant main effects. Data from square root transformation of percentage area stained was used for ANOVA to establish equal variance. There was a significant main effect of the FAD transgene on percentage area stained, cell size and GFAP staining intensity ($p < 0.0001$). *Post hoc* analysis indicated that while the trends for increased percentage area of GFAP staining ($p = 0.057$) and cell size ($p = 0.066$) in FAD, compared to WKY did not reach significance, percentage area stained ($p < 0.001$) and cell size ($p < 0.0001$) were robustly and significantly elevated in the hippocampal hilus of SHRSP/FAD rats, compared to WKY. Additionally, staining intensity was significantly elevated in SHRSP/FAD rats, compared to FAD ($p < 0.006$). Furthermore, *post hoc* analysis showed that percentage area ($p = 0.005$) and cell size ($p < 0.001$) were elevated in the dentate gyrus of SHRSP/FAD rats, compared to SHRSP. There were no SHRSP interactions, only a main SHRSP effect on cell size ($p = 0.024$), corresponding to a significant reduction of cell size in SHRSP, compared to FAD rats ($p < 0.05$). Percentage area stained, cell size and GFAP staining intensity all showed a strong region effect ($p < 0.0001$) corresponding to more robust increases in the plaque-enriched hilus of FAD and SHRSP/FAD rats.

GFAP Protein Levels in the Entorhinal Cortex and Hippocampus Are Increased in SHRSP/FAD Rats

The bottom panel of **Figure 5** depicts representative lanes of western blots for GFAP in two brain regions and the densitometric analysis of bands normalized to actin. Consistent

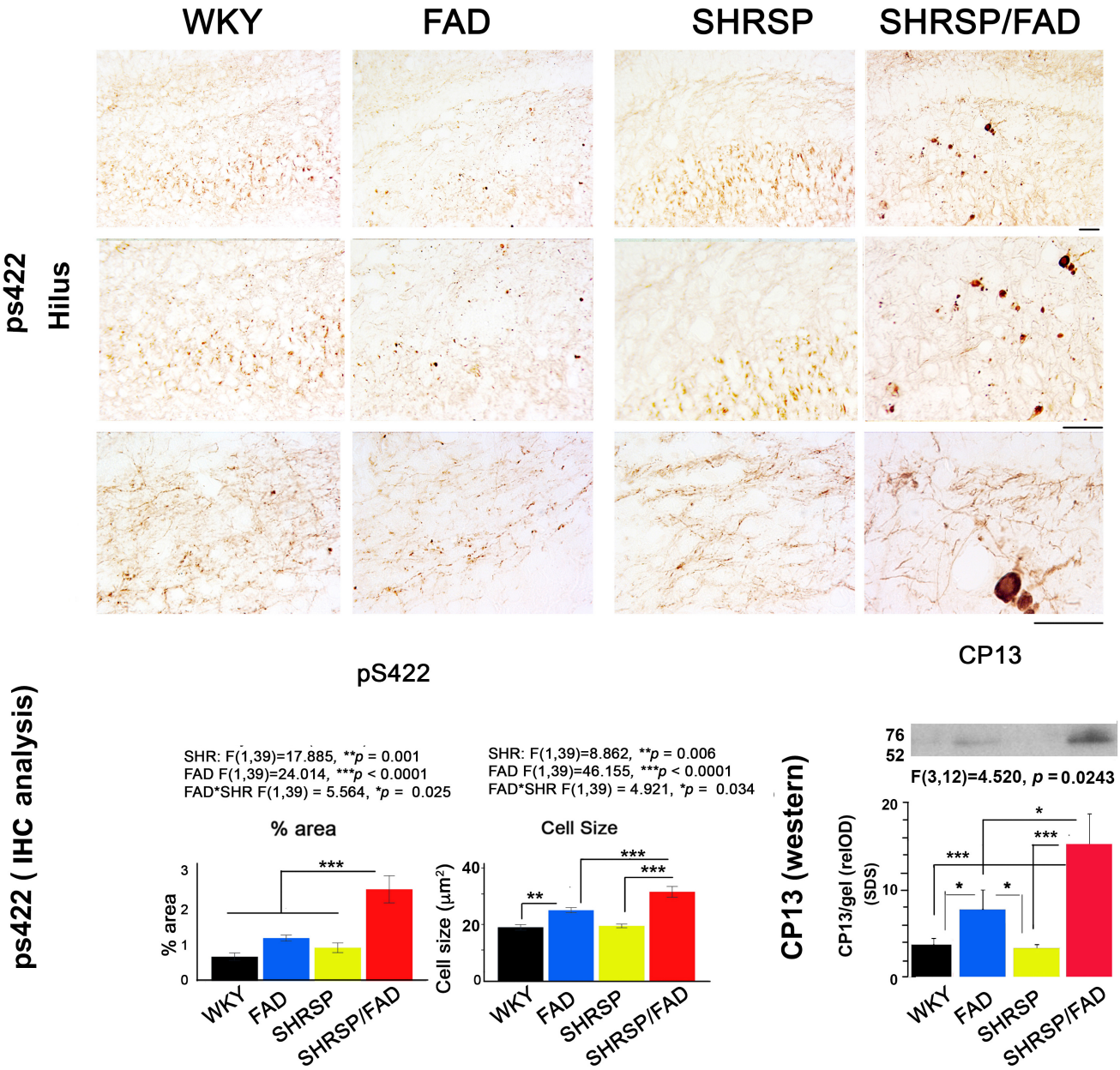

FIGURE 3 | Tau staining and insoluble protein levels are increased in SHRSP/FAD rats. Micrographs depict positive tau pS422 staining in the hilus of the hippocampus of WKY (n = 8), FAD (n = 11), SHRSP (n = 10), and SHRSP/FAD (n = 9) rats. Only SHRSP/FAD rats showed intense staining of neurons labeling globose neurofibrillary tangle-like structures extending tortuous neurites. Two-way ANOVA of percent area and cell size showed significant main effects of SHRSP (p = 0.001, p = 0.006), FAD (p = 0.0001, p = 0.0001) and SHRSP × FAD interactions (p = 0.025, p = 0.034), respectively. Percentage area stained positive for tau pS422 was increased more than two-fold in the SHRSP/FAD rats, compared to WKY, FAD and SHRSP rats ($p < 0.0001$). *Post hoc* analysis indicated that cell size was significantly elevated in the hilus of FAD rats, compared to WKY ($p < 0.01$), while further elevations of tau pS422 cell size were detected in SHRSP/FAD rats, compared to FAD and SHRSP rats ($p < 0.001$). The lower right panel shows representative lanes from a western blot analysis of CP13, an antibody to the serine 202 phospho-epitope of tau from the insoluble SDS fractions of hippocampal lysates. Two-way ANOVA showed a significant FAD effect and a FAD × SHR interaction. *Post hoc* analysis showed that there was a non-significant trend for increased CP13 levels in hippocampus from FAD compared to WKY rats (p = 0.08). However, in SHRSP/FAD rats, levels were significantly elevated compared to SHRSP rats ($p < 0.001$). Furthermore, CP13 levels were significantly elevated in the hippocampus of SHRSP/FAD rats, compared to FAD ($p < 0.05$). Data represent means ± SEM. *$p < 0.05$, **$p < 0.01$, ***$p < 0.001$; two-way ANOVA with LSD Fisher's *post hoc* test.

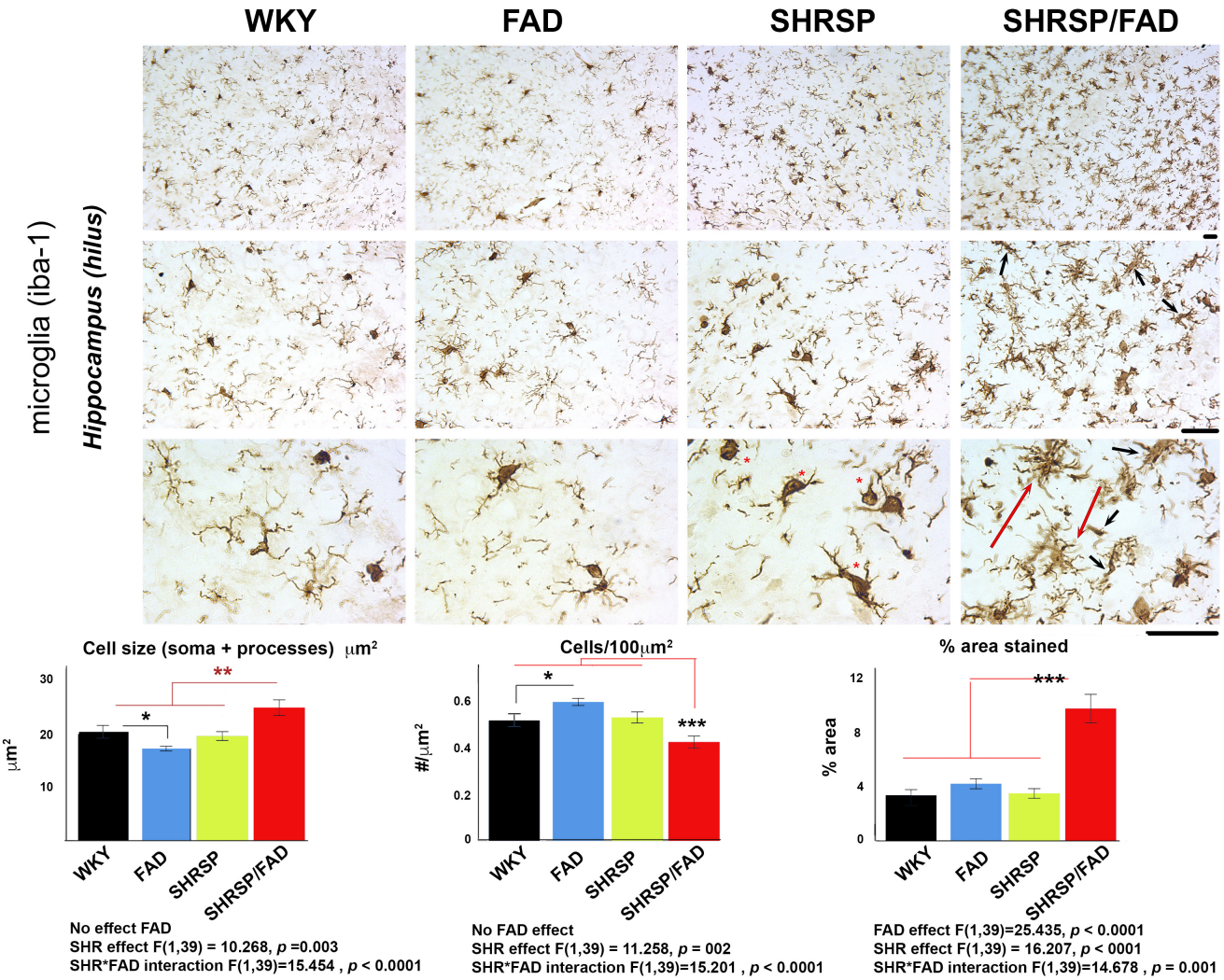

FIGURE 4 | Microglial staining and cell size are increased in SHRSP/FAD rats. Micrographs show Iba1-positive microglia in the hippocampus of the four strains. Microglia in SHRSP, FAD and WKY rats all showed normal ramified morphology with well-defined soma, which was more pronounced in the SHRSP rats (red asterisks). In contrast, microglia in the SHRSP/FAD rat showed hyper-ramified, thickened bushy processes (red arrows) and narrowed soma, some with rod morphology (black arrows). Two-way ANOVA (FAD × SHRSP) and showed a main FAD effect in percent area ($p < 0.0001$) and a significant SHRSP × FAD interaction ($p = 0.001$). *Post hoc* analysis showed that percent area stained for Iba1 was elevated in the hippocampus of SHRSP/FAD rats, compared to all other groups ($p < 0.001$). In fact this interaction was also seen with cell number and cell size, which *post hoc* analysis revealed was similarly due to significantly increased Iba1-positive cell number in SHRSP/FAD rats, compared to all other groups combined ($p = 0.005$). Number of microglia was significantly increased in FAD rats, compared to WKY, whereas cell count was significantly reduced in SHRSP/FAD rats, compared to SHRSP, despite increased area, associated with processes in SHRSP/FAD animals. Data represent means ± SEM. *$p < 0.05$, **$p < 0.01$, and ***$p < 0.001$; two-way ANOVA with LSD Fisher's *post hoc* test.

with observations by IHC, one-way ANOVA showed that there was a main effect of strain ($p < 0.001$). *Post hoc* analysis showed that levels of GFAP were significantly elevated in the lysis fraction from the entorhinal cortex and hippocampus of FAD rats, compared with WKY. However, in SHRSP/FAD rats, levels in both the entorhinal cortex and hippocampus were higher than in all other groups. Together, these data are consistent with multiple brain regions showing increased astrogliosis in FAD rats, which is exacerbated in SHRSP/FAD animals.

Aquaporin-4 Staining of Astrocyte End-Feet in the Hippocampus Indicates Disruption of Morphology in SHRSP/FAD Rats Along With Overall Increased Level of Staining

Figure 6 shows staining forAqp-4, a membrane-bound protein in astrocyte end-feet on vessels that regulates water permeability. In WKY rats, Aqp-4 staining was associated with evenly distributed small tubular vessels (black arrows), while in FAD rats, there were patches of staining of vessels that appeared to be fragmented, tortuous and thin astrocyte processes (red arrows) and swollen

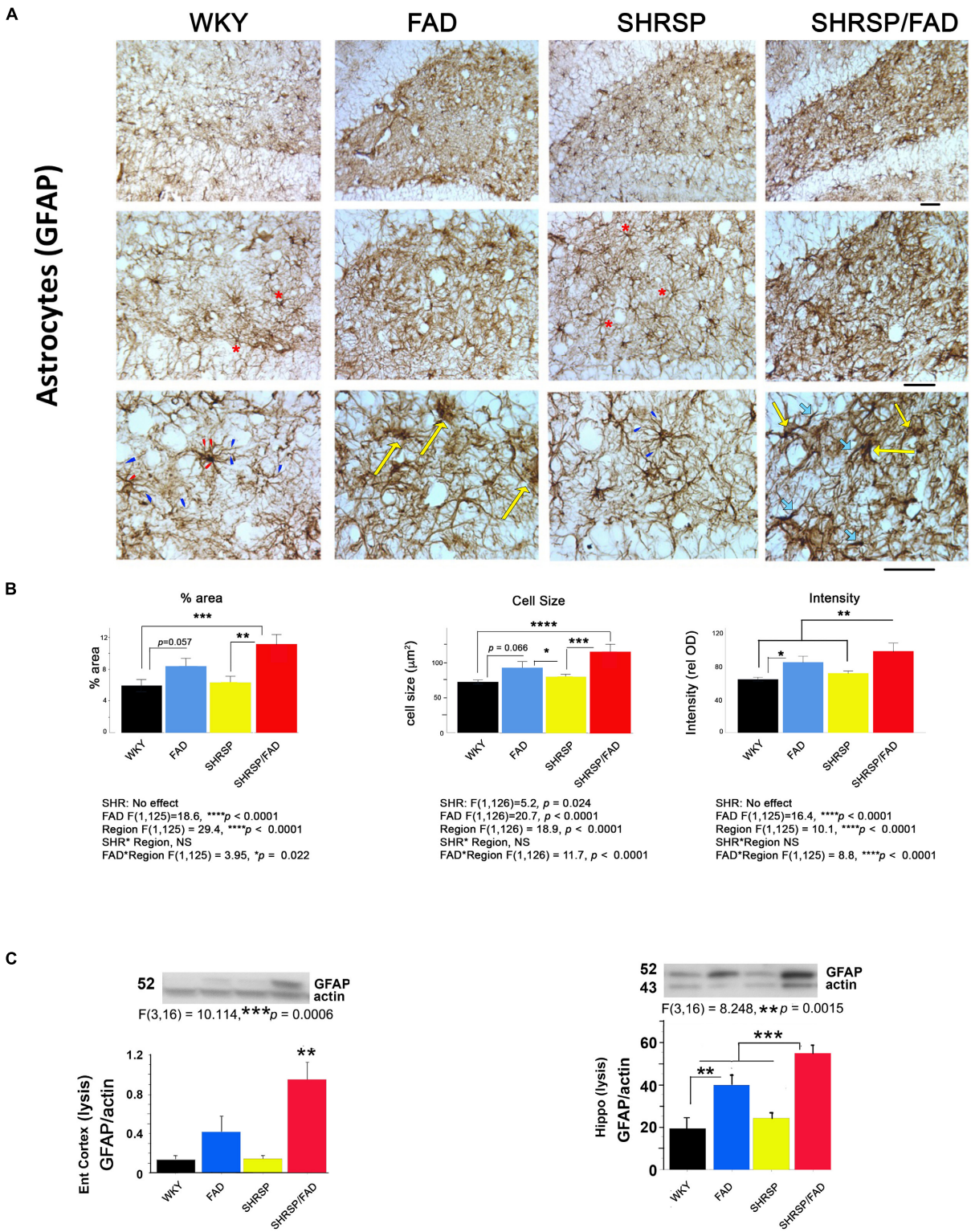

FIGURE 5 | Astrogliosis is augmented in SHRSP/FAD rats. **(A)** Micrographs show immunostaining of brain sections for the astrocytic antigen GFAP. In WKY rats, soma generally extended thick primary branches (red arrowheads), from which multiple secondary and tertiary processes (blue arrowheads) diverged with star-shaped soma typical (red asterisks) of quiescent astrocytes. There was increased GFAP staining throughout the hilus (similar to other regions, not shown) in SHRSP/FAD rats, manifested by hypertrophied soma (yellow arrows) and extended thickened and dense processes (thick light blue arrows) with fewer thin, secondary and tertiary processes, consistent with an activated state. **(B)** Quantitative image analysis showed that, percentage area of GFAP staining was

(Continued)

FIGURE 5 | Continued
significantly elevated in SHRSP ($p = 0.057$) and SHRSP/FAD ($p = 0.001$) rats when compared with WKY, and in SHRSP/FAD rats when compared with FAD ($p = 0.005$). Two-way ANOVA (region × SHRSP × FAD) revealed significant main effects for all variables ($p < 0.0001$), due to a robust increase in GFAP staining in the hilus of FAD rats relative to plaque-sparse regions. GFAP staining intensity was increased further in the hilus of SHRSP/FAD rats ($p < 0.006$). In SHRSP/FAD rats, however, all variables, including cell size, percentage area stained and GFAP staining intensity, were significantly elevated, compared to WKY and SHRSP rats. **(C)** The lower two panels show representative western blot gels from experiments measuring GFAP protein in the lysis fraction of tissue lysates from the entorhinal cortex and hippocampus. One-way ANOVA showed a significant effect of strain on GFAP protein levels in the entorhinal cortex ($p = 0.006$) and hippocampus ($p = 0.0015$) and *post hoc* analysis indicated that GFAP protein levels were significantly elevated in entorhinal cortex and hippocampal tissue from SHRSP/FAD rats, compared to all other groups. GFAP was also significantly elevated in the hippocampus of FAD rats, compared to WKY. Data represent means ± SEM. $^{*}p < 0.05$, $^{**}p < 0.01$, $^{***}p < 0.001$

vessels (blue asterisks). In SHRSP rats, there was an increase in staining of slightly distended but normally shaped tubular vessels (black arrows), compared to WKY.

The FAD-dependent increase in amorphous patches was exacerbated in SHRSP/FAD rats (red arrows). Two-way ANOVA showed no significant interaction of FAD × SHRSP effects for count and percentage area stained. *Post hoc* analysis showed that compared to FAD, there were more Aqp-4 puncta ($p < 0.01$) and higher percentage area stained ($p < 0.01$) in the hippocampus of SHRSP/FAD rats.

Aquaporin-4 Protein Levels Are Increased in the Hippocampus of FAD Rats

Lysates were prepared from hippocampal tissue, and levels of Aqp-4 were measured. Representative lanes of blots are shown in **Figure 6B** (right, mid panel). Since Aqp-4 is prone to multimeric aggregation, we used only 1 microgram of protein and did not boil the sample buffer. Three main bands were identified: 37, 50, and 150 kDa. Data from densitometric analysis were analyzed by two-way ANOVA (FAD × SHRSP × sex), which indicated a significant main effect of FAD on the 150 kDa Aqp-4 band. *Post hoc* analysis showed that total Aqp-4 was significantly elevated in FAD ($p < 0.01$) and SHRSP/FAD ($p < 0.01$), compared to WKY and SHRSP rats, respectively. There was also a sex effect, which *post hoc* analysis showed was due to higher Aqp-4 levels in females across groups. However, there were no differences between strains with sex. In conjunction with Aqp-4, GFAP was measured in the same blot after re-probing, and was found to positively correlate with levels of total ($r^2 = 0.379$, $p = 0.0003$) or monomeric Aqp-4 ($r^2 = 0.216$, $p = 0.0097$).

Aquaporin-4 Levels in Plasma Exosomes

Plasma exosomes were analyzed for Aqp-4 by western blot and relative optical density of the main band (150 kDa), was calculated (**Figure 6C**). The only significant effect observed in the two-way ANOVA was an interaction between FAD and SHRSP, which *post hoc* analysis showed was due to a robust increase in Aqp-4 in SHRSP/FAD rats that was higher than levels in FAD and SHRSP rats ($p < 0.05$).

Collagen IV and PECAM-1 Are Elevated in Brains of SHRSP/FAD Rats

Collagen IV Immunohistochemistry

Figure 7 depicts collagen IV staining in the brains of the four strains, specifically the stratum lucidum of the hippocampus and the globus pallidus of the basal ganglia. In all brain regions of WKY rats, vessels were lightly stained with no collagen IV staining in the vessel lumen. However, the lumen of capillaries in SHRSP rats showed sparse collagen IV immunoreactivity. Within the globus pallidus, a noticeable increase in collagen IV staining in FAD rats was observed, which was further increased in SHRSP/FAD rats, where vessel walls appeared distorted and thickened. Two-way ANOVA of percentage area of collagen IV staining was performed (region × FAD × SHRSP) (**Figure 7B**). Main SHRSP ($p < 0.0001$) and FAD ($p < 0.003$) effects on percentage area stained for collagen IV were significant as for region ($p = 0.003$) and the interaction between region and FAD ($p = 0.028$), likely reflecting regional differences in the percentage area stained for collagen IV (the hindlimb of somatosensory cortex showed the least staining) and the more pronounced group effects in the globus pallidus. The hindlimb of somatosensory 1 was minimally affected: compared to WKY rats, only the percentage area of collagen IV staining was significantly increased in SHRSP ($p < 0.05$). In the hippocampus (stratum lucidum), the SHRSP/FAD group showed the highest percentage area stained ($p < 0.05$). In contrast to these modest effects, there were several group differences within the globus pallidus. Compared to WKY, collagen IV staining was significantly elevated in FAD ($p < 0.001$) and SHRSP ($p < 0.05$) and SHRSP/FAD ($p < 0.0001$) groups, and percentage area stained was higher in the SHRSP/FAD group than in all other groups ($p < 0.0001$).

PECAM-1 (CD31) Is Elevated in Brains of SHRSP/FAD Rats

By western blot, we assessed changes in the endothelial cell tight junction marker PECAM-1 in the cytoskeletal/lysis fraction, to where PECAM-1 is redistributed in response to chronic neuroinflammation and associated with disruption of the BBB (Romer et al., 1995; Ferrero et al., 1996). We measured PECAM-1 by western blot in the lysis fraction from hippocampal tissue as a biomarker of BBB leakage (**Figure 7C**). Representative gel blots are shown in the lower panel (**Figure 7C**). Densitometric analysis of bands was performed and one-way ANOVA demonstrated a significant effect of strain on PECAM-1 levels. *Post hoc* analysis showed that levels of PECAM-1 were significantly elevated in the hippocampal lysis fraction from SHRSP/FAD rats, compared with FAD and SHRSP groups combined ($p < 0.01$). Furthermore, PECAM-1 protein was significantly lower in hippocampal tissue from FAD rats, compared to WKY ($p < 0.05$).

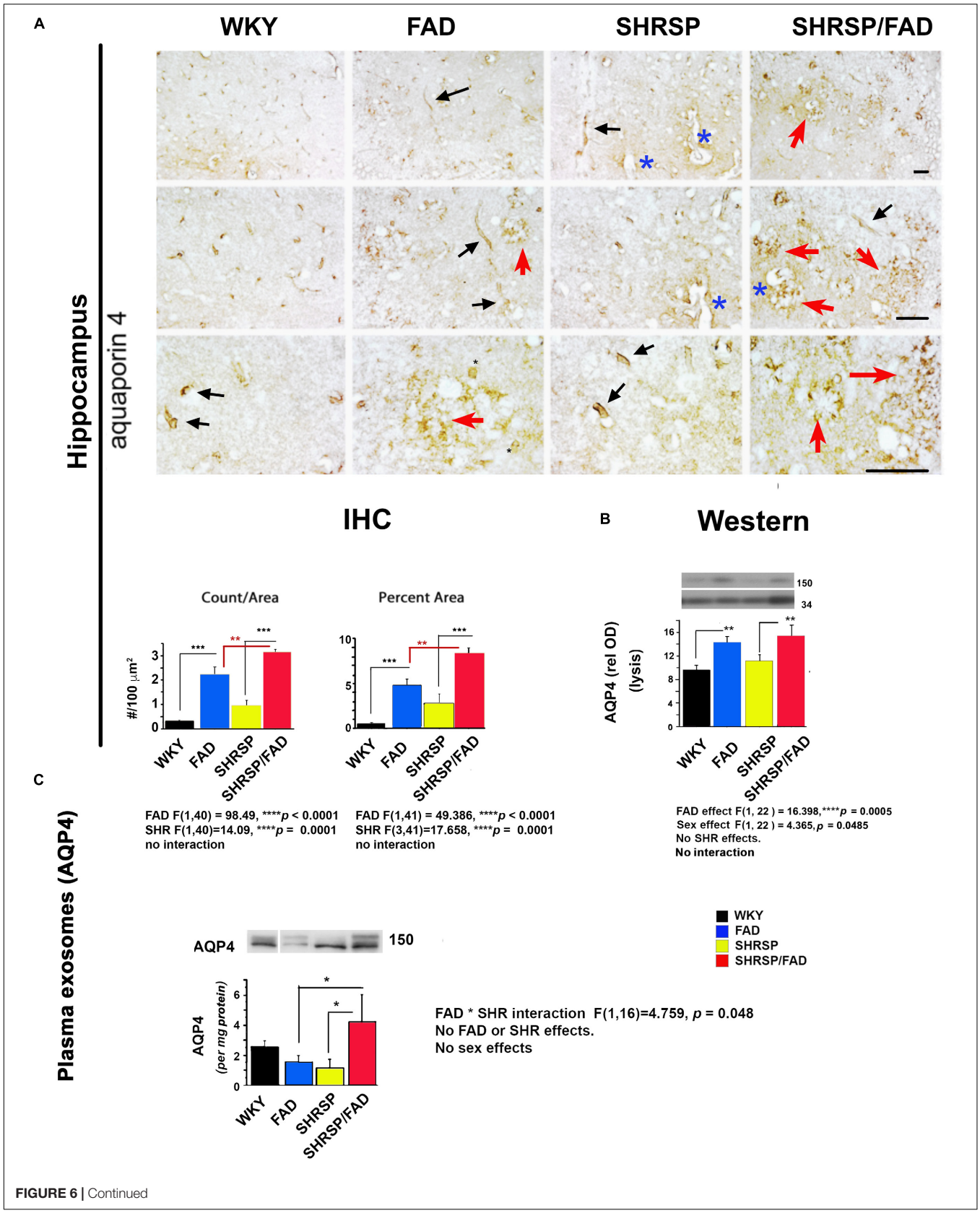

FIGURE 6 | Continued

FIGURE 6 | Aquaporin-4 is elevated in the brains of FAD, with a further increase in SHRSP/FAD rats, while aquaporin-4 protein levels in plasma exosomes were elevated in SHRSP/FAD rats only. **(A)** Micrographs illustrate staining for Aqp-4, a membrane-bound protein in astrocyte end-feet. In WKY rats, staining was associated with evenly distributed small tubular vessels (black arrows), while in FAD rats, staining was in patches of fragmented vessels, tortuous thin astrocyte processes (red arrows) and swollen vessels (blue asterisks). In SHRSP rats, Aqp-4 staining was slightly increased and labeled distended but normally shaped tubular vessels (black arrows). There were more Aqp-4-positive amorphous patches in the hippocampus of FAD rats, an effect that was exacerbated in SHRSP/FAD rats (red arrows). Two-way ANOVA showed FAD ($p < 0.0001$) and SHRSP ($p < 0.0001$) effects for count and percent area. *Post hoc* analysis showed that in the hippocampus, Aqp-4 count ($p < 0.001$) and percentage area stained ($p < 0.001$) were significantly elevated in FAD, compared to WKY rats. This effect was further increased in SHRSP/FAD rats in which Aqp-4 count ($p < 0.01$) and percentage area stained ($p < 0.01$) were significantly increased, compared to FAD rats. In SHRSP/FAD rats, there were more structures stained positively for Aqp-4 ($p < 0.001$) and a higher percentage area stained ($p < 0.001$), compared to SHRSP. **(B)** Aqp-4 was also measured in hippocampal tissue lysates (mid right panel) and analyzed by two-way ANOVA (FAD × SHRSP × sex), which showed a significant main effect of FAD on the 150 kDa Aqp-4. *Post hoc* analysis demonstrated that Aqp-4 (150 kDa) was significantly elevated in the hippocampal tissue from FAD, compared to WKY and SHRSP rats ($p < 0.01$). **(C)** The 150 kDa Aqp-4 protein was also measured in brain-derived plasma exosomes (bottom panel) and two-way ANOVA (FAD × SHRSP × sex) demonstrated a significant interaction between FAD and SHRSP. *Post hoc* analysis showed that Aqp-4 (150 kDa) was significantly elevated in plasma exosomes from SHRSP/FAD rats, compared to FAD and SHRSP rats ($p < 0.05$). Data represent means ± SEM. $^{*}p < 0.05$, $^{**}p < 0.01$, $^{***}p < 0.001$.

Calbindin Staining Is Reduced Slightly in SHRSP and Robustly in SHRSP/FAD Rats, While Caspase-Cleaved Actin Fractin Is Increased in SHRSP/FAD Rats

Calbindin Staining in the Thalamus and Hypothalamus Is Reduced in SHRSP/FAD Rats

To examine neuron damage we stained sections for calbindin, a neuroprotective calcium-binding peptide, which is predominantly enriched in GABAergic neurons, and its loss is associated with tangle pathology (Ahmadian et al., 2015). Images shown in **Figure 8A** illustrate positive calbindin staining in the reticular thalamus and the lateral hypothalamus. The intensity of staining of calbindin-immunoreactive neurons was variable across the strains, but the area stained was noticeably reduced in the SHRSP/FAD group. Two-way ANOVA of percentage area (SHRSP × FAD) in the thalamus showed a significant main effect of SHRSP, and *post hoc* analysis showed reduced calbindin levels in SHRSP ($p < 0.05$) and SHRSP/FAD ($p < 0.001$) rats, compared to WKY (**Figure 8B**). Furthermore, calbindin staining in the thalamus was significantly reduced in SHRSP/FAD rats, compared to FAD ($p < 0.01$), suggesting that calbindin-positive neuron loss in the thalamus was exacerbated in SHRSP/FAD rats, compared to FAD rats without hypertension. In the hypothalamus, there was a significant main effect of FAD ($p < 0.025$), in addition to a significant SHRSP effect ($p < 0.0001$). *Post hoc* analysis showed that percentage area of calbindin staining was significantly reduced in the hypothalamus of SHRSP/FAD rats, when compared to all other groups ($p < 0.01$) rats (**Figure 8B**). Together, these data support that the reduction of calbindin staining in the brains of SHRSP rats is exacerbated in SHRSP/FAD animals.

Levels of Most Synaptic Proteins Were Unchanged in the Hippocampus, While NR2B and Caspase-Cleaved Actin (Fractin) Were Elevated in SHRSP/FAD Rats

To further examine neurodegeneration, we measured synaptic proteins in membrane-enriched fractins in western blots (not shown). There were no changes in levels of pre-synaptic proteins SNAP25 and synaptophysin, nor in levels of the post-synaptic protein drebrin, however, levels of post-synaptic NR2B were different among strains (**Figure 8D**). *Post hoc* analysis showed that, although FAD showed a slight elevation in NR2B levels compared to WKY, NR2B levels were elevated in the SHRSP/FAD groups more than all other groups ($p < 0.01$).

We also measured caspase-cleaved actin (fractin (Yang et al., 1998), as an indicator of caspase-mediated apoptosis (**Figure 8**, lower panel). One-way analysis of relative optical density (relOD) of the bands showed a significant strain effect [$F(3,16) = 4.2$, $p = 0.045$] and *post hoc* analysis showed that levels of caspase-cleaved actin in the SHRSP/FAD rats were significantly higher than in WKY rats ($p < 0.05$).

Luxol Fast Blue Staining Shows Demyelination in White Matter Tracts in SHRSP Which Is Exacerbated in SHRSP/FAD Rats

Figure 9 depicts representative images of the retrosplenial cortex and hippocampus of all strains stained with Luxol fast blue, to visualize changes in myelin distribution between strains. Qualitative evaluation by an experimenter blinded to transgene, showed changes in myelin in both regions among the strains. In the cortex and corpus callosum (CC) (top panel) of WKY rats, there was extensive Luxol fast blue staining, which densely labeled the CC and was evenly spread. However, in FAD rats there were dark patches of Luxol fast blue, interspersed with white patches of demyelination. In contrast to these minor changes in FAD rats, there was notable loss of myelin patches in both SHRSP groups in the CC and cortex. In the SHRSP/FAD rat occasional lacunae appeared in the perirhinal cortex (not shown) and in the cortex-CC interface surrounded by a halo of demyelination (top right panel).

Selective layers of the hippocampus were affected differentially in the four strains. There was no change in Luxol fast blue in the stratum molecular among strains, but in the FAD and SHRSP rats, there was some loss of myelin in the stratum radiatum and lucidum reflected in irregular patches of blue in the FAD rat brain, with more extensive loss in the SHRSP/FAD rats. The most pronounced loss of myelin was seen in the hippocampal fissure of the SHRSP/FAD rat, when compared with all other strains.

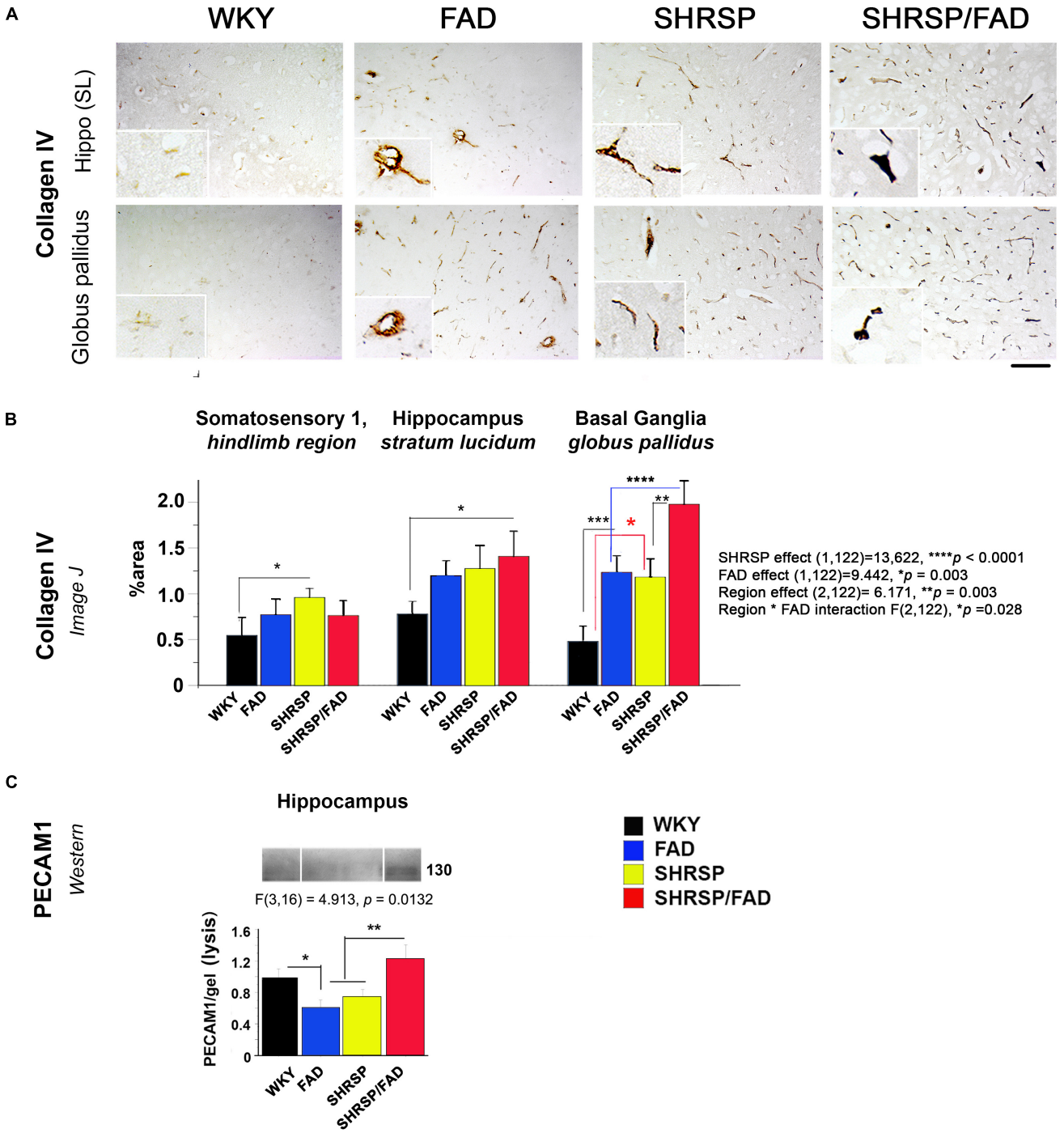

FIGURE 7 | Collagen IV deposition is increased in FAD and SHRSP rats, while PECAM-1 is increased in SHRSP/FAD rats only. **(A)** Micrographs depict collagen IV staining in stratum lucidum of the hippocampus and globus pallidus of the basal ganglia. In all brain regions of WKY rats, vessels were lightly stained, and there was no staining in the vessel lumen. However, in SHRSP rats, the lumen of capillaries showed sparse collagen IV immunoreactivity. There was increased staining in the globus pallidus of FAD rats, which was exacerbated in SHRSP/FAD rats, in which vessel walls appeared distorted and thickened. **(B)** Two-way ANOVA was performed [region (three brain regions) × FAD (Tg+ or Tg–) × SHRSP (non-SHRSP or WKY)].The main effects for both SHRSP were highly significant ($p < 0.0001$), and the effects for FAD, the effects of region and the interaction between FAD and region were also significant ($p = 0.003$, $p = 0.003$, and $p = 0.028$ respectively). *Post hoc* analysis with planned comparisons showed elevated intensity of collagen-IV staining in the hindlimb of SHRSP rats, compared to WKY ($p < 0.05$). In stratum lucidum of the hippocampus, collagen-IV staining was significantly elevated in SHRSP/FAD rats, compared to WKY ($p < 0.05$). Collagen-IV staining was

(Continued)

FIGURE 7 | Continued
increased significantly in the globus pallidus of FAD ($p < 0.001$) and SHRSP rats ($p < 0.0001$), compared to WKY. In SHRSP/FAD rats, collagen-IV staining was significantly increased further compared to FAD ($p < 0.001$) and SHRSP ($p < 0.01$) rats. **(C)** We also measured endothelial cell marker PECAM-1 in the lysis fraction of hippocampal tissue. Representative gel blots are shown and densitometry of bands was evaluated via one-way ANOVA, which demonstrated significant effects of strain on PECAM-1 levels. *Post hoc* analysis showed that levels of PECAM-1 were significantly elevated in the hippocampal lysis fraction from SHRSP/FAD rats, compared with FAD and SHRSP rats ($p < 0.01$). Levels of PECAM-1 were also significantly reduced in FAD rats, compared to WKY ($p < 0.05$). Data represent means ± SEM. $^{*}p < 0.05$, $^{**}p < 0.01$, $^{***}p < 0.001$, $^{****}p < 0.0001$.

Mitochondrial Complex I Is Reduced in Brains of SHRSP/FAD and FAD Rats, While Complex II Is Reduced in SHRSP/FAD Rats Only

Figure 10 shows representative lanes of the western blot of mitochondrial complexes I-V from hippocampal tissue. MANOVA was performed on protein band relOD of Complexes I (log transformation), and II -IV (Complexes I-IV × SHRSP × FAD). Results showed a significant main FAD effect [$F(4,23) = 3.421$, Wilks $\lambda = 0.627$, $p = 0.025$]. The univariate test showed significant FAD main effects on Complexes I and II ($p < 0.0001$ and $p < 0.039$, respectively), but not III or IV. Levels of Complex I were significantly reduced in FAD ($p < 0.01$) and SHRSP/FAD ($p < 0.01$) rats, compared to WKY, while Complex II was reduced three-fold in SHRSP/FAD rats only ($p < 0.05$). These data suggest that mitochondrial Complex I is depleted in the hippocampus of FAD rats only and Complex II is depleted in the SHRSP/FAD.

SHRSP Does Not Exacerbate FAD Deficits in Y Maze and Novel Object Recognition but Has Independent Effect on Hyperactivity

Novel Object Recognition Task

Two-way ANOVA (object preference × strain) demonstrated a significant preference for the novel object during the test phase of the NOR task in WKY rats ($p < 0.001$), however, in FAD animals, the recognition index (RI) [(time exploring novel object)/(time exploring both objects)] for the novel object did not differ significantly from that of the familiar object ($p > 0.05$) in any of the other strains, indicating a failure to recognize the novel object as a result of impaired working memory in SHRSP, FAD and SHRSP/FAD rats. Similar results were observed when calculating a discrimination index (DI) [(novel time –familiar time)/(novel time + familiar time)].

It is noteworthy that distance (**Figure 11A**) and speed (not shown) were significantly higher in SHRSP and SHRSP/FAD animals during the NOR test phase, when compared with control and FAD rats (**Figure 11**). Similar hyperactivity was evident in SHRSP and SHRSP/FAD animals during the open field task (OFT) (not shown). Collectively these data are consistent with SHRSP not affecting preference for novel object with or without FAD, but causing hyperactivity independent of FAD.

Y Maze

During an 8-min Y maze task, correct arm entries, speed, distance (**Figure 11B**), spontaneous alternation, and errors (not shown) were assessed. Two-way ANOVA (FAD × SHRSP) showed significant main effects of FAD on correct arm entries, speed and distance ($p < 0.005$), but no SHRSP effects or interactions.

Post hoc analysis showed a correct arm entries were significantly lower in FAD rats compared to WKY ($p = 0.0026$), and while there was also a reduction in correct arm entries in the SHRSP/FAD rats, this difference did not reach significance. *Post hoc* analysis also showed that SHRSP/FAD rats were significantly slower in the Y maze than SHRSP rats ($p = 0.0042$), while a slight reduction of speed in FAD rats, compared to WKY, was not significant. Finally, FAD-dependent reductions in speed were shown by *post hoc* analysis, whereby FAD and SHRSP/FAD rats were significantly slower in the Y maze, when compared with WKY ($p < 0.01$) and SHRSP ($p < 0.001$) rats, respectively.

DISCUSSION

Here we present an initial characterization of a novel rat model of MxD, exhibiting complex interactions between chronic hypertension and AD pathology. Crossing the SHRSP background into the FAD rats (SHRSP/FAD) produces a line that retains both the AD phenotype with extensive plaque pathology as well as the SHRSP hypertensive phenotype. Importantly to facilitate the investigation of direct effects of hypertension on AD dementia, we created a FAD+ control line, by introducing WKY background (non-hypertensive background strain for the SHRSP), which retained the FAD transgene-dependent neuritic plaque phenotype and behavioral deficits of the original F344 line.

Our data show region-dependent synergistic interactions, with exacerbated metabolic deficits, demyelination, gliosis, tau pathology and neurodegeneration in SHRSP/FAD rats, which is consistent with clinical and neuropathological data suggesting that coexistence of subclinical AD and SVD pathologies may lower the threshold for dementia risk (Fischer et al., 1991). We also observed exacerbation of SHRSP-dependent vascular changes in SHRSP/FAD rats, indicative of leakage and disruption of the BBB, but without greatly exacerbating AD plaque burden, consistent with the clinical neuropathological data on neuritic plaques in MxD (Petrovitch et al., 2005). This novel model should allow a better understanding of how hypertension may differentially affect neuritic and diffuse plaque and vascular amyloid pathology. It may provide a useful model for translation to identify how hypertensive phenotypes may interfere with the efficacy of some AD therapeutics, possibly even when vascular or AD pathological markers are below levels of detectability with standard neuroimaging (Fischer et al., 1991; Baker et al., 2012). This type of model is critical as undetected vascular damage could limit the efficacy of drugs that target AD pathology

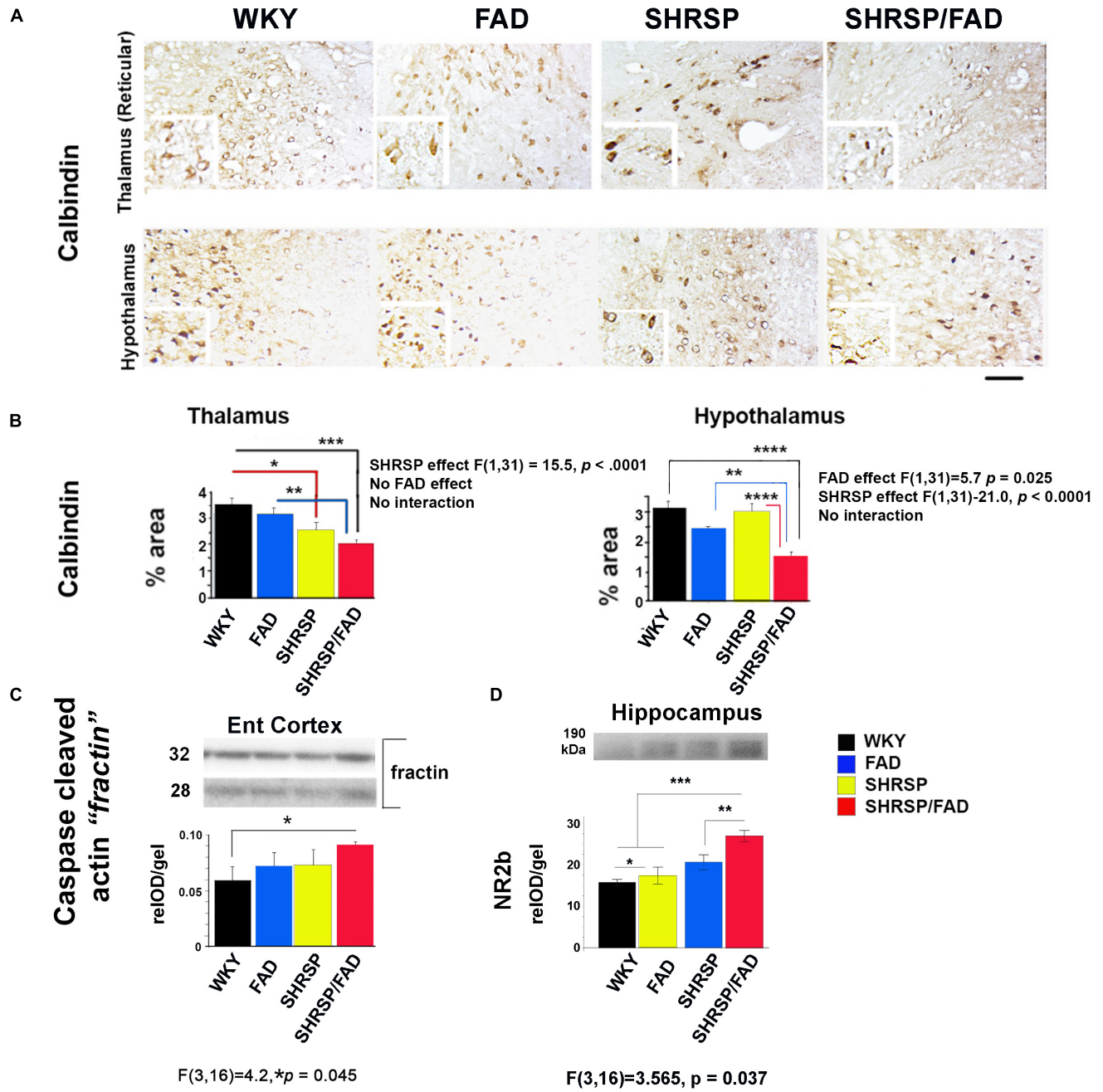

FIGURE 8 | Neuron-specific calbindin is reduced in SHRSP/FAD rats, while caspase-cleaved actin is increased. **(A)** Micrographs depict calbindin staining in the hypothalamus and thalamus showing numerous calbindin-immunoreactive neurons. **(B)** Two-way ANOVA of percentage area stained (SHRSP × FAD) in the reticular thalamus showed no effect of sex, but a significant main effect of SHRSP ($p < 0.0001$), consistent with *post hoc* analysis, which showed that calbindin staining was reduced in SHRSP ($p < 0.05$) and SHRSP/FAD ($p < 0.001$) rats, compared to WKY. Furthermore, calbindin staining was significantly reduced in SHRSP/FAD rats, compared to FAD ($p < 0.01$), suggesting that FAD exacerbates neuron loss in SHRSP rats. Changes in calbindin staining in the hypothalamus were similar, and while there was a main SHRSP effect ($p < 0.0001$), there was an additional FAD main effect ($p < 0.025$). *Post hoc* analysis showed that calbindin staining was significantly reduced in the hypothalamus of SHRSP/FAD rats, compared to SHRSP ($p < 0.0001$), FAD ($p < 0.01$), and WKY ($p < 0.0001$) rats. **(C)** We also measured caspase-cleaved actin in the entorhinal cortex as an indication of caspase activity by western blot (lower panel). One-way ANOVA of relative optical density showed a significant strain effect ($p = 0.045$), and *post hoc* analysis showed that levels of caspase-cleaved actin were increased in SHRSP/FAD rats compared to WKY rats ($p < 0.05$). **(D)** Levels of post-synaptic NR2B were significantly different among strains. There were main effects of strain, and *post hoc* analysis showed a slight elevation of NR2B levels in FAD compared to WKY, but levels in SHRSP/FAD groups were higher than all other groups ($p < 0.01$).Data represent means ± SEM. $^{*}p < 0.05$, $^{**}p < 0.01$, $^{***}p < 0.001$, $^{****}p < 0.0001$; one- and two-way ANOVA with LSD Fisher's *post hoc* test.

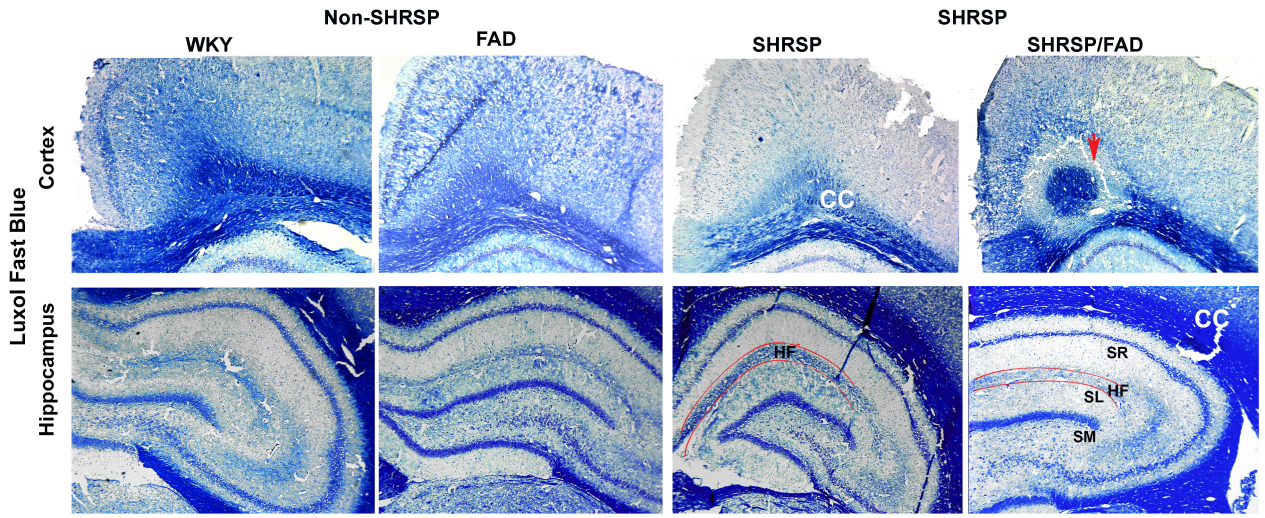

	cortex demyelination	Corpus Callosum demyelination	hippocampus (demyelination) lacuna	SR	HF	SL	SM
WKY	control	control	control	control	control	control	control
FAD	+	+	ns	ns	ns	+	ns
SHRSP	++	++	ns	+	ns	+	ns
SHRSP/FAD	+++	++	+	++	+++	++	ns

FIGURE 9 | Demyelination in the cortex, corpus callosum and the hippocampal fissure of SHRSP/FAD rats. Sections were stained with Luxol fast blue to visualize changes in myelin distribution between the different strains. Qualitative evaluation by a blinded experimenter showed changes in myelin in both regions among the strains. Top panels show extensive, evenly spread Luxol fast blue staining, which densely labeled the corpus callosum (CC) of WKY rats. However, in FAD rats, there were dark patches of Luxol fast blue, interspersed with white patches of demyelination. In contrast to these minor changes in FAD rats, there was a notable loss of myelin patches in the CC and cortex of SHRSP and SHRSP/FAD groups. The top right panel shows a lacuna in the cortex-CC interface surrounded by a halo of demyelination (red arrow). There was no change in Luxol fast blue in the stratum molecular (SM) among strains, but in the FAD and SHRSP rats, there was some loss of myelin in the stratum radiatum (SR) and lucidum (SL) reflected by irregular patches of blue in the FAD rat, with more extensive loss in the SHRSP/FAD rats. The most pronounced loss of myelin was seen in the hippocampal fissure of SHRSP/FAD rats.

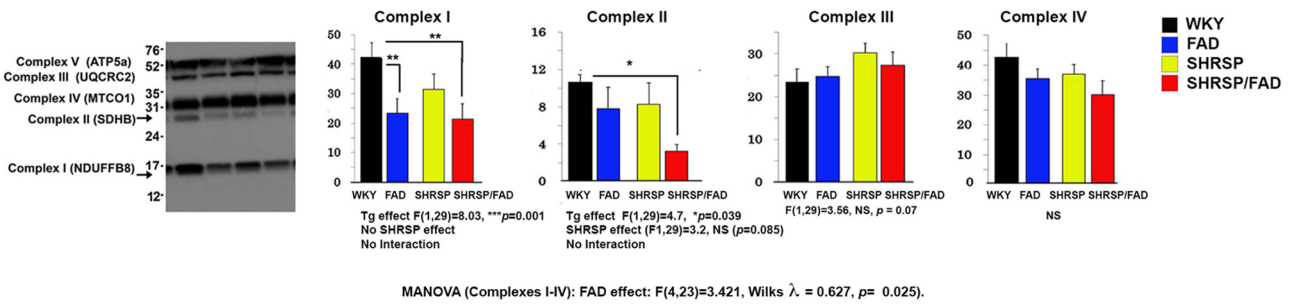

FIGURE 10 | Mitochondrial complex II is reduced in the hippocampus of SHRSP/FAD rats and mitochondrial complex I is reduced in FAD rats. We measured mitochondrial complexes I-IV from hippocampal tissue by western blot and MANOVA was performed on the relative optical densities of protein bands from complexes I (log transformation), and II-IV. Results showed no sex effects, but a significant main FAD effect ($p = 0.025$) and the univariate test showed significant FAD main effects for Complexes I and II ($p < 0.0001$ and $p < 0.039$, respectively), but not III and IV. Although complex I proteins were significantly reduced in SHRSP/FAD ($p < 0.01$) and FAD ($p < 0.01$) rats, compared to WKY, complex II levels, were significantly reduced more than threefold in SHRSP/FAD rats, compared to WKY ($p < 0.05$). Data represent means ± SEM. *$p < 0.05$, **$p < 0.01$; MANOVA with Wilks λ test and LSD Fisher's *post hoc* test.

alone. Moreover, this model may be useful for preclinical research aimed at delineating the pathophysiology of VaD and MxD and development of therapies for patients with MxD, in which the causes of cognitive decline are complex and therapeutic efficacy and safety may be limited by coexisting pathologies in MxD or VaD.

Subtle Changes in Plaque Pathology in the SHRSP/FAD Rat

SHRSP did not have an overwhelming impact on overall plaque burden in the FAD rats, as it slightly reduced Aβ staining in entorhinal and perirhinal cortices of SHRSP/FAD rats, increased Aβ in the hilus and vessel-rich hippocampal

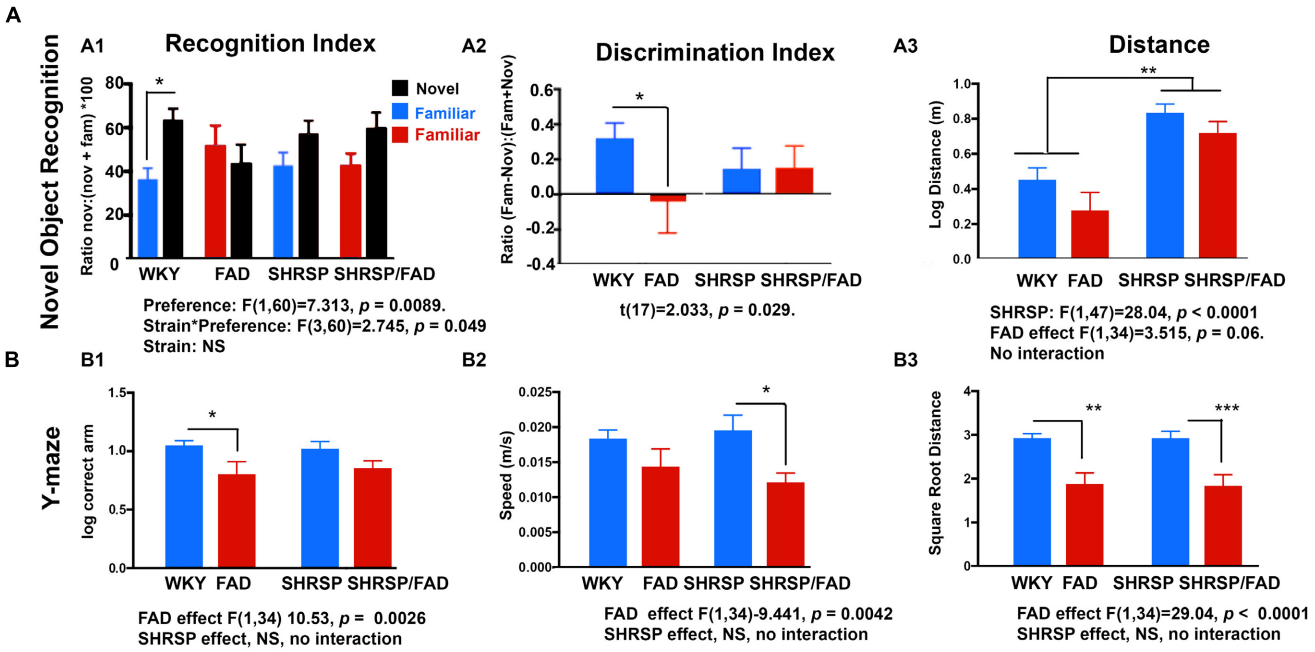

FIGURE 11 | Performance in the novel object recognition and Y maze tasks by WKY, FAD, SHRSP and SHRSP/FAD rats. Data were analyzed by two-way ANOVA (FAD × SHRSP). **(A)** The novel object recognition (NOR) task involved 2 days of habituation, followed by exposure of the rats to two identical objects in an acquisition phase, prior to a test phase, following a retention period of 1 h. Graphs depict recognition indices (RI; time exploring novel or familiar object/time exploring both objects × 100) and discrimination index [DI; (time exploring novel object – familiar object)/(time exploring novel object + familiar object)] in the test phase of the NOR task in FAD (n = 11), SHRSP (n = 10), SHRSP/FAD (n = 9) and non-transgenic (n = 8) rats. Two-way ANOVA showed no sex effect, but there was an interaction between strain and object preference ($p < 0.05$) and object preference ($p = 0.0089$). Fisher's LSD *post hoc* comparisons indicated that only WKY controls showed a significant preference for the novel object ($p < 0.05$). Similar results were seen with the two-way ANOVA with DI. Similarly, although two-way ANOVA showed that variation of the DI among groups in the test phase of the NOR task was not significant, t-tests within groups showed that the NOR test phase DI was significantly lower in FAD rats, compared to WKY ($p = 0.029$). However, the trends for lower DI in SHRSP and SHRSP/FAD rats, when compared with WKY, were non-significant. Two-way ANOVA of distance traveled during test phase of the NOR task showed a significant effect of SHRSP ($p < 0.0001$), and a trend for a main effect for FAD ($p = 0.06$). Fisher's LSD *post hoc* analysis showed that distance traveled in the SHRSP group was significantly higher than in WKY ($p < 0.01$). Since there was no interaction, the near significance of FAD is attributed to similar reductions in distance, independent of SHRSP. **(B)** Performance in the Y maze is shown for FAD, SHRSP, SHRSP/FAD and WKY rats. No differences in spontaneous alternation were seen between strains (not shown). Correct arm entries were assessed by two-way ANOVA showing no interaction between strain and FAD, although there was a significant FAD effect ($p < 0.0026$). *Post hoc* analysis revealed that the number of correct arm entries was significantly lower in FAD rats only, compared to WKY ($p < 0.05$). Similarly there was a significant FAD effect on speed ($p < 0.0042$) and distance ($p < 0.0001$) in the Y maze. *Post hoc* analysis showed that speed was significantly lower in SHRSP/FAD rats, compared to SHRSP, while distance was reduced in FAD and SHRSP/FAD rats, compared to WKY ($p < 0.01$) and SHRSP ($p < 0.001$), respectively. Data represent means ± SEM. $^*p < 0.05$, $^{**}p < 0.01$, $^{***}p < 0.001$; one-way ANOVA with Fisher's LSD *post hoc* test.

fissure and altered plaque morphology, reducing the plaque's neuritic dense-core plaques decorating FAD brain. This is contrast to the models with hypertension induced increases in Aβ discussed in the introduction. Although we lack rigorous clinical data describing differences in plaques between AD and MxD, our data is consistent with findings in the Honolulu Aging Study showing increased dementia risk developing in cognitively normal men with vascular pathology who were found to have increased tau pathology but fewer neuritic amyloid plaques (Petrovitch et al., 2005). Together these data support that, although hypertension exerts complex effects on Aβ pathology, it does not accelerate plaque pathogenesis in our model or in humans.

Whether or not hypertension attenuates the evolution of the diffuse plaque into a dense neuritic plaque or directly affects preexisting neuritic plaques, regional differences in neuroinflammatory responses could explain this effect. Compared to WKY, we observed relatively region-independent increased neuroinflammatory responses in SHRSP. FAD rats had much higher glial responses than SHRSP rats but this was region-dependent and particularly high in plaque-rich regions like the hilus, with disproportionate plaque burden, and less where there were fewer plaques (entorhinal, perirhinal), consistent with a strong inflammatory response to plaques. Therefore, the regional variations in plaques in SHRSP/FAD could be related regional glial responses to plaques, increasing or attenuating clearance. It should also be investigated whether diminished plaques could occur directly in response to hypertension as in the mutant APP crossed onto db/db mice which have hypertension and Type II diabetes and show a slight reduction in plaques (Ramos-Rodriguez et al., 2015; Infante-Garcia et al., 2016) or result secondary to enhanced clearance from lacunar stroke and increased monocyte/macrophage invasion (Frautschy et al., 1992).

In addition to possible innate immune clearance mechanisms, our model may impact LRP1 which mediates Aβ efflux in cerebral microvessels (Donahue et al., 2006; Kanekiyo et al., 2012) or receptor for advanced glycation end products (RAGE) in neurons which can mediate Aβ influx (Deane et al., 2003) or LDLR that can reduce Aβ (Kim et al., 2009; Katsouri and Georgopoulos, 2011). Specifically it would be important to examine redistribution of RAGE and LRP1 between microvasculature and neurons which appears Aβ or AD specific (Donahue et al., 2006; Shang et al., 2019) and increased expression of the low-density lipoprotein receptor (LDLR) which appears hypertension or SHRSP-specific (Ueno et al., 2010). However, whatever the mechanisms involved are, the Aβ effects are surprisingly small and regional and not the salient interactive feature in our model or in humans. The mechanisms determining potentially regional changes in Aβ clearance affecting plaque pathology include regional cerebral hypoperfusion and are clearly complex and poorly understood. Notably, two studies with surgically induced or angiotensin II infusion-induced hypertension did not show hypertension-associated amyloid reduction (Cifuentes et al., 2015; Shih et al., 2018). Although those studies did not evaluate plaque burden in the regions described here, they support our conclusions that the impact on plaques is subtle and requires more thorough examination of vascular amyloid and the relationship of vessels to focal changes in cerebral blood flow, neuroinflammation, lacunar or vascular changes, plaque size, texture and distribution in the SHRSP/FAD rat and in patients with MxD.

One limitation of our study is that because amyloid effects were small and regional, we did not pursue regional effects of SHRSP on amyloidogenic APP processing or changes in soluble oligomeric species. One might expect that there would be synergism between effects of hypertension and AD on APP processing, since hypertension models suggest that with aging hypertension increases the activity of β-secretase (not mRNA) as well as APP binding proteins (Csiszar et al., 2013; Zhang et al., 2018, 2019) and in AD models, expression of β-site amyloid precursor protein-cleaving enzyme 1 (BACE1) can be upregulated by oxidative damage or inflammation (Zhang et al., 2018). However, synergism between effects of hypertension and AD on APP processing as a primary mechanism, is not supported by the subtle differences in Aβ observed in our model and in human MxD data.

Diffuse extracellular Aβ has been reported in brains of SHRSP rats (Bueche et al., 2014; Schreiber et al., 2014) using anti-Rodent Aβ antibody, which binds to the three rodent specific amino acid differences present in Aβ 1-16, but also in full length APP and its C-terminal fragment. Unfortunately, labeling with this class of 1–16 region antibody also detects APP and its non-Aβ products associated with sites of axonal injury as well as Aβ. While we used polyclonal anti human Aβ (Launer et al., 2000; Petrovitch et al., 2000; Ferri et al., 2005; Petrovitch et al., 2005; Jellinger and Attems, 2007; Kalaria et al., 2012; Hebert et al., 2013; Rodrigue et al., 2013; Wimo et al., 2013; Gottesman et al., 2014; Oberlin et al., 2015; Khan et al., 2016; Custodio et al., 2017; Walker et al., 2017; Vinters et al., 2018; Wennberg et al., 2019) and showed that SHRSP rats showed rare sparse vascular Aβ pathology and rare diffuse plaques, our findings are still in agreement with Schreiber's group who found limited Aβ deposition or neuritic plaques in SHRSP rats in contrast to the extensive deposition observed in our FAD and SHRSP/FAD groups.

Robust Changes in Tau Pathology in the SHRSP/FAD Rat

The F344 Tg AD rat, from which our model was derived exhibits amyloid plaque pathology, insoluble tau and age-dependent cognitive deterioration, but surprisingly insoluble tau is reduced with age in the original report (Cohen et al., 2013). However, the introduction of hypertension in SHRSP/FAD rats robustly increased tau pathology. Importantly these data show that low levels of vascular pathology caused by hypertension may exacerbate tau pathology, despite minimal effects on amyloid pathology. There has not been research directly investigating hypertension and tau, however, there are two reports that indirectly support our observations. First, APP mice with the hypertensive db/db background show increased phospho- tau levels (Ramos-Rodriguez et al., 2015; Infante-Garcia et al., 2016), but increased Aβ and neuroinflammation associated with diabetes in this model could have driven tau hyperphosphorylation independent of hypertension. As described above, cognitively normal men with hypertension, who have fewer neuritic plaques but more tau pathology are at increased risk for AD (Petrovitch et al., 2005). Thus, if validated with further clinical and longitudinal neuropathological studies, our initial finding that hypertension increases tau pathogenesis in our MxD model would be an important advance in the field.

The Schreiber group reported that the SHRSP rat exhibits tau hyperphosphorylation (Schreiber et al., 2014), however, no evidence of unambiguous neurofibrillary tangles or detergent insoluble tau was established. Because hyperphosphorylation of tau is commonly observed with rodent brain injury and inflammation in the absence of detergent insoluble tau or tangles, findings of increased ptau by ICC or soluble ptau cannot be conflated with insoluble aggregating tau or tangles but it may indicate a relevant imbalance in tau kinases, phosphatases or clearance mechanisms. While p-tau levels in the present study were comparable between FAD and SHRSP rats, contrary to (Schreiber et al., 2014), several differences exist between their methods and ours. (1) the Schreiber laboratory used AT8 [to both Tau pSer202 and pThr205 (Schreiber et al., 2014) while we used pS422 and CP13 to Tau pSer422 and Tau pSer202, respectively; (2) they did not used phosphatase inhibitors that prevent post mortem phosphorylation, (3) they only used males which have more hypertension; and (4) they evaluated the cortex while we evaluated hippocampus. Nevertheless, our combined results suggest chronic hypertension may promote tauopathy, a known path to neurodegeneration.

Robust Increases in Microglial and Astrocytic Neuroinflammation in the SHRSP/FAD Rat

Similar to AD (Akiyama et al., 2000) and CBVD (Gallart-Palau et al., 2017), there was increased microgliosis and

hyperplasia of astrocytes in both FAD and SHRSP rats. Although increased neuroinflammation has previously been reported in both models (Sabbatini et al., 2002; Cohen et al., 2013; Tayebati et al., 2016), this is the first observation showing an additive response with the coexistence of robust AD pathology and hypertension. Specifically, brains of SHRSP/FAD rats showed increased glial density and percentage of positive staining. Notably, average microglia and astrocyte cell size were further elevated in the cross, indicative of reactive cells. Compared with SHRSP rats, which are not reported to show hypertrophy of astrocytes (Sabbatini et al., 2002; Tayebati et al., 2015), astrocytes in brains of SHRSP/FAD rats were significantly larger. Our data suggest that the combination of SHRSP phenotype with the AD transgene in the SHRSP/FAD rat enhances gliosis and possibly neuroinflammation generally in the brain beyond that seen with either alone which suggests a synergistic amplification of this pathology caused by the coexistence of AD pathology and hypertension. Further examination of the transcriptomic and functional profiles of glial cells in specific regions of these animals will help to clarify the effect that hypertension has on glial cells in the context of AD. Not only was microgliosis increased in SHRSP/FAD rats, microglial morphology was also different, compared with all other animals. Many microglia in the brains of SHRSP/FAD rats were rod-shaped and had more processes, such that there was more total Iba1-positive area stained, despite fewer microglial cells. Notably, several microglia had larger cell bodies, which typically associated with microvessels. Previously in a mouse model of stroke, it was found that microglia played a pathogenic role surrounding and phagocytosing endothelial cells leading to the disintegration of vessels, which was in part stimulated by fibrinogen or albumin, both indices of vessel leakage (Jolivel et al., 2015). While we did observe vessel-associated microglia and the density of vessels associated with Aqp-4 and collagen IV, we did not evaluate the density of all vessels. However, dysregulated Aqp-4 staining, an astrocytic endfoot protein that associates with cerebral blood vessels, in the SHRSP/FAD rat is consistent with damage to the neurovascular unit.

Aquaporin-4 in Microvessels in the SHRSP/FAD Rat

Parallel to GFAP changes, the astrocytic endfoot protein Aqp-4 was upregulated in the hippocampus of SHRSP/FAD rats. It is known that Aqp-4 is increased in brains of SHRSP rats (Tomassoni et al., 2010; Tayebati et al., 2015) and in AD brain, in association with amyloid plaques (Hoshi et al., 2012; Yang et al., 2017). Our data indicate that this upregulation of Aqp-4 is amplified in the SHRSP/FAD rat. A positive correlation between Aqp-4 and GFAP protein levels are consistent with prior reports of increased Aqp-4 corresponding with increased gliosis in a model of hypoglycemia (Zhao et al., 2018). Aqp-4 staining was redistributed to the neuropil, but it was unclear whether the loss of polarization was due to disintegration of vessels or retraction of endfeet. Dysregulation of Aqp-4 may be associated with cognitive dysfunction and pathology in AD and VaD (Lan et al., 2017). In fact in chronic traumatic encephalopathy (CTE), Aqp-4 is also increased and associated with perivascular tau (McKee and Robinson, 2014; Babcock, 2018) or age-related tau astrogliopathy (Kovacs et al., 2017). This similarity supports the concept the chronic damage to the neurovascular unit may contribute to tauopathy in both CTE and MxD.

Aquaporin-4 as a Blood Biomarker

Not only was there disruption of Aqp-4 distribution in the brain, elevated levels of Aqp-4 protein were additionally detected in brain-derived plasma exosomes from SHRSP/FAD rats. As such, Aqp-4 may prove to be a useful peripheral blood biomarker of MxD or VaD, reflecting vascular and inflammatory changes in the brain as a result of AD pathology with concomitant vascular dysfunction, thereby allowing for stratification of patients with a more complex dementia and guiding potential treatment options. In fact, others have shown in humans that neuron-derived plasma exosomes from traumatic brain injury (TBI) patients contain elevated levels of Aqp-4 protein, compared to controls and that Aqp-4 levels were significantly higher in exosomes from acute TBI patients, compared to chronic (Goetzl et al., 2019), suggesting that Aqp-4 levels in plasma exosomes may represent a robust marker with which to stratify patient groups or identify a clinically silent traumatic or indeed neurodegenerative brain disorder. Whether the findings in our model are relevant to serum changes in VaD or MxD patient samples should be examined.

Evidence of Loss of Microvessel Integrity

We observed excessive accumulation of collagen IV in brains of SHRSP/FAD rats, which may reflect the development of cerebral SVD, which is aggravated by AD pathology. Chronic hypertension increases collagen deposition in cerebral vessel walls (Zhou et al., 2015) and leads to deficient vessel integrity and function (Feihl et al., 2008; Grinberg and Thal, 2010; Heagerty et al., 2010). Similarly dysfunctional vessels are evident in brains of AD patients (Farkas et al., 2000; Bouras et al., 2006; Kitaguchi et al., 2007), and other hypertensive models with AD showed reduced vessel density (Cifuentes et al., 2015) or leakage (Shih et al., 2018). Interestingly, we found that SHRSP/FAD rats also showed elevations in the endothelial cell adhesion protein platelet endothelial cell adhesion molecule-1 (PECAM-1), which is involved with trans-endothelial leukocyte and monocyte migration across into the brain as part of the neuroinflammatory response (Giri et al., 2000, 2002; Kalinowska and Losy, 2006). Elevated PECAM-1 also implies that vascular inflammatory signaling at least plays a role in driving neuroinflammation in the brain of SHRSP/FAD rats. Our data show that long-term mild hypertension is associated with abnormal accumulation of vascular collagen IV, altered PECAM-1 and disruption of astrocyte end-feet associated with vessels. These findings suggest that AD pathology with concurrent chronic hypertension exacerbates a loss of CNS blood vessel integrity.

Mitochondrial Deficits Unique to the SHRSP/FAD Rat

Recent work has probed the involvement of dysfunctional mitochondria and bioenergetic deficits in AD pathophysiology. Mitochondrial dysfunction is an early event in AD pathogenesis (Yao et al., 2009; Calkins et al., 2011; Varghese et al., 2011; Du et al., 2012) leading to ATP depletion, which ultimately contributes to synapse and neuron degeneration (Vos et al., 2010; Swerdlow, 2018). In FAD rats, mitochondrial complex I (NADH:ubiquinone oxidoreductase) but not complex II (succinate dehydrogenase) was downregulated. The FAD effects on complex I are consistent with findings in AD patients, in which the 24 or 75 kDa subunits were reduced in the parietal, occipital and temporal cortices and caudate nucleus (Kim et al., 2001). This suggests that AD may have an early effect on mitochondrial complex I.

The FAD rats showed no changes in complex II consistent with reports that AD patients show no changes or even increased complex II protein expression (Bubber et al., 2005). Apparent increases in complex II specific to AD have been attributed to compensatory responses facilitating anaerobic metabolism as a result of loss of complexes, such as pyruvate dehydrogenase, involved in oxidative metabolism. Importantly SHRSP/FAD rats instead showed reductions in complex II, which would be predicted to compound bioenergetic deficits. Differences in complex II in MxD versus AD have not been looked at to the best of our knowledge, other than one report that found no changes in isolated VaD. However, complex II was found to be reduced in a rat model of VaD (Singh et al., 2015) and in a traumatic brain injury model in brain regions with disrupted cerebral blood flow (Jiang et al., 2000). Together these data warrant a more thorough examination of differential mitochondrial deficits in VaD, AD and MxD to determine if additional mitochondrial and fluorodeoxyglucose (FDG)-positron emission tomography (PET) deficits are promoted by the coexistence of both pathologies.

Evidence for Neuronal Damage in the SHRSP/FAD

Hypertension appeared to amplify neurodegenerative responses in AD rats. Here we showed that calbindin staining was reduced in brains of hypertensive SHRSP/FAD animals, possibly a reflection of increased neuronal vulnerability or loss as a result of the combination of hypertension with AD pathology. The FAD rats utilized in this study exhibit stereology-validated neuronal loss (Cohen et al., 2013), however, the SHRSP/FAD rats exhibited further reductions of calbindin, suggesting that neuron or calbindin loss might be intensified in the cross. Furthermore, caspase-cleaved actin levels were elevated in SHRSP/FAD brain, which had previously been reported in AD (Yang et al., 1998). Increased caspase activity may also relate to the hyper-inflammatory environment of the brain in SHRSP/FAD rats, through its interaction with the NOD-, LRR- and pyrin domain-containing protein 3 (NLRP3) inflammasome, a known hub of pathology in AD brain that drives interleukin-1β (IL-1β) production via TLR4 signaling (Burm et al., 2015). Although not investigated in this initial report, it will be important for future studies to assess inflammatory receptor signaling and cytokine profiles in the brain of SHRSP/FAD rats and potential correlations with tau hyperphosphorylation, tauopathy and neuron loss. Reduced brain volumes, including for the hippocampus and temporal lobes, have been found in individuals with elevated blood pressures, recorded several years prior (Beauchet et al., 2013; Power et al., 2016) and in animals in which hypertension was induced (Meissner et al., 2017). This may be due to neuron and pericyte loss as a result of chronic hypertension independent of tauopathy (Goel et al., 2015; Kruyer et al., 2015). Thus, our caspase and calbindin data add support for an amplification of neurodegenerative responses caused by the coexistence of both pathologies in SHRSP/FAD rats.

Pathological Elevations of NR2B in the SHRSP/FAD Rat

We observed significant increases in hippocampal NR2B protein detected by western blot in SHRSP/FAD rats. NR2B is a subunit of the *N*-methyl-D-aspartate receptor (NMDAR), an ionotropic glutamate receptor expressed at the post-synaptic membrane that can enhance memory (Cao et al., 2007; Wang et al., 2009; Vedder et al., 2013; Wang, 2014). Although AD typically shows disproportionate loss of post synaptic proteins, synaptic marker loss is both stage and region dependent as there can be compensatory sprouting which could be either pathological (aberrant sprouting) or transiently protective and an influx of aberrant terminals around plaques. Pathological elevations have been described associated with apoptosis in AD models (Liu et al., 2012). While overactivation of NR2B-containing NMDARs might improve some aspects of hippocampal-dependent memory, it can also contribute to excitotoxic calcium flux, hyperactivity and to the accumulation of hyperphosphorylated tau in the hippocampus following ischemic injury through disinhibition of glycogen synthase kinase-3β (GSK-3β), an important tau kinase (Xu et al., 2015). The elevated Tau pS422 staining and CP13 protein detected in our hypertensive AD rats is likely due to several factors, including neuroinflammation which has been shown to drive tau pathogenesis in AD models through effects on cytokine-induced tau hyperphosphorylation (Ghosh et al., 2013). Under normal conditions, neurons, but not astrocytes, express NMDARs; but following ischemic insult, expression of NMDARs is also evident in astrocytes (Krebs et al., 2003). Detailed longitudinal immunohistochemical studies are required to examine the regional changes in NR2B and phospho-NR2B and their possible relationship with cognitive performance.

Behavioral Changes in FAD and SHRSP Rats Were Not Exacerbated in SHRSP/FAD Rats

Limited behavioral testing was performed, and we found that independent effects of FAD and SHRSP were unaffected in SHRSP/FAD by the coexistence of both features and prominently

impacted by hyperactivity in SHRSP. In particular, hypoactivity in the Y maze was dependent on FAD and independent of SHRSP, while hyperactivity in both the OFT and NOR was dependent on SHRSP and independent of FAD. Neuropsychologically, little is understood about synergism of AD and vascular pathology in MxD as the current criteria for MxD would require fitting the diagnosis of both AD and VaD. For example one would expect declarative memory deficits related to AD and executive dysfunction relative to VaD, and predominantly with MxD this would be occurring in the older population (averaging 83 years old) (Custodio et al., 2017). It is speculated that the coexistence of both pathologies would lower the threshold of dementia, whereby less AD and less vascular pathology could cause dementia, even if neither pathology would by itself fulfill the pathological criteria for one or the other (Fischer et al., 1991).

There was a ceiling effect in NOR deficits, such that WKY rats, but none of the other groups showed preference. Thus, we could not evaluate whether the presence of hypertension affected severity of FAD deficits using the NOR task.

Limitations in the type of behavioral testing included not being able to complete more complex tests such as water maze or Barnes maze, that have been used to detect cognitive impairment in these models. We did, however, detect SHRSP-dependent hyperactivity, which is a recognized phenotype in this model (Gattu et al., 1997a,b; Terry et al., 2000; Hernandez et al., 2003; Kantak et al., 2008; Meneses et al., 2011). Since patients with MxD are typically older, another limitation in our study is that we do not have data on progression, so we do not know if there would be exacerbation of pathology with older ages or with strokes which we can but did not enhance with higher salt intake in our initial characterization. Therefore, although we identified independent behavioral changes associated with FAD transgene or SHRSP background with the minimal testing done, it is important to test these rats in the future with other behavioral tasks to determine which type of behaviors are exacerbated by the coexistence of both hypertension and FAD with and without higher salt intake. Future studies should focus on behavioral tests analogous to known differences in neuropsychological characteristics between MxD, VaD and AD such as behavioral testing in animals that reflects differences in episodic memory and executive function. Since VaD is associated with more anxiety and depression (reviewed by Cerejeira et al., 2012) we were not surprised to observe independent effects of AD and SHRSP, but we were surprised not to see more enhanced baseline cognitive deficits. For future studies we will explore whether a more comprehensive neuropsychological battery, assessing rat declarative memory (Engelmann et al., 2011) and executive dysfunction (Beas et al., 2013) or high salt challenge may reveal synergistic deficits caused by the hypertensive and FAD phenotypes. Finally, in tests where SHRSP show improved learning in young animals, a longitudinal evaluation of the age-related decline within strains rather than comparison of performance across strains will provide a better measure of the relationship of age-dependent pathology with age-dependent cognitive decline.

CONCLUSION

In conclusion, we show here that this novel rat model of MxD exhibits robust neuropathology, including amyloid and tau pathology, gliosis and behavioral alterations. In addition, exacerbation of several disease parameters was noted in SHRSP/FAD, compared to SHRSP and FAD rats, including increased astrocytosis, Aqp-4, collagen IV deposition, PECAM-1, caspase activity and qualitatively increased demyelination with reduced mitochondrial enzymes and calbindin levels. This novel model appears to be an advancement in mixed models of dementia, which have relied primarily on major vessel occlusion or mouse models of diabetes and AD that express Aβ but not tau pathology. Our model more accurately reflects pathology in the human syndrome of MxD associated with chronic hypertension, in the absence of diabetes, developing alongside classical amyloidogenic pathology, in addition to tauopathy and neuron loss. Further work is needed to characterize more completely any cognitive or behavioral abnormalities in the SHRSP/FAD rat and also to determine the extent to which degeneration of neurons and synapses develops in this rat with and without salt challenge and small strokes, another hallmark of MxD. We believe that this novel disease model will support researchers in delineating the association between cardiovascular abnormalities and dementia and will help bolster efforts to develop treatments for AD, VaD and CBVD.

DATA AVAILABILITY STATEMENT

All datasets generated for this study are included in the manuscript/supplementary files.

ETHICS STATEMENT

All experimentation was approved by the UCLA Chancellor's Animal Research Committee and the Veteran Administration Institutional Animal Care and Use Committee, and carried out in compliance with the National Institutes of Health "Guide for the Care and Use of Laboratory Animals" (NIH Publications No. 8023).

AUTHOR CONTRIBUTIONS

SF designed and supervised the experiments, and assisted in manuscript writing, figures preparation, and statistical analysis. PD assisted in manuscript writing, and behavioral testing and analysis. SH performed and analyzed the Western blot. MJ performed and analyzed the immunohistochemistry. HD'A assisted in writing the background and assessment of clinical aspects of the disease. HV assisted in interpretation of the plaque morphology. CO performed the metabolic studies. PK and DC assisted in creation of the model, behavioral testing, animal euthanasia, and tissue preparation. CL and MM assisted in behavioral testing, and tissue preparation and sectioning.

CZ performed the blood pressure measurement. EG assisted in writing background. BT assisted in blood pressure measurements. GC assisted in concepts for the study, and writing and editing of the manuscript. XZ prepared and analyzed the plasma exosomes.

FUNDING

This research was funded by VA Merit BX003485 (SF), VA MERIT RX000669 (SF), DOD AZ14016 (SF), Oskar Fisher Foundation, Dr. James Truchard (GC and SF), Mary S. Easton UCLA Alzheimer's Center (GC and SF), and Department of Defense (SF).

ACKNOWLEDGMENTS

We acknowledge Dr. Eddie Koo (University of San Diego, CA, United States and National University of Singapore, NUS) and Dr. Christopher Chen (NUS) for discussions and input into developing this model. We thank Dr. Robert Cohen, Emory University for generously providing us the F344Tg AD Rats (now available TgF344-19 rat, RRRC #00699, www.rrrc.us.)

REFERENCES

Ahmadian, S. S., Rezvanian, A., Peterson, M., Weintraub, S., Bigio, E. H., Mesulam, M. M., et al. (2015). Loss of calbindin-D28K is associated with the full range of tangle pathology within basal forebrain cholinergic neurons in Alzheimer's disease. *Neurobiol. Aging* 36, 3163–3170. doi: 10.1016/j.neurobiolaging.2015.09.001

Akiyama, H., Barger, S., Barnum, S., Bradt, B., Bauer, J., Cole, G. M., et al. (2000). Inflammation and Alzheimer's disease. *Neurobiol. Aging* 21, 383–421.

Areosa, S. A., Sherriff, F., and McShane, R. (2005). Memantine for dementia. *Coch. Database Syst. Rev.* CD003154. doi: 10.1002/14651858.CD003154.pub4

Attems, J., and Jellinger, K. A. (2014). The overlap between vascular disease and Alzheimer's disease–lessons from pathology. *BMC Med.* 12:206. doi: 10.1186/s12916-014-0206-2

Babcock, K. J. (2018). Histopathological assessment of atroglial aquaporin-4 expression in chronic traumatic encephalopathy. *Theses Dissert. Boston Univ.* 5238, 1–36.

Bailey, E. L., McCulloch, J., Sudlow, C., and Wardlaw, J. M. (2009). Potential animal models of lacunar stroke. a systematic review. *Stroke* 40, e451–e458. doi: 10.1161/STROKEAHA.108.528430

Baker, J. G., Williams, A. J., Ionita, C. C., Lee-Kwen, P., Ching, M., and Miletich, R. S. (2012). Cerebral small vessel disease: cognition, mood, daily functioning, and imaging findings from a small pilot sample. *Dement. Geriatr. Cogn. Dis. Extra* 2, 169–179. doi: 10.1159/000333482

Baumgart, M., Snyder, H. M., Carrillo, M. C., Fazio, S., Kim, H., and Johns, H. (2015). Summary of the evidence on modifiable risk factors for cognitive decline and dementia: a population-based perspective. *Alzheimers Dement.* 11, 718–726. doi: 10.1016/j.jalz.2015.05.016

Beas, B. S., Setlow, B., and Bizon, J. L. (2013). Distinct manifestations of executive dysfunction in aged rats. *Neurobiol. Aging* 34, 2164–2174. doi: 10.1016/j.neurobiolaging.2013.03.019

Beauchet, O., Celle, S., Roche, F., Bartha, R., Montero-Odasso, M., Allali, G., et al. (2013). Blood pressure levels and brain volume reduction: a systematic review and meta-analysis. *J. Hypertens.* 31, 1502–1516. doi: 10.1097/HJH.0b013e32836184b5

Biancardi, V. C., Son, S. J., Ahmadi, S., Filosa, J. A., and Stern, J. E. (2014). Circulating angiotensin II gains access to the hypothalamus and brain stem during hypertension via breakdown of the blood-brain barrier. *Hypertension* 63, 572–579. doi: 10.1161/HYPERTENSIONAHA.113.01743

Bouras, C., Kovari, E., Herrmann, F. R., Rivara, C. B., Bailey, T. L., von Gunten, A., et al. (2006). Stereologic analysis of microvascular morphology in the elderly: Alzheimer disease pathology and cognitive status. *J. Neuropathol. Exp. Neurol.* 65, 235–244. doi: 10.1097/01.jnen.0000203077.53080.2c

Bubber, P., Haroutunian, V., Fisch, G., Blass, J. P., and Gibson, G. E. (2005). Mitochondrial abnormalities in Alzheimer brain: mechanistic implications. *Ann. Neurol.* 57, 695–703. doi: 10.1002/ana.20474

Bueche, C. Z., Garz, C., Stanaszek, L., Niklass, S., Kropf, S., Bittner, D., et al. (2014). Impact of N-Acetylcysteine on cerebral amyloid-beta plaques and kidney damage in spontaneously hypertensive stroke-prone rats. *J. Alzheimer's Dis.* 42(Suppl. 3), S305–S313. doi: 10.3233/JAD-132615

Burm, S. M., Zuiderwijk-Sick, E. A., t Jong, A. E., van der Putten, C., Veth, J., Kondova, I., et al. (2015). Inflammasome-induced IL-1beta secretion in microglia is characterized by delayed kinetics and is only partially dependent on inflammatory caspases. *J. Neurosci.* 35, 678–687. doi: 10.1523/JNEUROSCI.2510-14.2015

Calkins, M. J., Manczak, M., Mao, P., Shirendeb, U., and Reddy, P. H. (2011). Impaired mitochondrial biogenesis, defective axonal transport of mitochondria, abnormal mitochondrial dynamics and synaptic degeneration in a mouse model of Alzheimer's disease. *Hum. Mol. Genet.* 20, 4515–4529. doi: 10.1093/hmg/ddr381

Cao, X., Cui, Z., Feng, R., Tang, Y. P., Qin, Z., Mei, B., et al. (2007). Maintenance of superior learning and memory function in NR2B transgenic mice during ageing. *Eur. J. Neurosci.* 25, 1815–1822. doi: 10.1111/j.1460-9568.2007.05431.x

Cerejeira, J., Lagarto, L., and Mukaetova-Ladinska, E. B. (2012). Behavioral and psychological symptoms of dementia. *Front. Neurol.* 3:73. doi: 10.3389/fneur.2012.00073

Cifuentes, D., Poittevin, M., Dere, E., Broqueres-You, D., Bonnin, P., Benessiano, J., et al. (2015). Hypertension accelerates the progression of Alzheimer-like pathology in a mouse model of the disease. *Hypertension* 65, 218–224. doi: 10.1161/HYPERTENSIONAHA.114.04139

Cohen, R. M., Rezai-Zadeh, K., Weitz, T. M., Rentsendorj, A., Gate, D., Spivak, I., et al. (2013). A transgenic Alzheimer rat with plaques, tau pathology, behavioral impairment, oligomeric abeta, and frank neuronal loss. *J. Neurosci.* 33, 6245–6256. doi: 10.1523/JNEUROSCI.3672-12.2013

Coisne, C., and Engelhardt, B. (2011). Tight junctions in brain barriers during central nervous system inflammation. *Antioxid. Redox. Signal.* 15, 1285–1303. doi: 10.1089/ars.2011.3929

Csiszar, A., Tucsek, Z., Toth, P., Sosnowska, D., Gautam, T., Koller, A., et al. (2013). Synergistic effects of hypertension and aging on cognitive function and hippocampal expression of genes involved in beta-amyloid generation and Alzheimer's disease. *Am. J. Physiol. Heart Circ. Physiol.* 305, H1120–H1130. doi: 10.1152/ajpheart.00288.2013

Custodio, N., Montesinos, R., Lira, D., Herrera-Perez, E., Bardales, Y., and Valeriano-Lorenzo, L. (2017). Mixed dementia: a review of the evidence. *Dement. Neuropsychol.* 11, 364–370. doi: 10.1590/1980-57642016dn11-040005

de la Torre, J. C. (2012). Cardiovascular risk factors promote brain hypoperfusion leading to cognitive decline and dementia. *Cardiovasc. Psychiatry Neurol.* 2012:367516. doi: 10.1155/2012/367516

De Reuck, J., Maurage, C. A., Deramecourt, V., Pasquier, F., Cordonnier, C., Leys, D., et al. (2018). Aging and cerebrovascular lesions in pure and in mixed neurodegenerative and vascular dementia brains: a neuropathological study. *Folia Neuropathol.* 56, 81–87. doi: 10.5114/fn.2018.76610

Deane, R., Du Yan, S., Submamaryan, R. K., LaRue, B., Jovanovic, S., Hogg, E., et al. (2003). RAGE mediates amyloid-beta peptide transport across the blood-brain barrier and accumulation in brain. *Nat. Med.* 9, 907–913. doi: 10.1038/nm890

Dey, A. K., Stamenova, V., Turner, G., Black, S. E., and Levine, B. (2016). Pathoconnectomics of cognitive impairment in small vessel disease: a systematic review. *Alzheimers Dement.* 12, 831–845. doi: 10.1016/j.jalz.2016.01.007

Di Marco, L. Y., Farkas, E., Martin, C., Venneri, A., and Frangi, A. F. (2015). Is Vasomotion in cerebral arteries impaired in Alzheimer's Disease? *J. Alzheimer's Dis.* 46, 35–53. doi: 10.3233/JAD-142976

Donahue, J. E., Flaherty, S. L., Johanson, C. E., Duncan, J. A. III, Silverberg, G. D., Miller, M. C., et al. (2006). RAGE, LRP-1, and amyloid-beta protein in

Alzheimer's disease. *Acta Neuropathol.* 112, 405–415. doi: 10.1007/s00401-006-0115-3

Du, H., Guo, L., and Yan, S. S. (2012). Synaptic mitochondrial pathology in Alzheimer's disease. *Antioxid. Redox Signal.* 16, 1467–1475. doi: 10.1089/ars.2011.4277

Engelmann, M., Hadicke, J., and Noack, J. (2011). Testing declarative memory in laboratory rats and mice using the nonconditioned social discrimination procedure. *Nat. Protoc.* 6, 1152–1162. doi: 10.1038/nprot.2011.353

Fan, Y., Lan, L., Zheng, L., Ji, X., Lin, J., Zeng, J., et al. (2015). Spontaneous white matter lesion in brain of stroke-prone renovascular hypertensive rats: a study from MRI, pathology and behavior. *Metab. Brain Dis.* 30, 1479–1486. doi: 10.1007/s11011-015-9722-9

Farkas, E., De Jong, G. I., de Vos, R. A., Jansen Steur, E. N., and Luiten, P. G. (2000). Pathological features of cerebral cortical capillaries are doubled in Alzheimer's disease and Parkinson's disease. *Acta Neuropathol.* 100, 395–402. doi: 10.1007/s004010000195

Feihl, F., Liaudet, L., Levy, B. I., and Waeber, B. (2008). Hypertension and microvascular remodelling. *Cardiovasc. Res.* 78, 274–285. doi: 10.1093/cvr/cvn022

Ferrero, E., Villa, A., Ferrero, M. E., Toninelli, E., Bender, J. R., Pardi, R., et al. (1996). Tumor necrosis factor alpha-induced vascular leakage involves PECAM1 phosphorylation. *Cancer Res.* 56, 3211–3215.

Ferri, C. P., Prince, M., Brayne, C., Brodaty, H., Fratiglioni, L., Ganguli, M., et al. (2005). Global prevalence of dementia: a Delphi consensus study. *Lancet* 366, 2112–2117. doi: 10.1016/S0140-6736(05)67889-0

Fiandaca, M. S., Kapogiannis, D., Mapstone, M., Boxer, A., Eitan, E., Schwartz, J. B., et al. (2015). Identification of preclinical Alzheimer's disease by a profile of pathogenic proteins in neurally derived blood exosomes: a case-control study. *Alzheimers Dement.* 11, 600.e1–607.e1. doi: 10.1016/j.jalz.2014.06.008

Fischer, P., Jellinger, K., Gatterer, G., and Danielczyk, W. (1991). Prospective neuropathological validation of Hachinski's Ischaemic score in dementias. *J. Neurol. Neurosurg. Psychiatry* 54, 580–583. doi: 10.1136/jnnp.54.7.580

Frautschy, S. A., Cole, G. M., and Baird, A. (1992). Phagocytosis and deposition of vascular beta-amyloid in rat brains injected with Alzheimer beta-amyloid. *Am. J. Pathol.* 140, 1389–1399.

Galisova, A., Baciak, L., Jozefovicova, M., Just Kukurova, I., Kebis, A., Ambrusova, K., et al. (2014). Pathophysiological rat model of vascular dementia: magnetic resonance spectroscopy, microimaging and behavioral study. *Brain Res.* 1568, 10–20. doi: 10.1016/j.brainres.2014.04.032

Gallart-Palau, X., Serra, A., Lee, B. S. T., Guo, X., and Sze, S. K. (2017). Brain ureido degenerative protein modifications are associated with neuroinflammation and proteinopathy in Alzheimer's disease with cerebrovascular disease. *J. Neuroinflamm.* 14:175. doi: 10.1186/s12974-017-0946-y

Gattu, M., Pauly, J. R., Urbanawiz, S., and Buccafusco, J. J. (1997a). Autoradiographic comparison of muscarinic M1 and M2 binding sites in the CNS of spontaneously hypertensive and normotensive rats. *Brain Res.* 771, 173–183. doi: 10.1016/s0006-8993(97)00691-4

Gattu, M., Terry, A. V. Jr., Pauly, J. R., and Buccafusco, J. J. (1997b). Cognitive impairment in spontaneously hypertensive rats: role of central nicotinic receptors. *Part II Brain Res.* 771, 104–114. doi: 10.1016/s0006-8993(97)00794-4

Ghosh, S., Wu, M. D., Shaftel, S. S., Kyrkanides, S., LaFerla, F. M., Olschowka, J. A., et al. (2013). Sustained interleukin-1beta overexpression exacerbates tau pathology despite reduced amyloid burden in an Alzheimer's mouse model. *J. Neurosci.* 33, 5053–5064. doi: 10.1523/JNEUROSCI.4361-12.2013

Giri, R., Selvaraj, S., Miller, C. A., Hofman, F., Yan, S. D., Stern, D., et al. (2002). Effect of endothelial cell polarity on beta-amyloid-induced migration of monocytes across normal and AD endothelium. *Am. J. Physiol. Cell Physiol.* 283, C895–C904. doi: 10.1152/ajpcell.00293.2001

Giri, R., Shen, Y., Stins, M., Du Yan, S., Schmidt, A. M., Stern, D., et al. (2000). beta-amyloid-induced migration of monocytes across human brain endothelial cells involves RAGE and PECAM-1. *Am. J. Physiol. Cell Physiol.* 279, C1772–C1781. doi: 10.1152/ajpcell.2000.279.6.C1772

Goel, R., Bhat, S. A., Rajasekar, N., Hanif, K., Nath, C., and Shukla, R. (2015). Hypertension exacerbates predisposition to neurodegeneration and memory impairment in the presence of a neuroinflammatory stimulus: protection by angiotensin converting enzyme inhibition. *Pharmacol. Biochem. Behav.* 133, 132–145. doi: 10.1016/j.pbb.2015.04.002

Goetzl, E. J., Peltz, C. B., Mustapic, M., Kapogiannis, D., and Yaffe, K. C. (2019). Neuron-derived plasma exosome proteins after remote Traumatic brain injury. *J. Neurotrauma* doi: 10.1089/neu.2019.6711 [Epub ahead of print].

Gottesman, R. F., Schneider, A. L., Albert, M., Alonso, A., Bandeen-Roche, K., Coker, L., et al. (2014). Midlife hypertension and 20-year cognitive change: the atherosclerosis risk in communities neurocognitive study. *JAMA Neurol.* 71, 1218–1227. doi: 10.1001/jamaneurol.2014.1646

Grammas, P., Martinez, J., and Miller, B. (2011). Cerebral microvascular endothelium and the pathogenesis of neurodegenerative diseases. *Expert Rev. Mol. Med.* 13:e19. doi: 10.1017/S1462399411001918

Gratton, J. A., Sauter, A., Rudin, M., Lees, K. R., McColl, J., Reid, J. L., et al. (1998). Susceptibility to cerebral infarction in the stroke-prone spontaneously hypertensive rat is inherited as a dominant trait. *Stroke* 29, 690–694. doi: 10.1161/01.str.29.3.690

Grinberg, L. T., and Thal, D. R. (2010). Vascular pathology in the aged human brain. *Acta Neuropathol.* 119, 277–290. doi: 10.1007/s00401-010-0652-7

Hainsworth, A. H., Brittain, J. F., and Khatun, H. (2012). Pre-clinical models of human cerebral small vessel disease: utility for clinical application. *J. Neurol. Sci.* 322, 237–240. doi: 10.1016/j.jns.2012.05.046

Hainsworth, A. H., and Markus, H. S. (2008). Do in vivo experimental models reflect human cerebral small vessel disease? A systematic review. *J. Cereb. Blood Flow Metab.* 28, 1877–1891. doi: 10.1038/jcbfm.2008.91

Harrison, D. G., Guzik, T. J., Lob, H. E., Madhur, M. S., Marvar, P. J., Thabet, S. R., et al. (2011). Inflammation, immunity, and hypertension. *Hypertension* 57, 132–140. doi: 10.1161/HYPERTENSIONAHA.110.163576

Heagerty, A. M., Heerkens, E. H., and Izzard, A. S. (2010). Small artery structure and function in hypertension. *J. Cell Mol. Med.* 14, 1037–1043. doi: 10.1111/j.1582-4934.2010.01080.x

Hebert, L. E., Weuve, J., Scherr, P. A., and Evans, D. A. (2013). Alzheimer disease in the United States (2010-2050) estimated using the 2010 census. *Neurology* 80, 1778–1783. doi: 10.1212/WNL.0b013e31828726f5

Held, F., Morris, A. W. J., Pirici, D., Niklass, S., Sharp, M. M. G., Garz, C., et al. (2017). Vascular basement membrane alterations and beta-amyloid accumulations in an animal model of cerebral small vessel disease. *Clin. Sci.* 131, 1001–1013. doi: 10.1042/CS20170004

Hernandez, C. M., Hoifodt, H., and Terry, A. V. Jr. (2003). Spontaneously hypertensive rats: further evaluation of age-related memory performance and cholinergic marker expression. *J. Psychiatry Neurosci.* 28, 197–209.

Hoshi, A., Yamamoto, T., Shimizu, K., Ugawa, Y., Nishizawa, M., Takahashi, H., et al. (2012). Characteristics of aquaporin expression surrounding senile plaques and cerebral amyloid angiopathy in Alzheimer disease. *J. Neuropathol. Exp. Neurol.* 71, 750–759. doi: 10.1097/NEN.0b013e3182632566

Iadecola, C. (2016). Vascular and metabolic factors in Alzheimer's disease and related Dementias: introduction. *Cell Mol. Neurobiol.* 36, 151–154. doi: 10.1007/s10571-015-0319-y

Infante-Garcia, C., Ramos-Rodriguez, J. J., Galindo-Gonzalez, L., and Garcia-Alloza, M. (2016). Long-term central pathology and cognitive impairment are exacerbated in a mixed model of Alzheimer's disease and type 2 diabetes. *Psychoneuroendocrinology* 65, 15–25. doi: 10.1016/j.psyneuen.2015.12.001

Jalal, F. Y., Yang, Y., Thompson, J., Lopez, A. C., and Rosenberg, G. A. (2012). Myelin loss associated with neuroinflammation in hypertensive rats. *Stroke* 43, 1115–1122. doi: 10.1161/STROKEAHA.111.643080

Jandke, S., Garz, C., Schwanke, D., Sendtner, M., Heinze, H. J., Carare, R. O., et al. (2018). The association between hypertensive arteriopathy and cerebral amyloid angiopathy in spontaneously hypertensive stroke-prone rats. *Brain Pathol.* 28, 844–859. doi: 10.1111/bpa.12629

Jellinger, K. A., and Attems, J. (2007). Neuropathological evaluation of mixed dementia. *J. Neurol. Sci.* 257, 80–87. doi: 10.1016/j.jns.2007.01.045

Jiang, X. B., Ohno, K., Qian, L., Tominaga, B., Kuroiwa, T., Nariai, T., et al. (2000). Changes in local cerebral blood flow, glucose utilization, and mitochondrial function following traumatic brain injury in rats. *Neurol. Med. Chir.* 40, 16–28.

Jolivel, V., Bicker, F., Biname, F., Ploen, R., Keller, S., Gollan, R., et al. (2015). Perivascular microglia promote blood vessel disintegration in the ischemic penumbra. *Acta Neuropathol.* 129, 279–295. doi: 10.1007/s00401-014-1372-1

Kaiser, D., Weise, G., Moller, K., Scheibe, J., Posel, C., Baasch, S., et al. (2014). Spontaneous white matter damage, cognitive decline and neuroinflammation

in middle-aged hypertensive rats: an animal model of early-stage cerebral small vessel disease. *Acta Neuropathol. Commun.* 2:169. doi: 10.1186/s40478-014-0169-8

Kalaria, R. N., Akinyemi, R., and Ihara, M. (2012). Does vascular pathology contribute to Alzheimer changes? *J. Neurol. Sci.* 322, 141–147. doi: 10.1016/j.jns.2012.07.032

Kalinowska, A., and Losy, J. (2006). PECAM-1, a key player in neuroinflammation. *Eur. J. Neurol.* 13, 1284–1290. doi: 10.1111/j.1468-1331.2006.01640.x

Kanekiyo, T., Liu, C. C., Shinohara, M., Li, J., and Bu, G. (2012). LRP1 in brain vascular smooth muscle cells mediates local clearance of Alzheimer's amyloid-beta. *J. Neurosci.* 32, 16458–16465. doi: 10.1523/JNEUROSCI.3987-12.2012

Kantak, K. M., Singh, T., Kerstetter, K. A., Dembro, K. A., Mutebi, M. M., Harvey, R. C., et al. (2008). Advancing the spontaneous hypertensive rat model of attention deficit/hyperactivity disorder. *Behav. Neurosci.* 122, 340–357. doi: 10.1037/0735-7044.122.2.340

Katsouri, L., and Georgopoulos, S. (2011). Lack of LDL receptor enhances amyloid deposition and decreases glial response in an Alzheimer's disease mouse model. *PLoS One* 6:e21880. doi: 10.1371/journal.pone.0021880

Kelly, P., Denver, P., Satchell, S. C., Ackermann, M., Konerding, M. A., and Mitchell, C. A. (2017). Microvascular ultrastructural changes precede cognitive impairment in the murine APPswe/PS1dE9 model of Alzheimer's disease. *Angiogenesis* 20, 567–580. doi: 10.1007/s10456-017-9568-3

Kelly, P., McClean, P. L., Ackermann, M., Konerding, M. A., Holscher, C., and Mitchell, C. A. (2015). Restoration of cerebral and systemic microvascular architecture in APP/PS1 transgenic mice following treatment with Liraglutide. *Microcirculation* 22, 133–145. doi: 10.1111/micc.12186

Khan, A., Kalaria, R. N., Corbett, A., and Ballard, C. (2016). Update on vascular Dementia. *J. Geriatr. Psychiatry Neurol.* 29, 281–301. doi: 10.1177/0891988716654987

Khoshnam, S. E., Sarkaki, A., Rashno, M., and Farbood, Y. (2018). Memory deficits and hippocampal inflammation in cerebral hypoperfusion and reperfusion in male rats: neuroprotective role of vanillic acid. *Life Sci.* 211, 126–132. doi: 10.1016/j.lfs.2018.08.065

Kim, J., Castellano, J. M., Jiang, H., Basak, J. M., Parsadanian, M., Pham, V., et al. (2009). Overexpression of low-density lipoprotein receptor in the brain markedly inhibits amyloid deposition and increases extracellular A beta clearance. *Neuron* 64, 632–644. doi: 10.1016/j.neuron.2009.11.013

Kim, S. H., Vlkolinsky, R., Cairns, N., Fountoulakis, M., and Lubec, G. (2001). The reduction of NADH ubiquinone oxidoreductase 24- and 75-kDa subunits in brains of patients with Down syndrome and Alzheimer's disease. *Life Sci.* 68, 2741–2750.

Kitaguchi, H., Ihara, M., Saiki, H., Takahashi, R., and Tomimoto, H. (2007). Capillary beds are decreased in Alzheimer's disease, but not in Binswanger's disease. *Neurosci. Lett.* 417, 128–131. doi: 10.1016/j.neulet.2007.02.021

Klakotskaia, D., Agca, C., Richardson, R. A., Stopa, E. G., Schachtman, T. R., and Agca, Y. (2018). Memory deficiency, cerebral amyloid angiopathy, and amyloid-beta plaques in APP+PS1 double transgenic rat model of Alzheimer's disease. *PLoS One* 13:e0195469. doi: 10.1371/journal.pone.0195469

Koundal, S., Liu, X., Sanggaard, S., Mortensen, K., Wardlaw, J., Nedergaard, M., et al. (2019). Brain morphometry and longitudinal relaxation time of spontaneously hypertensive Rats (SHRs) in early and intermediate stages of hypertension investigated by 3D VFA-SPGR MRI. *Neuroscience* 404, 14–26. doi: 10.1016/j.neuroscience.2019.01.030

Kovacs, G. G., Yousef, A., Kaindl, S., Lee, V. M., and Trojanowski, J. Q. (2017). Connexin-43 and aquaporin-4 are markers of ageing-related tau astrogliopathy (ARTAG)-related astroglial response. *Neuropathol. Appl. Neurobiol.* 44, 491–505. doi: 10.1111/nan.12427

Krebs, C., Fernandes, H. B., Sheldon, C., Raymond, L. A., and Baimbridge, K. G. (2003). Functional NMDA receptor subtype 2B is expressed in astrocytes after ischemia in vivo and anoxia in vitro. *J. Neurosci.* 23, 3364–3372. doi: 10.1523/jneurosci.23-08-03364.2003

Kruyer, A., Soplop, N., Strickland, S., and Norris, E. H. (2015). Chronic Hypertension leads to neurodegeneration in the TgSwDI Mouse Model of Alzheimer's disease. *Hypertension* 66, 175–182. doi: 10.1161/HYPERTENSIONAHA.115.05524

Kwon, K. J., Kim, M. K., Lee, E. J., Kim, J. N., Choi, B. R., Kim, S. Y., et al. (2014). Effects of donepezil, an acetylcholinesterase inhibitor, on neurogenesis in a rat model of vascular dementia. *J. Neurol. Sci.* 347, 66–77. doi: 10.1016/j.jns.2014.09.021

Lafosse, J. M., Reed, B. R., Mungas, D., Sterling, S. B., Wahbeh, H., and Jagust, W. J. (1997). Fluency and memory differences between ischemic vascular dementia and Alzheimer's disease. *Neuropsychology* 11, 514–522. doi: 10.1037//0894-4105.11.4.514

Lan, Y. L., Chen, J. J., Hu, G., Xu, J., Xiao, M., and Li, S. (2017). Aquaporin 4 in Astrocytes is a target for therapy in Alzheimer's Disease. *Curr. Pharm. Des.* 23, 4948–4957. doi: 10.2174/1381612823666170714144844

Launer, L. J., Ross, G. W., Petrovitch, H., Masaki, K., Foley, D., White, L. R., et al. (2000). Midlife blood pressure and dementia: the Honolulu-Asia aging study. *Neurobiol. Aging* 21, 49–55. doi: 10.1016/s0197-4580(00)00096-8

Liu, Y., Dong, Y. H., Lyu, P. Y., Chen, W. H., and Li, R. (2018). Hypertension-induced cerebral small vessel disease leading to cognitive impairment. *Chin. Med. J.* 131, 615–619. doi: 10.4103/0366-6999.226069

Liu, Z., Lv, C., Zhao, W., Song, Y., Pei, D., and Xu, T. (2012). NR2B-containing NMDA receptors expression and their relationship to apoptosis in hippocampus of Alzheimer's disease-like rats. *Neurochem. Res.* 37, 1420–1427. doi: 10.1007/s11064-012-0726-0

Looi, J. C., and Sachdev, P. S. (1999). Differentiation of vascular dementia from AD on neuropsychological tests. *Neurology* 53, 670–678.

Lukatela, K. A., Cohen, R. A., Kessler, H. A., Jenkins, M. A., Moser, D. J., Stone, W. F., et al. (2000). Dementia rating scale performance: a comparison of vascular and Alzheimer's dementia. *J. Clin. Exp. Neuropsychol.* 22, 445–454. doi: 10.1076/1380-3395(200008)22:4;1-0;FT445

Marfany, A., Sierra, C., Camafort, M., Domenech, M., and Coca, A. (2018). High blood pressure, Alzheimer disease and antihypertensive treatment. *Panminerva Med.* 60, 8–16. doi: 10.23736/S0031-0808.18.03360-8

McKee, A. C., and Robinson, M. E. (2014). Military-related traumatic brain injury and neurodegeneration. *Alzheimers Dement.* 10(3 Suppl.), S242–S253. doi: 10.1016/j.jalz.2014.04.003

Meissner, A., Minnerup, J., Soria, G., and Planas, A. M. (2017). Structural and functional brain alterations in a murine model of Angiotensin II-induced hypertension. *J. Neurochem.* 140, 509–521. doi: 10.1111/jnc.13905

Mendez, M. F., and Ashla-Mendez, M. (1991). Differences between multi-infarct dementia and Alzheimer's disease on unstructured neuropsychological tasks. *J. Clin. Exp. Neuropsychol.* 13, 923–932. doi: 10.1080/01688639108405108

Meneses, A., Perez-Garcia, G., Ponce-Lopez, T., Tellez, R., Gallegos-Cari, A., and Castillo, C. (2011). Spontaneously hypertensive rat (SHR) as an animal model for ADHD: a short overview. *Rev. Neurosci.* 22, 365–371. doi: 10.1515/RNS.2011.024

Moody, D. M., Brown, W. R., Challa, V. R., and Anderson, R. L. (1995). Periventricular venous collagenosis: association with leukoaraiosis. *Radiology* 194, 469–476. doi: 10.1148/radiology.194.2.7824728

Munoz-Moreno, E., Tudela, R., Lopez-Gil, X., and Soria, G. (2018). Early brain connectivity alterations and cognitive impairment in a rat model of Alzheimer's disease. *Alzheimers Res. Ther.* 10:16. doi: 10.1186/s13195-018-0346-2

Nabika, T., Ohara, H., Kato, N., and Isomura, M. (2012). The stroke-prone spontaneously hypertensive rat: still a useful model for post-GWAS genetic studies? *Hypertens. Res.* 35, 477–484. doi: 10.1038/hr.2012.30

Ngandu, T., Lehtisalo, J., Solomon, A., Levalahti, E., Ahtiluoto, S., Antikainen, R., et al. (2015). A 2 year multidomain intervention of diet, exercise, cognitive training, and vascular risk monitoring versus control to prevent cognitive decline in at-risk elderly people (FINGER): a randomised controlled trial. *Lancet.* 385, 2255–2263. doi: 10.1016/S0140-6736(15)60461-5

Oberlin, L. E., Manuck, S. B., Gianaros, P. J., Ferrell, R. E., Muldoon, M. F., Jennings, J. R., et al. (2015). Blood pressure interacts with APOE epsilon4 to predict memory performance in a midlife sample. *Neuropsychology* 29, 693–702. doi: 10.1037/neu0000177

Okamoto, K., and Aoki, K. (1963). Development of a strain of spontaneously hypertensive rats. *Jpn. Circ. J.* 27, 282–293. doi: 10.1253/jcj.27.282

Petrovitch, H., Ross, G. W., Steinhorn, S. C., Abbott, R. D., Markesbery, W., Davis, D., et al. (2005). AD lesions and infarcts in demented and non-demented Japanese-American men. *Ann. Neurol.* 57, 98–103. doi: 10.1002/ana.20318

Petrovitch, H., White, L. R., Izmirilian, G., Ross, G. W., Havlik, R. J., Markesbery, W., et al. (2000). Midlife blood pressure and neuritic plaques, neurofibrillary tangles, and brain weight at death: the HAAS. Honolulu-Asia aging Study. *Neurobiol. Aging* 21, 57–62. doi: 10.1016/s0197-4580(00)00106-8

Pirici, D., Stanaszek, L., Garz, C., Niklass, S., Heinze, H. J., Kalinski, T., et al. (2017). Common impact of chronic kidney disease and brain microhemorrhages on cerebral abeta pathology in SHRSP. *Brain Pathol.* 27, 169–180. doi: 10.1111/bpa.12384

Planton, M., Raposo, N., Albucher, J. F., and Pariente, J. (2017). Cerebral amyloid angiopathy-related cognitive impairment: the search for a specific neuropsychological pattern. *Rev. Neurol.* 173, 562–565. doi: 10.1016/j.neurol.2017.09.006

Power, M. C., Schneider, A. L., Wruck, L., Griswold, M., Coker, L. H., Alonso, A., et al. (2016). Life-course blood pressure in relation to brain volumes. *Alzheimers Dement.* 12, 890–899. doi: 10.1016/j.jalz.2016.03.012

Ramirez-Gomez, L., Zheng, L., Reed, B., Kramer, J., Mungas, D., Zarow, C., et al. (2017). Neuropsychological profiles differentiate alzheimer disease from subcortical ischemic vascular dementia in an autopsy-defined cohort. *Dement. Geriatr. Cogn. Disord.* 44, 1–11. doi: 10.1159/000477344

Ramos-Rodriguez, J. J., Jimenez-Palomares, M., Murillo-Carretero, M. I., Infante-Garcia, C., Berrocoso, E., Hernandez-Pacho, F., et al. (2015). Central vascular disease and exacerbated pathology in a mixed model of type 2 diabetes and Alzheimer's disease. *Psychoneuroendocrinology* 62, 69–79. doi: 10.1016/j.psyneuen.2015.07.606

Rizzi, L., Rosset, I., and Roriz-Cruz, M. (2014). Global epidemiology of dementia: Alzheimer's and vascular types. *Biomed Res. Int.* 2014:908915. doi: 10.1155/2014/908915

Rodrigue, K. M., Rieck, J. R., Kennedy, K. M., Devous, M. D. Sr., Diaz-Arrastia, R., and Park, D. C. (2013). Risk factors for beta-amyloid deposition in healthy aging: vascular and genetic effects. *JAMA Neurol.* 70, 600–606. doi: 10.1001/jamaneurol.2013.1342

Romer, L. H., McLean, N. V., Yan, H. C., Daise, M., Sun, J., and DeLisser, H. M. (1995). IFN-gamma and TNF-alpha induce redistribution of PECAM-1 (CD31) on human endothelial cells. *J. Immunol.* 154, 6582–6592.

Sabbatini, M., Catalani, A., Consoli, C., Marletta, N., Tomassoni, D., and Avola, R. (2002). The hippocampus in spontaneously hypertensive rats: an animal model of vascular dementia? *Mech. Ageing Dev.* 123, 547–559. doi: 10.1016/s0047-6374(01)00362-1

Sayed, F. A., Telpoukhovskaia, M., Kodama, L., Li, Y., Zhou, Y., Le, D., et al. (2018). Differential effects of partial and complete loss of TREM2 on microglial injury response and tauopathy. *Proc. Natl. Acad. Sci. U.S.A.* 115, 10172–10177. doi: 10.1073/pnas.1811411115

Schreiber, S., Drukarch, B., Garz, C., Niklass, S., Stanaszek, L., Kropf, S., et al. (2014). Interplay between age, cerebral small vessel disease, parenchymal amyloid-beta, and tau pathology: longitudinal studies in hypertensive stroke-prone rats. *J. Alzheimer's Dis.* 42(Suppl. 3), S205–S215. doi: 10.3233/JAD-132618

Sevigny, J., Chiao, P., Bussiere, T., Weinreb, P. H., Williams, L., Maier, M., et al. (2016). The antibody aducanumab reduces Abeta plaques in Alzheimer's disease. *Nature* 537, 50–56. doi: 10.1038/nature19323

Shang, J., Yamashita, T., Tian, F., Li, X., Liu, X., Shi, X., et al. (2019). Chronic cerebral hypoperfusion alters amyloid-beta transport related proteins in the cortical blood vessels of Alzheimer's disease model mouse. *Brain Res.* doi: 10.1016/j.brainres.2019.146379 [Epub ahead of print].

Shih, Y. H., Wu, S. Y., Yu, M., Huang, S. H., Lee, C. W., Jiang, M. J., et al. (2018). Hypertension accelerates Alzheimer's disease-related pathologies in Pigs and 3xTg Mice. *Front. Aging Neurosci.* 10:73. doi: 10.3389/fnagi.2018.00073

Sicard, P., Delemasure, S., Korandji, C., Segueira-Le Grand, A., Lauzier, B., Guilland, J. C., et al. (2008). Anti-hypertensive effects of Rosuvastatin are associated with decreased inflammation and oxidative stress markers in hypertensive rats. *Free Radic. Res.* 42, 226–236. doi: 10.1080/10715760701885380

Singh, P., Gupta, S., and Sharma, B. (2015). Melatonin receptor and KATP channel modulation in experimental vascular dementia. *Physiol. Behav.* 142, 66–78. doi: 10.1016/j.physbeh.2015.02.009

Smith, L. A., and McMahon, L. L. (2018). Deficits in synaptic function occur at medial perforant path-dentate granule cell synapses prior to Schaffer collateral-CA1 pyramidal cell synapses in the novel TgF344-Alzheimer's disease rat model. *Neurobiol. Dis.* 110, 166–179. doi: 10.1016/j.nbd.2017.11.014

Staals, J., Booth, T., Morris, Z., Bastin, M. E., Gow, A. J., Corley, J., et al. (2015). Total MRI load of cerebral small vessel disease and cognitive ability in older people. *Neurobiol. Aging* 36, 2806–2811. doi: 10.1016/j.neurobiolaging.2015.06.024

Stoiljkovic, M., Kelley, C., Stutz, B., Horvath, T. L., and Hajos, M. (2018). Altered cortical and hippocampal excitability in TgF344-AD Rats modeling Alzheimer's disease pathology. *Cereb. Cortex* 29, 2716–2727. doi: 10.1093/cercor/bhy140

Swerdlow, R. H. (2018). Mitochondria and mitochondrial cascades in Alzheimer's disease. *J. Alzheimer's Dis.* 62, 1403–1416. doi: 10.3233/JAD-170585

Sydow, A., Van der Jeugd, A., Zheng, F., Ahmed, T., Balschun, D., Petrova, O., et al. (2011). Reversibility of Tau-related cognitive defects in a regulatable FTD mouse model. *J. Mol. Neurosci.* 45, 432–437. doi: 10.1007/s12031-011-9604-5

Takemori, K., Murakami, T., Kometani, T., and Ito, H. (2013). Possible involvement of oxidative stress as a causative factor in blood-brain barrier dysfunction in stroke-prone spontaneously hypertensive rats. *Microvasc. Res.* 90, 169–172. doi: 10.1016/j.mvr.2013.08.005

Tang, J., Xiao, W., Li, Q., Deng, Q., Chu, X., Chen, Y., et al. (2015). A Cyclooxygenase-2 inhibitor reduces vascular wall thickness and ameliorates cognitive impairment in a cerebral small vessel diseases Rat Model. *Curr. Alzheimer Res.* 12, 704–710. doi: 10.2174/1567205012666150710104924

Tayebati, S. K., Amenta, F., and Tomassoni, D. (2015). Cerebrovascular and blood-brain barrier morphology in spontaneously hypertensive rats: effect of treatment with choline alphoscerate. *CNS Neurol. Disord. Drug Targets* 14, 421–429. doi: 10.2174/1871527314666150225140855

Tayebati, S. K., Tomassoni, D., and Amenta, F. (2012). Spontaneously hypertensive rat as a model of vascular brain disorder: microanatomy, neurochemistry and behavior. *J. Neurol. Sci.* 322, 241–249. doi: 10.1016/j.jns.2012.05.047

Tayebati, S. K., Tomassoni, D., and Amenta, F. (2016). Neuroinflammatory markers in spontaneously hypertensive Rat Brain: an immunohistochemical study. *CNS Neurol. Disord. Drug Targets* 15, 995–1000. doi: 10.2174/1871527315666160527155014

Terry, A. V. Jr., Hernandez, C. M., Buccafusco, J. J., and Gattu, M. (2000). Deficits in spatial learning and nicotinic-acetylcholine receptors in older, spontaneously hypertensive rats. *Neuroscience* 101, 357–368. doi: 10.1016/s0306-4522(00)00377-8

Tomassoni, D., Bramanti, V., and Amenta, F. (2010). Expression of aquaporins 1 and 4 in the brain of spontaneously hypertensive rats. *Brain Res.* 1325, 155–163. doi: 10.1016/j.brainres.2010.02.023

Traykov, L., Baudic, S., Thibaudet, M. C., Rigaud, A. S., Smagghe, A., and Boller, F. (2002). Neuropsychological deficit in early subcortical vascular dementia: comparison to Alzheimer's disease. *Dement. Geriatr. Cogn. Disord.* 14, 26–32. doi: 10.1159/000058330

Ueno, M., Wu, B., Nakagawa, T., Nagai, Y., Onodera, M., Huang, C. L., et al. (2010). The expression of LDL receptor in vessels with blood-brain barrier impairment in a stroke-prone hypertensive model. *Histochem. Cell Biol.* 133, 669–676. doi: 10.1007/s00418-010-0705-y

Valenti, R., Pantoni, L., and Markus, H. S. (2014). Treatment of vascular risk factors in patients with a diagnosis of Alzheimer's disease: a systematic review. *BMC Med.* 12:160. doi: 10.1186/s12916-014-0160-z

Varghese, M., Zhao, W., Wang, J., Cheng, A., Qian, X., Chaudhry, A., et al. (2011). Mitochondrial bioenergetics is defective in presymptomatic Tg2576 AD mice. *Transl. Neurosci.* 2, 1–5. doi: 10.2478/s13380-011-0011-8

Vedder, L. C., Smith, C. C., Flannigan, A. E., and McMahon, L. L. (2013). Estradiol-induced increase in novel object recognition requires hippocampal NR2B-containing NMDA receptors. *Hippocampus* 23, 108–115. doi: 10.1002/hipo.22068

Venkat, P., Chopp, M., and Chen, J. (2015). Models and mechanisms of vascular dementia. *Exp. Neurol.* 272, 97–108. doi: 10.1016/j.expneurol.2015.05.006

Venkat, P., Chopp, M., Zacharek, A., Cui, C., Zhang, L., Li, Q., et al. (2017). White matter damage and glymphatic dysfunction in a model of vascular dementia in rats with no prior vascular pathologies. *Neurobiol. Aging* 50, 96–106. doi: 10.1016/j.neurobiolaging.2016.11.002

Vinters, H. V., Zarow, C., Borys, E., Whitman, J. D., Tung, S., Ellis, W. G., et al. (2018). Review: Vascular dementia: clinicopathologic and genetic considerations. *Neuropathol. Appl. Neurobiol.* 44, 247–266. doi: 10.1111/nan.12472

Vos, M., Lauwers, E., and Verstreken, P. (2010). Synaptic mitochondria in synaptic transmission and organization of vesicle pools in health and disease. *Front. Syn. Neurosci.* 2:139. doi: 10.3389/fnsyn.2010.00139

Walker, K. A., Power, M. C., and Gottesman, R. F. (2017). Defining the relationship between hypertension, cognitive decline, and dementia: a review. *Curr. Hypertens. Rep.* 19, 24. doi: 10.1007/s11906-017-0724-3

Wang, D., Cui, Z., Zeng, Q., Kuang, H., Wang, L. P., Tsien, J. Z., et al. (2009). Genetic enhancement of memory and long-term potentiation but not CA1 long-term depression in NR2B transgenic rats. *PLoS One* 4:e7486. doi: 10.1371/journal.pone.0007486

Wang, H. (2014). Establishment of an animal model of vascular dementia. *Exp. Ther. Med.* 8, 1599–1603. doi: 10.3892/etm.2014.1926

Wardlaw, J. M., Smith, C., and Dichgans, M. (2013). Mechanisms of sporadic cerebral small vessel disease: insights from neuroimaging. *Lancet Neurol.* 12, 483–497. doi: 10.1016/S1474-4422(13)70060-7

Weaver, J., Jalal, F. Y., Yang, Y., Thompson, J., Rosenberg, G. A., and Liu, K. J. (2014). Tissue oxygen is reduced in white matter of spontaneously hypertensive-stroke prone rats: a longitudinal study with electron paramagnetic resonance. *J. Cereb. Blood Flow Metab.* 34, 890–896. doi: 10.1038/jcbfm.2014.35

Wennberg, A. M., Whitwell, J. L., Tosakulwong, N., Weigand, S. D., Murray, M. E., Machulda, M. M., et al. (2019). The influence of tau, amyloid, alpha-synuclein, TDP-43, and vascular pathology in clinically normal elderly individuals. *Neurobiol. Aging* 77, 26–36. doi: 10.1016/j.neurobiolaging.2019.01.008

Wimo, A., Guerchet, M., Ali, G.-C., Wu, Y.-T., Prina, A. M., Winblad, B., et al. (2017). The worldwide costs of dementia 2015 and comparisons with 2010. *Alzheimers Dement.* 13, 1–7. doi: 10.1016/j.jalz.2016.07.150

Wimo, A., Jonsson, L., Bond, J., Prince, M., Winblad, B., and Alzheimer Disease International. (2013). The worldwide economic impact of dementia 2010. *Alzheimers Dement.* 9, 1.e3–11.e3. doi: 10.1016/j.jalz.2012.11.006

Xu, Z., Xiao, N., Chen, Y., Huang, H., Marshall, C., Gao, J., et al. (2015). Deletion of aquaporin-4 in APP/PS1 mice exacerbates brain Abeta accumulation and memory deficits. *Mol. Neurodegener.* 10:58. doi: 10.1186/s13024-015-0056-1

Yang, F., Sun, X., Beech, W., Teter, B., Wu, S., Sigel, J., et al. (1998). Antibody to caspase-cleaved actin detects apoptosis in differentiated neuroblastoma and plaque-associated neurons and microglia in Alzheimer's disease. *Am. J. Pathol.* 152, 379–389.

Yang, J., Zhang, R., Shi, C., Mao, C., Yang, Z., Suo, Z., et al. (2017). AQP4 Association with amyloid deposition and astrocyte pathology in the Tg-ArcSwe Mouse model of Alzheimer's Disease. *J. Alzheimer's Dis.* 57, 157–169. doi: 10.3233/JAD-160957

Yao, J., Irwin, R. W., Zhao, L., Nilsen, J., Hamilton, R. T., and Brinton, R. D. (2009). Mitochondrial bioenergetic deficit precedes Alzheimer's pathology in female mouse model of Alzheimer's disease. *Proc. Natl. Acad. Sci. U.S.A.* 106, 14670–14675. doi: 10.1073/pnas.0903563106

Yasar, S., Xia, J., Yao, W., Furberg, C. D., Xue, Q. L., Mercado, C. I., et al. (2013). Antihypertensive drugs decrease risk of Alzheimer disease: Ginkgo evaluation of memory study. *Neurology* 81, 896–903. doi: 10.1212/WNL.0b013e3182a35228

Yu, P., Venkat, P., Chopp, M., Zacharek, A., Shen, Y., Ning, R., et al. (2018). Role of microRNA-126 in vascular cognitive impairment in mice. *J. Cereb. Blood Flow Metab.* doi: 10.1177/0271678X18800593 [Epub ahead of print].

Zhang, H. Y., Li, J., Guo, N., and Zhang, B. Y. (2019). Brain functions and unusual beta-amyloid accumulation in the hypertensive white matter lesions of rats. *J. Biol. Regul. Homeost. Agents* 33, 1073–1084.

Zhang, L., Zheng, H., Luo, J., Li, L., Pan, X., Jiang, T., et al. (2018). Inhibition of endothelial nitric oxide synthase reverses the effect of exercise on improving cognitive function in hypertensive rats. *Hypertens. Res.* 41, 414–425. doi: 10.1038/s41440-018-0033-5

Zhao, F., Deng, J., Xu, X., Cao, F., Lu, K., Li, D., et al. (2018). Aquaporin-4 deletion ameliorates hypoglycemia-induced BBB permeability by inhibiting inflammatory responses. *J. Neuroinflamm.* 15:157. doi: 10.1186/s12974-018-1203-8

Zhou, M., Mao, L., Wang, Y., Wang, Q., Yang, Z., Li, S., et al. (2015). Morphologic changes of cerebral veins in hypertensive rats: venous collagenosis is associated with hypertension. *J. Stroke Cerebrovasc. Dis.* 24, 530–536. doi: 10.1016/j.jstrokecerebrovasdis.2014.09.038

Conflict of Interest: The authors declare that the research was conducted in the absence of any commercial or financial relationships that could be construed as a potential conflict of interest.

frontiers in Physiology

MINI REVIEW
published: 04 February 2020
doi: 10.3389/fphys.2019.01587

Neutrophil-Related Oxidants Drive Heart and Brain Remodeling After Ischemia/Reperfusion Injury

Federico Carbone[1,2], *Aldo Bonaventura*[1,3] *and Fabrizio Montecucco*[2,4]*

[1] First Clinic of Internal Medicine, Department of Internal Medicine, University of Genoa, Genoa, Italy, [2] IRCCS Ospedale Policlinico San Martino Genoa – Italian Cardiovascular Network, Genoa, Italy, [3] Pauley Heart Center, Division of Cardiology, Department of Internal Medicine, Virginia Commonwealth University, Richmond, VA, United States, [4] First Clinic of Internal Medicine, Department of Internal Medicine and Centre of Excellence for Biomedical Research, University of Genoa, Genoa, Italy

The inflammatory response associated with myocardial and brain ischemia/reperfusion injury (IRI) is a critical determinant of tissue necrosis, functional organ recovery, and long-term clinical outcomes. In the post-ischemic period, reactive oxygen species (ROS) are involved in tissue repair through the clearance of dead cells and cellular debris. Neutrophils play a critical role in redox signaling due to their early recruitment and the large variety of released ROS. Noteworthy, ROS generated during IRI have a relevant role in both myocardial healing and activation of neuroprotective pathways. Anatomical and functional differences contribute to the responses in the myocardial and brain tissue despite a significant gene overlap. The exaggerated activation of this signaling system can result in adverse consequences, such as cell apoptosis and extracellular matrix degradation. In light of that, blocking the ROS cascade might have a therapeutic implication for cardiomyocyte and neuronal loss after acute ischemic events. The translation of these findings from preclinical models to clinical trials has so far failed because of differences between humans and animals, difficulty of agents to penetrate into specific cellular organs, and specifically unravel oxidant and antioxidant pathways. Here, we update knowledge on ROS cascade in IRI, focusing on the role of neutrophils. We discuss evidence of ROS blockade as a therapeutic approach for myocardial infarction and ischemic stroke.

Keywords: inflammation, reactive oxygen species, neutrophils, acute myocardial infarction, stroke

OPEN ACCESS

Edited by:
Mansoureh Eghbali, University of California, Los Angeles, United States

Reviewed by:
Houzao Chen, Chinese Academy of Medical Sciences, China
Germano Guerra, University of Molise, Italy

***Correspondence:**
Fabrizio Montecucco
fabrizio.montecucco@unige.it

Specialty section:
This article was submitted to Oxidant Physiology, a section of the journal Frontiers in Physiology

Received: *29 October 2018*
Accepted: *18 December 2019*
Published: *04 February 2020*

Citation:
Carbone F, Bonaventura A and Montecucco F (2020) Neutrophil-Related Oxidants Drive Heart and Brain Remodeling After Ischemia/Reperfusion Injury. Front. Physiol. 10:1587. doi: 10.3389/fphys.2019.01587

INTRODUCTION

Neutrophil (PMN) activation is strongly implicated in the pathogenesis of cardiovascular (CV) disease (Bonaventura et al., 2019). In addition to favoring atherosclerotic plaque vulnerability and rupture (Carbone et al., 2015a, 2018b), PMNs enhance thrombosis through different mechanisms, which include generation of neutrophil extracellular traps (NETs) (Bonaventura et al., 2018), release of proteases, and direct PMN–platelet interactions (Lisman, 2018). PMNs also have a critical role in ischemia/reperfusion injury (IRI) (Carbone et al., 2013; Garcia-Culebras et al., 2018) and tissue repair (Montecucco et al., 2017) (e.g., in the myocardium and the brain). Oxidative burst characterizes PMN activation and generates several classes of reactive oxygen species (ROS). Among the different subtypes of NADPH oxidases (NOX), NOX2 is prevalent but not specific of PMNs, being commonly expressed in cardiomyocytes, endothelial cells, fibroblasts, and neurons (El-Benna et al., 2009). Components of NOX2 enzymatic complex are located either

in the cytosol ($p47^{phox}$/$p67^{phox}$/$p40^{phox}$ and the GTPase Rac1/Rac2) or in the plasma membrane (flavocytochrome subunits $gp91^{phox}$ and $p22^{phox}$). Once assembled, the glycosylated $gp91^{phox}$ subunit undergoes a conformational change which allows catalytic activity. Activated NOX2 then generates high concentration of superoxide anion ($O_2^{\cdot-}$), which exerts a prevalent local effect due to the short life span. In addition, $O_2^{\cdot-}$ dismutation may generate hydrogen peroxide (H_2O_2), which, in turn, reacts to produce the hydroxyl radical ($^{\cdot}OH$). The phagocyte-specific enzyme myeloperoxidase (MPO) catalyzes the formation of hypochlorous acid (HClO) and promotes the generation of chloramines, aldehydes, $^1O_2$, ozone (O^3), and $^{\cdot}OH$ (Prokopowicz et al., 2012). Nitric oxide synthase (NOS) is another ROS-generating enzyme active in PMNs. Through the conversion of the L-arginine to L-citrulline, NOS produces nitric oxide (NO), which may generate peroxynitrite by interacting with $O_2^{\cdot-}$ (Szabo et al., 2007). On this basis, it is not surprising that oxidative stress largely contributes to IRI. Conversely, less is known about the potential involvement in tissue repair. In the next paragraphs, we will focus on both myocardial and brain remodeling, also discussing the potential therapeutic implication of oxidative stress modulation.

NEUTROPHIL OXIDATIVE BURST: TARGETS AND SIGNALING

Neutrophil-derived ROS show a specific diffusion range, determined by their life span and reactivity, whereas $O_2^{\cdot-}$ has a short life span. The non-radical compound H_2O_2 generated by its dismutation readily diffuses across membranes. Therefore, ROS may differently oxidize DNA, RNA, protein, and lipids. Nucleic acids undergo direct oxidative processes (e.g., nitrosative deamination, oxidation, and halogenation) or alternatively generate adducts with oxidized polyunsaturated fatty acids, protein, carbohydrates, and even nucleic acids themselves (Lonkar and Dedon, 2011). Posttranslational modification of proteins may occur through a direct oxidation of amino acids or other cellular components. Endoplasmic reticulum is extremely sensitive to the redox stress, which may determine disruption of the protein folding mechanism and the production of misfolded proteins (Cao and Kaufman, 2014). Also, catabolic processes are under the control of oxidative stress, which modulates protein degradation and autophagy (Pajares et al., 2015). By targeting polyunsaturated fatty acids, ROS may also determine membrane permeability, cytosol efflux, loss of membrane protein activities, and even biomembrane disruption with loss of cell viability (Jaganjac et al., 2016).

Finally, ROS may themselves act as second messengers and then transduce signals. Mitogen-activated protein kinases (MAPKs) are regulated by oxidative stress via different signaling cascades, involving Jun, p38 or extracellular signal-regulated kinase (ERK) 1/2 pathways, protein kinase C (PKC) and phosphoinositide 3-kinase (PI3K) activation (Hotamisligil and Davis, 2016). By adding an additional level of control, oxidative stress regulates a large amount of transcription factors (e.g., hypoxia-inducible factor [HIF]-1, activator protein [AP]-1, nuclear factor κ-light-chain-enhancer of activated B cells [NF-kB], and p53). It is then not surprising that ROS strongly influence in both autocrine and paracrine manner different PMN functions including phagocytosis, cytokine secretion, and apoptosis. Noteworthy, PMN-derived ROS also drive tissue response to IRI by modulating pathophysiological processes of resident cells (e.g., cardiomyocytes, endothelial and microglial cells, and neurons). The following paragraph will focus on this complex interaction between PMNs and the surrounding environment (**Figure 1**).

NEUTROPHIL OXIDANTS AND MYOCARDIAL REMODELING

Myocardial reperfusion after an acute myocardial infarction (AMI) is recommended to save as much myocardium as possible from necrosis and dysfunction. Anyway, when the coronary flux is re-established, and the myocardium reperfused after ischemia, the hypercontracture of cardiac myocytes and their cytolysis may be paradoxically increased in response to reoxygenation. This phenomenon, known as "oxygen paradox," forms a complementary dyad with the oxidative stress (Davies, 2016). The term "myocardial reperfusion injury" (MRI) describes myocardial injury and cardiomyocyte death usually occurring between 6 and 24 h after reperfusion of an ischemic area (Hausenloy and Yellon, 2016). Importantly, MRI is the main cause of death for stunned cardiomyocytes and ultimately accounts for more than half of the final size of myocardial ischemia. As widely reported in clinical and experimental studies, cardiomyocyte exposure to ROS causes apoptosis through different mechanisms. The leading one is likely the cytosolic and mitochondrial calcium overload that determines rapid alteration of intracellular pH. This, in turn, triggers the activation of MAPKs (Ong et al., 2015). Of interest, recent studies hypothesized oxidative stress as a promoter of myocardial fibrosis after ischemic injury, and both angiotensin 1 and the $K^{Ca3.1}$ channel have been suggested as involved pathways (Somanna et al., 2016; Wang et al., 2017). PMNs are recruited very early to the infarcted area (nearly after 30 min), and their actions are mediated by adhesive interactions with vascular endothelial cells, such as selectins, integrins, and molecules belonging to the immunoglobulin superfamily (Bonaventura et al., 2016). Selectin-dependent adhesion of PMNs mainly involves L-selectin (CD62L), E-selectin (CD62E), and P-selectin (CD62P). They play a critical role in neutrophil rolling so that their blocking is effective in reducing PMN recruitment and infarct size (Weyrich et al., 1993; Palazzo et al., 1998). However, selectins alone do not allow transmigration until the integrins start to play. PMNs express a combination of the β-chain CD18 with the α-chains CD11a [LFA-1 (lymphocyte function-associated antigen-1)], CD11b (macrophage-1 antigen), or CD11c (p150,95). PMN adhesion occurs with the binding of CD11/CD18 to the ligand intercellular adhesion molecule (ICAM)-1 expressed on the endothelial surface (Jordan et al., 1999). Hence, PMNs change shape to motile cells, and transendothelial migration takes

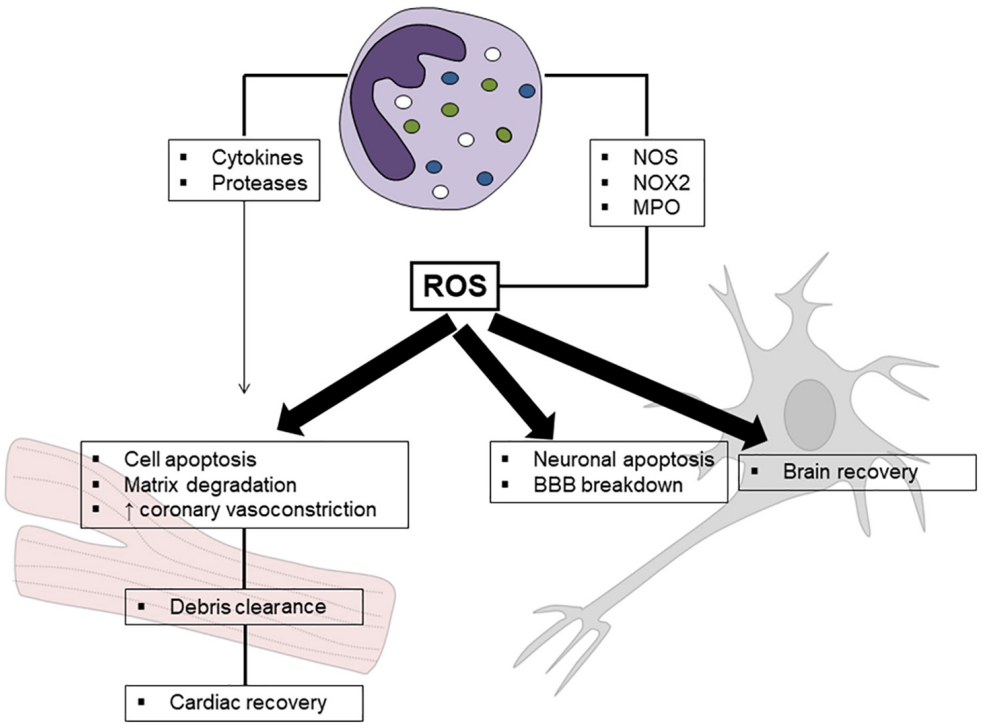

FIGURE 1 | Schematic mechanism of neutrophil-related oxidative stress in ischemia/reperfusion injury. Reactive oxygen species (ROS) released by neutrophils are mainly produced by nitric oxide synthase (NOS), NADPH oxidase type 2 (NOX2), and myeloperoxidase (MPO). Although their detrimental role in ischemia reperfusion injury has been clearly established, a potential effect in promoting tissue healing has been suggested, especially in myocardial injury.

place (Smith, 2000). The latter occurs via paracellular route through junctions between adjacent endothelial cells and involves various molecules (PECAM-1, CD99, ICAM-2, endothelial cell-selective adhesion molecule, and members of the junctional adhesion molecule family). Once the infarcted zone is infiltrated, PMNs release ROS alongside cytokines and proteolytic enzymes, ultimately feeding a vicious circle through a positive feedback loop (Panth et al., 2016; Montecucco et al., 2017). MPO is detected within the infarcted myocardium, including the luminal thrombi on eroded plaques (Ferrante et al., 2010), and MPO-generated oxidants are likely to have a negligible impact on infarct size and impact largely on the adverse left ventricle remodeling and function (Vasilyev et al., 2005). In experimental models, the mechanism of neutrophil-dependent MRI was shown to be further dependent on CD18 integrin activation and ICAM-1 expression by injured cardiac cells (Albelda et al., 1994). *In vivo*, ROS are mainly released by adherent PMNs, thus suggesting the crucial role of the PMN ligand-specific adhesion to cardiomyocytes in MRI (Frangogiannis, 2015). The generation of ROS peaks within 2–10 min from coronary artery reperfusion and acts as a trigger for immune cell chemotaxis – particularly PMN – through complement activation and upregulation of cytokines and chemokines via the NF-κB pathway (Hensley et al., 2000). The role of ROS is of utmost importance in cardiac healing after AMI as it promotes the clearance of dead cells and cellular debris. However, exaggerated oxidative stress may result in detrimental consequences, such as cell apoptosis and degradation of the extracellular matrix. This occurs when antioxidant systems (i.e., catalase, glutathione peroxidase, and superoxide dismutase) and intracellular antioxidants are overcome and the catastrophic actions of ROS may take place (Frangogiannis, 2015).

Cytochrome P-450 (CYP), xanthine oxidase (XO), NOX, monoamine oxidase (MAO), and the mitochondrial electron transport chain (METC) are the most common enzymes involved in ROS production. CYP is likely the most known source of ROS in reperfused infarcted heart (Vinten-Johansen, 2004). CYP-derived ROS increase in an oxygen-dependent way following increased uncoupling reaction and oxygen supply (Hernandez-Resendiz et al., 2018). In particular, the release of O^{-2} and H_2O_2 by CYP 2C9 activates the NF-κB pathway which in turn upregulates the production of proinflammatory cytokines and the expression of adhesion molecules (Fleming et al., 2001). Similarly, the overexpression of CYP 2C8 was reported to favor ROS generation, finally exacerbating coronary vasoconstriction and increasing infarct size (Edin et al., 2011). XO derives from xanthine dehydrogenase upon myocardial reperfusion and reacts with purine substrates and O_2 to finally generate O_2^- and H_2O_2. XO is usually abundant within the vascular endothelium of normal hearts and is referred to as a primary source of ROS (Hernandez-Resendiz et al., 2018). This finding is largely based on the evidence that allopurinol, a known xanthine oxidoreductase, is effective in limiting the injury occurring during MRI and reducing the infarcted size (Pisarenko et al., 1994). Furthermore, XO was described to have a role

in leukocyte recruitment and neutrophil adhesion in hypoxic conditions (Matsumura et al., 1998). Concerning NOX, the subtype NOX2 plays a central role and is typically overexpressed during MRI. Apart from the role in ROS generation, NOX can also indirectly provide damages via the activation of PKC-mediated phosphorylation of the cytosolic p47phox (Patterson et al., 1999). MAOs can catalyze oxidative deamination of several monoamines leading to a great production of ROS. Moreover, MAOs have a role in the production of H_2O_2 in the very early reperfusion period (Kunduzova et al., 2002). Finally, METC complexes are very important sources and targets of ROS arising during MRI, particularly complexes I and III (Hernandez-Resendiz et al., 2018). Mitochondrial complex I is formed by an active A-form and a deactivated D-form, the latter being the most abundant during MRI and producing O_2^- and H_2O_2 (Gorenkova et al., 2013). Mitochondrial complex III is another fundamental source of ROS during reperfusion as demonstrated by the reduced activity in ischemic hearts compared to healthy ones. Interestingly, ROS burst from the mitochondria can induce the oxidation of cholesterol and the production of oxysterols, which induce interleukin-1β release in the vascular endothelial cells and the following expression of adhesion molecules for the recruitment of immune cells (Lemaire et al., 1998; Poli et al., 2013).

Apart from the known detrimental effects of PMNs in the ischemic area, current evidence suggests that PMNs can also display reparative functions by recruiting and activating mononuclear cells (Alard et al., 2015). Recently, neutrophil depletion by a specific monoclonal antibody has been reported to not affect infarct size, but rather favor the progressive deterioration of the post-AMI cardiac function (Horckmans et al., 2017). Accordingly, the positive influence of PMNs in this setting may be due to the polarization of macrophages toward a reparative phenotype mediated, at least partially, by neutrophil gelatinase-associated lipocalin.

In line with these findings, many antioxidants were studied, although clinical trials reported some controversial results, especially with mitochondria-targeted antioxidants (coenzyme Q10, mitoQ, and MTP-131) (**Table 1**; Argaud et al., 2005; Karlsson et al., 2010; Skyschally et al., 2010; Chiari et al., 2014; Hausenloy et al., 2014; Cung et al., 2015; Dare et al., 2015; Eleawa et al., 2015; Hernandez-Resendiz et al., 2015; Gibson et al., 2016; Ottani et al., 2016). Coenzyme Q10 was shown to decrease the infarcted area, the inflammatory burden, and the oxidative stress and to normalize left ventricle function following AMI (Eleawa et al., 2015). MitoQ was studied in IRI after heart transplantation to reduce ROS production showing to block graft oxidative damage and blunt the early proinflammatory response in the recipient. This effect would be dependent on reducing mitochondrial DNA damage and H_2O_2 (Dare et al., 2015). On the contrary, no reduction in myocardial infarct size was found in the EMBRACE STEMI trial with MTP-131 (also known as Szeto-Schiller-31 or elamipretide), a cell-permeable mitochondria-targeting peptide selectively binding to cardiolipin and optimizing mitochondrial electron transport by reducing ROS generation (Gibson et al., 2016). The EMBRACE STEMI was a multicenter, randomized, double-blind phase IIa trial evaluating the efficacy and safety of MTP-131 vs. placebo infused at a rate of 0.05 mg/kg/h for 1 h among first-time anterior STEMI subjects undergoing primary percutaneous coronary intervention for a proximal or mid left anterior descending artery occlusion. No reduction of the primary endpoint (infarct size by creatine kinase–myocardial band and area under the curve over 72 h) was reached as well as no improvement in prespecified magnetic resonance imaging, angiographic, electrocardiographic, or clinical outcomes was shown (Gibson et al., 2016). In a similar manner, cyclosporine A, a potent inhibitor of the mitochondrial permeability transition pore, showed to significantly reduce myocardial infarction size in most, but not all, experimental studies (Argaud et al., 2005; Karlsson et al., 2010; Skyschally et al., 2010). As well, in some phase II clinical trials, cyclosporine A was likely to protect the heart following an AMI (Chiari et al., 2014; Hausenloy et al., 2014). On the contrary, two large clinical trials reported disappointing results, although a clear explanation is still lacking. The CYCLE (CYCLosporinE A in Reperfused Acute Myocardial Infarction) trial of 410 patients ST elevation AMI did not find any benefit with cyclosporine A administered prior to primary percutaneous coronary intervention in terms of ST-segment resolution and enzymatic myocardial infarct size (Ottani et al., 2016). In the CIRCUS (Does Cyclosporine Improve Clinical Outcome in ST Elevation Myocardial Infarction Patients) trial conducted among 970 patients with anterior ST elevation AMI, cyclosporine A immediately before primary percutaneous coronary intervention failed to improve clinical outcomes (all-cause death, heart failure hospitalization, and adverse left ventricle remodeling) at 1 year (Cung et al., 2015). For a wider explanation on this topic, readers can be referred to the review by Hausenloy et al. (2017). Among natural molecules, curcumin was largely studied as an antioxidant molecule, with promising direct and indirect effects on ROS scavenging and myocardial remodeling. An extensive discussion on this topic can be found elsewhere (Hernandez-Resendiz et al., 2015).

NEUTROPHIL OXIDANTS AND BRAIN REMODELING

Differently from other peripheral organs, the brain parenchyma does not elicit stereotypic immune responses. This is largely due to the unique anatomical composition, as endothelial, epithelial, and glial barriers tightly regulate the accessibility of immune cells. The anatomical and functional characteristics of this immune-privileged organ then imply a different response to IRI despite a significant gene overlapping (Zhang et al., 2014). The low levels of antioxidants associated with high polyunsaturated fatty acids in cellular membranes make the brain more susceptible to oxidative damage (Adibhatla and Hatcher, 2010). In the early phase of ischemic IRI, mitochondrial depolarization and activation of XO determine a first oxidative burst with ROS generation (mainly $O_2^{\cdot}$ and H_2O_2). They trigger PMN recruitment and activation, further precipitating IRI, even more when thrombolytic drugs are administered. Indeed, we have previously demonstrated how recombinant tissue-type plasminogen activator induces an early neutrophil degranulation via PI3K/Akt, which contributes

TABLE 1 | Efficacy of antioxidant compounds in myocardial ischemia/reperfusion injury.

Author	Year	Compound	Study protocol	Correlation with stroke
Eleawa et al., 2015	2015	CoQ10	Male Wistar rats (control, sham, MI without treatment, CoQ10 then MI)	CoQ10 pre-administration significantly reduced LV infarct area and normalized LV hemodynamic parameters. CoQ10 also decreased serum BNP and circulating inflammatory markers (TNF-α, IL-6). These effects were associated with lowered TBARS scores and concurrent increase in SOD and GSSH
Dare et al., 2015	2014	MitoQ	Heart transplant model in C57BL/6 mice [control, MitoQ; all exposed to short (30 min) or prolonged (4 h) cold preservation]	MitoQ to the donor heart protected against this I/R injury by blocking graft oxidative damage and dampening the early pro-inflammatory response in the recipient.
Gibson et al., 2016	2016	MTP-131	118 patients with anterior STEMI undergoing first-time PCI plus stenting within <4 h (i.v. MTP-131 at 0.05 mg/kg/h or appearing placebo)	MTP-131 failed in significantly reducing infarct size. MTP-131 was not associated with any improvement in magnetic resonance imaging, angiographic, electrocardiographic, or clinical outcomes
Argaud et al., 2005	2005	NIM811 (cyclosporin A derivative)	NZW rabbit [sham or I/R (10/5 min) preconditioned or not].	NIM811 increases the Ca^{2+} overload required to induce MPTP opening. NIM811 also reduced both necrotic and apoptotic cardiomyocyte death.
Skyschally et al., 2010	2010	Cyclosporin A	Göttinger minipigs [sham or I/R (90/120 min) or post-conditioning]	Both cyclosporine A at reperfusion and ischemic post-conditioning failed to reduced infarct size more than controls
Karlsson et al., 2010	2010	Cyclosporin A	Pigs [CsA (10 mg/kg) or placebo]	Cyclosporine A did not reduce IS/AAR compared with placebo. Rather, apoptosis-inducing factor protein expression was higher in the cyclosporine A group, thus suggesting a potential deleterious effect.
Hausenloy et al., 2014	2014	Cyclosporin A	78 patients undergoing elective CABG surgery [CsA (2.5 mg/kg) or placebo]	There was no significant difference in mean peak cTnT. However, in higher-risk patients peri-operative myocardial injury (post-operative cTnT) was reduced in the cyclosporine A group.
Chiari et al., 2014	2017	Cyclosporin A	61 patients undergoing elective aortic valve surgery [CsA (2.5 mg/kg) or placebo]	A significant 35% reduction of area under the curve for cTnI was observed in the cyclosporine group
Ottani et al., 2016	2016	Cyclosporin A	410 patients with anterior STEMI undergoing PCI [CsA (2.5 mg/kg) or placebo]	The two groups did not differ in TnI rise or LVEF both at day 4 and at 6 months. IS did not influence CsA efficacy.
Cung et al., 2015	2015	Cyclosporin A	970 patients with large STEMI within 6 h from onset [CsA (2.5 mg/kg) or placebo]	Cyclosporine A failed to reduce the rate of composite outcome as well as that of separate clinical components. No significant difference in the safety profile was observed between the two treatment groups.
Hernandez-Resendiz et al., 2015	2015	Curcumin	Male Wistar rats [curcumin (120 mg/kg/day) after 5/6 nephrectomy]	Curcumin restored sBP, myocardial wall thickening, LVEDV, and LVEF in nephrectomized rats. Also, it diminished MMP-2 levels and overall gelatinase activity, oxidative stress, and MPTP opening.

AAR, area at risk; BP, blood pressure; BNP, brain natriuretic peptide; CABG, coronary artery bypass graft; CsA, cyclosporin A; cTNI, cardiac troponin I; cTNT, cardiac troponin T; I/R, ischemia/reperfusion; IL, interleukin; IS, infarct size; LV, left ventricle; LVEDV, left ventricle end diastolic volume; LVEF, left ventricle ejection fraction; MMP, metalloproteinase; MPTP, mitochondrial permeability transition pore; PCI, percutaneous coronary intervention; SOD, superoxide dismutase; STEMI, ST elevation myocardial infarction; TBARS, thiobarbituric acid reactive substances; TNF, tumor necrosis factor.

to the increased risk of hemorrhagic transformation (Carbone et al., 2015b,c). PMNs then represent the leading source of ROS in the subacute phase of stroke. Experimental models largely emphasized the detrimental effect of NOX2 activation in the ischemic brain, being brain swelling and infarct size significantly reduced in $NOX2^{-/-}$ mice. In this context, especially $^{\cdot}OH$ has been described as typical phagocyte ROS and amplifier of ischemic injury on neuronal cells. $^{\cdot}OH$ is generated via the Fenton reaction and has great affinity for unsaturated fatty acids, ultimately leading to peroxyl radical (ROOS) generation. In turn, ROOS trigger a cycle of lipid peroxidation that destroys cellular membranes. Products of lipid peroxidation further sustain oxidative stress by generating aldehydes, dienals, or alkanes (e.g., malondialdehyde and 4-hydroxynonenal). The consequent redox unbalance leads to neuronal apoptosis and blood–brain barrier (BBB) breakdown.

More recently, NO has been suggested as an additional mediator of IRI. At low oxygen concentrations, NO accumulates and reacts with $O_2^{\cdot}$ to generate peroxynitrite. Nitrosative stress may lead to BBB breakdown, inflammation, and caspase activation, which ultimately lead to cell apoptosis through interacting with different cellular signaling pathways including matrix metalloproteinase, high-mobility group box 1, toll-like receptors 2 and 4, poly(ADP-ribose) polymerase, Src, Rho-associated protein kinase (ROCK), and glycogen synthase kinase (GSK)-3β (Radi et al., 2015). Oxidative stress may also influence epigenetic mechanisms (i.e., DNA methylation, histone modification, microRNAs) (Zhao et al., 2016; Narne et al., 2017),

TABLE 2 | Efficacy of antioxidant compounds in stroke.

Author	Year	Number of patient	Study design (follow-up)	Correlation with stroke
Edaravone				
Kono et al., 2013	2013	129 stroke patients	Retrospective analysis (7 and 90 days)	Edaravone was associated with higher recanalization rate ($p < 0.01$) and better mRS ($p < 0.01$).
Wada et al., 2014	2014	6336 stroke patients	Retrospective analysis (discharge)	Edaravone improved mRS score at discharge [OR 0.74 (95% CI 0.57–0.96); $p = 0.024$], without modifying length of hospital stay, hemorrhagic transformation, or in-hospital mortality.
Yamaguchi et al., 2017	2017	8274 stroke patients from PROTECT4.5 and SITS-ISTR studies	Retrospective analysis (90 days)	The combination of edaravone with r-tPA is associated with mRS improvement in patients with NIHSS score $\geq$ 16 ($p < 0.05$).
Lee and Xiang, 2018	2018	38 stroke patients	Prospective randomized trial (7 and 14 days)	Edaravone group was characterized by improved NIHSS score both at days 7 and 14 ($p < 0.05$ for both). Edaravone group also showed higher recanalization and lower rate of hemorrhagic transformation and bleeding complications ($p < 0.05$ for all).
Uric acid				
Logallo et al., 2011	2011	1136 stroke patients	Observational (7 and 90 days)	After tertile categorization, SUA correlated with early clinical improvement ($r = 0.012$; $p = 0.02$) and long-term favorable outcome [OR 1.004 (95% CI 1.001–1.009); $p = 0.04$].
Liu et al., 2015	2015	216 stroke patients	Prospective observational (90 days)	In multivariate models, increased SUA levels were associated with excellent outcomes [OR 1.005 (95% CI 1.002–1.009); $p = 0.033$]
Llull et al., 2015	2015	411 stroke patients	Prospective interventional (90 days)	UA therapy doubled the effect of placebo in improving stroke outcome in women [OR 2.088 (95% CI 1.050–4.150); $p = 0.036$], but not in men.
Chamorro et al., 2017	2017	421 stroke patients from URICO-ICTUS trial	Prospective interventional (90 days)	The addition of UA to thrombolysis improved functional outcome [OR 6.12 (95% CI 1.08–34·56); $p < 0·05$] in absence on any safety concerns.

CI, confidence interval; mRS, modified Rankin Scale; NIHSS, National Institute of Health Stroke Scale; OR, odds ratio; r-tPA, recombinant tissue-type plasminogen activator; RR, relative risk; SUA, serum uric acid.

well known to be implicated in neuroprotection (Felling and Song, 2015; Simon, 2016; Chandran et al., 2017). Therefore, it has been suggested that ROS may contribute themselves to neuronal recovery after ischemic stroke. In line with this hypothesis, ROS-induced activation of HIF-1α/β-catenin pathway has been associated with neuronal recovery in rats (Hu et al., 2014), whereas a biphasic role of ROS has been recently suggested also in human beings (Yang et al., 2018). Furthermore, oxidative stress (mainly H_2O_2 and NOX signaling) regulates neural stem and progenitor cell proliferation, self-renewal, and neurogenesis (Le Belle et al., 2011). As compared with $^{\cdot}OH$, ROS are generated constantly as part of a normal aerobic life and are active players of several metabolic pathways ranging from cell adhesion to lipid metabolism (Roy et al., 2017). Nevertheless, the extent to which the redox status potentially contributes to brain recovery has not been established yet. Rather, a large body of evidence indicates the suppression of oxidative stress as a promising strategy to reduce brain injury. Improving reperfusion is certainly the best approach to reduce ROS generation (Carbone et al., 2018a; Chamorro, 2018; Taskiran-Sag et al., 2018). Furthermore, it is likely that antioxidant compounds tested in previous neuroprotection trials might be more effective if reperfusion therapies are co-administered (Chamorro, 2018). Among different antioxidant compounds, edaravone has already been used for years in the Far East countries. As a free radical scavenger with inhibitory effects on lipid peroxidation (Yamamoto, 2017), edaravone promotes neuroprotection when combined with thrombolysis (Logallo et al., 2011; Kono et al., 2013; Wada et al., 2014; Liu et al., 2015; Llull et al., 2015; Chamorro et al., 2017; Yamaguchi et al., 2017; Lee and Xiang, 2018; **Table 2**). Surprisingly, free radical scavenging properties have also been described for uric acid (UA). Serum levels of UA are classically associated with increased CV risk, but this association may rather be a compensatory mechanism (Li et al., 2015). Furthermore, when administered with recombinant tissue-type plasminogen activator, UA significantly improves the efficacy of thrombolysis (Logallo et al., 2011; Liu et al., 2015; Llull et al., 2015; Chamorro et al., 2017; **Table 2**). Other classes of compounds are currently under evaluation in preclinical studies and include a synthetic analog of vitamin E and specific inhibitors of NOX and NOS (Sun et al., 2018). Finally, some advances in nanomedicine are expected to improve drug delivery (Zhang et al., 2017; Shen et al., 2018) or even provide new nanoparticles with antioxidant potential (Hosoo et al., 2017).

CONCLUSION

Free radicals have strong oxidative properties in ischemic tissues. When reperfusion occurs, the massive generation of ROS and reactive nitrogen species leads to cell death via DNA damage, protein dysfunction, and lipid peroxidation. However, signaling pathways activated by oxidative stress are also likely to be involved in the healing processes. Appropriate consideration of the role of PMN-related oxidative stress in IRI

might potentially improve current therapeutic strategies. However, several critical points should be taken into account. PMN-generated ROS may have both detrimental and beneficial roles in different models of IRI. This dual role might depend on the cell and tissue types and the timing of response (Montecucco et al., 2017). ROS activity is not limited to nearby cells/tissues. Rather there is variability in the diffusion range due to the different life span and reactivity. Finally, the side effects induced by immune suppression should be considered (Horckmans et al., 2017). Addressing these issues may explain how the results of clinical trials have so far failed to reproduce the success of preclinical studies.

AUTHOR CONTRIBUTIONS

All the authors wrote, made substantial corrections and contribution, and approved the final version of the manuscript to be published.

FUNDING

This study was supported by a grant from the Italian Ministry of Health to the Italian Cardiovascular Network (#2754291) and a grant from the Fondazione CARIGE to FM.

REFERENCES

Adibhatla, R. M., and Hatcher, J. F. (2010). Lipid oxidation and peroxidation in CNS health and disease: from molecular mechanisms to therapeutic opportunities. *Antioxid. Redox. Signal.* 12, 125–169. doi: 10.1089/ARS.2009.2668

Alard, J. E., Ortega-Gomez, A., Wichapong, K., Bongiovanni, D., Horckmans, M., Megens, R. T., et al. (2015). Recruitment of classical monocytes can be inhibited by disturbing heteromers of neutrophil HNP1 and platelet CCL5. *Sci. Transl. Med.* 7:ra196. doi: 10.1126/scitranslmed.aad5330

Albelda, S. M., Smith, C. W., and Ward, P. A. (1994). Adhesion molecules and inflammatory injury. *FASEB J.* 8, 504–512.

Argaud, L., Gateau-Roesch, O., Muntean, D., Chalabreysse, L., Loufouat, J., Robert, D., et al. (2005). Specific inhibition of the mitochondrial permeability transition prevents lethal reperfusion injury. *J. Mol. Cell Cardiol.* 38, 367–374. doi: 10.1016/j.yjmcc.2004.12.001

Bonaventura, A., Liberale, L., Carbone, F., Vecchie, A., Diaz-Canestro, C., Camici, G. G., et al. (2018). The pathophysiological role of neutrophil extracellular traps in inflammatory diseases. *Thromb. Haemost.* 118, 6–27. doi: 10.1160/TH17-09-0630

Bonaventura, A., Montecucco, F., and Dallegri, F. (2016). Cellular recruitment in myocardial ischaemia/reperfusion injury. *Eur. J. Clin. Invest.* 46, 590–601. doi: 10.1111/eci.12633

Bonaventura, A., Montecucco, F., Dallegri, F., Carbone, F., Lüscher, T. F., Camici, G. G., et al. (2019). Novel findings in neutrophil biology and their impact on cardiovascular disease. *Cardiovasc. Res.* 115, 1266–1285. doi: 10.1093/cvr/cvz084

Cao, S. S., and Kaufman, R. J. (2014). Endoplasmic reticulum stress and oxidative stress in cell fate decision and human disease. *Antioxid. Redox. Signal.* 21, 396–413. doi: 10.1089/ars.2014.5851

Carbone, F., Busto, G., Padroni, M., Bernardoni, A., Colagrande, S., Dallegri, F., et al. (2018a). Radiologic cerebral reperfusion at 24 h predicts good clinical outcome. *Transl. Stroke Res.* 10, 178–188. doi: 10.1007/s12975-018-0637-8

Carbone, F., Mach, F., and Montecucco, F. (2015a). Update on the role of neutrophils in atherosclerotic plaque vulnerability. *Curr. Drug Targets* 16, 321–333. doi: 10.2174/1389450115666141110093013

Carbone, F., Nencioni, A., Mach, F., Vuilleumier, N., and Montecucco, F. (2013). Pathophysiological role of neutrophils in acute myocardial infarction. *Thromb. Haemost.* 110, 501–514. doi: 10.1160/TH13-03-0211

Carbone, F., Rigamonti, F., Burger, F., Roth, A., Bertolotto, M., Spinella, G., et al. (2018b). Serum levels of osteopontin predict major adverse cardiovascular events in patients with severe carotid artery stenosis. *Int. J. Cardiol.* 255, 195–199. doi: 10.1016/j.ijcard.2018.01.008

Carbone, F., Vuilleumier, N., Bertolotto, M., Burger, F., Galan, K., Roversi, G., et al. (2015b). Treatment with recombinant tissue plasminogen activator (r-TPA) induces neutrophil degranulation in vitro via defined pathways. *Vascul. Pharmacol.* 64, 16–27. doi: 10.1016/j.vph.2014.11.007

Carbone, F., Vuilleumier, N., Burger, F., Roversi, G., Tamborino, C., Casetta, I., et al. (2015c). Serum osteopontin levels are upregulated and predict disability after an ischaemic stroke. *Eur. J. Clin. Invest.* 45, 579–586. doi: 10.1111/eci.12446

Chamorro, A. (2018). Neuroprotectants in the era of reperfusion therapy. *J. Stroke* 20, 197–207. doi: 10.5853/jos.2017.02901

Chamorro, A., Amaro, S., Castellanos, M., Gomis, M., Urra, X., Blasco, J., et al. (2017). Uric acid therapy improves the outcomes of stroke patients treated with intravenous tissue plasminogen activator and mechanical thrombectomy. *Int. J. Stroke* 12, 377–382. doi: 10.1177/1747493016684354

Chandran, R., Mehta, S. L., and Vemuganti, R. (2017). Non-coding RNAs and neuroprotection after acute CNS injuries. *Neurochem. Int.* 111, 12–22. doi: 10.1016/j.neuint.2017.01.015

Chiari, P., Angoulvant, D., Mewton, N., Desebbe, O., Obadia, J. F., Robin, J., et al. (2014). Cyclosporine protects the heart during aortic valve surgery. *Anesthesiology* 121, 232–238. doi: 10.1097/ALN.0000000000000331

Cung, T. T., Morel, O., Cayla, G., Rioufol, G., Garcia-Dorado, D., Angoulvant, D., et al. (2015). Cyclosporine before PCI in patients with acute myocardial infarction. *N. Engl. J. Med.* 373, 1021–1031. doi: 10.1056/NEJMoa1505489

Dare, A. J., Logan, A., Prime, T. A., Rogatti, S., Goddard, M., Bolton, E. M., et al. (2015). The mitochondria-targeted anti-oxidant MitoQ decreases ischemia-reperfusion injury in a murine syngeneic heart transplant model. *J. Heart Lung Transplant.* 34, 1471–1480. doi: 10.1016/j.healun.2015.05.007

Davies, K. J. (2016). The oxygen paradox, oxidative stress, and ageing. *Arch. Biochem. Biophys.* 595, 28–32. doi: 10.1016/j.abb.2015.11.015

Edin, M. L., Wang, Z., Bradbury, J. A., Graves, J. P., Lih, F. B., DeGraff, L. M., et al. (2011). Endothelial expression of human cytochrome P450 epoxygenase CYP2C8 increases susceptibility to ischemia-reperfusion injury in isolated mouse heart. *FASEB J.* 25, 3436–3447. doi: 10.1096/fj.11-188300

El-Benna, J., Dang, P. M., Gougerot-Pocidalo, M. A., Marie, J. C., and Braut-Boucher, F. (2009). p47phox, the phagocyte NADPH oxidase/NOX2 organizer: structure, phosphorylation and implication in diseases. *Exp. Mol. Med.* 41, 217–225. doi: 10.3858/emm.2009.41.4.058

Eleawa, S. M., Alkhateeb, M., Ghosh, S., Al-Hashem, F., Shatoor, A. S., Alhejaily, A., et al. (2015). Coenzyme Q10 protects against acute consequences of experimental myocardial infarction in rats. *Int. J. Physiol. Pathophysiol. Pharmacol.* 7, 1–13.

Felling, R. J., and Song, H. (2015). Epigenetic mechanisms of neuroplasticity and the implications for stroke recovery. *Exp. Neurol.* 268, 37–45. doi: 10.1016/j.expneurol.2014.09.017

Ferrante, G., Nakano, M., Prati, F., Niccoli, G., Mallus, M. T., and Ramazzotti, V. (2010). High levels of systemic myeloperoxidase are associated with coronary plaque erosion in patients with acute coronary syndromes: a clinicopathological study. *Circulation* 122, 2505–2513. doi: 10.1161/CIRCULATIONAHA.110.955302

Fleming, I., Michaelis, U. R., Bredenkotter, D., Fisslthaler, B., Dehghani, F., Brandes, R. P., et al. (2001). Endothelium-derived hyperpolarizing factor synthase (Cytochrome P450 2C9) is a functionally significant source of reactive oxygen species in coronary arteries. *Circ. Res.* 88, 44–51. doi: 10.1161/01.res.88.1.44

Frangogiannis, N. G. (2015). Pathophysiology of myocardial infarction. *Compr. Physiol.* 5, 1841–1875. doi: 10.1002/cphy.c150006

Garcia-Culebras, A., Duran-Laforet, V., Pena-Martinez, C., Ballesteros, I., Pradillo, J. M., Diaz-Guzman, J., et al. (2018). cells as therapeutic targets in

neuroinflammation after stroke: specific roles of neutrophils and neutrophil-platelet interactions. *J. Cereb. Blood Flow Metab.* 38, 2150–2164. doi: 10.1177/0271678X18795789

Gibson, C. M., Giugliano, R. P., Kloner, R. A., Bode, C., Tendera, M., Janosi, A., et al. (2016). EMBRACE STEMI study: a Phase 2a trial to evaluate the safety, tolerability, and efficacy of intravenous MTP-131 on reperfusion injury in patients undergoing primary percutaneous coronary intervention. *Eur. Heart J.* 37, 1296–1303. doi: 10.1093/eurheartj/ehv597

Gorenkova, N., Robinson, E., Grieve, D. J., and Galkin, A. (2013). Conformational change of mitochondrial complex I increases ROS sensitivity during ischemia. *Antioxid. Redox. Signal.* 19, 1459–1468. doi: 10.1089/ars.2012.4698

Hausenloy, D., Kunst, G., Boston-Griffiths, E., Kolvekar, S., Chaubey, S., John, L., et al. (2014). The effect of cyclosporin-A on peri-operative myocardial injury in adult patients undergoing coronary artery bypass graft surgery: a randomised controlled clinical trial. *Heart* 100, 544–549. doi: 10.1136/heartjnl-2013-304845

Hausenloy, D. J., Botker, H. E., Engstrom, T., Erlinge, D., Heusch, G., Ibanez, B., et al. (2017). Targeting reperfusion injury in patients with ST-segment elevation myocardial infarction: trials and tribulations. *Eur. Heart J.* 38, 935–941.

Hausenloy, D. J., and Yellon, D. M. (2016). Ischaemic conditioning and reperfusion injury. *Nat. Rev. Cardiol.* 13, 193–209. doi: 10.1038/nrcardio.2016.5

Hensley, K., Robinson, K. A., Gabbita, S. P., Salsman, S., and Floyd, R. A. (2000). Reactive oxygen species, cell signaling, and cell injury. *Free Radic. Biol. Med.* 28, 1456–1462. doi: 10.1016/s0891-5849(00)00252-5

Hernandez-Resendiz, S., Chinda, K., Ong, S. B., Cabrera-Fuentes, H., Zazueta, C., and Hausenloy, D. J. (2018). The role of redox dysregulation in the inflammatory response to acute myocardial ischaemia-reperfusion injury - adding fuel to the fire. *Curr. Med. Chem.* 25, 1275–1293. doi: 10.2174/0929867324666170329100619

Hernandez-Resendiz, S., Correa, F., Garcia-Nino, W. R., Buelna-Chontal, M., Roldan, F. J., Ramirez-Camacho, I., et al. (2015). Cardioprotection by curcumin post-treatment in rats with established chronic kidney disease. *Cardiovasc. Drugs Ther.* 29, 111–120. doi: 10.1007/s10557-015-6581-x

Horckmans, M., Ring, L., Duchene, J., Santovito, D., Schloss, M. J., Drechsler, M., et al. (2017). Neutrophils orchestrate post-myocardial infarction healing by polarizing macrophages towards a reparative phenotype. *Eur. Heart J.* 38, 187–197. doi: 10.1093/eurheartj/ehw002

Hosoo, H., Marushima, A., Nagasaki, Y., Hirayama, A., Ito, H., Puentes, S., et al. (2017). Neurovascular unit protection from cerebral ischemia-reperfusion injury by radical-containing nanoparticles in mice. *Stroke* 48, 2238–2247. doi: 10.1161/STROKEAHA.116.016356

Hotamisligil, G. S., and Davis, R. J. (2016). Cell signaling and stress responses. *Cold Spring Harb. Perspect. Biol.* 8:a006072. doi: 10.1101/cshperspect.a006072

Hu, Q., Liang, X., Chen, D., Chen, Y., Doycheva, D., Tang, J., et al. (2014). Delayed hyperbaric oxygen therapy promotes neurogenesis through reactive oxygen species/hypoxia-inducible factor-1alpha/beta-catenin pathway in middle cerebral artery occlusion rats. *Stroke* 45, 1807–1814. doi: 10.1161/STROKEAHA.114.005116

Jaganjac, M., Cipak, A., Schaur, R. J., and Zarkovic, N. (2016). Pathophysiology of neutrophil-mediated extracellular redox reactions. *Front. Biosci.* 21, 839–855. doi: 10.2741/4423

Jordan, J. E., Zhao, Z. Q., and Vinten-Johansen, J. (1999). The role of neutrophils in myocardial ischemia-reperfusion injury. *Cardiovasc. Res.* 43, 860–878. doi: 10.1016/s0008-6363(99)00187-x

Karlsson, L. O., Zhou, A. X., Larsson, E., Astrom-Olsson, K., Mansson, C., Akyurek, L. M., et al. (2010). Cyclosporine does not reduce myocardial infarct size in a porcine ischemia-reperfusion model. *J. Cardiovasc. Pharmacol. Ther.* 15, 182–189. doi: 10.1177/1074248410362074

Kono, S., Deguchi, K., Morimoto, N., Kurata, T., Yamashita, T., Ikeda, Y., et al. (2013). Intravenous thrombolysis with neuroprotective therapy by edaravone for ischemic stroke patients older than 80 years of age. *J. Stroke Cerebrovasc. Dis.* 22, 1175–1183. doi: 10.1016/j.jstrokecerebrovasdis.2013.02.010

Kunduzova, O. R., Bianchi, P., Parini, A., and Cambon, C. (2002). Hydrogen peroxide production by monoamine oxidase during ischemia/reperfusion. *Eur. J. Pharmacol.* 448, 225–230. doi: 10.1016/s0014-2999(02)01913-1

Le Belle, J. E., Orozco, N. M., Paucar, A. A., Saxe, J. P., Mottahedeh, J., Pyle, A. D., et al. (2011). Proliferative neural stem cells have high endogenous ROS levels that regulate self-renewal and neurogenesis in a PI3K/Akt-dependant manner. *Cell Stem Cell* 8, 59–71. doi: 10.1016/j.stem.2010.11.028

Lee, X. R., and Xiang, G. L. (2018). Effects of edaravone, the free radical scavenger, on outcomes in acute cerebral infarction patients treated with ultra-early thrombolysis of recombinant tissue plasminogen activator. *Clin. Neurol. Neurosurg.* 167, 157–161. doi: 10.1016/j.clineuro.2018.02.026

Lemaire, S., Lizard, G., Monier, S., Miguet, C., Gueldry, S., Volot, F., et al. (1998). Different patterns of IL-1beta secretion, adhesion molecule expression and apoptosis induction in human endothelial cells treated with 7alpha-, 7beta-hydroxycholesterol, or 7-ketocholesterol. *FEBS Lett.* 440, 434–439. doi: 10.1016/s0014-5793(98)01496-3

Li, R., Huang, C., Chen, J., Guo, Y., and Tan, S. (2015). The role of uric acid as a potential neuroprotectant in acute ischemic stroke: a review of literature. *Neurol. Sci.* 36, 1097–1103. doi: 10.1007/s10072-015-2151-z

Lisman, T. (2018). Platelet-neutrophil interactions as drivers of inflammatory and thrombotic disease. *Cell Tissue Res.* 371, 567–576. doi: 10.1007/s00441-017-2727-4

Liu, X., Liu, M., Chen, M., Ge, M. Q., and Pan, S. M. (2015). Serum uric acid is neuroprotective in Chinese patients with acute ischemic stroke treated with intravenous recombinant tissue plasminogen activator. *J. Stroke Cerebrovasc. Dis.* 24, 1080–1086. doi: 10.1016/j.jstrokecerebrovasdis.2015.01.011

Llull, L., Laredo, C., Renu, A., Perez, B., Vila, E., Obach, V., et al. (2015). Uric acid therapy improves clinical outcome in women with acute ischemic stroke. *Stroke* 46, 2162–2167. doi: 10.1161/STROKEAHA.115.009960

Logallo, N., Naess, H., Idicula, T., Brogger, J., Waje-Andreassen, U., and Thomassen, L. (2011). Serum uri acid: neuroprotection in thrombolysis. The bergen NORSTROKE study. *BMC Neurol.* 11:114. doi: 10.1186/1471-2377-11-114

Lonkar, P., and Dedon, P. C. (2011). Reactive species and DNA damage in chronic inflammation: reconciling chemical mechanisms and biological fates. *Int. J. Cancer* 128, 1999–2009. doi: 10.1002/ijc.25815

Matsumura, F., Yamaguchi, Y., Goto, M., Ichiguchi, O., Akizuki, E., Matsuda, T., et al. (1998). Xanthine oxidase inhibition attenuates kupffer cell production of neutrophil chemoattractant following ischemia-reperfusion in rat liver. *Hepatology* 28, 1578–1587. doi: 10.1002/hep.510280618

Montecucco, F., Liberale, L., Bonaventura, A., Vecchie, A., Dallegri, F., and Carbone, F. (2017). The Role of inflammation in cardiovascular outcome. *Curr. Atheroscler. Rep.* 19:11. doi: 10.1007/s11883-017-0646-1

Narne, P., Pandey, V., and Phanithi, P. B. (2017). Interplay between mitochondrial metabolism and oxidative stress in ischemic stroke: an epigenetic connection. *Mol. Cell. Neurosci.* 82, 176–194. doi: 10.1016/j.mcn.2017.05.008

Ong, S. B., Samangouei, P., Kalkhoran, S. B., and Hausenloy, D. J. (2015). The mitochondrial permeability transition pore and its role in myocardial ischemia reperfusion injury. *J. Mol. Cell Cardiol.* 78, 23–34. doi: 10.1016/j.yjmcc.2014.11.005

Ottani, F., Latini, R., Staszewsky, L., La Vecchia, L., Locuratolo, N., Sicuro, M., et al. (2016). Cyclosporine a in reperfused myocardial infarction: the multicenter. Controlled, open-label CYCLE trial. *J. Am. Coll. Cardiol.* 67, 365–374. doi: 10.1016/j.jacc.2015.10.081

Pajares, M., Jimenez-Moreno, N., Dias, I. H., Debelec, B., Vucetic, M., Fladmark, K. E., et al. (2015). Redox control of protein degradation. *Redox Biol.* 6, 409–420. doi: 10.1016/j.redox.2015.07.003

Palazzo, A. J., Jones, S. P., Anderson, D. C., Granger, D. N., and Lefer, D. J. (1998). Coronary endothelial P-selectin in pathogenesis of myocardial ischemia-reperfusion injury. *Am. J. Physiol.* 275, H1865–H1872. doi: 10.1152/ajpheart.1998.275.5.H1865

Panth, N., Paudel, K. R., and Parajuli, K. (2016). Reactive oxygen species: a key hallmark of cardiovascular disease. *Adv. Med.* 2016:9152732.

Patterson, C., Ruef, J., Madamanchi, N. R., Barry-Lane, P., Hu, Z., Horaist, C., et al. (1999). Stimulation of a vascular smooth muscle cell NAD(P)H oxidase by thrombin. *Evidence that p47*(phox) may participate in forming this oxidase in vitro and in vivo. *J. Biol. Chem.* 274, 19814–19822. doi: 10.1074/jbc.274.28.19814

Pisarenko, O. I., Lakomkin, V. L., Studneva, I. M., Timoshin, A. A., Kuzmin, A. I., Ruuge, E. K., et al. (1994). Allopurinol-enhanced postischemic recovery in the

isolated rat heart involves repletion of high-energy phosphates. *Biochem. Med. Metab. Biol.* 51, 16–26. doi: 10.1006/bmmb.1994.1002

Poli, G., Biasi, F., and Leonarduzzi, G. (2013). Oxysterols in the pathogenesis of major chronic diseases. *Redox Biol.* 1, 125–130. doi: 10.1016/j.redox.2012.12.001

Prokopowicz, Z., Marcinkiewicz, J., Katz, D. R., and Chain, B. M. (2012). Neutrophil myeloperoxidase: soldier and statesman. *Arch. Immunol. Ther. Exp.* 60, 43–54. doi: 10.1007/s00005-011-0156-8

Radi, R., Beckman, J. S., Bush, K. M., and Freeman, B. A. (2015). When the good and the bad make the ugly: the discovery of peroxynitrite. *J. Biol. Chem.* 290, 30726–30727. doi: 10.1074/jbc.o115.000001

Roy, J., Galano, J. M., Durand, T., Le Guennec, J. Y., and Lee, J. C. (2017). Physiological role of reactive oxygen species as promoters of natural defenses. *FASEB J.* 31, 3729–3745. doi: 10.1096/fj.201700170R

Shen, Y., Cao, B., Snyder, N. R., Woeppel, K. M., Eles, J. R., and Cui, X. T. (2018). ROS responsive resveratrol delivery from LDLR peptide conjugated PLA-coated mesoporous silica nanoparticles across the blood-brain barrier. *J. Nanobiotechnol.* 16:13. doi: 10.1186/s12951-018-0340-7

Simon, R. P. (2016). Epigenetic modulation of gene expression governs the brain's response to injury. *Neurosci. Lett.* 625, 16–19. doi: 10.1016/j.neulet.2015.12.024

Skyschally, A., Schulz, R., and Heusch, G. (2010). Cyclosporine A at reperfusion reduces infarct size in pigs. *Cardiovasc. Drugs. Ther.* 24, 85–87. doi: 10.1007/s10557-010-6219-y

Smith, C. W. (2000). Introduction: functional polarity of motile neutrophils. *Blood* 95, 2459–2461. doi: 10.1182/blood.v95.8.2459.008a37_2459_2461

Somanna, N. K., Valente, A. J., Krenz, M., Fay, W. P., Delafontaine, P., and Chandrasekar, B. (2016). The Nox1/4 dual inhibitor GKT137831 or Nox4 knockdown inhibits angiotensin-II-induced adult mouse cardiac fibroblast proliferation and migration. *AT*1 physically associates with Nox4. *J. Cell. Physiol.* 231, 1130–1141. doi: 10.1002/jcp.25210

Sun, M. S., Jin, H., Sun, X., Huang, S., Zhang, F. L., Guo, Z. N., et al. (2018). Free radical damage in ischemia-reperfusion injury: an obstacle in acute ischemic stroke after revascularization therapy. *Oxid. Med. Cell Longev.* 2018:3804979. doi: 10.1155/2018/3804979

Szabo, C., Ischiropoulos, H., and Radi, R. (2007). Peroxynitrite: biochemistry, pathophysiology and development of therapeutics. *Nat. Rev. Drug Discov.* 6, 662–680. doi: 10.1038/nrd2222

Taskiran-Sag, A., Yemisci, M., Gursoy-Ozdemir, Y., Erdener, S. E., Karatas, H., Yuce, D., et al. (2018). Improving microcirculatory reperfusion reduces parenchymal oxygen radical formation and provides neuroprotection. *Stroke* 49, 1267–1275. doi: 10.1161/STROKEAHA.118.020711

Vasilyev, N., Williams, T., Brennan, M. L., Unzek, S., Zhou, X., Heinecke, J. W., et al. (2005). Myeloperoxidase-generated oxidants modulate left ventricular remodeling but not infarct size after myocardial infarction. *Circulation* 112, 2812–2820. doi: 10.1161/circulationaha.105.542340

Vinten-Johansen, J. (2004). Involvement of neutrophils in the pathogenesis of lethal myocardial reperfusion injury. *Cardiovasc. Res.* 61, 481–497. doi: 10.1016/j.cardiores.2003.10.011

Wada, T., Yasunaga, H., Inokuchi, R., Horiguchi, H., Fushimi, K., Matsubara, T., et al. (2014). Effects of edaravone on early outcomes in acute ischemic stroke patients treated with recombinant tissue plasminogen activator. *J. Neurol. Sci.* 345, 106–111. doi: 10.1016/j.jns.2014.07.018

Wang, L. P., Fan, S. J., Li, S. M., Wang, X. J., Gao, J. L., and Yang, X. H. (2017). Oxidative stress promotes myocardial fibrosis by upregulating KCa3.1 channel expression in AGT-REN double transgenic hypertensive mice. *Pflugers Archiv.* 469, 1061–1071. doi: 10.1007/s00424-017-1984-0

Weyrich, A. S., Ma, X. Y., Lefer, D. J., Albertine, K. H., and Lefer, A. M. (1993). In vivo neutralization of P-selectin protects feline heart and endothelium in myocardial ischemia and reperfusion injury. *J. Clin. Invest.* 91, 2620–2629. doi: 10.1172/jci116501

Yamaguchi, T., Awano, H., Matsuda, H., Tanahashi, N., and Investigators, P. (2017). edaravone with and without .6 Mg/Kg Alteplase within 4.5 hours after ischemic stroke: a prospective cohort study (PROTECT4.5). *J. Stroke Cerebrovasc. Dis.* 26, 756–765. doi: 10.1016/j.jstrokecerebrovasdis.2016.10.011

Yamamoto, Y. (2017). Plasma marker of tissue oxidative damage and edaravone as a scavenger drug against peroxyl radicals and peroxynitrite. *J. Clin. Biochem. Nutr.* 60, 49–54. doi: 10.3164/jcbn.16-63

Yang, J., Qi, J., Xiu, B., Yang, B., Niu, C., and Yang, H. (2018). Reactive oxygen species play a biphasic role in brain ischemia. *J. Invest. Surg.* 32, 97–102. doi: 10.1080/08941939.2017.1376131

Zhang, C., Ling, C. L., Pang, L., Wang, Q., Liu, J. X., Wang, B. S., et al. (2017). Direct macromolecular drug delivery to cerebral ischemia area using neutrophil-mediated nanoparticles. *Theranostics* 7, 3260–3275. doi: 10.7150/thno.19979

Zhang, Y., Kong, P., Chen, Y., Yu, Y., Liu, J., Yang, L., et al. (2014). Significant overlapping modules and biological processes between stroke and coronary heart disease. *CNS Neurol. Disord. Drug Targets* 13, 652–660. doi: 10.2174/1871527312666131223115112

Zhao, H., Han, Z., Ji, X., and Luo, Y. (2016). Epigenetic regulation of oxidative stress in ischemic stroke. *Aging Dis.* 7, 295–306. doi: 10.14336/AD.2015.1009

Conflict of Interest: The authors declare that the research was conducted in the absence of any commercial or financial relationships that could be construed as a potential conflict of interest.

frontiers in Physiology

ORIGINAL RESEARCH
published: 02 February 2021
doi: 10.3389/fphys.2020.622613

Proarrhythmic Electrical Remodeling by Noncardiomyocytes at Interfaces With Cardiomyocytes Under Oxidative Stress

*Yali Zhao†, Shankar Iyer†‡, Maryam Tavanaei†‡, Nicole T. Nguyen, Andrew Lin and Thao P. Nguyen**

Division of Cardiology, Department of Medicine, The Cardiovascular Research Laboratory, David Geffen School of Medicine at UCLA, Los Angeles, CA, United States

OPEN ACCESS

Edited by:
Olivier Bernus, Université de Bordeaux, France

Reviewed by:
Callum Michael Zgierski-Johnston, University Heart Center Freiburg, Germany
Lai-Hua Xie, Rutgers Biomedical and Health Sciences, United States

***Correspondence:**
Thao P. Nguyen
tpnguyen@mednet.ucla.edu

†These authors have contributed equally to this work

‡Present address:
Shankar Iyer, Medical College of Wisconsin, Wauwatosa, WI, United States
Maryam Tavanaei, Internal Medicine Department, Santa Barbara Cottage Hospital, Santa Barbara, CA, United States

Specialty section:
This article was submitted to Cardiac Electrophysiology, a section of the journal Frontiers in Physiology

Received: *29 October 2020*
Accepted: *17 December 2020*
Published: *02 February 2021*

Citation:
Zhao Y, Iyer S, Tavanaei M, Nguyen NT, Lin A and Nguyen TP (2021) Proarrhythmic Electrical Remodeling by Noncardiomyocytes at Interfaces With Cardiomyocytes Under Oxidative Stress. Front. Physiol. 11:622613. doi: 10.3389/fphys.2020.622613

Life-threatening ventricular arrhythmias, typically arising from interfaces between fibrosis and surviving cardiomyocytes, are feared sequelae of structurally remodeled hearts under oxidative stress. Incomplete understanding of the proarrhythmic electrical remodeling by fibrosis limits the development of novel antiarrhythmic strategies. To define the mechanistic determinants of the proarrhythmia in electrical crosstalk between cardiomyocytes and noncardiomyocytes, we developed a novel *in vitro* model of interface between neonatal rat ventricular cardiomyocytes (NRVMs) and controls [NRVMs or connexin43 (Cx43)-deficient HeLa cells] vs. $Cx43^+$ noncardiomyocytes [aged rat ventricular myofibroblasts (ARVFs) or HeLaCx43 cells]. We performed high-speed voltage-sensitive optical imaging at baseline and following acute H_2O_2 exposure. In NRVM-NRVM and NRVM-HeLa controls, no arrhythmias occurred under either experimental condition. In the NRVM-ARVF and NRVM-HeLaCx43 groups, $Cx43^+$ noncardiomyocytes enabled passive decremental propagation of electrical impulses and impaired NRVM activation and repolarization, thereby slowing conduction and prolonging action potential duration. Following H_2O_2 exposure, arrhythmia triggers, automaticity, and non-reentrant and reentrant arrhythmias emerged. This study reveals that myofibroblasts (which generate cardiac fibrosis) and other noncardiomyocytes can induce not only structural remodeling but also electrical remodeling and that electrical remodeling by noncardiomyocytes can be particularly arrhythmogenic in the presence of an oxidative burst. Synergistic electrical remodeling between H_2O_2 and noncardiomyocytes may account for the clinical arrhythmogenicity of myofibroblasts at fibrotic interfaces with cardiomyocytes in ischemic/non-ischemic cardiomyopathies. Understanding the enhanced arrhythmogenicity of synergistic electrical remodeling by H_2O_2 and noncardiomyocytes may guide novel safe-by-design antiarrhythmic strategies for next-generation iatrogenic interfaces between surviving native cardiomyocytes and exogenous stem cells or engineered tissues in cardiac regenerative therapies.

Keywords: fibrosis, remodeling, oxidative stress, H_2O_2, cardiomyocyte, myofibroblast, interface, arrhythmia

INTRODUCTION

In the normal adult mammalian left ventricle, electrically excitable (capable of firing all-or-none action potentials) cardiomyocytes comprise 80% of the volume but only 30% of the cell number (Vliegen et al., 1991). In contrast, ventricular noncardiomyocytes (predominantly fibroblasts and endothelial cells) are electrically non-excitable (incapable of firing action potentials), but they outnumber cardiomyocytes and comprise the cellular majority in the heart. Following fibrotic structural remodeling, the ratio of noncardiomyocytes to cardiomyocytes increases further, and the noncardiomyocyte composition changes as new active myofibroblasts over-replace old quiescent fibroblasts. Myofibroblasts are noncardiomyocytes that share features with both cardiomyocytes and fibroblasts. Myofibroblasts do not exist in healthy young myocardium. They only proliferate in the injured, diseased, aged, or therapeutically ablated myocardium, by phenotypic conversion of existing fibroblasts, epithelial–mesenchymal transition, or *de novo* production. Fibrosis develops as myofibroblasts deposit collagen bundles to salvage the compromised cardiac mechanical function, albeit at the cost of higher risk of life-threatening ventricular arrhythmias (Nguyen et al., 2014).

Traditionally, the role of myofibroblasts in arrhythmogenesis was deemed purely indirect and passive, attributed to the interference of collagen bundles with electrical propagation and source–sink relationships (Kucera et al., 1998). However, the last 15 years marks a growing recognition for a more direct and active role of myofibroblasts in arrhythmogenesis. Myofibroblasts may directly engage local cardiomyocytes in bidirectional crosstalk by secreting soluble paracrine factors (Pedrotty et al., 2009; Vasquez et al., 2010; Cartledge et al., 2015). They may also form connexin (Cx)-based gap junction coupling for short-range heterotypic intercellular connectivity or Cx-based nanotube coupling for long-range heterotypic intercellular connectivity (Gaudesius et al., 2003; He et al., 2011; Nguyen et al., 2012; Mahoney et al., 2016; Quinn et al., 2016; Ribeiro-Rodrigues et al., 2017; Rubart et al., 2018). Additionally, these two mechanisms may synergize. For example, soluble myofibroblast paracrine factors, such as TGF-β1, may promote heterotypic gap junction coupling and increase myofibroblast arrhythmogenicity (Salvarani et al., 2017). Yet how fibrosis causes proarrhythmic electrical remodeling of local cardiomyocytes is not completely understood.

We hypothesized that myofibroblasts are not unique in proarrhythmic remodeling of cardiomyocyte electrophysiology via electrical crosstalk, as other non-excitable cells may also be capable if they are equipped to conduct adequate intercellular electrical communication and are more depolarized than cardiomyocytes. To test this hypothesis, we selected three noncardiomyocyte cell types based on extensive literature evidence of the differences in their Cx43 expression, which is negligible in HeLa cells, moderate in myofibroblasts (higher than in fibroblasts), and high in HeLa cells engineered to overexpress Cx43 (HeLaCx43). Literature is replete with immunohistochemistry and cutting-edge imaging evidence of *in vitro* Cx43 detection at cardiomyocyte short- and long-range interfaces with fibroblasts and HeLaCx43 cells (Gaudesius et al., 2003; Miragoli et al., 2006; He et al., 2011; Quinn et al., 2016; Ribeiro-Rodrigues et al., 2017). However, immunohistochemical evidence of Cx presence (or absence) cannot prove (nor disprove) that functional gap junctions/nanotubes formed or that their function remained unchanged for the experimental duration. Indeed, like other ion channels, both the formation and functional state (open vs. closed) of gap junctions/nanotubes are dynamic, clinically and experimentally. They are transient by nature (Palacios-Prado and Bukauskas, 2009) and depend on a host of variables, including local environmental stress, pH, and local tissue stretch, just to name a few. Unfortunately, evidence of heterotypic gap junction function, and more importantly, of potential attendant functional consequences and clinical relevance is scant. Therefore, the objective of this study is to address this knowledge gap in the field. Furthermore, we postulated that local environmental stress, such as an acute H_2O_2-mediated oxidative burst, might synergize by further lowering the repolarization reserve of cardiomyocytes and the protective source-sink mismatch of the myocardium. This study aimed to provide functional proof-of-concept for our hypotheses using a novel *in vitro* model of cardiomyocyte–noncardiomyocyte interface that we developed.

METHODS

The experimental protocol was approved by the University of California, Los Angeles (UCLA) Institutional Animal Care and Use Committee and conformed to the National Institutes of Health (NIH) *Guide for the Care and Use of Laboratory Animals*.

Isolating Aged Rat Ventricular Myofibroblasts

Ventricular myofibroblasts were freshly isolated from aged (24- to 26-month-old) Fischer 344 (F344) rats (ARVFs) of the National Institute on Aging (NIA) according to standard protocols (Katwa, 2003; Zhou et al., 2017; Melzer et al., 2020). Rats were euthanized by intraperitoneal injection of heparin sulfate (1,000 U) and sodium pentobarbital (100 mg/kg). The adequacy of anesthesia was confirmed by the lack of pedal withdrawal reflex, corneal reflex, and motor response to pain stimuli by scalpel tip. Fibrotic aged hearts were perfused using the standard Langendorff retrograde perfusion method at 12 ml/min, 37°C with Ca^{2+}-free Tyrode's solution for 4 min to remove blood from the vessels, then with enzyme solution for 35–37 min, and finally with 0.05 mmol/l-Ca^{2+} Tyrode's solution to wash out the enzyme solution. The enzyme solution was a Ca-free Tyrode's solution containing 2.2 mg/ml of collagenase (Type II, Worthington) and 0.17 mg/ml of protease (type XIV, Sigma). Digested hearts were removed from the perfusion apparatus and gently agitated to dissociate cells. Digested ventricular tissue was filtered through 70-μm cell strainers and was centrifuged (500 g, 5 min) to remove cardiomyocytes. Single ARVFs thus obtained were suspended in growth medium

[Dulbecco's modified Eagle's medium (DMEM) 10% fetal bovine serum (FBS)] for seeding.

Overexpressing Cx43 in HeLa Cells

Stable gap junction-rich HeLa cells expressing Cx43 and the fluorescent reporter yellow fluorescent protein (YFP) were generated using the Sleeping Beauty transposon system with the transposase plasmid pCMV(CAT)T7-SB100 (pSB100X, Addgene #34879). The gene of interest vector pSBi-RP (Addgene #60513) was prepared by removing the endogenous dTomato and subcloning Cx43YFP into pSBi-RP. Cx43YFP expression within this construct was driven by the constitutively active mammalian promoter EF-1a. HeLa cells were co-transfected with both plasmids at a ratio of 20, Cx43YFPpSBiP:1, pSB100X, using the Bio-T transfection reagent (Bioland Scientific). The transfection complex [1 μg of total DNA and 1.5 μl of Bio-T in 50 μl phosphate-buffered saline (PBS)] was applied to HeLa cell cultures with 70% confluency in 35-mm dishes. Two days post-transfection, HeLa cells expressing Cx43YFP were selected by maintaining the transfected cells in a puromycin (1 μg/ml) selection medium for 1 week. Once the selected HeLa cells expressing Cx43YFP reached confluency, they were split at a ratio of 1:4. Thereafter, T25 flasks were seeded with HeLaCx43 cells, and cells were cultured to confluency without puromycin. HeLaCx43 cell stocks were stored at −140°C and used as needed.

Patterning Cardiomyocyte–Noncardiomyocyte Interface

In our interface design, an interface divides a 14-mm-diameter monolayer into two equal half-circular sides. Side 1 was seeded with Fischer 344 neonatal rat ventricular cardiomyocytes (NRVMs). Side 2 was seeded with either of four cell types with well-known ample or deficient Cx43 expression (**Figure 1A**). The two side-2 control cell types were $Cx43^+$ cardiomyocytes (NRVMs, positive control for robust support of impulse propagation) and $Cx43^-$ noncardiomyocytes (HeLa cells, negative control for absent support of impulse propagation). The two side-2 experimental cell types were both $Cx43^+$ noncardiomyocytes but from a cardiac vs. non-cardiac source: ARVFs and HeLaCx43 cells.

Monolayers were prepared on 14-mm-diameter glass bottoms inside 35-mm culture dishes (MatTek) following the protocol and schedule depicted in **Figure 1B**. Because NRVMs grew more slowly than noncardiomyocytes, to pattern our interface model, we used six physical, chemical, and chronological measures to curb successfully the co-cultured noncardiomyocyte overgrowth past the interface into side 1 of NRVMs. (1) During NRVM harvest, neonatal cardiomyocytes were separated from neonatal fibroblasts by centrifugation and plating. (2) Prior to cell seeding, a two-phase aqueous system was created as a chemical barrier by supplementing NRVM medium with dextran (12.8% wt/wt) and noncardiomyocyte medium with polyethylene glycol (5% wt/wt). (3) To promote NRVM adherence and proliferation, glass bottoms were precoated with laminin only on the half-side that would serve as side 1 of heterotypic co-cultures. (4) On day 0, a vertical coverslip was inserted as an additional physical barrier separating the two sides of the dish. (5) On day 1, NRVMs (0.5 million cells/cm^2) were seeded on the laminin-precoated side 3 days in advance of noncardiomyocyte seeding on day 4 (0.5 million cells/cm^2). (6) On day 5, the vertical coverslip was removed only in the last 48 h for NRVMs and noncardiomyocytes to make contact at the interface. By day 7, the monolayers were ready for optical mapping.

High-Speed Optical Imaging

Bright-field microscopy was performed for each monolayer at the start of optical mapping to rapidly locate the heterotypic interface and assess for freedom from macroscopic (large cell clusters as opposed to isolated single cells) invasion of side-1 NRVMs by side-2 noncardiomyocytes. High-speed, high-resolution voltage-sensitive fluorescent optical mapping was performed at 37.0°C after 48 h of co-culture using di-8-ANEPPS (40 μM, 10 min; Invitrogen). Monolayers were superfused at baseline with normal Tyrode's solution and then with H_2O_2 solution (100 μM, ≥4 min). The microscope (Nikon) was equipped with a high-speed CMOS camera (100 × 100-pixel resolution; MiCAM Ultima, SciMedia). The 20 × 20-mm^2 field of view yields a spatial resolution of 200 μm/pixel. Fluorescence was excited with blue light delivered by a 455-nm light-emitting diode through a 550/60-nm excitation filter (Semrock). Spontaneous optical action potentials were recorded at 1.0 ms/frame.

Data Analysis

We analyzed optical voltage signals using BVAna (SciMedia) as previously described (Nguyen et al., 2016; Zhao et al., 2020). We reduced noise by cubic filtering of signals (3 × 3 pixels). Optical voltage signals were present and analyzed not for HeLa cells but only for the three cell types that supported impulse propagation: NRVMs on either side, and ARVFs or HeLaCx43 cells on side 2.

We measured activation time and activation duration by either one of two quantitative methods: activation map (preferable) or wave display (useful for low peak voltage amplitudes). Wave display is a sensitive method that allows visualization and measurement of multiple selected impulses at once from a single location (selected by one point-cursor), multiple scattered locations (selected by multiple point-cursors), or multiple locations arranged continuously along a selected scanning line. For all 1D wave displays (selected by a point-cursor or a line), time is the independent variable (x-axis). However, the 2D wave display offers the additional information of location as the dependent variable (y-axis), thus a method to calculate the activation duration of the linear cell population along that scanning line. If the peak voltage amplitudes permit, a more elegant and preferable method to calculate activation time and activation duration of a monolayer is to construct an activation map to offer at once a comprehensive bird's-eye view of the entire monolayer (one side or both sides) during only one selected impulse (or depolarization wave). However, because the activation mapping method requires signals of

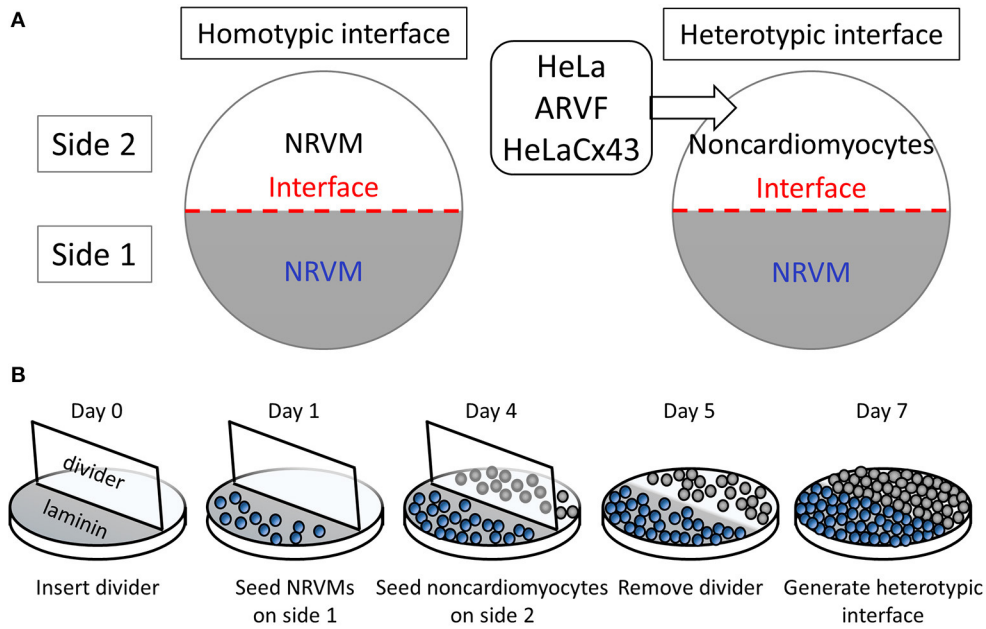

FIGURE 1 | Patterning cardiomyocyte–noncardiomyocyte interfaces. **(A)** Side-1 cell type for all monolayer groups was neonatal rat ventricular cardiomyocytes (NRVMs). Side-2 cell type was either NRVMs in homotypic interfaces (*left panel*) or noncardiomyocytes in heterotypic interfaces (*right panel*). **(B)** The protocol schedule allowed the formation of heterotypic coupling at the interface over 48 h prior to optical mapping of monolayers by day 7.

larger amplitudes (such as those generated by NRVMs or HeLaCx43 cells) than the wave display method, not all optical signals (such as those generated by ARVFs) could be mapped. We measured the activation time of a given location in the monolayer at the maximum positive dV/dt of the optical action potential. We measured the activation duration of the entire monolayer (one side or both sides) using activation map for the adequate voltage amplitudes of NRVMs and HeLaCx43 cells and using 2D wave display for the inadequate voltage amplitudes of ARVFs. The activation duration, or the time to activate that entire monolayer, is the difference between the latest and earliest activation time. Because the earliest activation time is the reference time 0 and reflects the focus of activation, the activation duration of a monolayer equals the latest activation time of that monolayer. We calculated NRVM conduction velocity by dividing the monolayer 7-mm radius by NRVM activation duration based on our finding of NRVM transverse conduction anisotropy, from the monolayer edge to the interface (as opposed to longitudinal conduction anisotropy along the monolayer interface).

We measured NRVM action potential duration at 80% of repolarization (APD_{80}) as the interval from maximal dV/dt to the moment at 80% of repolarization. Using the APD mapping method, we measured and mapped the APD_{80} distribution during a single excitation wavefront or the mean APD_{80} distribution during multiple excitation wavefronts. Using the wave display method, we calculated the mean of APD_{80} measurements from several successive excitation wavefronts corrected for the spontaneous NRVM beating rate (mean $APD_{80,c}$) by the Bazett formula.

Statistical Analysis

Statistical analysis was performed using GraphPad Prism8. Continuous variables were expressed as mean ± standard deviation (SD), and categorical variables as percentage. Due to H_2O_2 data non-normality as assessed by the Shapiro–Wilk test, non-parametric statistical tests were applied. Statistical significance of differences was evaluated using (1) one-way ANOVA with Tukey's *post-hoc* analysis for multiple-group comparisons of continuous variables under the same condition, (2) the Wilcoxon signed rank test for two-condition comparisons of continuous variables for the same group, and (3) two-tailed Fisher's exact test for comparisons of categorical variables. *P*-value and 95% confidence interval [95% CI] were estimated using the bootstrap-resampling method with 10,000 replications. $P < 0.05$ was the minimal standard for statistical significance.

RESULTS

Prior to optical mapping, the interface in each heterotypic monolayer was readily located using bright-field microscopy; and macroscopic (large cell clusters as opposed to isolated single cells) invasion of side-1 NRVMs by side-2 noncardiomyocytes was excluded. Single NRVMs are practically indistinguishable from single noncardiomyocytes in a mixture of both cell types. However, in our 2D model, visual distinction of the masses of these two different cell types under bright-field microscopy was readily apparent. Due to inherent cellular density differences, the population of thicker NRVMs appeared more attenuated (whiter) than that of neighboring thinner noncardiomyocytes. Additionally, optical voltage impulses of non-excitable

noncardiomyocytes if any were readily distinguished from optical action potentials of excitable NRVMs due to slower upstroke and diminished voltage amplitudes. Thus, besides visual confirmation of the heterotypic interface under bright-field microscopy, this discrepancy in optical voltage signals from excitable NRVMs vs. non-excitable noncardiomyocytes served as additional functional confirmation.

Of note, in this study, we avoided NRVM pacing by design because it can override the noncardiomyocyte-to-myocyte direction of the crosstalk and attenuate or negate potential chaotic electrotonic modulations of NRVMs by noncardiomyocytes and/or H_2O_2, such as repolarization impairment, multiple foci of spontaneous activation, or reentry. We found that hyperactivity (multiple rapid foci of spontaneous activation) did not arise in non-paced control NRVMs at baseline. If any, because we took great measures to purify NRVMs from neonatal rat ventricular fibroblasts (NRVFs) following NRVM harvest, non-paced "pure" (NRVF-devoid) NRVM monolayers displayed hypoactivity compared with typical "impure" NRVM monolayers richer in NRVFs.

Impulse Propagation by $Cx43^+$ Noncardiomyocytes Was Passive, Decremental, and Anisotropic

In this section, we focused on side 2 of the monolayer and the forward direction of the crosstalk, from NRVMs to noncardiomyocytes. We aimed to define the impact of NRVMs on noncardiomyocyte electrophysiological behavior, specifically regarding the capability of noncardiomyocytes for impulse propagation. Below, we presented evidence that although $Cx43^+$ noncardiomyocytes enabled impulse propagation across the heterotypic interface, impulse propagation by $Cx43^+$ noncardiomyocytes was passive, decremental, and anisotropic.

Figures 2A–H feature four pairs of 6-ms representative isochronal activation maps of four entire monolayers under baseline vs. H_2O_2 condition. Each activation map reflects the propagation of a given spontaneous excitation wavefront emerging from side-1 NRVMs, reaching the interface, and with or without success crossing the interface to reach side 2. To ease comparison of the two test conditions for the same monolayer (same row), both maps were constructed based on the longer activation duration of the entire monolayer, which was always under H_2O_2 condition. Thus, the four monolayers were mapped on four different ranges of activation times as indicated next to the corresponding color scales. The two activation durations of the two sides in a monolayer were indicated next to the corresponding sides in the monolayer activation map.

Intergroup comparisons of the four monolayers under the same test condition (same column, **Figure 2**) reveals which of the four side-2 cell types enabled continued propagation of impulses that emerged spontaneously from side-1 NRVMs and crossed the interface. Intercondition comparisons for the same monolayer reveal whether H_2O_2 modulated noncardiomyocyte capability to promote impulse propagation.

Under baseline condition, **Figure 2A** shows that in this NRVM-NRVM monolayer, the entire side-2 NRVM population was activated by an impulse emerging from side 1 in the same duration it had taken to activate the entire side-1 NRVM population. These findings indicate that side-2 NRVMs enabled rapid all-or-none active impulse propagation. In contrast, **Figure 2B** shows that in this NRVM-HeLa monolayer, the NRVM excitation wavefront from side 1 arrived at the interface but failed to reach the HeLa cells on side 2, indicating that as expected, HeLa cells failed to support impulse propagation. For the NRVM-ARVF monolayer in **Figure 2C**, ARVF activation by NRVM impulses was evidenced, not by activation mapping but by the more sensitive wave display method (which still did not detect impulse propagation by HeLa cells in **Figure 2B**). Using 2D wave display (**Supplementary Figure 1**), we ascertained the main propagation direction by line scan in multiple directions to be from left to right along the interface. The fact that ARVF voltage signals escaped detection by activation mapping underscores that ARVF-mediated impulse propagation was rapidly decremental. Compared with ARVFs in **Figure 2C**, HeLaCx43 cells in the NRVM-HeLaCx43 monolayer of **Figure 2D** enabled impulse propagation that decremented less rapidly. However, while impulses propagated through the entire side-2 NRVM monolayer (**Figure 2A**), impulses propagated through only a portion of the HeLaCx43 monolayer proximal to the interface. Yet it took 255% longer (780 vs. 220 ms) to activate that HeLaCx43 subpopulation than to activate the entire side-1 NRVM population in the same co-culture (**Figure 2D**). These comparisons underscore that impulse propagation mediated by HeLaCx43 cells was both passive and decremental.

Importantly, compared with side-1 NRVMs in the same monolayer (**Figure 2D**) or with side-2 NRVMs in an NRVM-NRVM monolayer (**Figure 2A**), HeLaCx43 cells and NRVMs have divergent anisotropies of impulse propagation, indicating that the electrical connectivity between the two cell types was non-uniform and weak. It is known that anisotropy of impulse propagation has important arrhythmogenic implications as dynamic functional regulation mediated by dynamic gap junctional conductance (Valderrábano, 2007). Within side 1 of **Figures 2A–D**, following the emergence of an NRVM activation focus in the midline farthest from the interface, the resultant action potentials propagated transversely toward the interface (vertical arrows), indicating that the depolarization wave reached the entire interface length almost simultaneously. In **Figure 2A**, strong homotypic coupling between NRVMs on both sides of the interface caused simultaneous activation of all side-2 NRVMs along the interface and consequent preservation of the original transverse conduction anisotropy of side-1 NRVMs. In contrast, in **Figure 2D**, HeLaCx43 cells failed to preserve the transverse conduction anisotropy of side-1 NRVMs. Instead, HeLaCx43 impulses propagated longitudinally along the interface (horizontal arrow) because the HeLaCx43 cells along the interface were not activated by NRVMs simultaneously. Longitudinal stacking of HeLaCx43 activation isochrones indicates that heterotypic NRVM-HeLaCx43 coupling was non-uniform and weaker than homotypic coupling among HeLaCx43

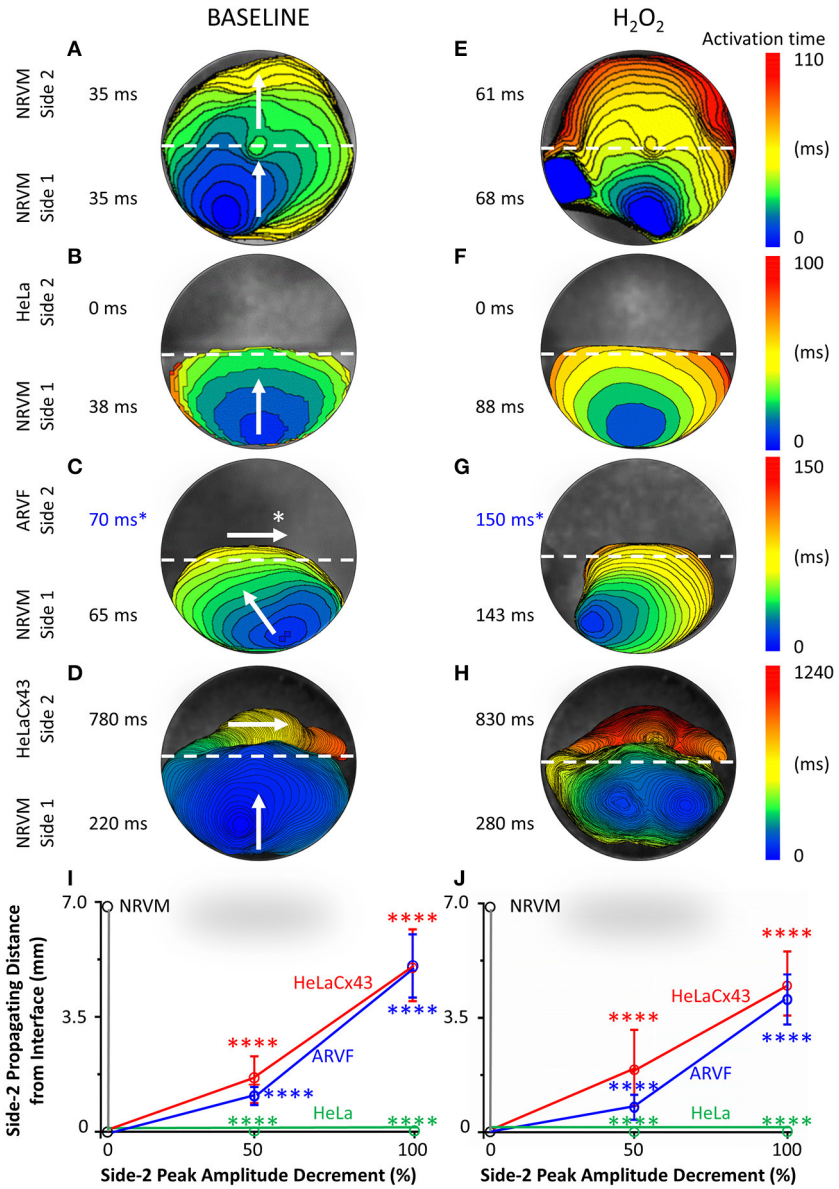

FIGURE 2 | Divergent anisotropies of impulse propagation by cardiomyocytes vs. $Cx43^+$ noncardiomyocytes. **(A–H)** Representative activation maps (6-ms isochrones) of the entire monolayer under baseline (left column) vs. H_2O_2 condition (right column) during a single spontaneous excitation wavefront emerging from side-1 NRVMs, reaching the interface, and with or without success crossing the interface to reach side 2. Note the longitudinal anisotropy of $Cx43^+$ noncardiomyocytes (horizontal arrows in **C,D**) in contrast to the transverse anisotropy of NRVMs (vertical/near vertical arrows in **A–D**). To ease comparison of the two test conditions for the same monolayer (same row), both activation maps were constructed based on the longer activation duration of the entire monolayer, which was always that under H_2O_2 condition. Thus, the four monolayers were mapped based on four different activation-time ranges indicated by numbers next to the color scales. The two activation durations of the two sides in a monolayer were indicated next to the corresponding sides in the monolayer activation map. *ARVF main activation direction and activation durations **(C,G)** were measured using the 2D wave display method (see **Supplementary Figure 1**). **(I,J)** Under baseline (left panel) vs. H_2O_2 condition (right panel), successful propagation of spontaneous action potentials from side-1 NRVMs across the interface to side 2 was supported only by the three $Cx43^+$ cell types, but not by $Cx43^-$ HeLa cells. Side-2 NRVMs supported active impulse propagation with no amplitude drop-off. In contrast, ARVFs and HeLaCx43 cells supported passive impulse propagation with substantial amplitude decrement. Number of monolayers: NRVM-NRVM, $n = 9$; NRVM-HeLa, $n = 5$; NRVM-ARVF, $n = 11$; NRVM-HeLaCx43, $n = 8$. ****$P < 0.0001$; one-way ANOVA with Tukey's *post-hoc* analysis for multiple-group comparisons under the same condition. $P > 0.05$ for all two-condition comparisons of the same group by the Wilcoxon signed rank test. NRVM, neonatal rat ventricular cardiomyocyte; ARVF, aged rat ventricular myofibroblast.

cells. This longitudinal conduction anisotropy was characteristic of all HeLaCx43 co-cultures tested in this study as well as of ARVF co-cultures (as determined by the wave display method; horizontal arrows, **Figure 2D** and **Supplementary Figure 1**). Of note, under H_2O_2 condition, the divergence in conduction anisotropy between NRVMs and HeLaCx43 cells may not be as

apparent because the intrinsic anisotropic conduction properties of both cell types (Valderrábano, 2007) were dynamically perturbed by H_2O_2 (**Figures 2E–H**).

Taken together, at baseline, in the NRVM-NRVM group ($n = 9$), spontaneous action potentials emerging from side 1 propagated actively across the interface to side 2 with preserved peak amplitude; therefore, side-2 NRVMs served as positive control (**Figure 2I**). This finding indicates that NRVMs on both sides of the homotypic interface were excitable and well coupled to one another. However, in the NRVM-HeLa group ($n = 5$), HeLa cells acted as an electrical barrier to impulse propagation, thus serving as negative control. Subsequent acute H_2O_2 exposure did not change the capability of either side-2 control NRVM or HeLa group for impulse propagation (**Figure 2J**).

In NRVM co-cultures with $Cx43^+$ noncardiomyocytes (NRVM-ARVF, $n = 11$ and NRVM-HeLaCx43, $n = 8$), spontaneous NRVM impulses succeeded in propagating across the interface to reach noncardiomyocytes, albeit with decremental peak amplitudes. Peak amplitudes of impulses propagated by ARVFs and HeLaCx43 cells dropped 50% by 1.1 $\pm$ 0.3 and 1.6 $\pm$ 0.7 mm from the interface and then became extinct by 5.1 $\pm$ 1.0 and 5.1 $\pm$ 1.1 mm, respectively (**Figure 2I**). These findings suggest that while $Cx43^+$ noncardiomyocytes could act as capacitors for passive NRVM impulse propagation, voltage signals deteriorated, most likely due to non-excitability and weak, variable electrical connectivity to NRVMs. Subsequent acute H_2O_2 exposure did not significantly change how far voltage signals could passively propagate past the interface or how fast they deteriorated (**Figure 2J**). However, in terms of propagating distances and peak amplitudes, HeLaCx43 cells were superior to ARVFs at enabling impulse propagation under both test conditions.

$Cx43^+$ Noncardiomyocytes and H_2O_2 Impaired Neonatal Rat Ventricular Cardiomyocyte Activation and Slowed Neonatal Rat Ventricular Cardiomyocyte Conduction

In this section, we focused on side 1 of the monolayer and the reverse direction of the crosstalk, from noncardiomyocytes to NRVMs. We aimed to define the impact of $Cx43^+$ noncardiomyocytes on NRVM electrophysiological behavior, specifically regarding NRVM activation and conduction. Below, we presented evidence that $Cx43^+$ noncardiomyocytes impaired NRVM activation (**Figures 2A–H**, **3A–H**, and **Supplementary Figure 2**), thereby slowing NRVM conduction (**Figures 3I,J**), independently and synergistically with H_2O_2.

Figures 3A–H features four pairs of representative 6-ms isochronal activation maps of only side-1 NRVMs (not of both sides as in **Figures 2A–H**) from four monolayers under baseline vs. H_2O_2 condition. To ease comparison of the two test conditions for the same side 1 (same row), both maps were constructed based on the longer of the two side-1 NRVM activation durations, which was always that under H_2O_2 condition. Thus, the four monolayers were mapped on four different activation-time ranges as indicated next to the corresponding color scales. The activation duration of side 1 in each monolayer was indicated next to its corresponding activation map.

At baseline, neither side-2 NRVMs nor HeLa cells impaired the rapid activation of co-cultured side-1 NRVMs (which measured 35–38 ms in **Figures 2A,B** and 40–43 ms in **Figures 3A,B**). In contrast, both ARVFs and HeLaCx43 cells independently prolonged NRVM activation duration by 74–86 and 412–529% over baseline, respectively (to 75 and 65 ms in **Figures 2C**, **3C** and 220 ms in **Figures 2D**, **3D**). These findings indicate that HeLaCx43 cells were more potent than ARVFs at impairing NRVM activation.

In subsequent exposure, H_2O_2 independently prolonged the activation duration of side-1 NRVMs in NRVM-NRVM monolayers by 94–123% over baseline (**Figure 2E** vs. **Figure 2A**, **Figure 3E** vs. **Figure 3A**) and of those in NRVM-HeLa monolayers to similar extent, by 125–132% over baseline (**Figure 3F** vs. **Figure 3B**, **Figure 2F** vs. **Figure 2B**). Note that the activation durations of NRVMs in co-cultures with HeLa cells (38–40 ms at baseline, 88–90 ms under stress) roughly matched the activation durations of NRVMs on each side of co-cultures with other NRVMs (35–43 ms at baseline; 61–96 ms under stress) under similar test conditions. These findings indicate that HeLa cells exerted no appreciable impact on the co-cultured NRVMs under either test condition. Importantly, H_2O_2-induced impairment of NRVM activation was heterogeneous and chaotic as evidenced by the mismatch in isochronal patterns of the same monolayers pre- and post-H_2O_2 exposure. Comparisons of **Figure 2E** with **Figure 2A**, **Figure 3E** with **Figure 3A**, **Figure 2F** with **Figure 2B**, and **Figure 3F** with **Figure 3B** reveal that H_2O_2 did not affect each NRVM in the same isochrone under prior baseline equally.

Evidence that the collective impairment of NRVM activation by both $Cx43^+$ noncardiomyocytes and H_2O_2 was synergistic came from adding up their individual impairment contributions. For example, independently, ARVFs and H_2O_2 prolonged NRVM activation by 86–94% (**Figures 2C,E**) over baseline (**Figure 2A**). Therefore, a simple sum of their individual impairment would have amounted to 180%. However, collectively (**Figure 2G**), they caused instead a synergistic impairment of 309%, or 71% greater than the sum of their individual impairment. Repeating these calculations with the three monolayers in **Figures 3A,C,E** confirms that, collectively, ARVFs and H_2O_2 delayed NRVM activation synergistically by 249%, or 26% greater than expected from the sum of their individual impairment of 198%.

Likewise, the collective impairment of NRVM activation by both HeLaCx43 cells and H_2O_2 was also synergistic. HeLaCx43 cells and H_2O_2 delayed NRVM activation markedly by 551–700% (**Figures 2H**, **3H**), or 3–12% greater than expected from the sums of their individual impairment of 535% (**Figures 3D,E**) and 623% (**Figures 2D,E**) over baseline (**Figures 2A**, **3A**). Note that although H_2O_2 synergistic impairment of NRVM activation with HeLaCx43 cells was more severe than that with ARVFs because the contribution by HeLaCx43 cells was larger than by ARVFs, H_2O_2 synergy with ARVFs (26 or 71%) was greater than with

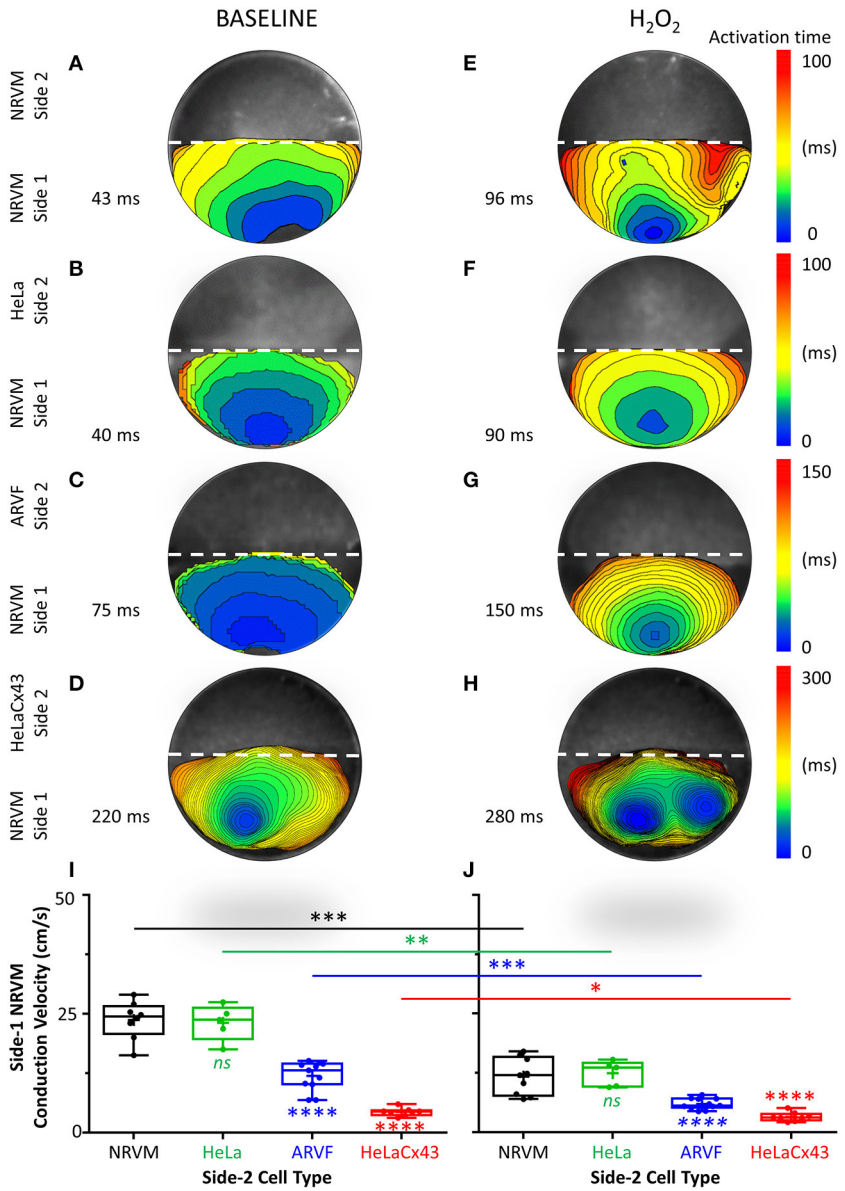

FIGURE 3 | Cx43$^+$ noncardiomyocytes and H_2O_2 impaired NRVM activation and slowed conduction. **(A–H)** Representative activation maps (6-ms isochrones) of side-1 NRVMs under baseline (left column) vs. H_2O_2 condition (right column) during a single spontaneous excitation wavefront sweeping across side 1 of the monolayer. To ease comparison of the two test conditions for the same side 1 (same row), both maps were constructed based on the longer of the two side-1 NRVM activation durations, which was always that under H_2O_2 condition. Thus, the four monolayers were mapped on four different activation-time ranges indicated by numbers next to the color scales. The activation duration of side 1 in each monolayer was indicated next to its corresponding activation map. Please refer to **Supplementary Figure 2** for a summary of independent and synergistic prolongation of NRVM activation duration by Cx43$^+$ noncardiomyocytes and H_2O_2. **(I,J)** Independent and synergistic slowing of NRVM conduction by Cx43$^+$ noncardiomyocytes and H_2O_2. Number of monolayers: NRVM-NRVM, $n = 9$; NRVM-HeLa, $n = 5$; NRVM-ARVF, $n = 11$; NRVM-HeLaCx43, $n = 8$. Symbols: box plots with mean (+), median, first and third quartiles (box), minimum and maximum (whiskers). $^{ns}P > 0.05$, $^{*}P < 0.05$, $^{**}P < 0.01$, $^{***}P < 0.001$, $^{****}P < 0.0001$; one-way ANOVA with Tukey's *post-hoc* analysis for multiple-group comparisons under the same condition and the Wilcoxon signed rank test for two-condition comparisons of the same group. NRVM, neonatal rat ventricular cardiomyocyte; ARVF, aged rat ventricular myofibroblast.

HeLaCx43 cells (3 or 12%). Importantly, synergistic impairment of NRVM activation by both Cx43$^+$ noncardiomyocytes and H_2O_2 led to dispersion of NRVM activation, increased NRVM activation gradient, and enhanced NRVM automaticity as evidenced by the emergence of thin, fractionated activation isochrones over longer activation durations, and multiple shifting foci of activation (**Figure 3G** and **Figure 3H** vs. **Figure 3E** and **Figure 3F**).

Taken together, Cx43$^+$ noncardiomyocytes impaired activation of co-cultured NRVMs independently or

synergistically with H_2O_2 (**Supplementary Figure 2**), thereby significantly slowing NRVM conduction (**Figures 3I,J**). However, because HeLaCx43 cells were superior to ARVFs at impairing NRVM activation under both test conditions, HeLaCx43 cells caused greater reduction in NRVM conduction velocity.

$Cx43^+$ Noncardiomyocytes and H_2O_2 Impaired Neonatal Rat Ventricular Cardiomyocyte Repolarization and Prolonged Action Potential Duration

Next, we examined the independent and collective impact of $Cx43^+$ noncardiomyocytes and H_2O_2 on NRVM repolarization and the consequences of such electrical remodeling on NRVM APD_{80}.

Figures 4A–H feature four pairs of APD_{80} maps of side-1 NRVMs from four representative monolayers under baseline vs. H_2O_2 condition. Each APD_{80} map reflects the APD_{80} distribution within side 1 of a monolayer during a single spontaneous excitation wavefront. Intergroup comparisons of the four monolayers under the same test condition (same column, **Figure 4**) reveal the modulation impact of noncardiomyocytes. Intercondition comparisons for the same monolayer reveal the modulation impact of H_2O_2. To ease intergroup and intercondition comparisons, all maps were constructed based on the longest APD_{80} range of 159–500 ms, which was the same as that of the side-1 NRVM monolayer in co-culture with HeLaCx43 cells under H_2O_2 condition. The mean of the APD_{80} distribution was indicated next to the corresponding APD_{80} map.

At baseline, neither side-2 NRVMs nor HeLa cells modulate repolarization of side-1 NRVMs (**Figures 4A,B**). In contrast, both ARVFs and HeLaCx43 cells impaired NRVM repolarization to similar extent as evidenced by APD_{80} prolongation from control value of 200 ms (**Figures 4A,B**) to 310–320 ms (a 55–60% prolongation over baseline, **Figures 4C,D**). Comparing **Figures 4E,F** with **Figures 4A,B** reveals that H_2O_2 prolonged APD_{80} to 310–315 ms in both control monolayers, indicating that H_2O_2 impaired NRVM repolarization and prolonged APD_{80} independently by 58% over baseline. Comparing **Figures 4G,H** with **Figures 4C,D** reveals that H_2O_2 prolonged APD_{80} synergistically with ARVFs and HeLaCx43 cells at roughly equal extent by 135–140% over baseline, corresponding to 15–24% increase over their respective summative impairment.

Figures 4I,J show the means of APD_{80} measurements from five successive excitation wavefronts corrected for the spontaneous NRVM beating rate by the Bazett formula under baseline vs. H_2O_2 condition, respectively. Taken together, impairment of NRVM repolarization by $Cx43^+$ noncardiomyocytes independently or synergistically with H_2O_2 significantly prolonged APD_{80}. However, HeLaCx43 cells and ARVFs were equally capable of impairing NRVM repolarization under both test conditions to cause similar prolongation of NRVM APD_{80}.

$Cx43^+$ Noncardiomyocytes and H_2O_2 Were Synergistically Arrhythmogenic

Finally, we determined whether independent or synergistic impairment of NRVM activation and repolarization by $Cx43^+$ noncardiomyocytes and H_2O_2 carries actual arrhythmogenic consequences.

Figure 5A summarizes the incidence of arrhythmia triggers (left panel) and non-reentrant (middle panel) and reentrant arrhythmias (right panel) of the four groups under baseline vs. H_2O_2 condition. The increase of arrhythmia triggers and non-reentrant arrhythmias from baseline to H_2O_2 in the two control groups reflects the independent arrhythmogenicity of H_2O_2 (**Figure 5A**, left and middle panels). The higher incidence of arrhythmia triggers, and non-reentrant and reentrant arrhythmias at baseline in the two experimental groups compared with the two control groups reflects the independent arrhythmogenicity of $Cx43^+$ noncardiomyocytes (**Figure 5A**, all three panels). Note that complex reentry mediated by dynamic functional conduction blocks developed only in the presence of $Cx43^+$ noncardiomyocytes (**Figure 5A**, right panel). However, the probabilities of successful arrhythmogenesis were the highest in the presence of both $Cx43^+$ noncardiomyocytes and H_2O_2. These findings suggest that $Cx43^+$ noncardiomyocytes and H_2O_2 must have synergized to reduce NRVM repolarization reserve enough for local arrhythmia triggers to overcome the protective local source–sink mismatch and propagate through the rest of the NRVM monolayers.

Figures 5B,C illustrate the synergistic arrhythmogenicity of HeLaCx43 cells and H_2O_2. Spontaneous optical action potentials of NRVMs distal to (blue traces) and proximal to (red traces) the interface with HeLaCx43 cells reveal the new emergence of various arrhythmias in the presence of H_2O_2. In **Figure 5B**, exposure of an NRVM-HeLaCx43 monolayer to H_2O_2 induced early (EADs) and delayed afterdepolarizations (DADs) and a burst of triggered activity, causing new tachy-bradyarrhythmia to emerge in NRVMs. In **Figure 5C**, H_2O_2 exposure of another NRVM-HeLaCx43 co-culture shortened NRVM spontaneous cycle length by 4.5-fold compared with baseline, precipitating an equivalent of monomorphic "ventricular tachycardia" in NRVMs distal to the interface. However, proximal to the interface, non-uniform functional conduction block and dispersion of refractoriness precipitated bradyarrhythmia.

Figures 5D,E illustrate the synergistic arrhythmogenicity of ARVFs and H_2O_2. Activation maps (6-ms isochrones) of NRVMs in co-cultures with ARVFs reveal the new emergence of non-reentrant and reentrant arrhythmias in the presence of H_2O_2.

In **Figure 5D** left panel, following H_2O_2 exposure, a spontaneous excitation wavefront emerging in NRVMs most distal to the interface (location 1) took 47 ms to reach NRVMs most proximal to the interface with ARVFs (location 7). **Figure 5D** right panel illustrates that subsequently as activation of the NRVM monolayer slow further to 88 ms, an EAD emerged near the interface (location 5), leading to non-uniform conduction block and non-reentrant arrhythmia, which reversed the course of impulse propagation away from the interface

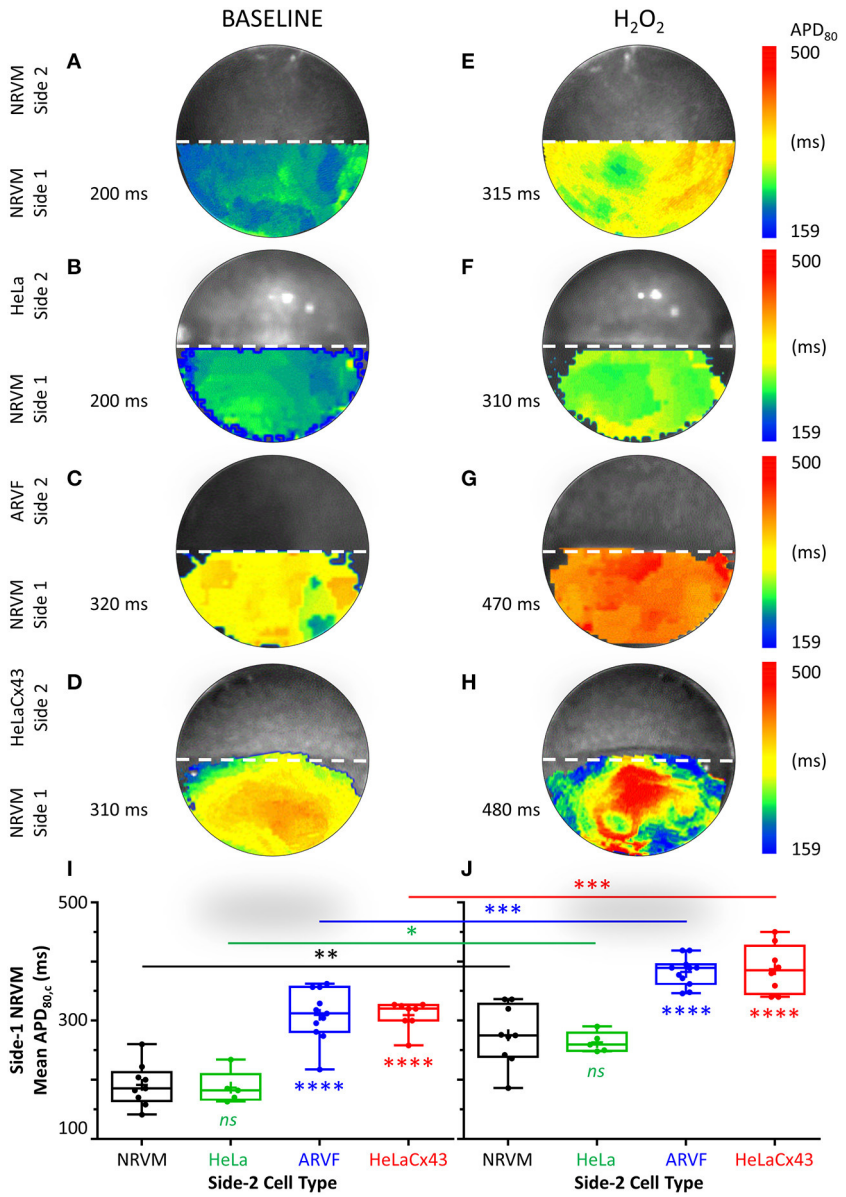

FIGURE 4 | $Cx43^+$ noncardiomyocytes and H_2O_2 prolonged APD by impairing NRVM repolarization. **(A–H)** Representative APD_{80} maps of side-1 NRVMs under baseline (left column) vs. H_2O_2 condition (right column) during a single excitation wavefront sweeping across side 1 of the monolayer. To ease intergroup and intercondition comparisons, all maps were constructed based on the longest APD_{80} range of 159–500 ms, which was that of the side-1 NRVM monolayer in co-culture with HeLaCx43 cells under H_2O_2 condition. The mean of the APD_{80} distribution was indicated next to the corresponding APD_{80} map. **(I,J)** Means of five APD_{80} measurements from five successive excitation wavefronts corrected for the spontaneous NRVM beating rate by Bazett formula under baseline vs. H_2O_2 condition. Note the independent and synergistic prolongation of mean $APD_{80,c}$ by $Cx43^+$ noncardiomyocytes and H_2O_2. Number of monolayers: NRVM-NRVM, $n = 9$; NRVM-HeLa, $n = 5$; NRVM-ARVF, $n = 11$; NRVM-HeLaCx43, $n = 8$. Symbols: box plots with mean (+), median, first and third quartiles (box), and minimum and maximum (whiskers). $^{ns}P > 0.05$, $^{*}P < 0.05$, $^{**}P < 0.01$, $^{***}P < 0.001$, $^{****}P < 0.0001$; one-way ANOVA with Tukey's *post-hoc* analysis for multiple-group comparisons under the same condition and the Wilcoxon signed rank test for two-condition comparisons of the same group. APD, action potential duration; NRVM, neonatal rat ventricular cardiomyocyte; ARVF, aged rat ventricular myofibroblast.

(from location 5 to 1). In another NRVM-ARVF co-culture exposed to H_2O_2 in **Figure 5E**, both ARVFs and H_2O_2 markedly slowed conduction and caused multiple shifting foci of activation, dynamic conduction block, and dispersion of refractoriness, thereby precipitating the dynamic emergence of a functional circuit of reentrant arrhythmia. In **Figure 5E** left panel, a major spontaneous excitation wavefront emerged left distally to the interface (location 1) and slowly reached the interface (location 4) after 65 ms via two general pathways, one proximal (1–2′-3′-4) and one distal to the interface (1–2–3–4). Note the

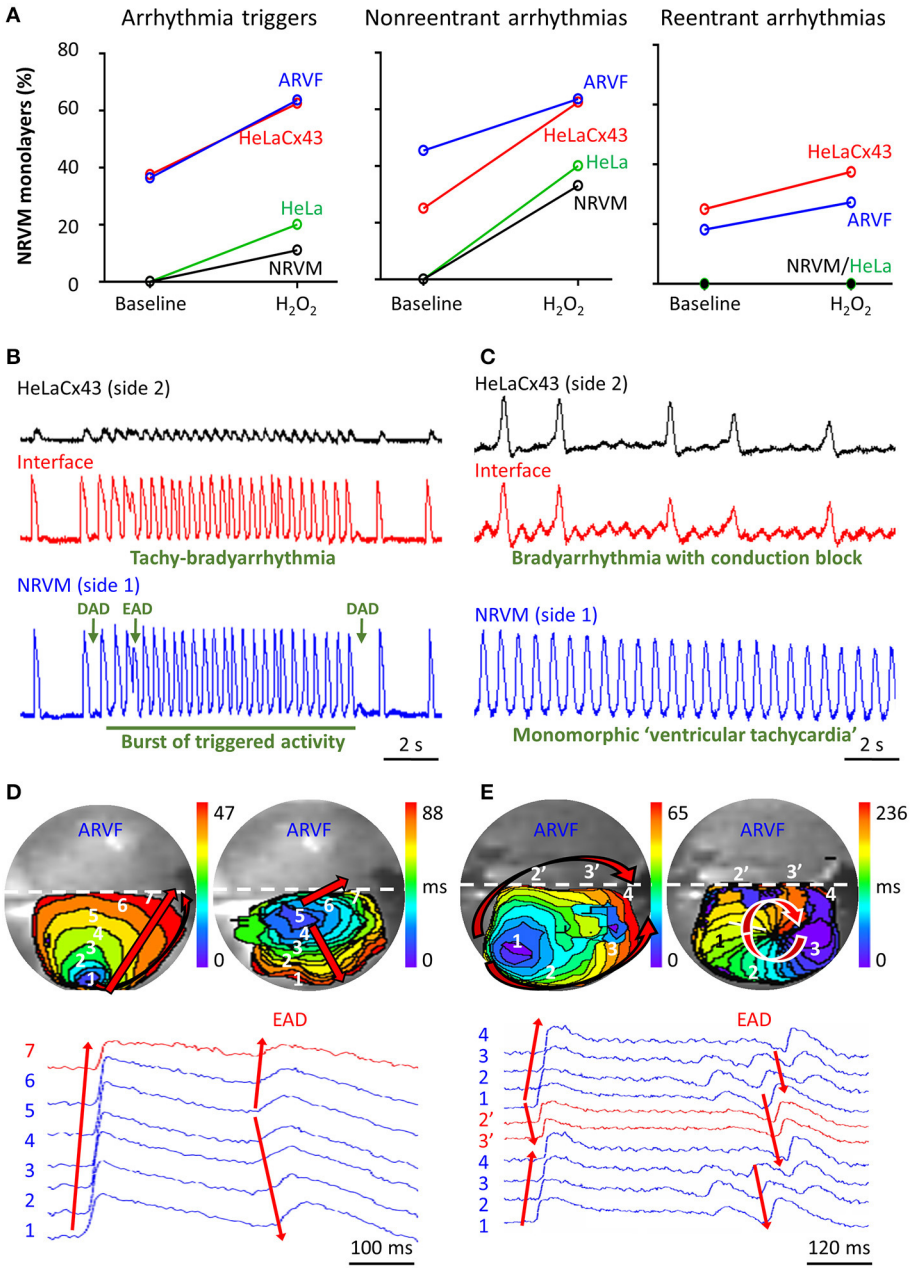

FIGURE 5 | $Cx43^+$ noncardiomyocytes and H_2O_2 were independently and synergistically arrhythmogenic. **(A)** $Cx43^+$ noncardiomyocytes and H_2O_2 independently and synergistically increased the likelihood of successful induction of new arrhythmia triggers, and non-reentrant and reentrant arrhythmias. Number of monolayers: NRVM-NRVM, $n = 9$; NRVM-HeLa, $n = 5$; NRVM-ARVF, $n = 11$; NRVM-HeLaCx43, $n = 8$. **(B,C)** Representative optical voltage tracings from two different monolayers illustrate how both HeLaCx43 cells and H_2O_2 successfully induced the emergence of new tachy-bradyarrhythmia mediated by arrhythmia triggers **(B)**, monomorphic "ventricular tachycardia," and bradyarrhythmia mediated by variable conduction block **(C)**. DAD/EAD, delayed/early afterdepolarization **(D,E)** NRVM activation maps (6-ms isochrones) and corresponding 2D wave displays from seven and six different locations within two different NRVM-ARVF monolayers exposed to H_2O_2. ARVFs and H_2O_2 synergistically induced the emergence of new EAD-mediated non-reentrant arrhythmia (5–4–3–2–1, D right panel) and a reentrant circuit (3–2–1–2′-3′-4, **E** right panel). NRVM, neonatal rat ventricular cardiomyocyte; ARVF, aged rat ventricular myofibroblast.

conduction block caused by an additional simultaneous minor focus of activation (a small purple isochrone) near location 3. In **Figure 5E** right panel, as activation of the NRVM monolayer slowed further to 236 ms, a new major focus of activation developed at location 3 (near the previously minor activation focus) and set the stage for a reentry circuit (3–2–1–2′-3′-4). The emergence of reentry indicates that the circuit path was longer than the impulse wavelength.

DISCUSSION

Dual Protective and Proarrhythmic Potentials of Myofibroblasts

During myocardial aging or wound healing, myofibroblasts secrete collagen and generate fibrosis. It is common knowledge that structural remodeling by fibrosis rescues myocardial mechanical stability but puts the heart at risk for lethal arrhythmias. Less commonly appreciated is how electrical remodeling by fibrosis accounts for its arrhythmogenicity. Here, we provided functional proof-of-concept for the underlying mechanisms. We demonstrated the dual adaptive and maladaptive contributions of myofibroblasts in rescuing impulse propagation yet impairing neighboring cardiomyocyte electrophysiology and rendering them more vulnerable to arrhythmias. Based on our findings, one may view myofibroblasts as "wannabe" cardiomyocytes, loaded with good intentions for structural and electrical remodeling but with imperfect means for successful risk-free execution.

For myofibroblasts in myocardial fibrosis, such as ARVFs, Cx43 was shown to play a critical role in their pathological differentiation from fibroblasts (Asazuma-Nakamura et al., 2009). It was well-established in the literature that myofibroblasts readily form functional gap junctions with cardiomyocytes *in vitro* (Jacquemet and Henriquez, 2008; Pedrotty et al., 2008; McCain et al., 2012; Nagaraju et al., 2019) and *in situ* (Driesen et al., 2005; He et al., 2011; Quinn et al., 2016). Once electrotonically coupled to cardiomyocytes, noncardiomyocytes can serve as sinks for electrotonic currents (Fast et al., 1996). Consistent with that observation, we found that, unlike Cx-deficient HeLa cells, myofibroblasts at the interface with NRVMs enabled 2D impulse conduction that would not have otherwise been possible. Thus, myofibroblasts can potentially rescue cardiac electrical activity by reconnecting electrically separate islands of surviving cardiomyocytes separated by collagen strands and dead cardiomyocytes. On the converse, we found that, unlike excitable NRVMs, non-excitable myofibroblasts at the interface with NRVMs impaired NRVM activation and repolarization. Thus, the cardiac electrical activity rescued by myofibroblasts was decremental, proarrhythmic, and maladaptive.

Our current work provides evidence supporting our hypothesis that arrhythmogenicity is not exclusive to myofibroblasts but pertains also to other $Cx43^+$ noncardiomyocyte types. HeLa cells are non-excitable cells that do not express Cx43 (Elfgang et al., 1995; Mesnil et al., 1995). By contrasting HeLa cells with HeLaCx43 cells, we demonstrated that Cx43 overexpression is necessary for non-excitable cells other than myofibroblasts to interface electrically with neighboring excitable cardiomyocytes and act as a capacitive load. This explains why in the normal heart, fibroblasts, which are Cx43-poor, hardly present any arrhythmogenic risk for neighboring cardiomyocytes. Cx43 expression is necessary for noncardiomyocytes not only to form heterotypic gap junction coupling (or nanotube coupling) with cardiomyocytes but also to form homotypic gap junction coupling among themselves for continued propagation of the depolarization wavefront across the noncardiomyocyte population to reach other neighboring viable cardiomyocytes downstream. The functional evidence in this study indicates that the limiting factor for passive electrical conduction was the heterogeneous heterotypic coupling strength along the interface rather than the homotypic coupling strength among HeLaCx43 cells. This observed difference in homotypic vs. heterotypic coupling strength is consistent with prior reports that homomeric–homotypic and homomeric–heterotypic channels differ markedly in their static and dynamic properties of transjunctional conductance and voltage, which dictate their different impulse-propagation capabilities and their respective symmetry vs. asymmetry of electrophysiological functions (Desplantez et al., 2004, 2007; Schulte et al., 2008). Another possible explanation for the difference in homotypic vs. heterotypic coupling strength is that homotypic coupling formation had 1-day advantage over heterotypic coupling formation (3 vs. 2 days, respectively; **Figure 1B**).

Our group and others (Zlochiver et al., 2008; Vasquez et al., 2010; Nguyen et al., 2012, 2015; Salvarani et al., 2017) previously demonstrated that myofibroblasts can be arrhythmogenic for neighboring cardiomyocytes. We show here that $Cx43^+$ non-excitable cells, including myofibroblasts, can impair cardiomyocyte activation and repolarization. This maladaptive role of myofibroblasts contributes to proarrhythmic electrical remodeling by fibrosis. Adult cardiomyocytes have hyperpolarized resting membrane potential ranging from −90 to −80 mV (Pinnell et al., 2007). NRVMs in monolayers have resting membrane potential ranging −80 to −70 mV as recorded by others (Chan et al., 2010) and our group (unpublished data). In contrast, myofibroblasts have depolarized (less negative) resting membrane potentials, widely ranging anywhere from −50 to −5 mV, depending on local microenvironments (Kiseleva et al., 1998; Kamkin et al., 2005). Like myofibroblasts, HeLaCx43 cells have depolarized resting membrane potentials, also widely ranging from −50 to −15 mV (Stein et al., 1996; Ando et al., 2009; Zhang et al., 2009; Hsu et al., 2010). By comparing co-cultures of cardiomyocytes with other cardiomyocytes vs. with $Cx43^+$ noncardiomyocytes, we found that a transjunctional cardiomyocyte–noncardiomyocyte gradient of resting membrane potentials is a sufficient condition for noncardiomyocytes to increase cardiomyocyte susceptibility to arrhythmias. This experimental finding validates our earlier prediction in a prior mathematical modeling study (Nguyen et al., 2012).

Dual Hits by Fibrosis and H_2O_2 for Arrhythmogenic Synergy

Here, simulating *in situ* fibrosis in the native heart, we found that *in vitro* interfaces between $Cx43^+$ noncardiomyocytes and cardiomyocytes created structural and functional heterogeneities, thereby exerting both passive and active arrhythmogenicity. Heterotypic interfaces lowered the protective source–sink mismatch (Xie et al., 2010; Nguyen et al., 2014) to create a vulnerable substrate (passive arrhythmogenicity). In addition, cardiomyocyte–noncardiomyocyte electrical crosstalk facilitates the initiation and maintenance of arrhythmias by promoting automaticity, causing dynamic functional conduction

block, slowing conduction, and prolonging APD (active arrhythmogenicity). We demonstrated that slow conduction by cardiomyocyte–noncardiomyocyte electrical crosstalk promotes the development of reentrant circuits within an area as small as 77 mm^2. Our finding is compatible with the dimension of the smallest microreentrant circuit of 50 mm^2 ever reported for the human heart (Spach et al., 1988). Since the impulse wavelength is the product of the conduction velocity and the refractory period, slow conduction reduces the wavelength. For reentry to succeed, the path length must exceed or at least equal the wavelength. Therefore, by reducing the wavelength, slow conduction reduces the minimal path length required for successful reentry (Antzelevitch and Burashnikov, 2011). This explains why a reentrant circuit can develop within such a small border zone area near the cardiomyocyte–noncardiomyocyte interface.

However, experimentally and clinically, not all fibrotic hearts develop arrhythmias until challenged by stress. For arrhythmia triggers to propagate and initiate arrhythmias, a second hit, such as H_2O_2-mediated oxidative stress as used in this study, is often required to lower the protective source–sink mismatch and repolarization reserve sufficiently. Xie et al. elegantly demonstrated the underlying cellular mechanisms of H_2O_2 arrhythmogenicity in single adult rabbit ventricular cardiomyocytes (Xie et al., 2009). The authors showed that successful induction of early afterdepolarizations by H_2O_2 relies on Ca^{2+}/calmodulin kinase II activation to impair inactivation of the Na^+ current (thereby reducing repolarization reserve) and to enhance the L-type Ca^{2+} current (thereby reversing repolarization). Following cardiac injury regardless of cause, oxidative stress contributes critically to pathological remodeling by fibrosis and the ensuing increased proarrhythmic risk at fibrotic border zones. Notably, increased oxidative stress to the heart may occur specifically post-infarction (Ide et al., 2001; Venditti et al., 2001; Carpi et al., 2009; Chi et al., 2017; Margaritis et al., 2017) and in heart failure (Nickel et al., 2015; Bertero and Maack, 2018b; Zhou and Tian, 2018). However, increased oxidative stress to the heart may also occur non-specifically in cardiac inflammation (Zhou et al., 2011), metabolic dysregulation (Nickel et al., 2015; Bertero and Maack, 2018a), and aging (Ander et al., 2007; Lisanti et al., 2011; Martín-Fernández and Gredilla, 2016). Oxidative stress causes the release of reactive oxygen species, such as H_2O_2. Importantly, H_2O_2 is also a well-recognized pathophysiological paracrine factor produced by activated myofibroblasts in the heart, the lungs (Waghray et al., 2005), and malignant tissues (Lisanti et al., 2011). Previously, we and other groups have tested higher (mM-range) experimental H_2O_2 concentrations (Nguyen et al., 2012, 2015; Wang et al., 2014). In this study, we chose the H_2O_2 concentration of 100 μM for its pathophysiological relevance (Wang et al., 2014). While low sustained H_2O_2 levels of 10–20 μM are routinely produced for baseline cellular signaling (Droge, 2002; Baek et al., 2012), H_2O_2 levels during an acute oxidative-stress burst can increase abruptly within 2–6 $\times$ 10^{-14} mol/h/cell to hundreds of μM (Granger, 1988; Droge, 2002; Rhee, 2006).

However, we found that the stressor needed as the second hit for arrhythmogenic synergy does not have to be H_2O_2 or oxidative stress. We have previously showed that angiotensin II-mediated oxidative stress or hypokalemic stress can also synergize with fibrosis to induce arrhythmias (Bapat et al., 2012; Nguyen et al., 2012; Pezhouman et al., 2015). Other groups have shown that other soluble myofibroblast paracrine factors, such as TGF-β1 (Salvarani et al., 2017) and those from infarcted hearts (Vasquez et al., 2010), can also promote cardiomyocyte–myofibroblast electrical crosstalk and further increased myofibroblast arrhythmogenicity. Our study excluded potential arrhythmogenic contribution by paracrine factors secreted by the cultured myofibroblasts. Instead, we demonstrated that HeLaCx43, which does not secrete myofibroblast paracrine factors at all, can be just as arrhythmogenic as myofibroblasts. Conversely, if HeLa cells secrete different paracrine factors, those factors are not arrhythmogenic by themselves because HeLa cells that do not overexpress Cx43 are not arrhythmogenic.

Experimental Caveats and Nuances

Several caveats and nuances of the experimental design of this functional study are worth mentioning. Here, we did not seek to reproduce well-established evidence of Cx43 detection at cardiomyocyte–noncardiomyocyte interfaces (Traub et al., 1994; Delorme et al., 1997; Gaudesius et al., 2003; Miragoli et al., 2006; He et al., 2011; Quinn et al., 2016). Instead of seeking indirect speculative structural evidence for heterotypic gap junction/nanotube presence, we provided functional evidence of their existence and, more importantly, their functional consequences.

We chose neonatal, instead of adult cardiomyocytes, as representative cardiomyocytes. While adult cardiomyocytes would offer higher clinical relevance, they unfortunately lose the ability to proliferate in culture to form monolayers. However, we have functional evidence that adult cardiomyocytes retain the ability to form functional heterotypic gap junctions with adult fibroblasts, not only of the same but also of different species, to allow bidirectional passage of macromolecules (**Supplementary Figure 3**), presumably including ions, which are necessary for bidirectional electrical crosstalk. Therefore, findings using NRVMs in monolayers can be judiciously extrapolated to adult cardiomyocytes in tissue or whole heart settings.

We chose myofibroblasts, instead of fibroblasts, as representative cardiac $Cx43^+$ noncardiomyocytes for two reasons: higher clinical relevance and stronger modulation of NRVM electrophysiology. In fact, we initially employed fibroblasts from young adult rat ventricular fibroblasts (YRVFs; 3–6 months of age) in our pilot studies but found negative results, like those with HeLa cells. This finding suggests that at least in our 2D model, while fibroblasts might form functional heterotypic gap junctions with NRVMs (as they did with adult cardiomyocytes shown in **Supplementary Figure 3**), the net NRVM-fibroblast gap junction current generated did not produce an appreciable arrhythmogenic "source" effect powerful enough to significantly modulate the electrophysiology of the neighboring large NRVM "sink."

Interestingly, the proarrhythmic electrical remodeling of NRVMs by YRVFs can be captured by a 1D model instead of a

2D model. In our 1D model, 12-mm-long, 1-mm-wide cultured NRVM strands were centrally interrupted by 200-μm-long, 1-mm-wide YRVF inserts (**Supplementary Figure 4**). YRVFs enabled impulse conduction over a 500-μm distance but markedly impaired NRVM depolarization and repolarization. Consequently, YRVFs slowed NRVM maximal upstroke velocity, delayed NRVM conduction, prolonged APD_{75} and APD_{90}, and perturbed impulse propagation. With the synergy from hypokalemic (2 mM) or isoproterenol (1 μM) stress, YRVFs induced early afterdepolarizations and conduction blocks. Our 1D findings are consistent with Gaudesius et al.'s findings in their 1D model of 10-mm-long, 80-μm-wide NRVM strands that centrally located 80-μm-long, 80-μm-wide NRVF inserts permitted impulse conduction over a 300-μm distance (Gaudesius et al., 2003). Interestingly, when HeLaCx43 replaced NRVFs in the inserts, HeLaCx43 cells could double the impulse propagating distance to 600 μm (Gaudesius et al., 2003). Reminiscent of Gaudesius et al.'s finding that HeLaCx43 cells were superior to neonatal fibroblasts in 1D impulse propagating distance, we found that HeLaCx43 cells were superior to ARVFs both in 2D impulse propagating distance (**Figure 2**) and in NRVM modulation impact, such as more severe NRVM activation delay and greater reduction of NRVM conduction velocity (**Figure 3**). Nevertheless, what are the underlying determinants? In a prior hybrid biological-computational study of cardiomyocyte–myofibroblast coupling, we identified four critical determinants of higher noncardiomyocyte potential for EAD induction: more depolarized noncardiomyocyte resting membrane potential (which translates to larger transjunctional voltage gradient), larger noncardiomyocyte membrane capacitance and conductance, and larger transjunctional conductance (Nguyen et al., 2012). It is likely that the same four critical factors also played a role to some extent in determining the superior potency of HeLaCx43 cells over ARVFs in certain NRVM proarrhythmic electrical remodeling aspects in our 2D model and over NRVFs in Gaudesius et al.'s 1D model.

Our findings of the contrasting positive vs. negative impacts of YRVFs on NRVM electrical remodeling in the respective 1D vs. 2D model support Xie et al.'s two insightful predictions regarding the importance of structural remodeling on electrophysiological remodeling (Xie et al., 2010). In this classic simulation study, the authors elegantly showed how the minimal numbers of contiguous susceptible cardiomyocytes required to overcome the protective source–sink mismatch for arrhythmia tissue propagation increase drastically as the tissue is scaled up from 1D to 2D and 3D and how all these numbers decrease drastically in the presence of tissue fibrosis. Thus, the presence of heterotypic gap junctions between cardiomyocytes and noncardiomyocytes, even when proven functional, is prognostically meaningless by itself unless properly interpreted in the context of structural remodeling (1D vs. 2D or 3D, absence or presence of fibrosis and local stressors, etc.).

Clinical Implications for Disease

While our results may have clinical relevance for post-infarction arrhythmogenesis, the clinical relevance of our findings likely extends broadly to arrhythmogenesis in hearts structurally remodeled by fibrosis in general, irrespective of fibrosis etiology. The clinical literature on the mechanisms of arrhythmogenesis at scar border zones in human structural heart disease regardless of cause has demonstrated that conduction of surviving cardiomyocytes at scar border zones is slow and that slow conduction promotes reentrant ventricular tachycardia (De Bakker et al., 1988, 1993; Van Dessel et al., 2001; Patterson et al., 2017). These clinical findings are compatible with two key findings in this study that NRVM conduction at interfaces with noncardiomyocytes is slow and slow conduction promotes reentry.

In a prior review (Nguyen et al., 2012), we discussed that not all myocardial fibrosis patterns are equally arrhythmogenic. Compact fibrosis, characterized by dense areas of collagen and myofibroblasts that are devoid of cardiomyocytes, has the least arrhythmogenicity. In contrast, patchy fibrosis and interstitial fibrosis, associated with border zones of an infarct or a scar in non-ischemic heart disease, have the most arrhythmogenicity. Here, our novel design of cardiomyocyte–noncardiomyocyte interface simulates a short (14-mm) linear scar border zone. The homotypic NRVM monolayer simulates healthy myocardium devoid of structural or electrical remodeling. The heterotypic NRVM-HeLa interface simulates myocardial structural remodeling to demonstrate its effect on passive proarrhythmic electrical remodeling by non-conducting noncardiomyocytes. The heterotypic NRVM-ARVF and NRVM-HeLaCx43 interfaces simulate myocardial structural remodeling to demonstrate its effect on active proarrhythmic electrical remodeling by conducting noncardiomyocytes. The addition of acute H_2O_2 exposure simulates how an acute oxidative-stress burst can amplify the combined arrhythmogenicity of structural and electrical remodeling in the fibrotic heart and explain why not all fibrotic hearts develop arrhythmias until challenged by adequate stress.

Our findings further suggest that the strength of gap junction coupling between cardiomyocytes and noncardiomyocytes, if present, is likely to be markedly heterogeneous. Heterogeneous gap junction coupling is an important aspect of tissue inhomogeneity. It was postulated that heterogeneous gap junction coupling contributes critically to ventricular arrhythmogenesis in patients with congestive heart failure (Boulaksil et al., 2011) and non-ischemic dilated cardiomyopathy (Kitamura et al., 2002).

Lastly, while our study concerns ventricular cardiomyocytes, the findings here may also account for the synergistic contribution of myofibroblasts and oxidative stress in the genesis and maintenance of atrial fibrillation in vulnerable fibrotic atrial substrates.

Clinical Implications for Therapeutics

Our findings may have clinical implications for therapeutics. Like myofibroblasts, exogenous stem cells and progenitor cells (introduced by reparative/regenerative cellular or tissue therapies) express Cx43 and have more depolarized resting membrane potentials than native cardiomyocytes. For example, human induced pluripotent stem cell-derived cardiomyocytes

(hiPSC-CMs) have flourished as a powerful tool for drug discovery, disease modeling (Chow et al., 2013; Rocchetti et al., 2017; Chai et al., 2018; Wong et al., 2020), and regenerative medicine (Rhee and Wu, 2018; Sadahiro, 2019; Huang et al., 2020). However, in contrast to adult cardiomyocytes that have stable and more negative resting membrane potential (around −85 mV), hiPSC-CMs do not achieve sufficiently negative membrane potential (−40 to −70 mV), presumably due to inadequate expression of inward rectifier current I_{K1} (Goversen et al., 2018; Horváth et al., 2018). Consequently, although hiPSC-CMs are excitable cardiomyocytes that can provide all-or-none impulse propagation support for endogenous cardiomyocytes, they may have no less arrhythmogenic potential than endogenous myofibroblasts.

Our findings have clinical implications for the engraftment process of cardiac regeneration and tissue engineering therapies. To increase the probability of successful electrical integration, exogenous stem cells and progenitor cells can be engineered prior to transplant to overexpress Cx43. To minimize the arrhythmogenic risk for recipient hearts, exogenous cells can be engineered to overexpress I_{K1} or other stabilizing currents that can hyperpolarize their resting membrane potential to match that of endogenous cardiomyocytes. The caveat is that the three factors—the gradient of resting membrane potentials between noncardiomyocytes and cardiomyocytes, the noncardiomyocyte resistive and capacitive loads, and the cardiomyocyte–noncardiomyocyte electrical coupling strength—all individually and collectively contribute to slowing cardiomyocyte conduction. Therefore, novel antiarrhythmic strategies may need to consider all these three factors to minimize the arrhythmogenic consequences of cell-based or tissue-based cardiac regeneration therapy.

Study Limitations

This *in vitro* functional proof-of-concept study has limitations. First, although the six precaution measures taken in developing our heterotypic interface model successfully prevented macroscopic invasion of side-1 NRVMs by side-2 noncardiomyocytes, we could not completely exclude microscopic seepage. However, microscopic invasion lacks clinical relevance because isolated single noncardiomyocytes could hardly cause significant impact on the much larger mass of neighboring well-coupled NRVM syncytium. Therefore, the heterotypic interface in our *in vitro* model should not be construed as absolute demarcation dividing cardiomyocytes and noncardiomyocytes. In fact, this design imperfection is superior at recapitulating clinical dynamic 4D cardiac fibrosis border zones, which are not absolute divides between fibrosis and surviving cardiomyocytes. Comparison with the NRVM-HeLa negative control further supports that the low extent of noncardiomyocyte seepage in our interface model made no significant electrophysiological contribution. Second, the interface in our current model was designed to simulate only one specific pattern of structural remodeling, a static 14-mm linear border zone. However, in clinical cardiomyopathies, infinite possibilities of scar border zone patterns exist. By nature, clinical myocardial fibrosis is permanent because it cannot regress in human and other mammalian hearts, which lack the capability to regenerate meaningfully. Yet clinical myocardial fibrosis patterns are transient because they evolve and expand dynamically with time in response to changing local environmental stress and new insults or injuries. This continued evolution of dynamic structural remodeling shapes and is shaped by dynamic electrical remodeling as these two interdependent remodeling processes beget further remodeling. Lastly, this study employed an *in vitro* approach, common to proof-of-concept mechanistic studies. Therefore, additional *ex vivo* 4D studies in intact hearts are necessary to establish relevance to native interfaces of endogenous cardiomyocytes with endogenous noncardiomyocytes (following heart disease, injury, or aging) or with exogenous cardiomyocytes (following cell or tissue transplantation in cardiac regeneration therapies).

DATA AVAILABILITY STATEMENT

The original contributions presented in the study are included in the article/**Supplementary Materials**, further inquiries can be directed to the corresponding author/s.

ETHICS STATEMENT

The animal study was reviewed and approved by UCLA Institutional Animal Care and Use Committee.

AUTHOR CONTRIBUTIONS

SI, MT, and NN performed the experiments. YZ, SI, MT, AL, and NN analyzed and interpreted the data and assisted with manuscript preparation. TN conceived the study, designed the experiments, interpreted the data, and prepared the manuscript. All authors contributed to manuscript revision, approved the submitted version, and agreed to be accountable for all aspects of the work.

FUNDING

This work was supported by the National Institutes of Health R01 HL141452 to TN.

ACKNOWLEDGMENTS

We thank Dr. Scott John for his generous expert technical assistance with the preparation of the genetically engineered HeLaCx43 cell line.

SUPPLEMENTARY MATERIAL

The Supplementary Material for this article can be found online at: https://www.frontiersin.org/articles/10.3389/fphys.2020.622613/full#supplementary-material

REFERENCES

Ander, B. P., Hurtado, C., Raposo, C. S., Maddaford, T. G., Deniset, J. F., Hryshko, L. V., et al. (2007). Differential sensitivities of the NCX1.1 and NCX1.3 isoforms of the Na^+-Ca^{2+} exchanger to alpha-linolenic acid. *Cardiovasc. Res.* 73, 395–403. doi: 10.1016/j.cardiores.2006.09.013

Ando, J., Smith, N. I., Fujita, K., and Kawata, S. (2009). Photogeneration of membrane potential hyperpolarization and depolarization in non-excitable cells. *Eur. Biophys. J.* 38, 255–262. doi: 10.1007/s00249-008-0397-6

Antzelevitch, C., and Burashnikov, A. (2011). Overview of basic mechanisms of cardiac arrhythmia. *Card. Electrophysiol. Clin.* 3, 23–45. doi: 10.1016/j.ccep.2010.10.012

Asazuma-Nakamura, Y., Dai, P., Harada, Y., Jiang, Y., Hamaoka, K., and Takamatsu, T. (2009). Cx43 contributes to TGF-beta signaling to regulate differentiation of cardiac fibroblasts into myofibroblasts. *Exp. Cell Res.* 315, 1190–1199. doi: 10.1016/j.yexcr.2008.12.021

Baek, J. Y., Han, S. H., Sung, S. H., Lee, H. E., Kim, Y. M., Noh, Y. H., et al. (2012). Sulfiredoxin protein is critical for redox balance and survival of cells exposed to low steady-state levels of H2O2. *J. Biol. Chem.* 287, 81–89. doi: 10.1074/jbc.M111.316711

Bapat, A., Nguyen, T. P., Lee, J. H., Sovari, A. A., Fishbein, M. C., Weiss, J. N., et al. (2012). Enhanced sensitivity of aged fibrotic hearts to angiotensin II- and hypokalemia-induced early afterdepolarization-mediated ventricular arrhythmias. *Am. J. Physiol. Heart Circ. Physiol.* 302, H2331–H2340. doi: 10.1152/ajpheart.00094.2012

Bertero, E., and Maack, C. (2018a). Calcium signaling and reactive oxygen species in mitochondria. *Circ. Res.* 122, 1460–1478. doi: 10.1161/CIRCRESAHA.118.310082

Bertero, E., and Maack, C. (2018b). Metabolic remodelling in heart failure. *Nat. Rev. Cardiol.* 15, 457–470. doi: 10.1038/s41569-018-0044-6

Boulaksil, M., Jungschleger, J. G., Antoons, G., Houtman, M. J., De Boer, T. P., Wilders, R., et al. (2011). Drug-induced torsade de pointes arrhythmias in the chronic AV block dog are perpetuated by focal activity. *Circ. Arrhythm. Electrophysiol.* 4, 566–576. doi: 10.1161/CIRCEP.110.958991

Carpi, A., Menabo, R., Kaludercic, N., Pelicci, P., Di Lisa, F., and Giorgio, M. (2009). The cardioprotective effects elicited by p66(Shc) ablation demonstrate the crucial role of mitochondrial ROS formation in ischemia/reperfusion injury. *Biochim. Biophys. Acta* 1787, 774–780. doi: 10.1016/j.bbabio.2009.04.001

Cartledge, J. E., Kane, C., Dias, P., Tesfom, M., Clarke, L., Mckee, B., et al. (2015). Functional crosstalk between cardiac fibroblasts and adult cardiomyocytes by soluble mediators. *Cardiovasc. Res.* 105, 260–270. doi: 10.1093/cvr/cvu264

Chai, S., Wan, X., Ramirez-Navarro, A., Tesar, P. J., Kaufman, E. S., Ficker, E., et al. (2018). Physiological genomics identifies genetic modifiers of long QT syndrome type 2 severity. *J. Clin. Invest.* 128, 1043–1056. doi: 10.1172/JCI94996

Chan, Y. C., Tse, H. F., Siu, C. W., Wang, K., and Li, R. A. (2010). Automaticity and conduction properties of bio-artificial pacemakers assessed in an *in vitro* monolayer model of neonatal rat ventricular myocytes. *Europace* 12, 1178–1187. doi: 10.1093/europace/euq120

Chi, R. F., Wang, J. P., Wang, K., Zhang, X. L., Zhang, Y. A., Kang, Y. M., et al. (2017). Progressive Reduction in Myocyte Autophagy After Myocardial Infarction in Rabbits: Association with oxidative stress and left ventricular remodeling. *Cell. Physiol. Biochem.* 44, 2439–2454. doi: 10.1159/000486167

Chow, M., Boheler, K. R., and Li, R. A. (2013). Human pluripotent stem cell-derived cardiomyocytes for heart regeneration, drug discovery and disease modeling: from the genetic, epigenetic, and tissue modeling perspectives. *Stem Cell Res. Ther.* 4:97. doi: 10.1186/scrt308

De Bakker, J. M., Van Capelle, F. J., Janse, M. J., Tasseron, S., Vermeulen, J. T., De Jonge, N., et al. (1993). Slow conduction in the infarcted human heart. 'Zigzag' course of activation. *Circulation* 88, 915–926. doi: 10.1161/01.CIR.88.3.915

De Bakker, J. M. T., Van Capelle, F. J. L., Janse, M. J., Wilde, A. A. M., Coronel, R., Becker, A. E., et al. (1988). Reentry as a cause of ventricular tachycardia in patients with chronic ischemic heart disease: electrophysiologic and anatomic correlation. *Circulation* 77, 589–606. doi: 10.1161/01.CIR.77.3.589

Delorme, B., Dahl, E., Jarry-Guichard, T., Briand, J. P., Willecke, K., Gros, D., et al. (1997). Expression pattern of connexin gene products at the early developmental stages of the mouse cardiovascular system. *Circ. Res.* 81, 423–437. doi: 10.1161/01.RES.81.3.423

Desplantez, T., Dupont, E., Severs, N. J., and Weingart, R. (2007). Gap junction channels and cardiac impulse propagation. *J. Membr. Biol.* 218, 13–28. doi: 10.1007/s00232-007-9046-8

Desplantez, T., Halliday, D., Dupont, E., and Weingart, R. (2004). Cardiac connexins Cx43 and Cx45: formation of diverse gap junction channels with diverse electrical properties. *Pflugers Arch.* 448, 363–375. doi: 10.1007/s00424-004-1250-0

Driesen, R. B., Dispersyn, G. D., Verheyen, F. K., Van Den Eijnde, S. M., Hofstra, L., Thoné, F., et al. (2005). Partial cell fusion: a newly recognized type of communication between dedifferentiating cardiomyocytes and fibroblasts. *Cardiovasc. Res.* 68, 37–46. doi: 10.1016/j.cardiores.2005.05.020

Droge, W. (2002). Free radicals in the physiological control of cell function. *Physiol. Rev.* 82, 47–95. doi: 10.1152/physrev.00018.2001

Elfgang, C., Eckert, R., Lichtenberg-Frate, H., Butterweck, A., Traub, O., Klein, R. A., et al. (1995). Specific permeability and selective formation of gap junction channels in connexin-transfected HeLa cells. *J. Cell Biol.* 129, 805–817. doi: 10.1083/jcb.129.3.805

Fast, V. G., Darrow, B. J., Saffitz, J. E., and Kléber, A. G. (1996). Anisotropic activation spread in heart cell monolayers assessed by high-resolution optical mapping. Role of tissue discontinuities. *Circ. Res.* 79, 115–127. doi: 10.1161/01.RES.79.1.115

Gaudesius, G., Miragoli, M., Thomas, S. P., and Rohr, S. (2003). Coupling of cardiac electrical activity over extended distances by fibroblasts of cardiac origin. *Circ. Res.* 93, 421–428. doi: 10.1161/01.RES.0000089258.40661.0C

Goversen, B., Van Der Heyden, M. A. G., Van Veen, T. A. B., and De Boer, T. P. (2018). The immature electrophysiological phenotype of iPSC-CMs still hampers *in vitro* drug screening: special focus on I(K1). *Pharmacol. Ther.* 183, 127–136. doi: 10.1016/j.pharmthera.2017.10.001

Granger, D. N. (1988). Role of xanthine oxidase and granulocytes in ischemia-reperfusion injury. *Am. J. Physiol.* 255, H1269–H1275. doi: 10.1152/ajpheart.1988.255.6.H1269

He, K., Shi, X., Zhang, X., Dang, S., Ma, X., Liu, F., et al. (2011). Long-distance intercellular connectivity between cardiomyocytes and cardiofibroblasts mediated by membrane nanotubes. *Cardiovasc. Res.* 92, 39–47. doi: 10.1093/cvr/cvr189

Horváth, A., Lemoine, M. D., Löser, A., Mannhardt, I., Flenner, F., Uzun, A. U., et al. (2018). Low resting membrane potential and low inward rectifier potassium currents are not inherent features of hiPSC-derived cardiomyocytes. *Stem Cell Rep.* 10, 822–833. doi: 10.1016/j.stemcr.2018.01.012

Hsu, K., Han, J., Shinlapawittayatorn, K., Deschenes, I., and Marban, E. (2010). Membrane potential depolarization as a triggering mechanism for Vpu-mediated HIV-1 release. *Biophys. J.* 99, 1718–1725. doi: 10.1016/j.bpj.2010.07.027

Huang, C. Y., Peres Moreno Maia-Joca, R., Ong, C. S., Wilson, I., Disilvestre, D., Tomaselli, G. F., et al. (2020). Enhancement of human iPSC-derived cardiomyocyte maturation by chemical conditioning in a 3D environment. *J. Mol. Cell. Cardiol.* 138, 1–11. doi: 10.1016/j.yjmcc.2019.10.001

Ide, T., Tsutsui, H., Hayashidani, S., Kang, D., Suematsu, N., Nakamura, K., et al. (2001). Mitochondrial DNA damage and dysfunction associated with oxidative stress in failing hearts after myocardial infarction. *Circ. Res.* 88, 529–535. doi: 10.1161/01.RES.88.5.529

Jacquemet, V., and Henriquez, C. S. (2008). Loading effect of fibroblast-myocyte coupling on resting potential, impulse propagation, and repolarization: insights from a microstructure model. *Am. J. Physiol. Heart Circ. Physiol.* 294, H2040–H2052. doi: 10.1152/ajpheart.01298.2007

Kamkin, A., Kiseleva, I., Lozinsky, I., and Scholz, H. (2005). Electrical interaction of mechanosensitive fibroblasts and myocytes in the heart. *Basic Res. Cardiol.* 100, 337–345. doi: 10.1007/s00395-005-0529-4

Katwa, L. C. (2003). Cardiac myofibroblasts isolated from the site of myocardial infarction express endothelin *de novo*. *Am. J. Physiol. Heart Circ. Physiol.* 285, H1132–H1139. doi: 10.1152/ajpheart.01141.2002

Kiseleva, I., Kamkin, A., Pylaev, A., Kondratjev, D., Leiterer, K. P., Theres, H., et al. (1998). Electrophysiological properties of mechanosensitive atrial fibroblasts from chronic infarcted rat heart. *J. Mol. Cell. Cardiol.* 30, 1083–1093. doi: 10.1006/jmcc.1998.0673

Kitamura, H., Ohnishi, Y., Yoshida, A., Okajima, K., Azumi, H., Ishida, A., et al. (2002). Heterogeneous loss of connexin43 protein in nonischemic dilated

cardiomyopathy with ventricular tachycardia. *J. Cardiovasc. Electrophysiol.* 13, 865–870. doi: 10.1046/j.1540-8167.2002.00865.x

Kucera, J. P., Kleber, A. G., and Rohr, S. (1998). Slow conduction in cardiac tissue, II: effects of branching tissue geometry. *Circ. Res.* 83, 795–805. doi: 10.1161/01.RES.83.8.795

Lisanti, M. P., Martinez-Outschoorn, U. E., Lin, Z., Pavlides, S., Whitaker-Menezes, D., Pestell, R. G., et al. (2011). Hydrogen peroxide fuels aging, inflammation, cancer metabolism and metastasis: the seed and soil also needs "fertilizer". *Cell Cycle* 10, 2440–2449. doi: 10.4161/cc.10.15.16870

Mahoney, V. M., Mezzano, V., Mirams, G. R., Maass, K., Li, Z., Cerrone, M., et al. (2016). Connexin43 contributes to electrotonic conduction across scar tissue in the intact heart. *Sci. Rep.* 6:26744. doi: 10.1038/srep26744

Margaritis, M., Sanna, F., Lazaros, G., Akoumianakis, I., Patel, S., Antonopoulos, A. S., et al. (2017). Predictive value of telomere length on outcome following acute myocardial infarction: evidence for contrasting effects of vascular vs. blood oxidative stress. *Eur. Heart J.* 38, 3094–3104. doi: 10.1093/eurheartj/ehx177

Martín-Fernández, B., and Gredilla, R. (2016). Mitochondria and oxidative stress in heart aging. *Age* 38, 225–238. doi: 10.1007/s11357-016-9933-y

McCain, M. L., Desplantez, T., Geisse, N. A., Rothen-Rutishauser, B., Oberer, H., Parker, K. K., et al. (2012). Cell-to-cell coupling in engineered pairs of rat ventricular cardiomyocytes: relation between Cx43 immunofluorescence and intercellular electrical conductance. *Am. J. Physiol. Heart Circ. Physiol.* 302, H443–H450. doi: 10.1152/ajpheart.01218.2010

Melzer, M., Beier, D., Young, P. P., and Saraswati, S. (2020). Isolation and characterization of adult cardiac fibroblasts and myofibroblasts. *J. Vis. Exp*, 157. doi: 10.3791/60909

Mesnil, M., Krutovskikh, V., Piccoli, C., Elfgang, C., Traub, O., Willecke, K., et al. (1995). Negative growth control of HeLa cells by connexin genes: connexin species specificity. *Cancer Res.* 55, 629–639.

Miragoli, M., Gaudesius, G., and Rohr, S. (2006). Electrotonic modulation of cardiac impulse conduction by myofibroblasts. *Circ. Res.* 98, 801–810. doi: 10.1161/01.RES.0000214537.44195.a3

Nagaraju, C. K., Dries, E., Gilbert, G., Abdesselem, M., Wang, N., Amoni, M., et al. (2019). Myofibroblast modulation of cardiac myocyte structure and function. *Sci. Rep.* 9:8879. doi: 10.1038/s41598-019-45078-2

Nguyen, T. P., Qu, Z., and Weiss, J. N. (2014). Cardiac fibrosis and arrhythmogenesis: the road to repair is paved with perils. *J. Mol. Cell. Cardiol.* 70, 83–91. doi: 10.1016/j.yjmcc.2013.10.018

Nguyen, T. P., Singh, N., Xie, Y., Qu, Z., and Weiss, J. N. (2015). Repolarization reserve evolves dynamically during the cardiac action potential: effects of transient outward currents on early afterdepolarizations. *Circ. Arrhythm. Electrophysiol.* 8, 694–702. doi: 10.1161/CIRCEP.114.002451

Nguyen, T. P., Sovari, A. A., Pezhouman, A., Iyer, S., Cao, H., Ko, C. Y., et al. (2016). Increased susceptibility of spontaneously hypertensive rats to ventricular tachyarrhythmias in early hypertension. *J. Physiol.* 594, 1689–1707. doi: 10.1113/JP271318

Nguyen, T. P., Xie, Y., Garfinkel, A., Qu, Z., and Weiss, J. N. (2012). Arrhythmogenic consequences of myofibroblast-myocyte coupling. *Cardiovasc Res.* 93, 242–251. doi: 10.1093/cvr/cvr292

Nickel, A. G., Von Hardenberg, A., Hohl, M., Löffler, J. R., Kohlhaas, M., Becker, J., et al. (2015). Reversal of mitochondrial transhydrogenase causes oxidative stress in heart failure. *Cell Metab.* 22, 472–484. doi: 10.1016/j.cmet.2015.07.008

Palacios-Prado, N., and Bukauskas, F. F. (2009). Heterotypic gap junction channels as voltage-sensitive valves for intercellular signaling. *Proc. Natl. Acad. Sci. U.S.A.* 106, 14855–14860. doi: 10.1073/pnas.0901923106

Patterson, E., Scherlag, B. J., Berbari, E. J., and Lazzara, R. (2017). Slow conduction through an arc of block: a basis for arrhythmia formation postmyocardial infarction. *J. Cardiovasc. Electrophysiol.* 28, 1203–1212. doi: 10.1111/jce.13300

Pedrotty, D. M., Klinger, R. Y., Badie, N., Hinds, S., Kardashian, A., and Bursac, N. (2008). Structural coupling of cardiomyocytes and noncardiomyocytes: quantitative comparisons using a novel micropatterned cell pair assay. *Am. J. Physiol. Heart Circ. Physiol.* 295, H390–H400. doi: 10.1152/ajpheart.91531.2007

Pedrotty, D. M., Klinger, R. Y., Kirkton, R. D., and Bursac, N. (2009). Cardiac fibroblast paracrine factors alter impulse conduction and ion channel expression of neonatal rat cardiomyocytes. *Cardiovasc. Res.* 83, 688–697. doi: 10.1093/cvr/cvp164

Pezhouman, A., Singh, N., Song, Z., Nivala, M., Eskandari, A., Cao, H., et al. (2015). Molecular basis of hypokalemia-induced ventricular fibrillation. *Circulation* 132, 1528–1537. doi: 10.1161/CIRCULATIONAHA.115.016217

Pinnell, J., Turner, S., and Howell, S. (2007). Cardiac muscle physiology. *Continu. Educ. Anaesth. Crit. Care Pain* 7, 85–88. doi: 10.1093/bjaceaccp/mkm013

Quinn, T. A., Camelliti, P., Rog-Zielinska, E. A., Siedlecka, U., Poggioli, T., O'Toole, E. T., et al. (2016). Electrotonic coupling of excitable and nonexcitable cells in the heart revealed by optogenetics. *Proc. Natl. Acad. Sci. U.S.A.* 113, 14852–14857. doi: 10.1073/pnas.1611184114

Rhee, J. W., and Wu, J. C. (2018). Cardiac cell cycle activation as a strategy to improve iPSC-derived cardiomyocyte therapy. *Circ. Res.* 122, 14–16. doi: 10.1161/CIRCRESAHA.117.312287

Rhee, S. G. (2006). Cell signaling. H_2O_2, a necessary evil for cell signaling. *Science* 312, 1882–1883. doi: 10.1126/science.1130481

Ribeiro-Rodrigues, T. M., Martins-Marques, T., Morel, S., Kwak, B. R., and Girão, H. (2017). Role of connexin 43 in different forms of intercellular communication - gap junctions, extracellular vesicles and tunnelling nanotubes. *J. Cell Sci.* 130, 3619–3630. doi: 10.1242/jcs.200667

Rocchetti, M., Sala, L., Dreizehnter, L., Crotti, L., Sinnecker, D., Mura, M., et al. (2017). Elucidating arrhythmogenic mechanisms of long-QT syndrome CALM1-F142L mutation in patient-specific induced pluripotent stem cell-derived cardiomyocytes. *Cardiovasc. Res.* 113, 531–541. doi: 10.1093/cvr/cvx006

Rubart, M., Tao, W., Lu, X. L., Conway, S. J., Reuter, S. P., Lin, S. F., et al. (2018). Electrical coupling between ventricular myocytes and myofibroblasts in the infarcted mouse heart. *Cardiovasc. Res.* 114, 389–400. doi: 10.1093/cvr/cvx163

Sadahiro, T. (2019). Cardiac regeneration with pluripotent stem cell-derived cardiomyocytes and direct cardiac reprogramming. *Regen. Ther.* 11, 95–100. doi: 10.1016/j.reth.2019.06.004

Salvarani, N., Maguy, A., De Simone, S. A., Miragoli, M., Jousset, F., and Rohr, S. (2017). TGF-beta1 (Transforming Growth Factor-beta1) plays a pivotal role in cardiac myofibroblast arrhythmogenicity. *Circ. Arrhythm. Electrophysiol.* 10:e004567. doi: 10.1161/CIRCEP.116.004567

Schulte, J. S., Scheffler, A., Rojas-Gomez, D., Mohr, F. W., and Dhein, S. (2008). Neonatal rat cardiomyocytes show characteristics of nonhomotypic gap junction channels. *Cell Commun. Adhes.* 15, 13–25. doi: 10.1080/15419060802014404

Spach, M. S., Dolber, P. C., and Heidlage, J. F. (1988). Influence of the passive anisotropic properties on directional differences in propagation following modification of the sodium conductance in human atrial muscle. A model of reentry based on anisotropic discontinuous propagation. *Circ. Res.* 62, 811–832. doi: 10.1161/01.RES.62.4.811

Stein, M. A., Mathers, D. A., Yan, H., Baimbridge, K. G., and Finlay, B. B. (1996). Enteropathogenic *Escherichia coli* markedly decreases the resting membrane potential of Caco-2 and HeLa human epithelial cells. *Infect. Immun.* 64, 4820–4825. doi: 10.1128/IAI.64.11.4820-4825.1996

Traub, O., Eckert, R., Lichtenberg-Fraté, H., Elfgang, C., Bastide, B., Scheidtmann, K. H., et al. (1994). Immunochemical and electrophysiological characterization of murine connexin40 and−43 in mouse tissues and transfected human cells. *Eur. J. Cell Biol.* 64, 101–112.

Valderrábano, M. (2007). Influence of anisotropic conduction properties in the propagation of the cardiac action potential. *Prog. Biophys. Mol. Biol.* 94, 144–168. doi: 10.1016/j.pbiomolbio.2007.03.014

Van Dessel, P. F., De Bakker, J. M., Van Hemel, N. M., Linnenbank, A. C., Jessurun, E. R., and Defauw, J. A. (2001). Pace mapping of postinfarction scar to detect ventricular tachycardia exit sites and zones of slow conduction. *J. Cardiovasc. Electrophysiol.* 12, 662–670. doi: 10.1046/j.1540-8167.2001.00662.x

Vasquez, C., Mohandas, P., Louie, K. L., Benamer, N., Bapat, A. C., and Morley, G. E. (2010). Enhanced fibroblast-myocyte interactions in response to cardiac injury. *Circ. Res.* 107, 1011–1020. doi: 10.1161/CIRCRESAHA.110.227421

Venditti, P., Masullo, P., and Di Meo, S. (2001). Effects of myocardial ischemia and reperfusion on mitochondrial function and susceptibility to oxidative stress. *Cell. Mol. Life Sci.* 58, 1528–1537. doi: 10.1007/PL00000793

Vliegen, H. W., Van Der Laarse, A., Cornelisse, C. J., and Eulderink, F. (1991). Myocardial changes in pressure overload-induced left ventricular hypertrophy. A study on tissue composition, polyploidization and multinucleation. *Eur. Heart J.* 12, 488–494. doi: 10.1093/oxfordjournals.eurheartj.a059928

Waghray, M., Cui, Z., Horowitz, J. C., Subramanian, I. M., Martinez, F. J., Toews, G. B., et al. (2005). Hydrogen peroxide is a diffusible paracrine signal for the induction of epithelial cell death by activated myofibroblasts. *FASEB J.* 19, 854–856. doi: 10.1096/fj.04-2882fje

Wang, Z. H., Liu, J. L., Wu, L., Yu, Z., and Yang, H. T. (2014). Concentration-dependent wrestling between detrimental and protective effects of H_2O_2 during myocardial ischemia/reperfusion. *Cell Death Dis.* 5:e1297. doi: 10.1038/cddis.2014.267

Wong, A. O., Wong, N., Geng, L., Chow, M. Z., Lee, E. K., Wu, H., et al. (2020). Combinatorial treatment of human cardiac engineered tissues with biomimetic cues induces functional maturation as revealed by optical mapping of action potentials and calcium transients. *Front. Physiol.* 11:165. doi: 10.3389/fphys.2020.00165

Xie, L. H., Chen, F., Karagueuzian, H. S., and Weiss, J. N. (2009). Oxidative-stress-induced afterdepolarizations and calmodulin kinase II signaling. *Circ. Res.* 104, 79–86. doi: 10.1161/CIRCRESAHA.108.183475

Xie, Y., Sato, D., Garfinkel, A., Qu, Z., and Weiss, J. N. (2010). So little source, so much sink: requirements for afterdepolarizations to propagate in tissue. *Biophys. J.* 99, 1408–1415. doi: 10.1016/j.bpj.2010.06.042

Zhang, X., Jin, Y., Plummer, M. R., Pooyan, S., Gunaseelan, S., and Sinko, P. J. (2009). Endocytosis and membrane potential are required for HeLa cell uptake of R.I.-CKTat9, a retro-inverso Tat cell penetrating peptide. *Mol. Pharm.* 6, 836–848. doi: 10.1021/mp800121f

Zhao, Y., James, N. A., Beshay, A. R., Chang, E. E., Lin, A., Bashar, F., et al. (2020). Adult zebrafish ventricular electrical gradients as tissue mechanisms of ECG patterns under baseline vs. oxidative stress. *Cardiovasc. Res.* doi: 10.1093/cvr/cvaa238. [Epub ahead of print].

Zhou, B., and Tian, R. (2018). Mitochondrial dysfunction in pathophysiology of heart failure. *J. Clin. Invest.* 128, 3716–3726. doi: 10.1172/JCI120849

Zhou, R., Yazdi, A. S., Menu, P., and Tschopp, J. (2011). A role for mitochondria in NLRP3 inflammasome activation. *Nature* 469, 221–225. doi: 10.1038/nature09663

Zhou, Y., Richards, A. M., and Wang, P. (2017). Characterization and standardization of cultured cardiac fibroblasts for *ex vivo* models of heart fibrosis and heart ischemia. *Tissue Eng. Part C Methods* 23, 422–433. doi: 10.1089/ten.tec.2017.0169

Zlochiver, S., Munoz, V., Vikstrom, K. L., Taffet, S. M., Berenfeld, O., and Jalife, J. (2008). Electrotonic myofibroblast-to-myocyte coupling increases propensity to reentrant arrhythmias in two-dimensional cardiac monolayers. *Biophys. J.* 95, 4469–4480. doi: 10.1529/biophysj.108.136473

Conflict of Interest: The authors declare that the research was conducted in the absence of any commercial or financial relationships that could be construed as a potential conflict of interest.

Advantages of publishing in Frontiers

OPEN ACCESS
Articles are free to read for greatest visibility and readership

FAST PUBLICATION
Around 90 days from submission to decision

HIGH QUALITY PEER-REVIEW
Rigorous, collaborative, and constructive peer-review

TRANSPARENT PEER-REVIEW
Editors and reviewers acknowledged by name on published articles

Frontiers
Avenue du Tribunal-Fédéral 34
1005 Lausanne | Switzerland

Visit us: www.frontiersin.org
Contact us: frontiersin.org/about/contact

REPRODUCIBILITY OF RESEARCH
Support open data and methods to enhance research reproducibility

DIGITAL PUBLISHING
Articles designed for optimal readership across devices

FOLLOW US
@frontiersin

IMPACT METRICS
Advanced article metrics track visibility across digital media

EXTENSIVE PROMOTION
Marketing and promotion of impactful research

LOOP RESEARCH NETWORK
Our network increases your article's readership